



HAL
open science

Fabrication of semipolar GaN-based μ LEDs on SOI substrates

Beatrice Wannous

► **To cite this version:**

Beatrice Wannous. Fabrication of semipolar GaN-based μ LEDs on SOI substrates. Micro and nanotechnologies/Microelectronics. Université Grenoble Alpes [2020-..], 2023. English. NNT : 2023GRALT092 . tel-04541757

HAL Id: tel-04541757

<https://theses.hal.science/tel-04541757>

Submitted on 11 Apr 2024

HAL is a multi-disciplinary open access archive for the deposit and dissemination of scientific research documents, whether they are published or not. The documents may come from teaching and research institutions in France or abroad, or from public or private research centers.

L'archive ouverte pluridisciplinaire **HAL**, est destinée au dépôt et à la diffusion de documents scientifiques de niveau recherche, publiés ou non, émanant des établissements d'enseignement et de recherche français ou étrangers, des laboratoires publics ou privés.

THÈSE

Pour obtenir le grade de

DOCTEUR DE L'UNIVERSITÉ GRENOBLE ALPES

École doctorale : EEATS - Electronique, Electrotechnique, Automatique, Traitement du Signal (EEATS)

Spécialité : Nano électronique et Nano technologies

Unité de recherche : Laboratoire d'Electronique et de Technologie de l'Information (LETI)

Fabrication de μ LEDs à base de GaN semi-polaire sur des substrats SOI

Fabrication of semipolar GaN-based μ LEDs on SOI substrates

Présentée par :

Beatrice WANNOUS

Direction de thèse :

François TEMPLIER
Directeur de Recherche, CEA
Fabian ROL
ingénieur de recherche, CEA
Pierre-Marie COULON
Ingénieur de recherche, CRHEA

Directeur de thèse
Co-encadrant de thèse
Co-encadrant de thèse

Rapporteurs :

Maria TCHERNYCHEVA
DIRECTRICE DE RECHERCHE, CNRS DELEGATION ILE-DE-FRANCE SUD
Genevieve CHADEYRON
PROFESSEURE DES UNIVERSITES, SIGMA CLERMONT FERRAND

Thèse soutenue publiquement le **12 décembre 2023**, devant le jury composé de :

François TEMPLIER DIRECTEUR DE RECHERCHE, CEA CENTRE DE GRENOBLE	Directeur de thèse
Maria TCHERNYCHEVA DIRECTRICE DE RECHERCHE, CNRS DELEGATION ILE-DE-FRANCE SUD	Présidente
Genevieve CHADEYRON PROFESSEURE DES UNIVERSITES, SIGMA CLERMONT FERRAND	Rapporteure
Norbert FRUEHAUF FULL PROFESSOR, Universität Stuttgart	Examineur
Christophe DURAND MAITRE DE CONFERENCES HDR, Université Grenoble Alpes	Examineur

Invités :

Christophe Figuet
INGENIEUR DOCTEUR, Soitec



Acknowledgments

To avoid listing endless names, I'll keep things general since I've already thanked those directly involved in person.

First off, a big thanks to my director and supervisors, both those who stayed and those who moved on during my PhD. Your guidance, support, trust, patience, and knowledge meant everything to me. It was truly an honor to work with each of you.

I also want to thank the researchers who contributed to the results of this thesis, whether by conducting experiments or helping with the analysis.

I can't imagine this thesis turning out the same without my office mates, cleanroom colleagues, and friends at CRHEA and CEA. The good times we've shared over the past three years made the work feel easier and more enjoyable.

And of course, I owe immense gratitude to my entire family for their unwavering support from day one. And last but definitely not least, a huge thank you to Elias, who helped me through it all and handled my breakdowns smoothly 😊

With Love!

Introduction

In the early 1900s, the concept of spontaneous emission was introduced, which is known to occur when an electron de-excites from a high-energy state to a lower one by emitting a photon. This principle applied to semiconductors allowed researchers to develop practical light-emitting diodes (LEDs) in 1962 when Nick Holonyak [1] from General Electric obtained the first visible LED emitting red light. Following this breakthrough, researchers continued to develop this technology by reaching a wider range of colors. In 1994, the Nichia team led by Shuji Nakamura obtained the first high-brightness blue LED when they used gallium nitride (GaN) as a semiconductor material. This invention enabled the completion of the visible emission spectrum, which then made it possible to obtain white light by combining the blue LED with yellow phosphor, achieving external efficiencies of over 70%. Shuji Nakamura, Hiroshi Amano, and Isamu Akasaki were the three pioneers awarded the 2014 Nobel Prize for their contribution to the Blue LED invention.[2]–[4] In the early 2000s, these white LEDs started to be commercially available and replaced traditional lighting sources, such as incandescent light bulbs, due to their better efficiency, longer lifetime, and lower heat generation. LED technology is constantly evolving, and more innovative applications are being developed, such as automotive lighting, general lighting, displays, and water purification.

During the same years, liquid crystal displays (LCDs) progressed enough to become the dominant technology in large displays, replacing cathode ray tubes (CRTs). Despite their dominance, LCDs require a backlight unit because they are non-emissive, which limits their size flexibility. Therefore, the development of organic LEDs (OLEDs) has emerged and started to compete with LCDs in many display applications. However, both technologies presented advantages and disadvantages. For instance, LCDs offer lower cost, better lifespan, and higher brightness, while OLEDs are self-emissive, have better contrast, and are more flexible in size. Both technologies are being improved to overcome their disadvantages.

Lately, researchers have started to direct their attention to micro-LEDs (μ LEDs), which are considered the next-generation displays. μ LED displays are made up of miniature LEDs, smaller than 50 micrometers in diameter and down to $1\mu\text{m}$. [5] These LEDs are arranged in any pattern to create a display. Despite being in their early stages of development, μ LEDs have proven to be compact, reliable, and capable of high pixel density, high brightness, and high contrast ratio. [6]

In fact, there is an increased demand for various applications, such as augmented reality, smartphones, smartwatches, and TVs, that can benefit from these μ LEDs due to their advantages over LCDs and OLEDs. In the early 2000s, researchers demonstrated a display of $12\mu\text{m}$ InGaN μ LEDs. Since then, many laboratory teams and companies, such as Apple, Google, Sony, and Samsung, have worked on developing this technology. For instance, Samsung has demonstrated a 146-inch microLED TV and Sony has created a flat panel microLED display up to 21 meters by 5.5 meters. [7]

Interestingly, from a theoretical point of view, μ LEDs were expected to have higher efficiency and better energy consumption than LCDs and OLEDs. However, this has not yet been achieved due to the high density of defects at the edges of the etched μ LEDs, which causes non-radiative recombination of carriers. The higher the perimeter-to-surface ratio, the less efficient the μ LED is.

It has been around 20 years now that InGaN/GaN quantum wells (QWs) based LEDs have been used in the field of lighting. With their continuous development over the years, they reached a level of maturity that enabled them to be used in μ LEDs for display applications. However, there are still

several challenges to fabricating the three primary colors (red, green, and blue (RGB)) required to obtain white light emission. Besides the decrease of the μ LED size, an efficiency loss is observed when trying to reach higher wavelength emission. Even on large-size LEDs, the external quantum efficiency decreases from 80% in the blue to nearly 50% when reaching the green color[8], [9]. On the other hand, the efficiency in the red hardly exceeds 10% [10] because higher Indium content is needed in the QWs to reach the red, thus more defects will be generated due to the lattice mismatch between InN and GaN. Although better efficiency in the red is achieved when using AlGaInP/GaInP-based large LEDs[11], the aim is to fabricate RGB pixels on the same semiconductor to facilitate the mass transfer.

Researchers have been trying several approaches while implementing InGaN/GaN quantum wells (QWs) to reach longer wavelengths without degrading the quality of the micro-LEDs (μ LEDs). One of these approaches is the use of different GaN crystallographic orientations. The most mature and most commonly used orientation is known as the polar one, which is also responsible for the aforementioned device's performance limitation. Therefore, in this Ph.D., we will be using $(10\bar{1}1)$ semipolar GaN, which can offer several advantages over the polar GaN to improve the performance of μ LEDs for display and μ display applications.

First, semipolar orientation has a reduced internal electric field within its QWs, which results in faster electron-hole recombination. This should yield a reduction of the efficiency loss at high current density, compared to polar orientations. Even at low current density, the fast recombination will limit the carriers from recombining non-radiatively on the edges of the μ LEDs, thus improving the efficiency. Additionally, the $(10\bar{1}1)$ semipolar orientation has proven to be able to incorporate the highest indium concentration, hence achieving longer wavelength emission.

All the aforementioned advantages that can accompany the implementation of the semipolar orientation address fields of interest such as displays and μ LED-based communication applications. However, from an industrial point of view, semipolar GaN is either grown on sapphire or on silicon substrates, which results in a high defect density due to the growth on foreign substrates. Several studies have been conducted to reach high-quality material while maintaining a low cost. For the same crystallographic orientation, Mantach *et al.* were able to reach the lowest defect density when using an aspect-ratio-trapping technique on a silicon-on-insulator (SOI) substrate to grow semipolar GaN.

In this context, this work aims to fabricate $(10\bar{1}1)$ semipolar GaN-based μ LEDs on SOI substrates following the approach adopted by Mantach *et al.* [12].

This thesis is organized into five chapters described as follows:

Chapter I: the first chapter provides an overview of the essential physical concepts that are relevant to this thesis and highlights the key principles that support this work.

Chapter II: the second chapter describes the development and optimization of SOI substrate patterning in the PFP cleanroom of CEA-LETI and the $(10\bar{1}1)$ semipolar GaN template growth performed in the CRHEA laboratory.

Chapter III: the third chapter covers the investigation of the structural and optical properties of the grown MQW and LED epitaxial structures.

Chapter IV: The fourth chapter presents the design and fabrication of the photolithography mask set that includes all the needed devices. In addition, it describes the development of the μ LED process flow and the device fabrication.

Chapter V: The fifth chapter addresses the electro-optical characterization of the fabricated semipolar μ LEDs and correlates their characteristics with the obtained epitaxial structure properties.

Table of Contents

LIST OF ACRONYMS.....	8
CHAPTER I	10
I.1 III-Nitrides semiconductors	11
<i>I.1.a Structural Properties of III-Nitrides.....</i>	<i>11</i>
<i>I.1.b GaN Crystallographic Orientations.....</i>	<i>12</i>
<i>I.1.c Polarization.....</i>	<i>13</i>
I.2 InGaN Quantum Wells	15
<i>I.2.a InGaN QW properties</i>	<i>15</i>
I.3 Recombination mechanisms in QWs	20
<i>I.3.a Radiative recombination.....</i>	<i>21</i>
<i>I.3.b Non-radiative recombination</i>	<i>21</i>
I.4 Light-emitting diode	23
<i>I.4.a GaN-based LED Structure.....</i>	<i>24</i>
<i>I.4.b Optoelectrical LED Characteristics.....</i>	<i>25</i>
<i>I.4.c LED Properties.....</i>	<i>28</i>
I.5 μLED	30
I.6 Heteroepitaxial Semipolar Growth	33
I.7 References.....	37
CHAPTER II	42
II.1 Introduction.....	43
II.2 MOVPE	43
<i>II.2.a Thomas Swan Reactor</i>	<i>43</i>
<i>II.2.b Growth Mechanism</i>	<i>45</i>
<i>II.2.c Selective area growth principle</i>	<i>46</i>
II.3 Patterning Process	49
<i>II.3.a First method: Regular-SOI with thin SiO₂ mask.....</i>	<i>50</i>
<i>II.3.b Second method: ART-SOI</i>	<i>51</i>
II.4 Regular SOI Template Growth:	55
<i>II.4.a GaN stripes:</i>	<i>56</i>
<i>II.4.b GaN coalescence.....</i>	<i>59</i>

II.4.c	<i>Impact of the AlN/SiO₂ and SiO₂/AlN approaches on GaN growth</i>	62
II.4.d	<i>Growth parameter summary</i>	63
II.5	ART-SOI Template Growth:	63
II.5.a	<i>GaN Stripes</i>	64
II.5.b	<i>GaN Coalescence</i>	65
II.5.c	<i>Optical Characterization</i>	66
II.6	Conclusion	69
II.7	References	71
CHAPTER III	72
III.1	Introduction	73
III.2	Characterization techniques	73
III.2.a	<i>Cathodo-Luminescence (CL)</i>	73
III.2.b	<i>Transmission Electron Microscopy (TEM)</i>	74
III.2.c	<i>Photo-Luminescence (PL)</i>	75
III.2.d	<i>Time Resolved Photo-Luminescence (TRPL)</i>	77
III.2.e	<i>Optical Differential Lifetime Measurement (ODL)</i>	78
III.3	Multi-Quantum Well (MQW) Growth	79
III.3.a	<i>MQW structure</i>	79
III.3.b	<i>Characterization of MQW grown on the TS</i>	80
III.3.c	<i>TS and Aixtron reactor comparison</i>	83
III.3.d	<i>Characterization of MQW grown on the Aixtron</i>	84
III.3.e	<i>Red MQW characterization</i>	90
III.4	LED Growth :	94
III.4.a	<i>LED structure</i>	94
III.4.b	<i>LED characterization</i>	95
III.5	Conclusion	97
III.6	References	99
CHAPTER IV	100
IV.1	Introduction	101
IV.2	An overview of the process steps involved in the device fabrication	101
IV.3	Mask set fabrication	104
IV.3.a	<i>Mask Description</i>	104

IV.3.b	Alignment	109
IV.4	Process steps description.....	111
IV.4.a	P-GaN Activation	111
IV.4.b	MARKS.....	112
IV.4.c	P-contact deposition.....	112
IV.4.d	MESA	113
IV.4.e	P-Contact (CTP).....	115
IV.4.f	N-Contact (CTN).....	115
IV.4.g	ISOL.....	116
IV.4.h	PAD (Electrical Wiring)	117
IV.4.i	TEST	118
IV.5	Process verification.....	118
IV.5.a	Linear TLM.....	119
IV.5.b	Optoelectrical Measurements on LEDs.....	122
IV.6	Conclusion	124
IV.7	References.....	125
CHAPTER V	127
V.1	μLED Electro-optical measurements	128
V.1.a	4x4μm ² μLEDs.....	128
V.1.b	Coalescence lines impact on 4x4μm ² blue μLED	130
V.1.c	Size-dependent characteristics of semi-polar μLEDs	131
V.2	Study of the origin of the device leakage	132
V.2.a	Micro-electroluminescence measurements	132
V.2.b	Photoluminescence measurements.....	134
V.2.c	Transmission electron microscopy.....	135
V.3	Wavelength shift study.....	136
V.3.a	Transmission electron microscopy.....	137
V.3.b	SiLENSe Simulation	138
V.3.c	μPhotoluminescence.....	140
V.3.d	μElectroluminescence	141
V.4	μLED-based applications.....	142
V.4.a	μLED Matrix	142
V.4.b	Frequency response of semi-polar μLED.....	143

V.5	Conclusion	144
V.6	References.....	145
	GENERAL CONCLUSION	146
	APPENDIX A	148
	Résumé	149

List of Acronyms

AFM	atomic force microscopy
ART	aspect ratio trapping
BOE	buffer oxide etching
BOX	buffer oxide
BSF	basal stacking fault
CL	cathodoluminescence
CTN	N contact
CTP	P contact
CVD	chemical vapor deposition
EDX	energy dispersive X-ray
EL	electroluminescence
ELO	epitaxial lateral overgrowth
EQE	external quantum efficiency
FIB	focused ion beam
FWHM	full width at half maximum
IBS	ion beam sputtering
IQE	internal quantum efficiency
LED	light-emitting diode
MD	misfit dislocation
MOVPE	metal-organic vapor phase epitaxy
NBE	near band edge
ODL	optical differential lifetime
PL	photoluminescence
PVD	physical vapor deposition
QCSE	quantum confined stark effect
QW	quantum well
RF	radio frequency
RMS	root mean square
SAG	selective area growth

SEM	scanning electron microscopy
SOI	silicon on insulator
SRH	shockley read hall
STEM	scanning transmission electron microscopy
TD	threading dislocation
TLM	transmission line model
VLC	visible light communication
WZ	wurtzite

Chapter I

I.1 III-Nitrides semiconductors

The III-nitrides semiconductors are composed of the nitride (N) of column V of the periodic table and metal atoms such as aluminum (Al), indium (In), and gallium (Ga) of column III. The importance of these materials in optoelectronic devices arises from their direct bandgap. A band gap energy determines the minimum energy required to excite an electron from its bound state. Additionally, it determines the energy of a photon produced when an electron from the conduction band recombines with a hole in the valence band. The direct bandgap allows an efficient direct photon emission without the assistance of phonons. Additionally, they can cover emission from the infrared (IR) at 0.7V to the ultraviolet (UV) at 6.2V (**Figure 1-1**). This can be achieved by combining the binaries GaN, AlN, and InN to make ternary and quaternary alloys.[13]

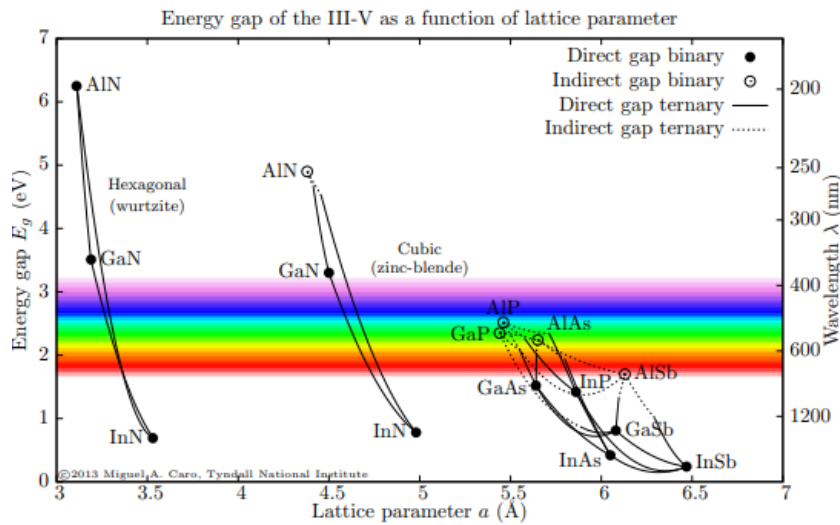


Figure 1-1: Band gap energy as a function of the in-plane lattice parameter a for direct and indirect band gap materials.[13]

I.1.a Structural Properties of III-Nitrides

The III-nitride semiconductor materials exhibit three crystal structures: hexagonal wurtzite (WZ), cubic zinc-blende (ZB), and rock salt. In this study, we will primarily focus on the wurtzite structure, as it is the most commonly grown in III-nitride devices due to its thermodynamic stability.

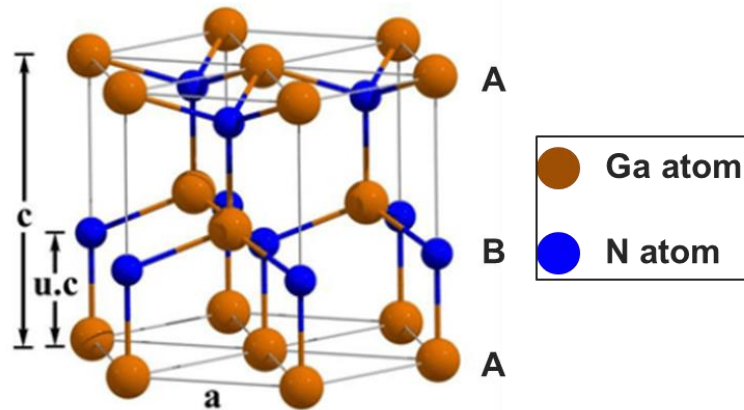


Figure 1-2: A GaN wurtzite structure representation identifying the two close-packed sublattices occupied by metal (Ga) atoms in brown and nitrogen atoms in blue. The lattice parameters a , c , and u are shown along the c -axis.[14]

The wurtzite (WZ) structure consists of two interpenetrating hexagonal close-packed sublattices, one composed of cations (Ga, Al, or In atoms) and the other of anions (N atoms) as presented in **Figure 1-2**. These sublattices are stacked in an ABAB sequential arrangement. Each metal atom is bonded to four surrounding N atoms, forming tetrahedral covalent bonds. The hexagonal unit cell is defined by two lattice constants: ' a ' represents the in-plane distance between neighboring metal or N atoms, while ' c ' represents the out-of-plane distance between the parallel $\pm c$ planes formed by N or Ga atoms. The two sublattices are displaced by a constant $u=(3/8)c$ along the c direction. The values of these lattice parameters of the GaN wurtzite structure are listed in **Table 1-1** below.

Lattice parameters	GaN
a (Å)	3.189
c (Å)	5.185
u	1.944

Table 1-1: Lattice parameters of the wurtzite structure for GaN semiconductors.[15]

In the hexagonal unit cell, crystallographic planes are denoted using Miller-Bravais indices in the form of (h, k, i, l) , where $i = -(h+k)$. The c -plane is represented by (0001) , which is perpendicular to the c -direction $[0001]$.

I.1.b GaN Crystallographic Orientations

The wurtzite crystal structure of GaN exhibits a lack of inversion symmetry which leads to nonequivalent dangling bonds at the surface of (0001) and $(000\bar{1})$ as seen in **Figure 1-3.a**. Consequently, polarities formed along the $\pm c$ -directions are determined by the bonding direction between Ga and N atoms. When the three bonds of the Ga atom are in the direction opposite to the growth direction, it is referred to as Ga-polar (+ c). On the other hand, when the three bonds of N are along the growth direction, it is referred to as N-polar (- c). These polarities significantly impact the growth mechanism of the crystal, including aspects such as indium incorporation, surface morphology, and optoelectronic properties. [16], [17]

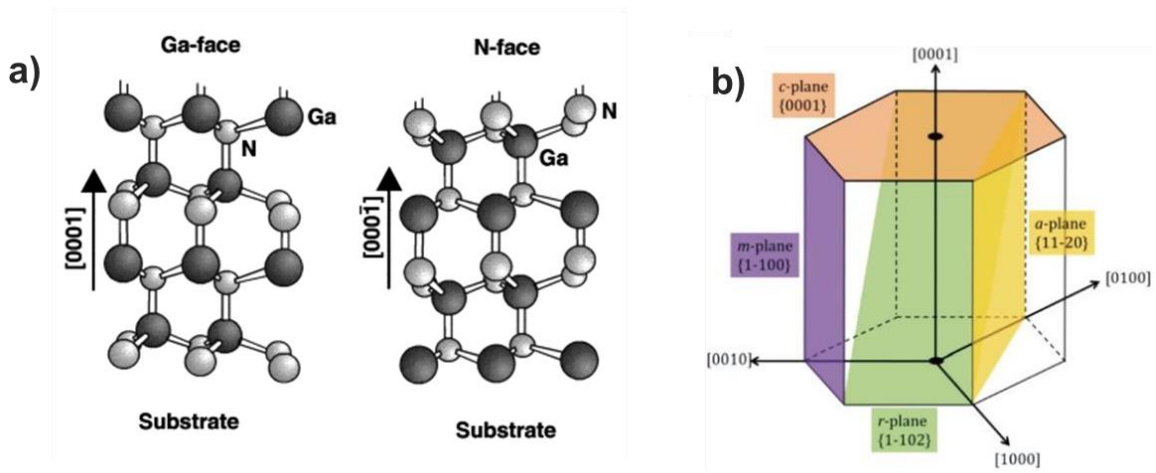


Figure 1-3: a) Ga and N polarities of the GaN wurtzite structure[18]. b)The different wurtzite planes are distinguished by their Bravais-Miller notation.[19]

GaN-based material is essentially grown along the +c direction. However, it is possible to achieve crystal growth along other orientations. These orientations can be parallel to [0001], which is referred to as non-polar. It is also possible to epitaxially grow a surface that exhibits an intermediate angle between the polar and non-polar orientations referred to as semipolar planes. The three different crystallographic planes for the GaN wurtzite structure are represented in the schematic of **Figure 1-3. b.**

The semipolar GaN, and specifically the $(10\bar{1}1)$ orientation, will be used throughout this work and will be highlighted in each upcoming section of this chapter. In the next paragraph, we will discuss the spontaneous and piezoelectric polarizations of the different GaN planes.

1.1.c **Polarization**

A macroscopic polarization is found in the WZ III-nitrides semiconductors, which highly impacts the optoelectrical properties of the material. It is the sum of two components: spontaneous polarization (P_{sp}), and piezoelectric polarization denoted as P_{pz} .

The P_{sp} is an intrinsic property of the WZ material. It is related to the asymmetry of the GaN crystal structure and the difference in electronegativity between Ga and N atoms along the [0001] axis in the crystal. The nitrogen is more electronegative than gallium resulting in an unequal charge distribution which generates an electric dipole along [0001] in each unit cell. This polarization is present in the crystal at equilibrium in the absence of any external stress.

The P_{pz} occurs when the semiconductor undergoes mechanical strain. This strain is particularly generated when III-nitrides are grown heteroepitaxially on III-nitrides-based layers such as InGaN on GaN. As a result, the in-plane lattice constants (listed in **Table 1-2**) of the epilayer are forced to match that of the substrate layer. This phenomenon is referred to as pseudomorphic growth.

Material	In-plane constant a (Å)
GaN	3.189
AlN	3.112
InN	3.533

Table 1-2: Summary of the in-plane lattice constants of GaN, AlN and InN.[15]

The lattice can be undergoing different strain states: tensile such as AlGaIn/GaN seen in **Figure 1-4. a,** or compressive such as InGaIn/GaN seen in **Figure 1-4. b,** leading to a positive and a negative P_{pz} along [0001] respectively.

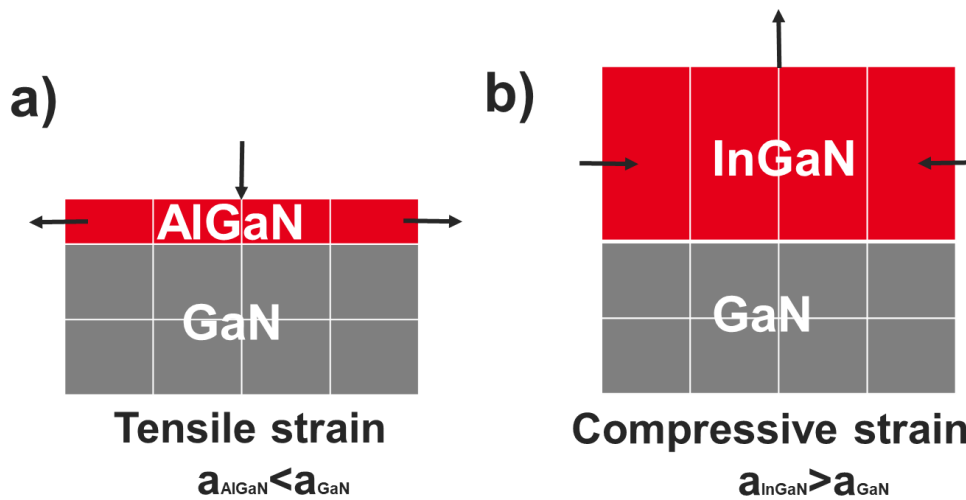


Figure 1-4: Schematic representation of the strain in a) tensile and b) compressive states function of the lattice mismatch.

Strain can also arise from thermal expansion when growing III-nitrides on foreign substrates such as sapphire (Al_2O_3) and silicon (Si). These foreign substrates are used due to the lack of native and affordable substrates such as freestanding GaN. Hence, the piezoelectric polarization is caused by the lattice mismatch and thermal expansion between the materials.

In the case of InGaIn/GaN, the total polarization is highly dependent on the difference of P_{pz} contribution compared to the P_{sp} which remains the same no matter the In concentration. In the case of polar GaN, a difference of polarization generates two sheets of charges ($\pm\sigma$) of opposite values which create an internal field at the heterointerfaces perpendicular to the growth plane as represented in **Figure 1-5. a**. The formula of the stress (σ) generated by the difference in polarization is expressed as follows:

$$\sigma = \Delta P \times n$$

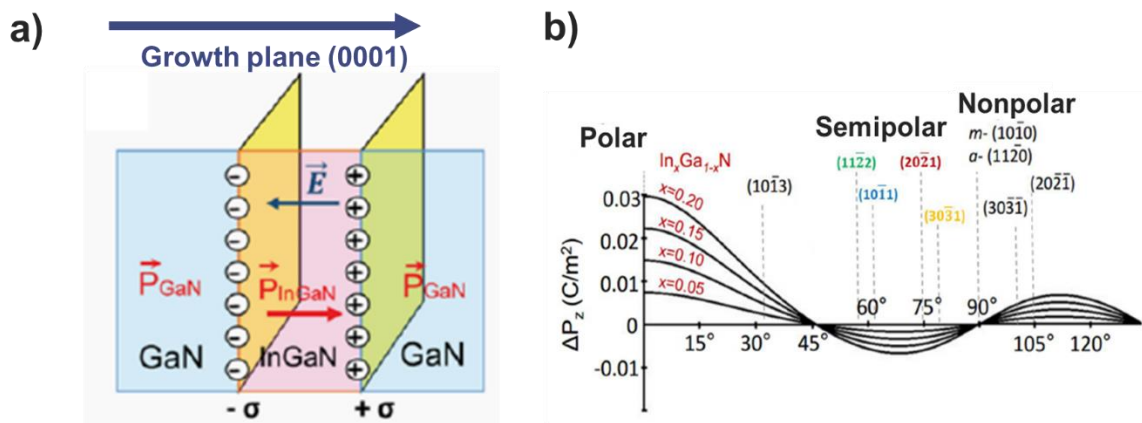


Figure 1-5: a) Schematic of GaN/InGaIn/GaN heterostructure grown along (0001)[19]. b) Difference of the total polarization on different GaN plane orientations for various In compositions.[20]

However, Romanov et al. [21] proved the dependence of the total polarization discontinuity concerning the growth plane having an angle from the c-axis, such as along semipolar or non-polar orientations as illustrated in **Figure 1-5. b**. The orientation used in this work ($10\bar{1}1$) has an inclination angle of $\sim 61^\circ$, which results in a relatively small negative total polarization discontinuity.

I.2 InGaN Quantum Wells

The active region of an LED is constituted of quantum wells (QWs). A QW is a thin layer of lower bandgap energy semiconductor sandwiched between two similar layers of higher bandgap energies referred to as quantum barriers (QBs). As shown in **Figure 2-1**, charge carriers tend to reduce their potential energies and become localized within the QW region.

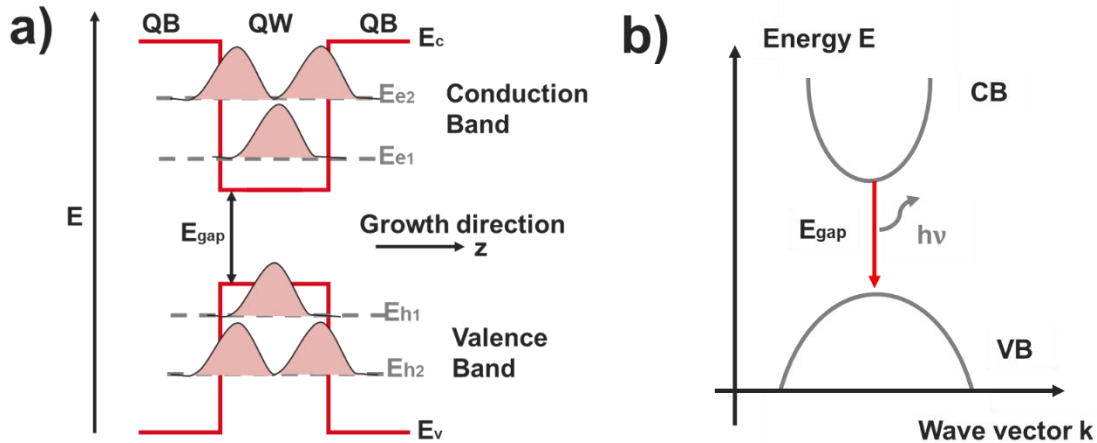


Figure 2-1: a) Schematic representation of the first and second energy levels of a QW with their corresponding wavefunctions in a real space along the growth direction. b) The energy band diagram of a direct photon emission in the in-plane k wave vector

Multiple quantum wells (MQWs) can be also achieved by having the same properties of a group of isolated single QW. These structures, classified as type-I systems, enable the confinement of both electrons and holes within a single layer of material along the growth direction. This means having both carriers localized in the same in-plane k -space (at the maxima and minima of the valence and conduction band energies respectively) as depicted in **Figure 2-1.b**. The confinement in the z direction leads to the formation of discrete energy levels, denoted as subbands, which can be calculated using the simple one-dimensional Schrödinger equation:

$$\frac{\partial^2 \psi(z)}{\partial z^2} + \left(\frac{2m^*}{\hbar^2} \right) (E - V(z)) \psi(z) = 0$$

Where $\psi(z)$ represents the wavefunction, m^* is the effective mass, and $V(z)$ is the potential energy along the growth direction.

In our work, In incorporation in GaN leads to the formation of a thin InGaN layer which will be the QW sandwiched between GaN QBs. By adjusting the In composition and layer thickness of the QW, the bandgap energies can be precisely controlled allowing a tunable wavelength emission in InGaN-based devices.

I.2.a InGaN QW properties

I.2.a.i InGaN characteristics

Considerable difficulties exist to grow homogeneous InGaN with high In concentrations which are related to the phase separation that is predicted for InGaN. The thermodynamic GaN/InN phase diagrams showed large miscibility gaps at temperatures between 600°C and 850°C making it hard to

incorporate In [22]–[24]. Additionally, experimental studies have shown that if the In content is greater than 25%, phase separation is likely to occur.[25][26]

Atomic probe tomography measurements have shown that In is randomly distributed in InGaN alloy for low In concentrations in polar GaN [27]. This randomly distributed Indium will generate potential fluctuations in MQW structures where carriers will be localized. This fluctuation was shown to vary between 10 and 22% within a 30nm distance as seen in **Figure 2-2**. [28]

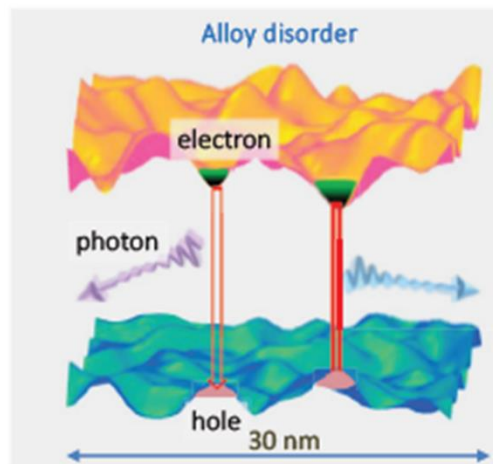


Figure 2-2: Illustration of the In fluctuations in InGaN structures generating potential minima [28].

The effect of carrier localization on the device performance is still under investigation. Some explain that the high internal quantum efficiency (IQE) in InGaN QW despite the high dislocation density is due to the localization that decreases the carrier diffusion to a non-radiative recombination center.[29] However, recent studies showed that high IQE was achieved despite carriers diffusion towards the dislocations which means that localization itself cannot be the only cause of elevated IQE. [30]

I.2.a.ii Quantum Confined Stark Effect

The polarization-induced electric field when growing InGaN/GaN along the c-plane causes the formation of the so-called Quantum Confined Stark Effect (QCSE). This phenomenon results in a bending of the energy bands in the QW and leads to spatial separation of the charge carriers' wavefunctions thereby reducing their radiative recombination rate. In addition, the wavefunction separation causes the reduction of the transition energy resulting in wavelength redshifting as shown in **Figure 2-3**.

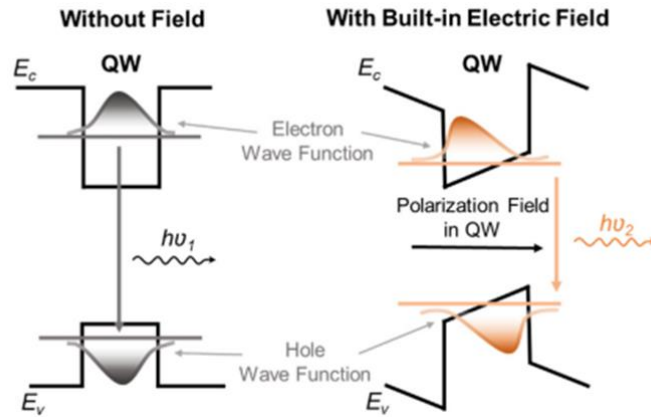


Figure 2-3: The schematic diagram of the quantum-confined Stark effect (QCSE) in InGaN QW [31].

Different strategies have been employed to mitigate the QCSE phenomenon such as the use of nanowire structures, quantum dots, and superlattice as a strain-relaxed layer [32] or the use of thin QW. Having a thin InGaN QWs (2-3nm) enhances carrier confinement and hence the wave function overlapping between the carriers. However, a poor carrier injection is caused by this thin QW. Other methods such as the choice of the crystal orientation of GaN proved to mitigate or even remove the QCSE by reducing or eliminating the induced internal electric field.[33] As illustrated in **Figure 1-5**, as the sheet of charge between InGaN and GaN decreases for semipolar and non-polar orientations, the induced electric field is also decreased resulting in enhancement of the wavefunction overlapping as presented in **Figure 2-4**.

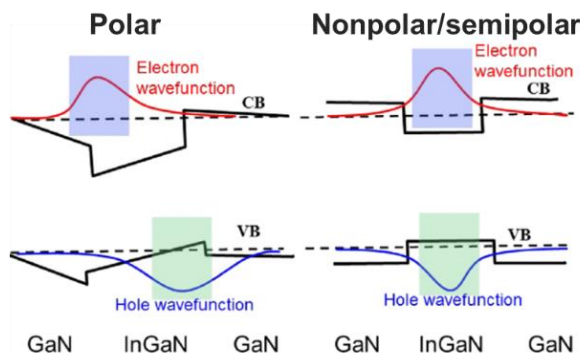


Figure 2-4: Visualization of the QCSE in InGaN/GaN quantum well structures (a) polar GaN that suffers from QCSE and (b) non-polar GaN that is free from it [34].

I.2.a.iii GaN Defects

- Dislocations:

During the process of growing epitaxial layers, it is important to minimize structural defects in the crystal lattice, such as dislocations and stacking faults. Dislocations are considered as non-radiative recombination centers that also affect the diffusion length of minority carriers [35]. They can behave differently depending on the crystallographic orientations or the growth approaches, they can either interact with other defects, annihilate, or even form dislocation loops. These defects can have a negative impact on the optoelectronic properties of semiconducting materials, specifically affecting the quantum efficiency of light emission.

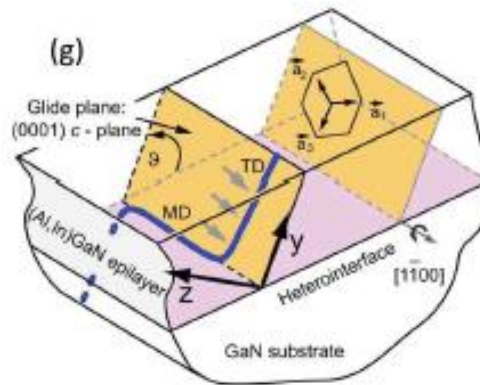


Figure 2-5: Schematic explaining the formation of misfit and threading dislocations resulting from slip in the inclined basal (0001) plane in semi-polar structures.[36]

There are two groups of dislocations present: threading dislocation (TD) and misfit dislocation (MD). Threading dislocations can occur during the growth process and can propagate throughout the entire crystal lattice. Misfit dislocations, on the other hand, are generated at the interface between the substrate and the grown epilayer due to strain relaxation between the two materials such as InGaN on GaN. This generation of misfit dislocations is caused by the thickness of the InGaN epilayer exceeding the critical thickness, beyond which plastic relaxation occurs. The critical thickness can be calculated using the Matthews-Blakeslee model [37].

In addition, dislocations are characterized by their Burgers vector, denoted as \vec{b} , which represents the magnitude and direction of the lattice distortion caused by the dislocation. There are three types of dislocations:

- i. Edge dislocations: They are characterized by an extra half-plane of atoms inserted into the crystal lattice **Figure 2-6.a**. They have a Burgers vector that is parallel to \vec{a} seen in **Figure 2-6.c**.
- ii. Screw dislocations: They are characterized by a spiral-like motion of the crystal lattice around the dislocation axis **Figure 2-6.b**. They have a Burgers vector parallel to the c-axis.
- iii. Mixed dislocation: They are a combination of screw and edge dislocation components. They follow the vector $\vec{a}+\vec{c}$ shown in **Figure 2-6.c**.

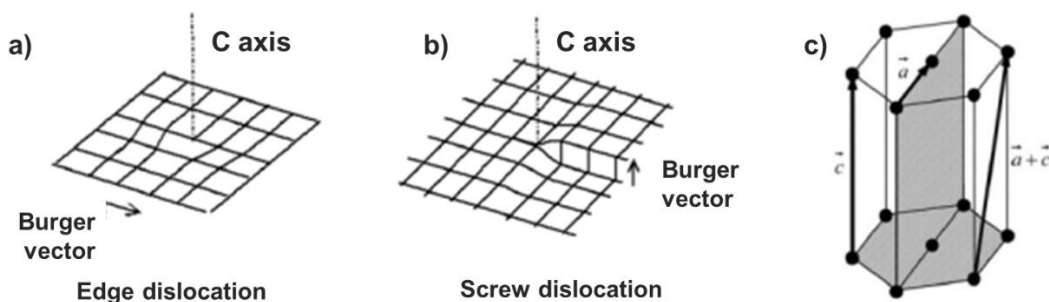


Figure 2-6: Illustration of a) edge dislocations, b) screw dislocations, and c) the direction of the burgers vectors.[38]

- Basal-Stacking-Faults:

Basal stacking faults (BSFs) are another type of extended GaN defects that are aligned parallel and perpendicular to the growth plane for polar and nonpolar GaN, respectively. Whereas, BSFs are aligned in an inclined angle to the growth for semipolar GaN. They occur when the stacking sequence of the atomic layers deviates from the previously explained ideal ABAB WZ arrangement. Instead, insertion of the cubic stacking sequence (ZB) takes place within the hexagonal crystal lattice creating three different types of BSFs. Type I_1 and I_2 are two intrinsic faults that consist of an inserted single and a double ABC cubic sequence respectively, along the polar plane. The third type E is an extrinsic fault that involves in this case a triple or even more cubic insertions. The energies associated with these 3 types are affected by the number of cubic insertions, hence the formation energy of I_1 is the lowest ($10 < 24 < 38$ meV)[39]. These different energy formations along the structure can negatively impact the crystal quality by leading to carrier localization within the QWs. The highest density of BSFs was observed by TEM near the interface of the film/substrate, especially in non- and semi-polar, or they are terminated by a partial dislocation at each end[40]. Several explanations were adapted for the cause of BSF formation such as GaN 3D nucleation or variation of growth conditions when, for example, introducing new material or changing from 3D to 2D growth. The latter case causes a different growth rate in a way that the adatoms diffusion is slower along the -c direction compared to the +c, where BSFs are formed.

Studies have shown that these BSFs can be characterized not only by TEM but also using low-temperature PL and CL techniques as these defects are optically active. Local PL spectra at low temperatures showed a weaker emission from the active region grown on $(10\bar{1}1)$ semipolar GaN at the BSFs compared to the rest of the sample, as well as a slight red shift that was suggested to be caused by the BSFs.[41] Therefore, these defects faults have important implications for the properties of GaN materials.

- V-pits:

V-pits, also known as inverted hexagonal pyramids (IHPs), are commonly observed defects in InGaN-based structures grown on the c-plane. These defects have inclined planes of the $\{10\bar{1}1\}$ type. Several research groups have attempted to explain the mechanism behind their formation. Shiojiri et al.,[42] proposed that these defects originate from threading dislocations that reach the InGaN regions (**Figure 2-7.a**). Consequently, the QWs are thinner at the facets of these V-pits due to a slower growth along the semipolar planes compared to the c-plane as illustrated in **Figure 2-7.b**. This results in an effective band gap higher by several hundred meV compared to normal c-plane QWs.[43] The relatively high growth temperature of GaN (around 1050°C) compared to the temperature required for the growth of multi-quantum wells (typically between 650°C and 800°C) may explain why these defects are rarely observed in GaN.

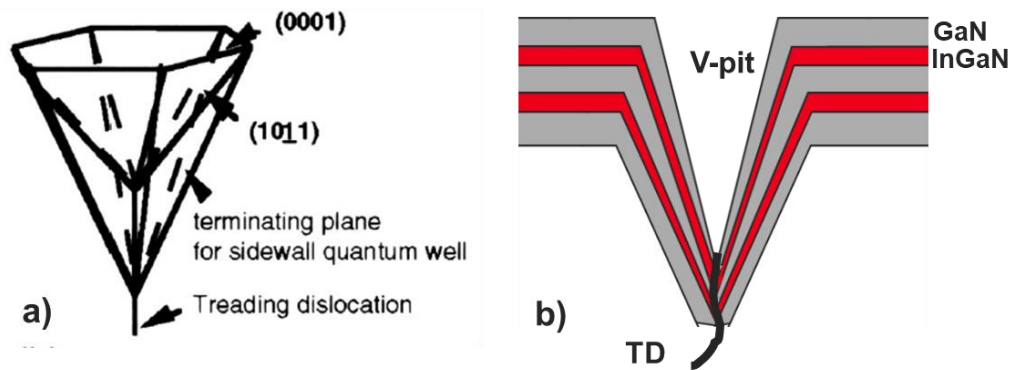


Figure 2-7: An illustration of a perspective view in a)[44] and a cross-section view in b) of the V-pit.

Despite the reported advantages of the V-pits such as their contribution to strain relaxation in polar GaN, [45] and better carrier injection into deeper QWs, they can also introduce various problems. These problems include the generation of deep traps at the center of the pits blocking the electron injections[46], non-uniformity in QW layer thickness and composition, an increase in the work function of n-type GaN [47], and a leakage current [48]. Some experiments suggest that the V-defects act as non-radiative recombination centers, while others suggest that they result in longer minority carrier lifetimes.[46].

- Point defects:

Point defects are disturbances occurring at a single point within the atomic lattice. They can be referred to as vacancy atoms and impurity atoms that can be either interstitial (found in between the matrix atoms) or substitutional (replacing an atom in the matrix). Two types of vacancies are present either have an ion leaving a lattice site to move to an interstitial position (Frenkel defect) or have an ion and a cation migrating to the surface (Schottky defect).

Point defects can introduce deep energy levels leading to unintentional doping of the semiconductor. Consequently, this is often observed by PL spectroscopy as a yellow band emission[49]. Therefore, these defects have a direct impact on the device's efficiency as they are considered one of the main causes of non-radiative recombination.[50] Haller et al. suggested that these defects are mainly nitrogen vacancies that are created during the growth of GaN at high temperatures and segregate on the GaN surface even during InGaN growth at lower temperatures.[51] Few approaches were used to trap these defects and avoid their incorporation in the active region such as the growth of an InGaN underlayer (UL) or an InGaN/GaN superlattice just before the growth of the QW layer.[50], [52] These layers allow the point defects to be buried before they reach the quantum wells where they act as non-radiative recombination centers.

I.3 Recombination mechanisms in QWs

Recombination refers to the process in which an electron in the conduction band and a hole in the valance band annihilate which results in the release of excess energy. Recombination can occur in two ways: radiative recombination and non-radiative recombination.

Radiative recombination involves the emission of photons as the excess energy is released. In this process, the released energy is converted into light.

On the other hand, non-radiative recombination involves the release of excess energy in the form of phonons. Phonons are vibrations or lattice distortions within the material, and the excess energy is

dissipated as heat rather than being converted into light. We are going to detail these recombination mechanisms within the InGaN QWs in the following paragraphs.

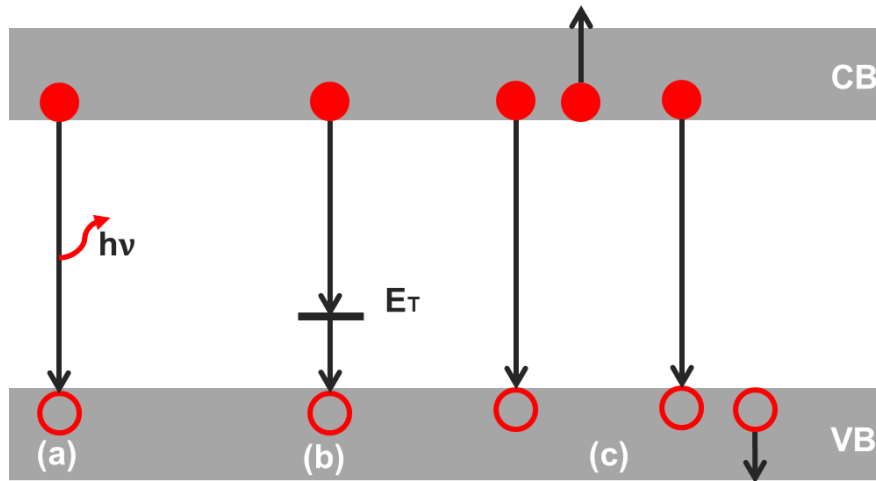


Figure 3-1: Schematic of both radiative and nonradiative recombination mechanisms. a) band-band, b) SRH, and c) Auger recombinations.

I.3.a Radiative recombination

I.3.a.i Band-Band recombination:

This process involves the direct radiative recombination of an electron from the conduction band with a hole in the valence band (**Figure 3-1.a**), resulting in the emission of a photon with an energy equivalent to the bandgap energy (E). For recombination to occur, the electrons and holes must have matching momentum states in k -space, which explains the preference for direct bandgap semiconductors. The rate of radiative recombination, which represents the number of recombination events per unit time and volume, is directly proportional to the concentrations of free electrons (n) in the conduction band and holes (p) in the valence band:

$$R_{rad} = Bnp$$

The constant B corresponds to the coefficient of bimolecular recombination and typically has values on the order of $10^{-12} \text{ cm}^3/\text{s}$ for InGaN QWs.[53]

I.3.b Non-radiative recombination

I.3.b.i Trap-assisted or Shockley-Read-Hall (SRH) recombination:

Shockley–Read–Hall (SRH) recombination is a nonradiative recombination where an electron or hole recombines with a deep-level defect within the band gap of a semiconductor (**Figure 3-1.b**).[54], [55] For this type of recombination, a trap in the forbidden energy bandgap of the semiconductor is necessary. Deep-level defects can arise from vacancies, interstitials, unwanted impurities, dislocations, or combinations of different types of defects.[56]

As a result, the presence of these new energy levels within the bandgap can locally alter the energy transitions. For instance, a free electron from the conduction band can be captured by one of these defects. A hole can be subsequently captured by the same defect creating an electron-hole pair annihilation. However, it's important to note that these energy transitions may not necessarily involve the emission of radiation. The excess energy of the carriers can be thermally dissipated through phonon interactions. These processes are quantified by the Shockley-Read-Hall (SRH)

statistics, named after Shockley, Read [43], and Hall [42], who first proposed an analytical description of these phenomena.

$$R_{SRH} = \frac{p_0 \Delta n + n_0 \Delta p + \Delta p \Delta n}{(N_T v_p \sigma_p)^{-1} [n_0 + n_1 + \Delta n] + (N_T v_n \sigma_n)^{-1} [p_0 + p_1 + \Delta p]}$$

Where Δn and Δp are the excess of electron and hole concentrations respectively. n_0 and p_0 are concentrations of electrons and holes respectively at equilibrium. v_p and v_n are the electron and hole thermal velocities, σ_n and σ_p are the capture cross sections of the traps. n_1 and p_1 represent the concentrations of electrons and holes, respectively, when the Fermi level coincides with the trap level E_T .

$$n_1 = n_i \exp\left(\frac{E_T - E_{Fi}}{kT}\right)$$

and

$$p_1 = n_i \exp\left(\frac{E_{Fi} - E_T}{kT}\right)$$

where n_i is the intrinsic carrier density and E_{Fi} is the intrinsic Fermi level.

The traps in the Shockley-Read-Hall (SRH) recombination process are located near the middle of the semiconductor's bandgap. The energy required to remove a carrier from these traps to the allowed bands is much greater than the thermal energy (kT). Deep-level trap states also typically exhibit similar capture coefficients for both electrons and holes.[56]

In the case of doped semiconductors, such as those with n-type doping ($n_0 > n_i > p_0$), and for a relatively small deviation from equilibrium ($n = n_0 + \Delta n \approx n_0$ and $p = p_0 + \Delta p < n_0$), it can be demonstrated that the non-radiative lifetime of minority carriers is determined by:

$$\tau = \tau_{n0} = \frac{1}{N_T v_n \sigma_n} = \frac{\Delta n}{R_{SRH}} \quad (\text{for n-type doping})$$

$$\tau = \tau_{p0} = \frac{1}{N_T v_p \sigma_p} = \frac{\Delta p}{R_{SRH}} \quad (\text{for p-type doping})$$

This implies that the SRH rate is primarily limited by the capture rate of minority carriers written as :

$$R_{SRH} = An$$

I.3.b.ii Auger recombination:

The auger recombination is when an electron and a hole undergo direct band transition. However, unlike radiative recombination, where the energy is emitted as a photon, in Auger recombination, the energy generated during the recombination process is transferred to another free electron or hole (Figure 3-1.c). The excited carrier will then lose energy in the form of phonons. The specific equation for Auger recombination involving an excited free electron and hole depends on the approximation that $n=p$ and it is expressed as follows:

$$R_{Auger} = C_n p n^2 + C_p n p^2 = (C_n + C_p) n^3 = C n^3$$

Where C is the Auger coefficient.

I.4 Light-emitting diode

The light-emitting diode (LED) is the basic component of solid-state lighting technology. It is a semiconductor device that emits light when an electric current is passed through it. It involves combining a p-doped semiconductor with its n-doped counterpart to form a p-n junction. There are two types of p-n junction, a homo-junction is formed by the same semiconductor material, as presented in the scheme of **Figure 4-1**, and a hetero-junction by using different semiconductors.

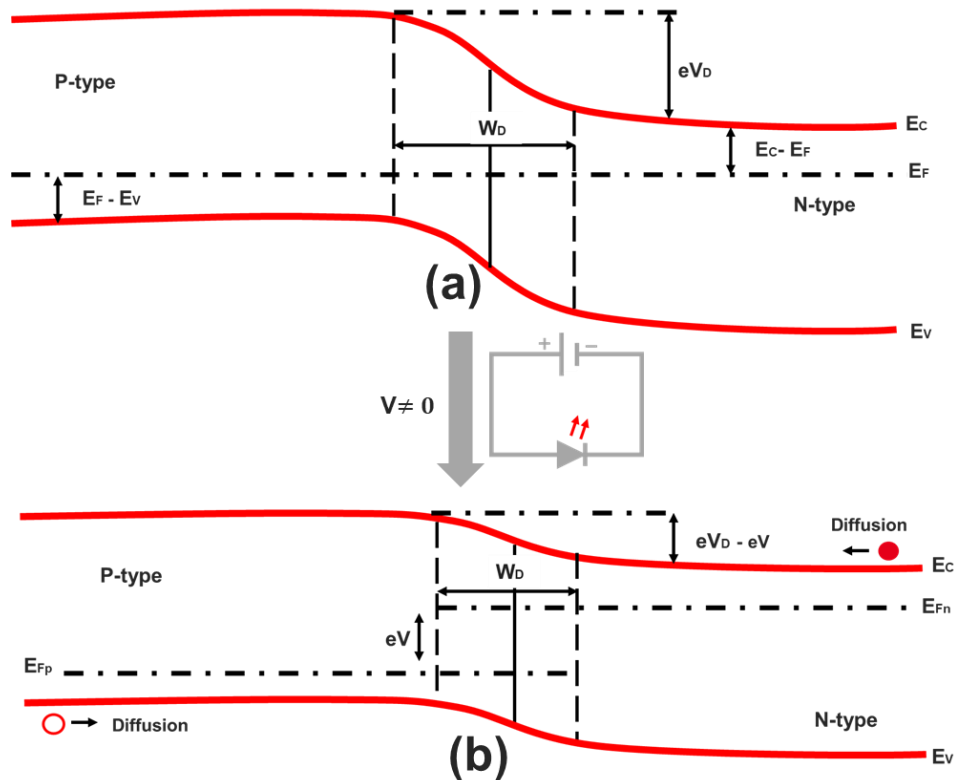


Figure 4-1: A schematic of the p-n homojunction a) under no bias and b) under a forward bias.

For the homojunction case, when no bias is applied, electrons in the conduction band flow across the junction from the n-doped side, and holes in the valence band flow from the p-doped side to recombine (**Figure 4-1.a**). Upon recombination, free carriers are reduced from a region in between the p-n junction known as the depletion region. The width W_d of this region is indicated by the dashed vertical lines in the **Figure 4-1.a** and is dependent on the doping level. The higher the doping, the more free carriers are present which leads to a narrower region. The only charges present in the depletion area are from the remaining ionized dopants. This creates an electric field causing carrier drifts to the opposite direction of the carrier diffusion. This generates a potential barrier for free carriers known as the diffusion voltage V_D .

When a voltage is applied to the diode (**Figure 4-1.b**), the Fermi level on the p-side (E_{Fp}) is separated by eV from the Fermi level on the n-side (E_{Fn}). Thus the charge carriers start to diffuse allowing a reduction of the potential barrier and hence a narrower depletion region. This results in a recombination of electrons and holes at the p-n junction, emitting light with an energy equal to the bandgap energy $E = h\nu = \frac{hc}{\lambda}$. [57] However, these junction types do not allow achieving significant light output which is not ideal for LED fabrications. The recombination along this junction occurs over a large area which will favor a low carrier concentration and nonradiative recombination.

Therefore, the use of heterojunctions seems to be the solution for better LED characteristics to confine the carriers in a smaller area. One of the heterojunction structures is the type I- QW presented previously. The InGaN MQWs (active region) are placed in between the p and n-side of the junction, where carriers will be recombined. MQWs in these cases present an improvement in the number of carriers that recombine radiatively due to the carrier's confinement within the well. [56]

I.4.a GaN-based LED Structure

A typical schematic of a planar LED structure with its corresponding band structure is illustrated in **Figure 4-2.a** and **b** respectively. It begins by growing a GaN template on a substrate, followed by an upper layer of n-doped GaN. Silicon (Si) is commonly used as an n-type dopant for GaN due to its easy incorporation, high concentration, and low activation energy (12-17meV)[58]. Si is added as an impurity to generate an excess of electrons and establish the desired conductivity. An InGaN underlayer is often used just after the nGaN layer to trap point defects as mentioned in subsection **I.2.a.i**. Subsequently, the active region is grown, consisting of multiple quantum well (MQW) InGaN structures. Just before the final p-doped GaN layer, an electron-blocking layer (EBL) is typically incorporated to create a potential barrier for electrons.

The concentration of electrons in GaN is higher than the hole concentration due to better doping. In addition, the mobility of electrons is significantly higher than that of holes. Consequently, the active region quickly becomes saturated with electrons, which struggle to find sufficient holes for recombination, resulting in an electron overflow. This is one of the reasons the concentration of minority carriers in p-GaN is significant, unlike in n-GaN. Therefore the primary purpose of the EBL is to minimize electron overflow into p-GaN, which is generally more dominant than hole overflow due to the lower mobility of holes. A commonly used material for this purpose is p-doped AlGaIn, where the aluminum proportion (relative to Ga) typically ranges from 15% to 30% effectively increasing the band gap.

P-doping in GaN poses challenges due to the high activation energy required to ionize the dopants. Currently, magnesium (Mg) is the preferred acceptor for p-doping GaN, with an activation energy of 155 meV. In addition, the presence of hydrogen atoms introduced during growth, mainly through ammonia (NH₃), can easily passivate magnesium, leading to poor conductivity. Thermal annealing is employed before LED fabrication to enhance p-type conductivity by activating the dopants. Additionally, a p++ doped layer having a higher Mg concentration is often added on top of the p-GaN to further improve the conductivity. Following the addition of metal contacts on the p and n sides, electrons and holes can be injected into the LED, leading to their confinement within the active region of the multi-quantum wells.

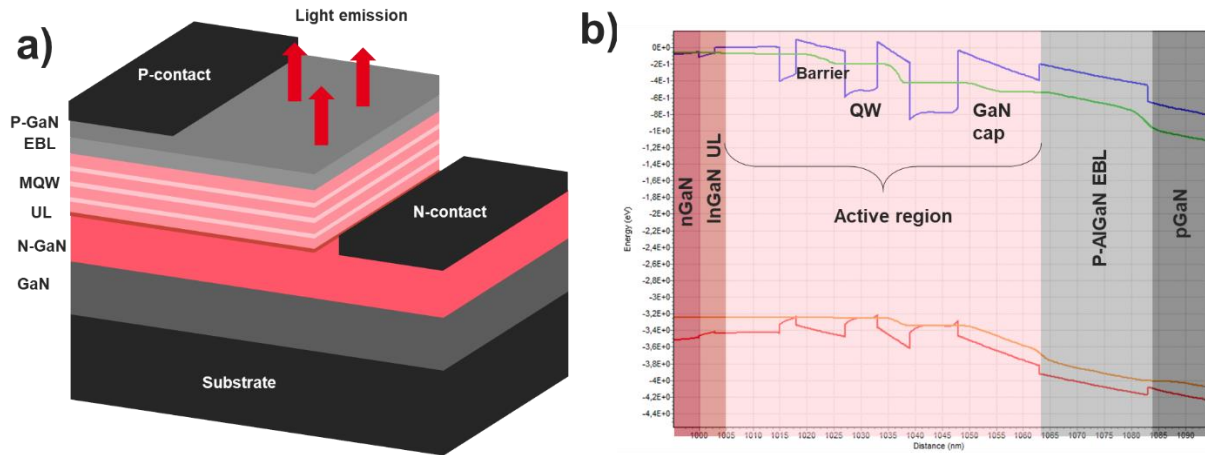


Figure 4-2: a) Schematic representation of a semipolar GaN-based LED structure with its corresponding energy band diagram simulated using SiLENSe in b).

I.4.b Optoelectrical LED Characteristics

The current flowing through the p-n junction is modeled by the Shockley equation[56] :

$$I = I_s \left(e^{\frac{qV}{n_c kT}} - 1 \right)$$

Here, I_s represents the saturation current, q is the electron charge, V is the applied voltage, T is the temperature expressed in Kelvin (K) and k is the Boltzmann constant expressed in eV/K. The parameter n_c is known as the ideality factor, which usually gives insight into the recombination mechanisms occurring under forward bias.

Ideally, when the current is dominated by the radiative recombination the ideality factor is equal to 1 whereas for non-radiative recombination, it is equal to 2. However, in reality, in nitride semiconductors the ideality factor varies over a wider range where there is currently no scientific explanation for the values exceeding 2. In practice, LED characteristics can deviate from this idealized equation due to various factors such as series resistance (R_s) that arise from contact resistances or the resistivity of the semiconductor material, and parallel resistance (R_p) that is associated with a pathway that bypasses the p-n junction, particularly due to surface, sidewalls and process-induced defects. The modified form of the Shockley equation, which incorporates these factors, is presented in the following equation:

$$I - \frac{V - IR_s}{R_p} = I_s \left(e^{\frac{q(V-IR_s)}{n_c kT}} \right)$$

I.4.b.i Contacts

The contact is directly related to the metal's work function (Φ_M) and the semiconductor material's electron affinity (χ_{sc}). The work function corresponds to the difference between the vacuum level and the Fermi level for the metal or the semiconductor as illustrated in **Figure 4-3** for the n-type material. The electron affinity is the difference between the vacuum level and the conduction band.

Thus, the electrons from the metal will perceive a potential barrier (known as the Schottky barrier) expressed as follows:

$$\Phi_b = \Phi_M - \chi_{SC}$$

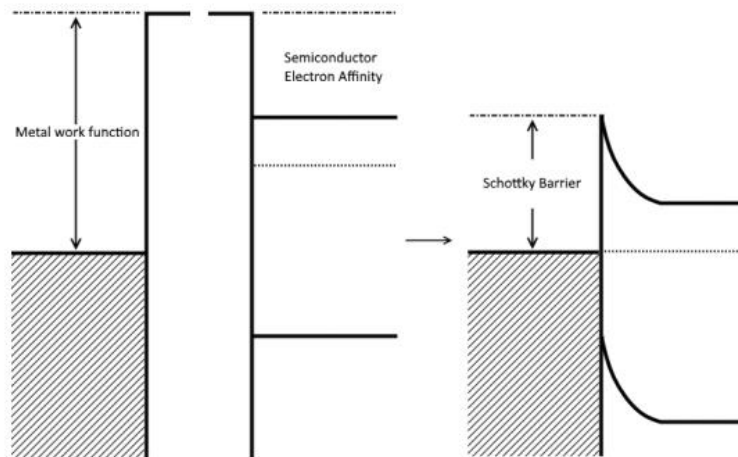


Figure 4-3: Band structure of n-type Schottky barrier formation [59]

An LED must have positive and negative electrical contacts, which allow for the injection of holes from the p-doped side and electrons from the n-doped side of the LED. The choice of a metal contact is crucial and directly depends on the doped material on which it needs to be deposited. **Figure 4-3** presents the resultant Schottky barrier for the n-type. The carrier travels this barrier either by thermal excitation or by tunneling. The tunneling leads to an ohmic contact where the Fermi level is aligned with respect to the energy bands which results in a linear current-voltage characteristic as seen in **Figure 4-4**. Otherwise, the contact is Schottky that needs thermal energy to tunnel through the contact.

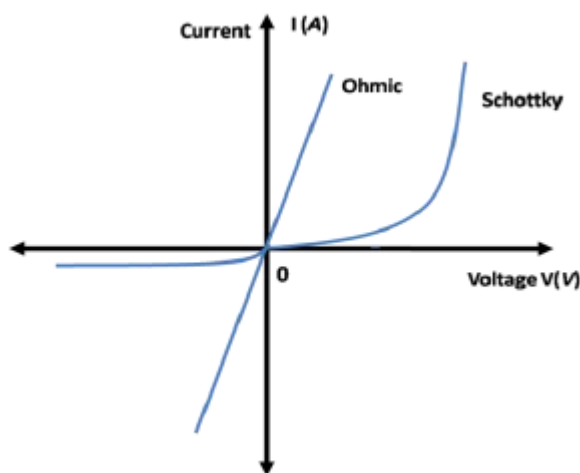


Figure 4-4: The I-V characteristics of an ohmic and a Schottky contact.[60]

The contact behavior is dependent on the surface defect which can cause inhomogeneity in the transport current, while GaN quality, doping, and metal-GaN reactions are additional contributing factors [61]. An ohmic contact is relatively easy to achieve on n-GaN, but it is much more challenging in the case of p-GaN. Usually, particularly for p-GaN, a Schottky barrier is commonly obtained because of the lack of a metal work function material that matches what is needed to bend the

energy bands and tunnel the carriers. To improve the contact, better doping should be used such as a higher dopant concentration p++ layer previously mentioned to help tunnel the carriers and decrease the Schottky barrier.

I.4.b.ii Device Efficiency

Studying the device's efficiency is essential to improve the optoelectrical LED performance. Starting with the **internal quantum efficiency (IQE)** that represents the ratio of the number of photons emitted by the active region to the number of injected electrons into the LED.

$$IQE = \frac{P_{int}/h\nu}{I/q}$$

Where P_{int} is the optical power emitted by the active region, the current injected into the LED is expressed as I , and the electron charge as q . h is Planck's constant (6.63×10^{-34} joule seconds), and ν is the frequency of the photon in hertz (Hz).

The IQE of an InGaN/GaN LED depends on the crystal quality and structural design of the active region. It is the radiative rate over the total recombination rate (radiative and non-radiative recombinations). A simplified theoretical model, known as ABC, is widely used to analyze the IQE by using the recombination mechanisms previously explained, where the IQE can be expressed in function of the three coefficients as follows:

$$IQE = \frac{Bn^2}{An + Bn^2 + Cn^3}$$

The number of photons emitted by the active region won't be totally extracted through the LED. This is a limiting factor to be taken into account, as photons have the possibility of total reflection within the LED, due to the large difference between the GaN and air refractive indices. Therefore, some strategies such as using patterned substrates and surface roughening [62] have been applied to improve the extraction. To quantify this, the light extraction efficiency is also calculated.

The **light extraction efficiency (LEE)** of an LED represents the ratio of the total emitted light from the LED with respect to the light generated within the active region. It is expressed as follows:

$$LEE = \frac{P/h\nu}{P_{int}/h\nu}$$

The combination of IQE and LEE gives information about the **external quantum efficiency (EQE)** expressed as follows:

$$EQE = IQE \times LEE$$

The EQE represents the ratio of the number of photons emitted by the LED to the number of electrons injected into the LED which can be extracted using this equation:

$$EQE = \frac{P/h\nu}{I/q}$$

Where P is the optical power emitted into the free space.

Finally, the **wall plug efficiency (WPE)** is the ratio of the emitted optical power over the input electrical power expressed as follows:

$$WPE = \frac{P}{P_{elec}} = \frac{P}{IV}$$

The impact of the WPE is significant on LED applications in terms of cost-effectiveness. For instance, a high WPE results in an efficient LED that provides the same amount of light emission with low electrical power consumption.

I.4.c LED Properties

GaN-based LEDs suffer from several performance limitations, such as droop, green gap, quantum-confined Stark effect (QCSE), and thermal droop. This paragraph will discuss these properties and their impact on LED performance.

I.4.c.i Droop:

Efficiency droop refers to an intrinsic phenomenon observed in GaN-based LEDs where the efficiency of the device decreases as the current density (J) increases. The exact mechanism behind this droop is still ongoing research, but several theories tried to explain this phenomenon. One widely accepted theory is the Auger recombination which I described in paragraph **I.3**. The impact of the Auger appears in the Cn^3 term in the previous IQE formula as well as the current density formula by using the ABC model previously explained:

$$J = qd(An + Bn^2 + Cn^3)$$

Where d is the active region thickness, and q is the electron charge.

The J is directly proportional to the Auger parameter C and a cubic number of carriers (n^3) so at high J we are at high carrier density hence the impact of the Auger is higher. Based on the IQE equation in **I.4.b.ii**, as J increases, Auger increases therefore the IQE decreases.

The Auger carriers were also been evidenced experimentally in InGaN QWs by electron emission spectroscopy at the current density where an efficiency drop was observed [63]. It has been also demonstrated that the droop is composed of two contributions: the Auger scattering and a defect-assisted droop process which is more prevalent at long wavelengths.

The droop is a significant challenge to overcome in GaN LED, therefore, researchers have suggested the use of wider quantum wells to reduce the carrier density for a given current density thereby reducing the droop. However, wide wells on the c-plane suffer from a poor wavefunction overlap and low radiative recombination rate because of the QCSE. As previously mentioned, semipolar and nonpolar orientations exhibit a reduction or elimination of this effect, therefore, wider wells can be grown on these planes since efficiency does not significantly degrade from QCSE in thicker wells.[20] Results on $(20\bar{2}\bar{1})$ and $(30\bar{3}\bar{1})$ semipolar GaN showed efficient and low droop performance for thick QWs [33], [64]. In addition, semipolar and nonpolar orientations exhibit faster recombination even for thinner QWs, and that allows as well an increase of J at maximum EQE.

I.4.c.ii Green Gap:

The "green gap" refers to the drop in efficiency for green-yellow emission in LEDs as observed in **Figure 4-5**.

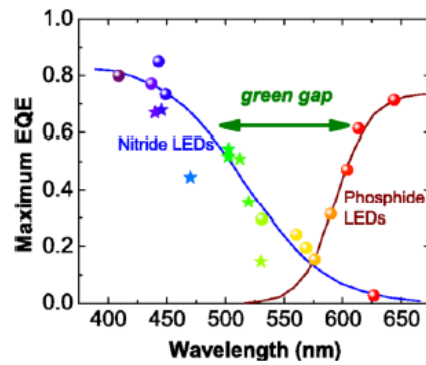


Figure 4-5: Maximum EQE as a function of the wavelength emission of different nitride and phosphide LEDs illustrating the green gap problem [65].

Increasing the In content in the active region leads to InGaN inhomogeneity and defects, which cause the reduction of efficiency. Additionally, the strain induced by the increase of In leads to more QCSE causing an early efficiency droop at a lower current. Various explanations are given for the green gap as it is still an ongoing investigation. However, a few solutions were suggested to tackle this problem such as a high-quality MQW structure. The reduction of defect density has proven to contribute to the improvement of the IQE at high wavelengths hence reducing the green gap effect.[53] Or by using the semipolar/non-polar planes which help eliminate the QCSE issue. Additionally, semipolar planes proved a high indium incorporation [66] which gives promising solutions for the green gap.

I.4.c.iii QCSE:

The previously explained QCSE phenomenon has a direct impact on the LED performance. When applying a forward bias in an LED, the QCSE will be dominating at low current density resulting in a red shift and a longer recombination lifetime. Despite being able to reach a longer wavelength compared to non-polar, when excess carriers are injected at a higher current, a screening of the electric field takes place leading to a wavelength blue shift as demonstrated in **Figure 4-6** [31].

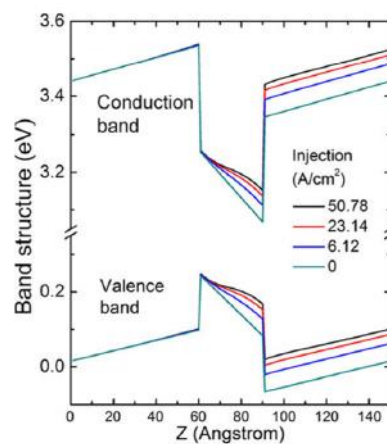


Figure 4-6: The screening of the internal electric field at different injection currents. [44]

The wavelength blueshifting prevents reaching longer wavelength emission at higher current which limits the LED color performance. In addition, a slower recombination rate is an important problem when using InGaN/GaN LEDs for data communication applications. However, the reduction of

electron-hole wavefunction overlap has a low effect on the IQE_{max} as it impacts the radiative and the non-radiative recombinations, hence the max IQE remains the same when considering the ABC model. On the other hand, because of the wavefunction separation, the decay time of the recombination increases so the carriers tend to accumulate in the QW region and the carrier density corresponding to the maximum EQE is reached at a lower current density.[53], [67] This is also directly related to the efficiency droop appearing at lower current density when aiming higher wavelength.

Similarly, as for the droop and green gap problems, the use of the semipolar and nonpolar orientations might lead to an improvement in the device performance as it can significantly improve the wavefunction overlapping when mitigating the QCSE. This can offer promising solutions for VLC applications as it proves a higher modulation bandwidth especially at low current densities proved along these orientations.[68]

I.4.c.iv Thermal droop:

Thermal droop, also referred to as temperature-dependent efficiency droop, is the reduction of the LED efficiency as the operation temperature rises. The impact of this phenomenon is important to be taken into account however, the cause is yet to be understood. David et al. point to transport effects ruling out a temperature dependence of IQE by showing that the droop is affected by the active region recombination [53], [69]. Having a thick QW on semipolar GaN was able to reduce the thermal effect when increasing the current density from 1 to 40 A/cm² which proved superior performance compared to conventional c-plane LEDs for identical conditions. [70]

I.5 μLED

In recent years, the rapid development of μLED-based display applications and μLED-based data communication applications further promotes the outbreak of μLED market[71]. Despite the remarkable features that μLEDs can offer, it is evident that some obstacles accompany their implementation. For example, the key technologies for color conversion and mass transfer, and the decrease of efficiency with size reduction. Focusing on the latter problem, estimation demonstrated a higher efficiency for μLEDs, which is one of the main advantages over LEDs in displays, but it has not been achieved experimentally until today. Hwang et al. [72] demonstrated the best reported blue 10x10μm² μLED on patterned sapphire with an EQE of 40.02% which was still lower than 48.6% observed for a 60x60μm². LEDs suffer a reduction of efficiency when their sizes decrease to a few

micrometers. Oliver et al. showed that the max EQE is reached at higher current densities having a lower value as the LED size decreases as illustrated in **Figure 5-1.a.**[73]

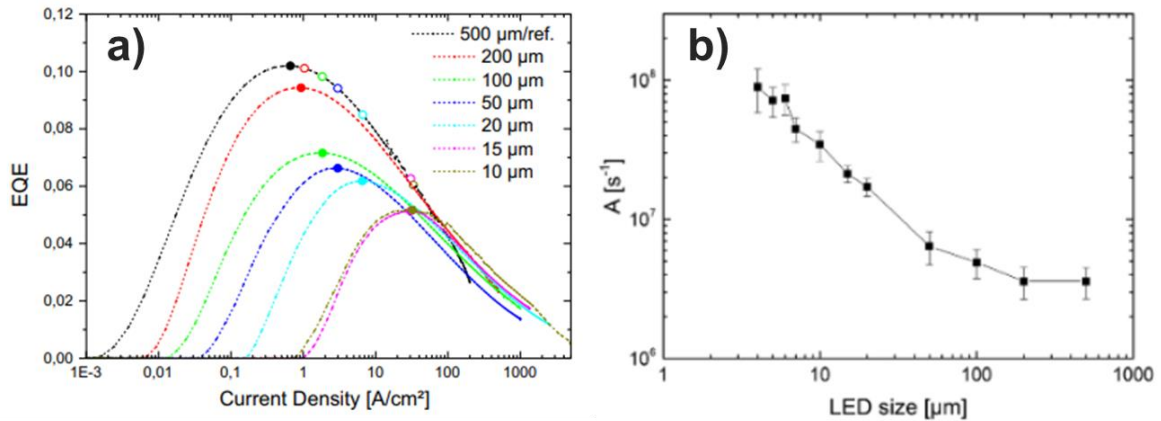


Figure 5-1: a) EQE curves of the different μ LED sizes where the experimental and calculated maximum are indicated by the solid and empty circles, respectively. b) The extracted SRH parameter (A) for the different μ LED sizes.[73], [74]

This was explained by the sidewall defects impacting more significantly the efficiency for μ LEDs because of the increase of the perimeter/surface ratio with respect to bigger sizes LEDs. The defects on the sidewalls are generally induced by the dry etching when defining the LED dimensions, called a mesa. μ LEDs proved to have a large carrier diffusion length (μm range) which facilitates the carriers to reach the mesa edges when current is injected in the quantum wells. Therefore, these defects consume part of the charge carriers, which leads to SRH recombination hence, a decrease in efficiency. **Figure 5-1. b** presents the increase of the value of the SRH coefficient A extracted from a fit of experimental data with the ABC model with the decrease of LED sizes[74]. To improve the efficiency of the μ LEDs, several surface passivation and treatment approaches have been used to successfully mitigate the impact of the sidewall defects.[75], [76] Wong et al. showed an improved efficiency for a $20 \times 20 \mu\text{m}^2$ μ LED when its sidewalls were passivated with SiO_2 by using an atomic layer deposition (**Figure 5-2**).[77]

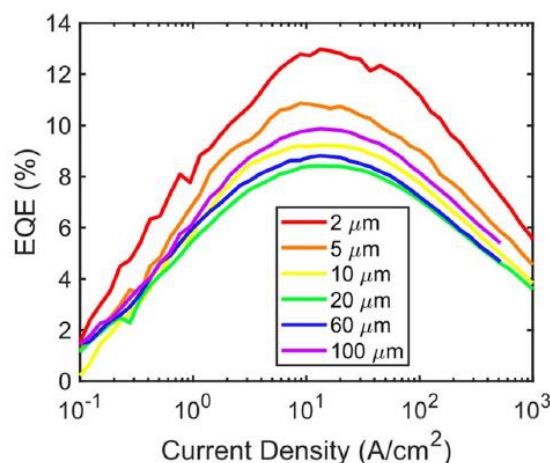


Figure 5-2: EQE curves for different μ LED sizes.[78]

In this work, we will focus on the efficiency decrease at longer wavelengths as we aim to fabricate RGB μ LEDs. However, the efficiency of In-rich green-red μ LEDs is also impacted by several other factors listed in section 1.4. By changing the GaN crystallographic orientation to semipolar instead of

the commercially used polar plane, we can increase the In incorporation. A study on the In incorporation dependence for different orientations has proved the best performance for $(10\bar{1}1)$ among the rest as illustrated in **Figure 5-3**.

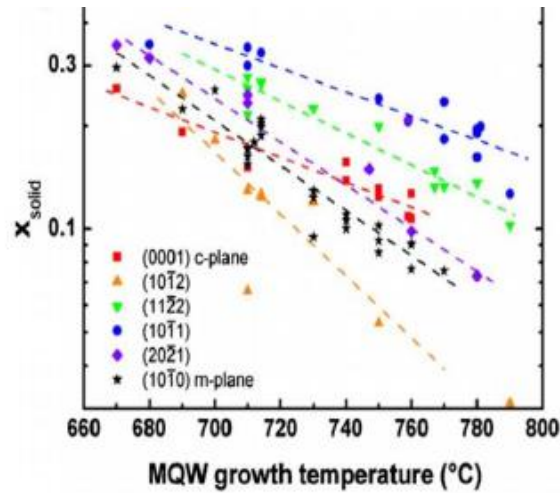


Figure 5-3: The In incorporation with respect to the MQW growth temperature for the different GaN crystallographic orientations.

As mentioned earlier, the semipolar orientation offers also a good solution to decrease the QCSE, as well as the possibility of reducing the droop by growing thicker wells. Hence, the ability to reach longer wavelength emission.

Chen *et al.* have observed decent J-V characteristics for a $50 \times 50 \mu\text{m}^2$ semipolar $(20\bar{2}1)$ μLED grown on sapphire (**Figure 5-4. a**) and the proof of a lower droop at high current density. Furthermore, they have been able to demonstrate a narrow spectrum with a full width at half maximum (FWHM) and wavelength stability [79] when increasing the current density (**Figure 5-4. b**). Similar improvements in the semipolar μLED characteristics compared to the c-plane orientation were observed for different semipolar orientations.[80], [81] Green $(20\bar{2}1)$ μLED grown on sapphire was also achieved with a 2.5% EQE by Khoury et al.[82]

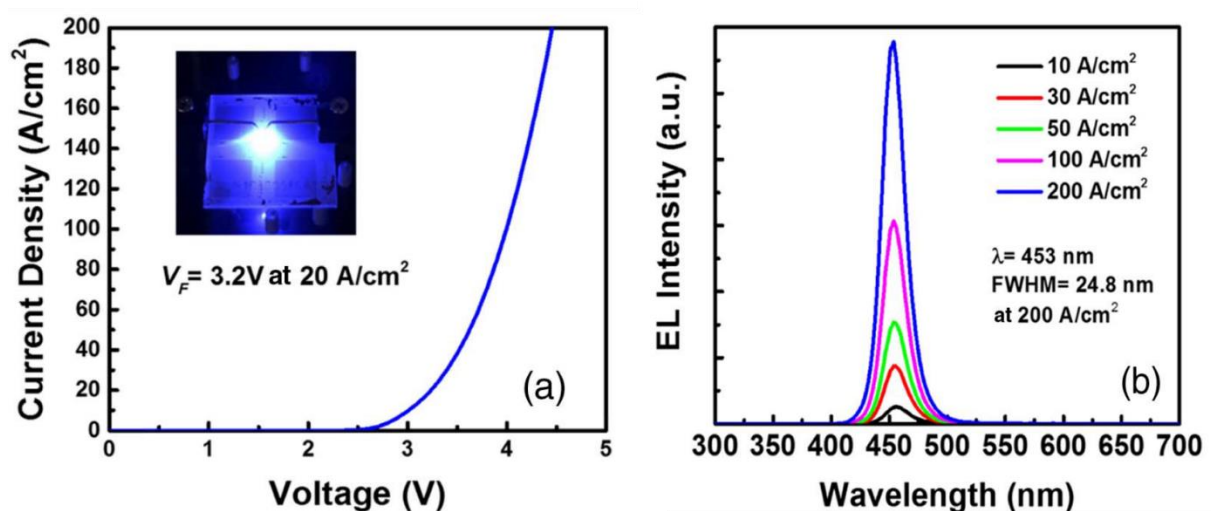


Figure 5-4: a) Current density-voltage characteristics of a $50 \times 50 \mu\text{m}^2$ semipolar μLED with its corresponding EL spectra while increasing J in b).

Besides display application, μ LEDs grown on semipolar substrates were able to compete in data communication by ensuring shorter lifetime due to the better electron-hole wavefunction overlapping than c -plane μ LEDs which led to a larger bandwidth at lower currents and thus faster frequency responses. [68], [83]–[86]

I.6 Heteroepitaxial Semipolar Growth

As elaborated previously, semipolar ($10\bar{1}1$) GaN orientation shows great promise to improve optoelectronic devices performance compared to c -plane. Due to the high cost and limited size of freestanding GaN, semipolar GaN is grown on foreign substrates with all the challenges it implies. However, independently of the substrate used (Si or sapphire), growing heteroepitaxially induces a large density of TDs and BSFs. Several attempts to reduce these defects such as growing low-temperature AlN interlayers helped block the BSF propagation.[87] This technique was only efficient for low semipolar angle orientations. Another one is using the epitaxial lateral overgrowth (ELO) and asymmetric lateral epitaxy, which were similar to the c -plane defect reduction techniques. These techniques were able to reduce the BSFs and TDs to the order of 10^5 cm^{-1} and 10^8 cm^{-2} respectively[88]. Nonetheless, these techniques were not efficient in eliminating the BSFs or even reducing them. Therefore, using the knowledge gained on polar GaN, the inclined growth approach was adopted, which consists of patterning the substrate to achieve inclined c -plane facets where GaN will be nucleated.[89] Following this nucleation, GaN bands (stripes) will be formed and coalesced to reach a 2D surface. The inclined approach on patterned sapphire substrates reduced the density of TDs to 10^7 cm^{-2} and BSFs to 10^2 cm^{-1} . [90] This is due to the reduced interaction between GaN and the substrate, which normally leads to the generation of these defects.

Several semipolar orientations were grown on patterned sapphire substrates with their corresponding inclination angle (seen in **Table 6-1**). The inclined angle from the c -plane is needed to achieve the specific semipolar orientations. The growth on patterned sapphire proved a lower defect density than the techniques implemented on Si substrates.

Semipolar GaN top plane	Angle to c -plane	Foreign substrate	Sidewall nucleation facet	Required substrate surface facet	Angle between the sidewall facet and the surface
$\{10\bar{1}1\}$	61.9°	Silicon	$\{111\}$	$\{001\}$ 7° off	61.7°
$\{11\bar{2}2\}$	58.4°	Silicon	$\{111\}$	$\{113\}$	60.5°
$\{11\bar{2}2\}$	58.4°	Sapphire	$\{0001\}$ c -plane	$\{10\bar{1}2\}$ r -plane	57.6°
$\{10\bar{1}1\}$	61.9°	Sapphire	$\{0001\}$ c -plane	$\{11\bar{2}6\}$ n -plane	61.2°

Table 6-1: The different semipolar orientations achieved by growing on foreign substrates with an inclination angle.[91]

However, silicon can be available commercially at low cost reaching 12" which is double the size found commercially for sapphire. Another advantage is the easy removal of Si using grinding and wet etching methods instead of laser lift-off (LLO) in the case of sapphire[92]. Therefore, investigations have been performed to explore the growth of ($10\bar{1}1$) on patterned Si.

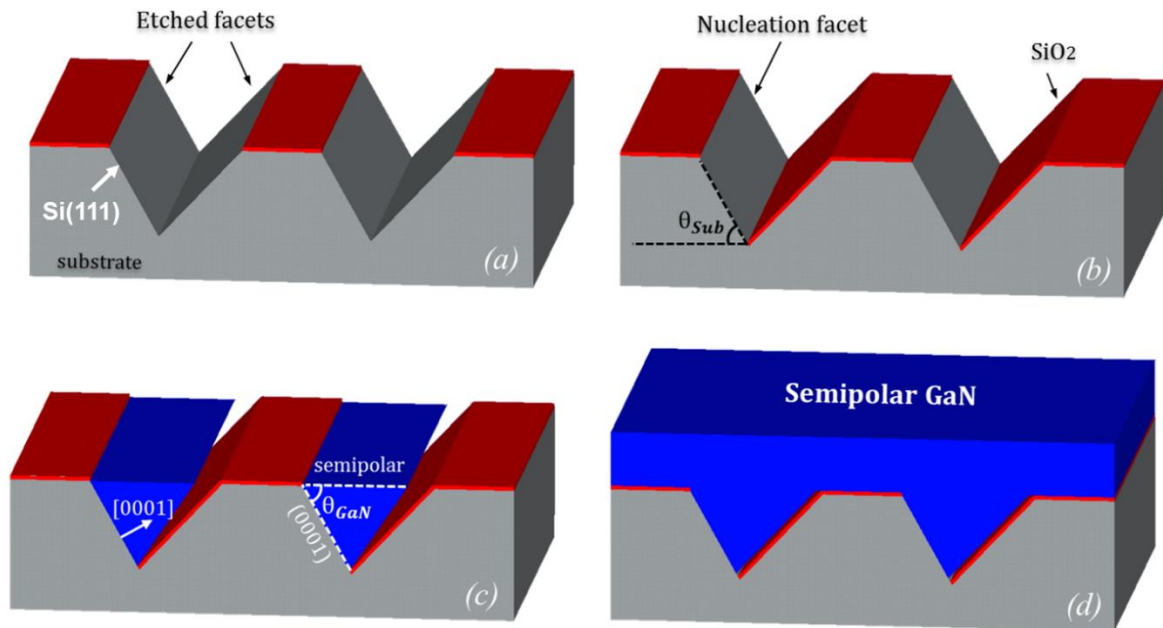


Figure 6-1: Schematic of the silicon (001)7° off substrate processing steps: (a) KOH anisotropic etching and (b) inclined IBS deposition. This is followed by the inclined growth of GaN stripes in c) and d) after coalescence.[93]

This approach as illustrated with its different steps in **Figure 6-1**, is achieved on silicon substrates. It is based on processing V-grooves onto the Si substrate, which are etched in a way to reveal (111) crystal facet (**Figure 6-1. a**) which is known as a good nucleation facet for c-plane growth.[91] An inclined SiO₂ deposition on the entire surface except on the facet where GaN will be grown as illustrated in **Figure 6-1. b**. GaN is grown selectively on the nucleated facet in an inclined direction along the c-direction until reaching coalescence **Figure 6-1 c-d**.

This method accomplished by Khoury et al. showed that TDs propagated along the +c growth direction during the stripe growth **Figure 6-1. c**. Once the TDs meet an inclined facet, they bend and propagate in the basal plane. This approach helped reduce the density of TDs by limiting their propagation towards the coalesced surface. This was consistent with Tian et al.[94] that proved numerically and experimentally that using patterned substrate along with lateral growth helps in reducing the strain and the dislocation density.

However, when growing GaN on Si at high temperatures, a chemical reaction, referred to as “meltback etching”, between Ga and Si atoms may occur when GaN diffuses into the Si facet. This reaction can propagate toward the surface and perturb it. To prevent it, an AlN layer is typically grown on top of the Si substrate which was not sufficient on patterned as it is on planar substrates. Khoury et al. suggested that fabrication errors of the patterns might be one of the causes that the AlN layer is not perfectly covering the Si. The meltback was then mitigated by a variation of carrier gas fraction (H₂/N₂) during growth.

Nonetheless, still not sufficient enough to block all the TDs (seen in **Figure 6-2. a**) that are disadvantageous for device fabrication as TDs act as non-radiative recombination centers and decrease quantum efficiency[95], and result in lowering crystal quality.[96]–[98] Another approach was adopted by Mantach et al. to further reduce the dislocation by using a silicon-on-insulator (SOI) substrate as presented in **Figure 6-2.b**.[99]

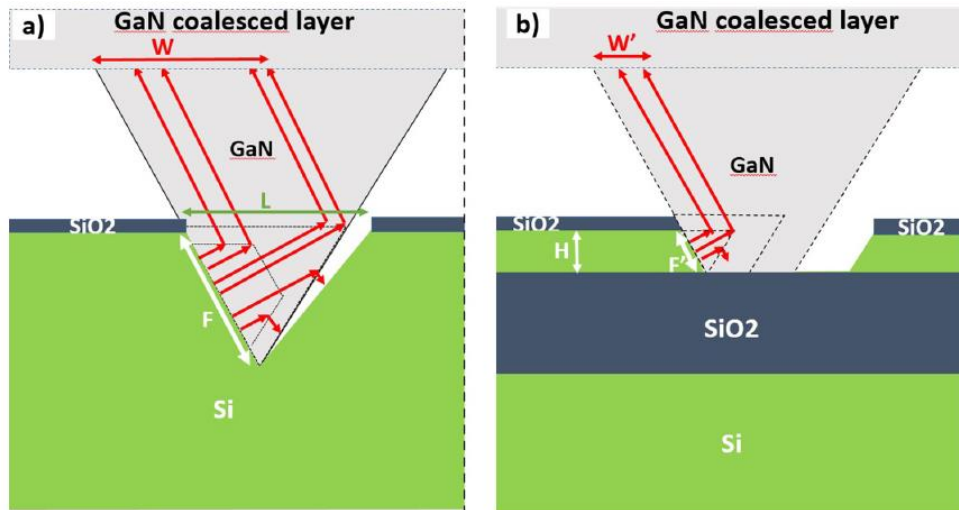


Figure 6-2: Scheme showing the dislocation bending phenomenon and the high dislocation region “W” of a) on Si buffer substrate and b) on SOI substrate.[99]

In addition, having a thin Si layer will help further mitigate or even eliminate the meltback etching formation by reducing the surface of exposed Si in case of imperfect AlN coverage. Initially, the principle consisted of an SOI substrate having a 500nm silicon oxide (SiO₂) buffer oxide (BOX) with a 150nm top Si (001) layer having an angle of 6° off instead of 7° as supposed to for (10 $\bar{1}$ 1) orientation due to the unavailability of the latter one. The schematic of **Figure 6-3** demonstrates the silicon layer having a 7° off-axis.

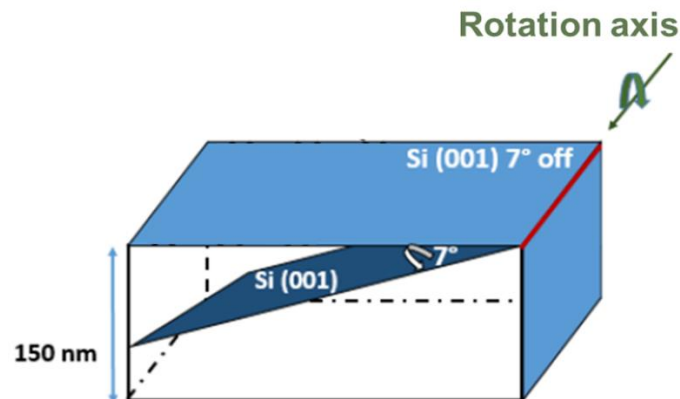


Figure 6-3: A schematic demonstrating the 150nm thick silicon layer having a 7° off axis.[49]

A thin SiO₂ layer is then deposited on the top Si layer to be then etched along with the Si layer to form the needed trenches for subsequent inclined growth on Si (111) facets. Although using an SOI substrate proved to reduce the defect density, TDs were still able to escape and reach the surface. Therefore, an increase in thickness of the deposited SiO₂ layer on top was found to block the propagated defects as presented in the schematic of **Figure 6-4.a**. This approach is known as aspect-ratio-trapping (ART)-SOI.

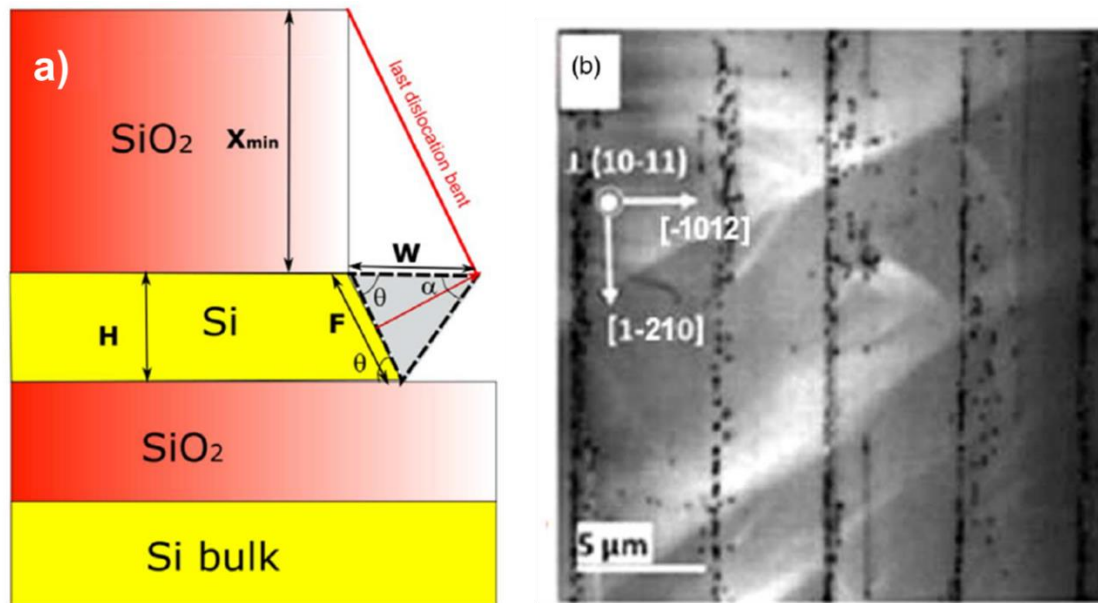


Figure 6-4: a) A schematic of the ART-SOI approach illustrating the dislocation bending. b) CL image at room temperature showing the TDs (black dots) along the coalescence line of the stripes. [12]

The distribution of the TDs is along the stripes at the coalescence line as illustrated by the black dots in the CL image of **Figure 6-4. b**. Although not observed at room temperature, the BSFs are seen as white lines along the stripes near the coalescence line at low-temperature CL. Mantach et al. were able to reach a TDs density below 10^7 cm^{-2} which is similar to the c-plane one and a BSF density of 10^5 cm^{-1} . They have achieved a state-of-the-art level in terms of defect density on semipolar GaN grown on SOI.

Hence, in this work, our goal is first to find the right conditions to reproduce and optimize the aforementioned regular and ART-SOI approaches to reach similar defect densities. The next step is to proceed toward device fabrication, to fabricate μLEDs down to $4 \times 4 \mu\text{m}^2$. This will require locating the μLEDs in a defect-free area, between the BSFs lines and TDs described in **Figure 6-4.b**. Fabricating a μLED on a high crystal quality substrate, in addition to the previously reported advantages of the $(10\bar{1}1)$ semipolar, opens the possibility of achieving a μLED with high performance and efficiency at longer wavelengths on an industry-compatible substrate.

I.7 References

- [1] M. G. Craford, « From Holonyak to Today », *Proc. IEEE*, vol. 101, n° 10, p. 2170-2175, oct. 2013, doi: 10.1109/JPROC.2013.2274911.
- [2] S. Nakamura, T. Mukai, M. S. M. Senoh, et N. I. N. Iwasa, « Thermal Annealing Effects on P-Type Mg-Doped GaN Films », *Jpn. J. Appl. Phys.*, vol. 31, n° 2B, p. L139, févr. 1992, doi: 10.1143/JJAP.31.L139.
- [3] H. Amano, M. Kito, K. Hiramatsu, et I. Akasaki, « P-Type Conduction in Mg-Doped GaN Treated with Low-Energy Electron Beam Irradiation (LEEBI) », *Jpn. J. Appl. Phys.*, vol. 28, n° 12A, p. L2112, déc. 1989, doi: 10.1143/JJAP.28.L2112.
- [4] H. Amano, N. Sawaki, I. Akasaki, et Y. Toyoda, « Metalorganic vapor phase epitaxial growth of a high-quality GaN film using an AlN buffer layer », *Appl. Phys. Lett.*, vol. 48, n° 5, p. 353-355, févr. 1986, doi: 10.1063/1.96549.
- [5] Z. Chen, S. Yan, et C. Danesh, « MicroLED technologies and applications: characteristics, fabrication, progress, and challenges », *J. Phys. Appl. Phys.*, vol. 54, n° 12, p. 123001, mars 2021, doi: 10.1088/1361-6463/abcfe4.
- [6] Z. Lu *et al.*, « Recent progress of InGaN-based red light emitting diodes », *Micro Nanostructures*, vol. 183, p. 207669, nov. 2023, doi: 10.1016/j.micrna.2023.207669.
- [7] J. Y. Lin et H. X. Jiang, « Development of microLED », *Appl. Phys. Lett.*, vol. 116, n° 10, p. 100502, mars 2020, doi: 10.1063/1.5145201.
- [8] C. A. Hurni, « Bulk GaN flip-chip violet light-emitting diodes with optimized efficiency for high-power operation ».
- [9] Q. Lv *et al.*, « Realization of Highly Efficient InGaN Green LEDs with Sandwich-like Multiple Quantum Well Structure: Role of Enhanced Interwell Carrier Transport », *ACS Photonics*, vol. 6, n° 1, p. 130-138, janv. 2019, doi: 10.1021/acsp Photonics.8b01040.
- [10] A. Dussaigne *et al.*, « Full InGaN red (625 nm) micro-LED (10 μ m) demonstration on a relaxed pseudo-substrate », *Appl. Phys. Express*, vol. 14, n° 9, p. 092011, sept. 2021, doi: 10.35848/1882-0786/ac1b3e.
- [11] P. Li *et al.*, « Size-independent peak external quantum efficiency (>2%) of InGaN red micro-light-emitting diodes with an emission wavelength over 600 nm », *Appl. Phys. Lett.*, vol. 119, n° 8, p. 081102, août 2021, doi: 10.1063/5.0061940.
- [12] R. Mantach, P. Vennéguès, J. Zuniga-Perez, P. De Mierry, M. Portail, et G. Feuillet, « Freestanding-quality dislocation density in semipolar GaN epilayers grown on SOI: aspect ratio trapping », *Appl. Phys. Express*, vol. 13, n° 11, p. 115504, nov. 2020, doi: 10.35848/1882-0786/abc1cd.
- [13] C. Bayo et M. Ángel, « Theory of elasticity and electric polarization effects in the group-III nitrides », 2013, Consulté le: 10 août 2023. [En ligne]. Disponible sur: <https://hdl.handle.net/10468/1344>
- [14] T. Wonglakhon et D. Zahn, « Interaction potentials for modelling GaN precipitation and solid state polymorphism », *J. Phys. Condens. Matter*, vol. 32, n° 20, p. 205401, mai 2020, doi: 10.1088/1361-648X/ab6cbe.
- [15] I. Vurgaftman et J. R. Meyer, « Band parameters for nitrogen-containing semiconductors », *J. Appl. Phys.*, vol. 94, n° 6, p. 3675-3696, sept. 2003, doi: 10.1063/1.1600519.
- [16] A. R. Arehart, T. Homan, M. H. Wong, C. Poblenz, J. S. Speck, et S. A. Ringel, « Impact of N- and Ga-face polarity on the incorporation of deep levels in n-type GaN grown by molecular beam epitaxy », *Appl. Phys. Lett.*, vol. 96, n° 24, p. 242112, juin 2010, doi: 10.1063/1.3453660.
- [17] F. Tuomisto *et al.*, « Polarity dependent properties of GaN layers grown by hydride vapor phase epitaxy on GaN bulk crystals », *Phys. Status Solidi B*, vol. 240, n° 2, p. 289-292, 2003, doi: 10.1002/pssb.200303259.
- [18] O. Ambacher *et al.*, « Two-dimensional electron gases induced by spontaneous and piezoelectric polarization charges in N- and Ga-face AlGaIn/GaN heterostructures », *J. Appl. Phys.*, vol. 85, n° 6, p. 3222-3233, mars 1999, doi: 10.1063/1.369664.
- [19] A. Kapoor, « Core-shell InGaN/GaN wires for flexible LEDs ».

- [20] M. Monavarian, A. Rashidi, et D. Feezell, « A Decade of Nonpolar and Semipolar III-Nitrides: A Review of Successes and Challenges », *Phys. Status Solidi A*, p. 1800628, déc. 2018, doi: 10.1002/pssa.201800628.
- [21] A. E. Romanov, T. J. Baker, S. Nakamura, J. S. Speck, et ERATO/JST UCSB Group, « Strain-induced polarization in wurtzite III-nitride semipolar layers », *J. Appl. Phys.*, vol. 100, n° 2, p. 023522, juill. 2006, doi: 10.1063/1.2218385.
- [22] I. Ho et G. B. Stringfellow, « Solid phase immiscibility in GaInN », *Appl. Phys. Lett.*, vol. 69, n° 18, p. 2701-2703, oct. 1996, doi: 10.1063/1.117683.
- [23] T. Matsuoka, « Calculation of unstable mixing region in wurtzite $\text{In}_{1-x-y}\text{Ga}_x\text{Al}_y\text{N}$ », *Appl. Phys. Lett.*, vol. 71, n° 1, p. 105-106, juill. 1997, doi: 10.1063/1.119440.
- [24] V. A. Elyukhin, E. A. Avrutin, J. H. Marsh, et E. L. Portnoi, « Decomposition and stability of group-III nitride ternary cubic spontaneously ordered alloys », *IEEE J. Sel. Top. Quantum Electron.*, vol. 4, n° 3, p. 531-536, mai 1998, doi: 10.1109/2944.704114.
- [25] A. Koukitsu et H. Seki, « Thermodynamic study on phase separation during MOVPE growth of $\text{In}_x\text{Ga}_{1-x}\text{N}$ ».
- [26] T. Saito et Y. Arakawa, « Atomic structure and phase stability of $\text{In}_x\text{Ga}_{1-x}\text{N}$ random alloys calculated using a valence-force-field method », *Phys. Rev. B*, vol. 60, n° 3, p. 1701-1706, juill. 1999, doi: 10.1103/PhysRevB.60.1701.
- [27] C. J. Humphreys *et al.*, « The atomic structure of polar and non-polar InGaN quantum wells and the green gap problem », *Ultramicroscopy*, vol. 176, p. 93-98, mai 2017, doi: 10.1016/j.ultramic.2017.01.019.
- [28] C. Weisbuch, S. Nakamura, Y.-R. Wu, et J. S. Speck, « Disorder effects in nitride semiconductors: impact on fundamental and device properties », *Nanophotonics*, vol. 10, n° 1, p. 3-21, nov. 2020, doi: 10.1515/nanoph-2020-0590.
- [29] S. F. Chichibu *et al.*, « Origin of defect-insensitive emission probability in In-containing (Al,In,Ga)N alloy semiconductors », *Nat. Mater.*, vol. 5, n° 10, p. 810-816, oct. 2006, doi: 10.1038/nmat1726.
- [30] A. David, « Long-Range Carrier Diffusion in (In , Ga) N Quantum Wells and Implications from Fundamentals to Devices », *Phys. Rev. Appl.*, vol. 15, n° 5, p. 054015, mai 2021, doi: 10.1103/PhysRevApplied.15.054015.
- [31] W.-C. Miao *et al.*, « Modified Distributed Bragg Reflectors for Color Stability in InGaN Red Micro-LEDs », *Nanomaterials*, vol. 13, n° 4, p. 661, févr. 2023, doi: 10.3390/nano13040661.
- [32] Z. Zhuang, D. Iida, et K. Ohkawa, « InGaN-based red light-emitting diodes: from traditional to micro-LEDs », *Jpn. J. Appl. Phys.*, vol. 61, n° SA, p. SA0809, janv. 2022, doi: 10.35848/1347-4065/ac1a00.
- [33] D. F. Feezell, J. S. Speck, S. P. DenBaars, et S. Nakamura, « Semipolar ($\bar{1}10$) InGaN/GaN Light-Emitting Diodes for High-Efficiency Solid-State Lighting », *J. Disp. Technol.*, vol. 9, n° 4, p. 190-198, avr. 2013, doi: 10.1109/JDT.2012.2227682.
- [34] V. N. Bessolov, E. V. Konenkova, S. A. Kukushkin, A. V. Osipov, et S. N. Rodin, « SEMIPOLAR GALLIUM NITRIDE ON SILICON: TECHNOLOGY AND PROPERTIES », p. 19.
- [35] K. Kumakura, T. Makimoto, N. Kobayashi, T. Hashizume, T. Fukui, et H. Hasegawa, « Minority carrier diffusion length in GaN: Dislocation density and doping concentration dependence », *Appl. Phys. Lett.*, vol. 86, n° 5, p. 052105, janv. 2005, doi: 10.1063/1.1861116.
- [36] A. E. Romanov *et al.*, « Basal plane misfit dislocations and stress relaxation in III-nitride semipolar heteroepitaxy », *J. Appl. Phys.*, vol. 109, n° 10, p. 103522, mai 2011, doi: 10.1063/1.3590141.
- [37] J. Matthews, « Defects in epitaxial multilayers I. Misfit dislocations », *J. Cryst. Growth*, vol. 27, p. 118-125, déc. 1974, doi: 10.1016/0022-0248(74)90424-2.
- [38] P. C. Barbier, « Epitaxie de GaN sur substrat de graphène ».
- [39] C. Stampfl et C. G. Van de Walle, « Energetics and electronic structure of stacking faults in AlN, GaN, and InN », *Phys. Rev. B*, vol. 57, n° 24, p. R15052-R15055, juin 1998, doi: 10.1103/PhysRevB.57.R15052.

- [40] J. Lähnemann, U. Jahn, O. Brandt, T. Flissikowski, P. Dogan, et H. T. Grahn, « Luminescence associated with stacking faults in GaN », *J. Phys. Appl. Phys.*, vol. 47, n° 42, p. 423001, oct. 2014, doi: 10.1088/0022-3727/47/42/423001.
- [41] M. Monavarian, « Beyond conventional c-plane GaN-based light emitting diodes: A systematic exploration of LEDs on semi-polar orientations », p. 314.
- [42] M. Shiojiri, C. C. Chuo, J. T. Hsu, J. R. Yang, et H. Saijo, « Structure and formation mechanism of V defects in multiple InGaN/GaN quantum well layers », *J. Appl. Phys.*, vol. 99, n° 7, p. 073505, avr. 2006, doi: 10.1063/1.2180532.
- [43] A. Hangleiter *et al.*, « Suppression of Nonradiative Recombination by V-Shaped Pits in GaInN / GaN Quantum Wells Produces a Large Increase in the Light Emission Efficiency », *Phys. Rev. Lett.*, vol. 95, n° 12, p. 127402, sept. 2005, doi: 10.1103/PhysRevLett.95.127402.
- [44] X. H. Wu *et al.*, « Structural origin of V-defects and correlation with localized excitonic centers in InGaN/GaN multiple quantum wells », *Appl. Phys. Lett.*, vol. 72, n° 6, p. 692-694, févr. 1998, doi: 10.1063/1.120844.
- [45] A. V. Lobanova, A. L. Kolesnikova, A. E. Romanov, S. Yu. Karpov, M. E. Rudinsky, et E. V. Yakovlev, « Mechanism of stress relaxation in (0001) InGaN/GaN via formation of V-shaped dislocation half-loops », *Appl. Phys. Lett.*, vol. 103, n° 15, p. 152106, oct. 2013, doi: 10.1063/1.4824835.
- [46] P. H. Weidlich, M. Schnedler, H. Eisele, U. Strauß, R. E. Dunin-Borkowski, et Ph. Ebert, « Evidence of deep traps in overgrown v-shaped defects in epitaxial GaN layers », *Appl. Phys. Lett.*, vol. 103, n° 6, p. 062101, août 2013, doi: 10.1063/1.4816969.
- [47] A. Lochthofen *et al.*, « Electrical investigation of V-defects in GaN using Kelvin probe and conductive atomic force microscopy », *Appl. Phys. Lett.*, vol. 93, n° 2, p. 022107, juill. 2008, doi: 10.1063/1.2953081.
- [48] L. C. Le *et al.*, « Carriers capturing of V-defect and its effect on leakage current and electroluminescence in InGaN-based light-emitting diodes », *Appl. Phys. Lett.*, vol. 101, n° 25, p. 252110, déc. 2012, doi: 10.1063/1.4772548.
- [49] R. Mantach, « Croissance de pseudo-substrats GaN semi polaire (10-11) sur silicium sur isolant (SOI) », Université Côte d'Azur.
- [50] C. Haller, J.-F. Carlin, G. Jacopin, D. Martin, R. Butté, et N. Grandjean, « Burying non-radiative defects in InGaN underlayer to increase InGaN/GaN quantum well efficiency », *Appl. Phys. Lett.*, vol. 111, n° 26, p. 262101, déc. 2017, doi: 10.1063/1.5007616.
- [51] C. Haller *et al.*, « GaN surface as the source of non-radiative defects in InGaN/GaN quantum wells », *Appl. Phys. Lett.*, vol. 113, n° 11, p. 111106, sept. 2018, doi: 10.1063/1.5048010.
- [52] T. Akasaka, H. Gotoh, T. Saito, et T. Makimoto, « High luminescent efficiency of InGaN multiple quantum wells grown on InGaN underlying layers », *Appl. Phys. Lett.*, vol. 85, n° 15, p. 3089-3091, oct. 2004, doi: 10.1063/1.1804607.
- [53] A. David, N. G. Young, C. Lund, et M. D. Craven, « Review—The Physics of Recombinations in III-Nitride Emitters », *ECS J. Solid State Sci. Technol.*, vol. 9, n° 1, p. 016021, janv. 2020, doi: 10.1149/2.0372001JSS.
- [54] R. N. Hall, « Electron-Hole Recombination in Germanium », *Phys. Rev.*, vol. 87, n° 2, p. 387-387, juill. 1952, doi: 10.1103/PhysRev.87.387.
- [55] W. Shockley et W. T. Read, « Statistics of the Recombinations of Holes and Electrons », *Phys. Rev.*, vol. 87, n° 5, p. 835-842, sept. 1952, doi: 10.1103/PhysRev.87.835.
- [56] E. F. Schubert, *Light-Emitting Diodes (3rd Edition)*. E. Fred Schubert, 2018.
- [57] F. A. Ponce et D. P. Bour, « Nitride-based semiconductors for blue and green light-emitting devices », *Nature*, vol. 386, n° 6623, p. 351-359, mars 1997, doi: 10.1038/386351a0.
- [58] W. Götz, N. M. Johnson, C. Chen, H. Liu, C. Kuo, et W. Imler, « Activation energies of Si donors in GaN », *Appl. Phys. Lett.*, vol. 68, n° 22, p. 3144-3146, mai 1996, doi: 10.1063/1.115805.
- [59] Y. Wang, « Fabrication and Characterization of Gallium Nitride Based Diodes », Graduate Faculty of Auburn University, Auburn, Alabama, 2011.
- [60] F. Olivier, « Etude des caractéristiques électro-optiques de micro-LED GaN pour application aux micro-écrans haute-luminance ».
- [61] Q. Z. Liu et S. S. Lau, « A REVIEW OF THE METAL±GaN CONTACT TECHNOLOGY ».
- [62] T. Fujii, « Increase in the extraction efficiency of GaN-based light-emitting diodes.pdf ».

- [63] J. Iveland, L. Martinelli, J. Peretti, J. S. Speck, et C. Weisbuch, « Direct Measurement of Auger Electrons Emitted from a Semiconductor Light-Emitting Diode under Electrical Injection: Identification of the Dominant Mechanism for Efficiency Droop », *Phys. Rev. Lett.*, vol. 110, n° 17, p. 177406, avr. 2013, doi: 10.1103/PhysRevLett.110.177406.
- [64] D. L. Becerra *et al.*, « High-power low-droop violet semipolar (303⁻1⁻) InGa_N/Ga_N light-emitting diodes with thick active layer design », *Appl. Phys. Lett.*, vol. 105, n° 17, p. 171106, oct. 2014, doi: 10.1063/1.4900793.
- [65] M. Auf der Maur, « Efficiency Drop in Green InGa_N=Ga_N Light Emitting Diodes: The Role of Random Alloy Fluctuations ».
- [66] T. Wernicke *et al.*, « Indium incorporation and emission wavelength of polar, nonpolar and semipolar InGa_N quantum wells », *Semicond. Sci. Technol.*, vol. 27, n° 2, p. 024014, févr. 2012, doi: 10.1088/0268-1242/27/2/024014.
- [67] A. David et M. J. Grundmann, « Influence of polarization fields on carrier lifetime and recombination rates in InGa_N-based light-emitting diodes », *Appl. Phys. Lett.*, vol. 97, n° 3, p. 033501, juill. 2010, doi: 10.1063/1.3462916.
- [68] M. Monavarian *et al.*, « Impact of crystal orientation on the modulation bandwidth of InGa_N/Ga_N light-emitting diodes », *Appl. Phys. Lett.*, vol. 112, n° 4, p. 041104, janv. 2018, doi: 10.1063/1.5019730.
- [69] A. David, « Thermal droop in high-quality InGa_N LEDs ».
- [70] C.-C. Pan *et al.*, « Reduction in Thermal Droop Using Thick Single-Quantum-Well Structure in Semipolar (2⁻1⁻) Blue Light-Emitting Diodes », *Appl. Phys. Express*, vol. 5, n° 10, p. 102103, sept. 2012, doi: 10.1143/APEX.5.102103.
- [71] S. Hang *et al.*, « A review on the low external quantum efficiency and the remedies for Ga_N-based micro-LEDs », *J. Phys. Appl. Phys.*, vol. 54, n° 15, p. 153002, avr. 2021, doi: 10.1088/1361-6463/abd9a3.
- [72] D. Hwang, A. Mughal, C. D. Pynn, S. Nakamura, et S. P. DenBaars, « Sustained high external quantum efficiency in ultrasmall blue III–nitride micro-LEDs », *Appl. Phys. Express*, vol. 10, n° 3, p. 032101, mars 2017, doi: 10.7567/APEX.10.032101.
- [73] « Influence of size-reduction on the performances of Ga_N-based micro-LEDs for display application | Elsevier Enhanced Reader ». Consulté le: 16 février 2023. [En ligne]. Disponible sur: <https://reader.elsevier.com/reader/sd/pii/S0022231316308547?token=498369E7286369064FA5D62EC13A4A52A1E7DA32FDE37841E5A223BBF2D314FEE2F4C9CBEAE07EB3B4387412DB65F6A9&originRegion=eu-west-1&originCreation=20230216161806>
- [74] F. Olivier, A. Daami, C. Licitra, et F. Templier, « Shockley-Read-Hall and Auger non-radiative recombination in Ga_N based LEDs: A size effect study », *Appl. Phys. Lett.*, vol. 111, n° 2, p. 022104, juill. 2017, doi: 10.1063/1.4993741.
- [75] J. M. Smith *et al.*, « Comparison of size-dependent characteristics of blue and green InGa_N microLEDs down to 1 μm in diameter », *Appl. Phys. Lett.*, vol. 116, n° 7, p. 071102, févr. 2020, doi: 10.1063/1.5144819.
- [76] M. Sheen *et al.*, « Highly efficient blue InGa_N nanoscale light-emitting diodes », *Nature*, vol. 608, n° 7921, p. 56-61, août 2022, doi: 10.1038/s41586-022-04933-5.
- [77] M. S. Wong *et al.*, « High efficiency of III-nitride micro-light-emitting diodes by sidewall passivation using atomic layer deposition », *Opt. Express*, vol. 26, n° 16, p. 21324, août 2018, doi: 10.1364/OE.26.021324.
- [78] R. T. Ley *et al.*, « Revealing the importance of light extraction efficiency in InGa_N/Ga_N microLEDs via chemical treatment and dielectric passivation », *Appl. Phys. Lett.*, vol. 116, n° 25, p. 251104, juin 2020, doi: 10.1063/5.0011651.
- [79] S.-W. H. Chen *et al.*, « Full-color micro-LED display with high color stability using semipolar (20-21) InGa_N LEDs and quantum-dot photoresist », *Photonics Res.*, vol. 8, n° 5, p. 630, mai 2020, doi: 10.1364/PRJ.388958.
- [80] H. Li *et al.*, « Study of efficient semipolar (11-22) InGa_N green micro-light-emitting diodes on high-quality (11-22) Ga_N/sapphire template », *Opt. Express*, vol. 27, n° 17, p. 24154, août 2019, doi: 10.1364/OE.27.024154.

- [81] R.-H. Horng, S. Sinha, Y.-R. Wu, F.-G. Tarntair, J. Han, et D.-S. Wu, « Characterization of semi-polar (20 $\overline{2}$) InGa \overline{N} microLEDs », *Sci. Rep.*, vol. 10, n° 1, p. 15966, déc. 2020, doi: 10.1038/s41598-020-72720-1.
- [82] M. Khoury *et al.*, « 560 nm InGa \overline{N} micro-LEDs on low-defect-density and scalable (20-21) semipolar Ga \overline{N} on patterned sapphire substrates », *Opt. Express*, vol. 28, n° 12, p. 18150, juin 2020, doi: 10.1364/OE.387561.
- [83] G. N. Arvanitakis *et al.*, « Gb/s Underwater Wireless Optical Communications Using Series-Connected Ga \overline{N} Micro-LED Arrays », *IEEE Photonics J.*, vol. 12, n° 2, p. 1-10, avr. 2020, doi: 10.1109/JPHOT.2019.2959656.
- [84] S. Rajbhandari *et al.*, « A review of gallium nitride LEDs for multi-gigabit-per-second visible light data communications », *Semicond. Sci. Technol.*, vol. 32, n° 2, p. 023001, févr. 2017, doi: 10.1088/1361-6641/32/2/023001.
- [85] A. Rashidi, M. Monavarian, A. Aragon, A. Rishinaramangalam, et D. Feezell, « Nonpolar $\{m\}$ -Plane InGa \overline{N} /Ga \overline{N} Micro-Scale Light-Emitting Diode With 1.5 GHz Modulation Bandwidth », *IEEE Electron Device Lett.*, vol. 39, n° 4, p. 520-523, avr. 2018, doi: 10.1109/LED.2018.2803082.
- [86] A. Rashidi *et al.*, « High-Speed Nonpolar InGa \overline{N} /Ga \overline{N} LEDs for Visible-Light Communication », *IEEE Photonics Technol. Lett.*, vol. 29, n° 4, p. 381-384, févr. 2017, doi: 10.1109/LPT.2017.2650681.
- [87] A. Dadgar *et al.*, « Eliminating stacking faults in semi-polar Ga \overline{N} by AlN interlayers », *Appl. Phys. Lett.*, vol. 99, n° 2, p. 021905, juill. 2011, doi: 10.1063/1.3610467.
- [88] Z. Bougrioua *et al.*, « Reduction of stacking faults in (11 $\overline{2}$) and (11 $\overline{2}$) Ga \overline{N} films by ELO techniques and benefit on Ga \overline{N} wells emission », *Phys. Status Solidi A*, vol. 204, n° 1, p. 282-289, janv. 2007, doi: 10.1002/pssa.200673585.
- [89] P. Vennéguès, « Defect reduction methods for III-nitride heteroepitaxial films grown along nonpolar and semipolar orientations », *Semicond. Sci. Technol.*, vol. 27, n° 2, p. 024004, févr. 2012, doi: 10.1088/0268-1242/27/2/024004.
- [90] F. Tendille, « Ingénierie des défauts cristallins pour l'obtention ».
- [91] F. Scholz, « Semipolar Ga \overline{N} grown on foreign substrates: a review », *Semicond. Sci. Technol.*, vol. 27, n° 2, p. 024002, févr. 2012, doi: 10.1088/0268-1242/27/2/024002.
- [92] Z. Chen, S. Yan, et C. Danesh, « MicroLED technologies and applications: characteristics, fabrication, progress, and challenges », *J. Phys. Appl. Phys.*, vol. 54, n° 12, p. 123001, mars 2021, doi: 10.1088/1361-6463/abcfe4.
- [93] M. Khoury, « Metal Organic Vapor Phase Epitaxy of Semipolar Ga \overline{N} on Patterned Silicon Substrates », l'UNIVERSITE de Nice-Sophia Antipolis.
- [94] Z. Tian *et al.*, « Phosphor-free microLEDs with ultrafast and broadband features for visible light communications », *Photonics Res.*, vol. 9, n° 4, p. 452, avr. 2021, doi: 10.1364/PRJ.413069.
- [95] W. Chen *et al.*, « High-performance, single-pyramid micro light-emitting diode with leakage current confinement layer », *Appl. Phys. Express*, vol. 8, n° 3, p. 032102, mars 2015, doi: 10.7567/APEX.8.032102.
- [96] T. Hino, S. Tomiya, T. Miyajima, K. Yanashima, S. Hashimoto, et M. Ikeda, « Characterization of threading dislocations in Ga \overline{N} epitaxial layers », *Appl. Phys. Lett.*, vol. 76, n° 23, p. 3421-3423, juin 2000, doi: 10.1063/1.126666.
- [97] N. G. Weimann, L. F. Eastman, D. Doppalapudi, H. M. Ng, et T. D. Moustakas, « Scattering of electrons at threading dislocations in Ga \overline{N} », *J. Appl. Phys.*, vol. 83, n° 7, p. 3656-3659, avr. 1998, doi: 10.1063/1.366585.
- [98] C. Stampfl et C. G. Van de Walle, « Energetics and electronic structure of stacking faults in AlN, Ga \overline{N} , and In \overline{N} », *Phys. Rev. B*, vol. 57, n° 24, p. R15052-R15055, juin 1998, doi: 10.1103/PhysRevB.57.R15052.
- [99] R. Mantach *et al.*, « Semipolar (10-11) Ga \overline{N} growth on silicon-on-insulator substrates: Defect reduction and meltback etching suppression », *J. Appl. Phys.*, vol. 125, n° 3, p. 035703, janv. 2019, doi: 10.1063/1.5067375.

Chapter II

II.1 Introduction

In this chapter, we will discuss the growth of semipolar GaN on textured SOI substrates, building on the work of Mantach *et al.* First, I will introduce the epitaxial growth method used, including a brief explanation of the selective area growth approach. Then I will detail the patterning process in order to obtain textured SOI substrates enabling regular and high aspect ratio trapping (ART). Regular patterned SOI substrates will be used to investigate the impact of growth conditions on the formation of GaN stripes and their subsequent coalescence. The growth parameters will be then transferred to the ART SOI substrates and will be used as a starting point to further optimize them in order to get GaN coalescence on such deep textured substrates. The quality of the final semipolar GaN template on SOI will be assessed by secondary electron microscopy, atomic force microscopy, photoluminescence spectroscopy, and cathodoluminescence.

II.2 MOVPE

II.2.a Thomas Swan Reactor

Metal-Organic Vapor Phase Epitaxy (MOVPE) is widely and mostly employed in the III-V-based opto- and microelectronics industry as it can be used to manufacture several wafers with sizes ranging from 2 to 12 inches, with high growth rates and good crystal quality, at least for certain materials. For GaN deposition to take place, a chemical reaction occurs between organometallic (OM) compounds of the group-III column and the precursor of the group-V elements at the surface of the wafer.

The OM compounds are precursors made of a metallic atom bonded to an organic alkyl radical. In the case of III-N material growth, the precursors used are trimethylgallium (TMGa) or $((CH_3)_3Ga)$, trimethylaluminum (TMAI), and trimethylindium (TMIIn) for the group III element and ammonia (NH_3) under gaseous form as the group-V precursor.

The OM compounds are usually found in the reactor in their liquid phase stored in containers (bubblers), in which the liquid-vapor phases are maintained in thermodynamic equilibrium. These bubblers are placed in a water bath to control their temperatures. Tubes are dipped in the bubblers to create a path for the transportation of these precursors in their vapor phase toward the growth chamber with the help of carrier gases such as hydrogen (H_2) and nitrogen (N_2). The V-elements are stored outside the reactor and transported to the chamber by the same carrier gases. The flow rate of these carrier gases is controlled by mass flow controllers (MFC).

Two MOVPE reactors were employed throughout this work: a 3x2" Thomas Swan Closed-Coupled Showerhead (CCS) and a 7x2" AIXTRON CCS. Note that only the Thomas Swan reactor was employed to achieve the growth of the semipolar GaN templates, as presented in this chapter. On the contrary, both reactors were used to grow MQW and LED structures, which will be discussed in **Chapter III**.

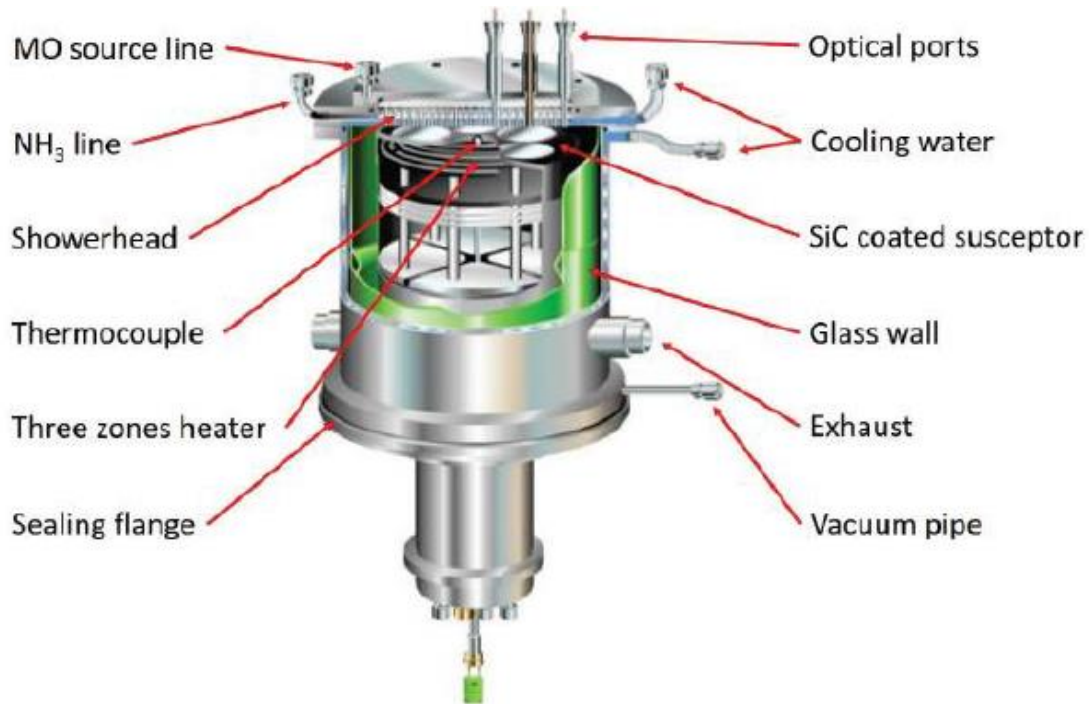


Figure 2- 1: Schematic of the 3x2" Thomas Swan CCS reactor chamber.

A schematic of the Thomas Swan reactor's chamber is presented in **Figure 2- 1**. The substrates are positioned on a SiC-coated susceptor, which rotates throughout the growth process to ensure a uniform distribution of the species on the surface. OM and NH_3 precursors are injected separately at the surface of the substrate through a showerhead. The heating is performed via a three-zone heater made of tungsten in order to maximize temperature uniformity across the susceptor. The thermocouple positioned below the susceptor will follow the set temperature given by the user but doesn't provide the real temperature (T) at the surface of the wafer. Instead, an *in-situ* optical reflectometry system is installed outside the reactor to monitor the surface temperature of the wafer and the reflectivity throughout the growth. The temperature obtained through reflectivity is around 150°C lower than the set temperature and might derive depending on the susceptor employed, the position of the thermocouple, the calibration of the reflectivity, and the state of the reactor. The temperature calibration is thus essential, as it determines the maximum growth rate (see section **II.4**), and it was performed before every new growth series.

II.2.b Growth Mechanism

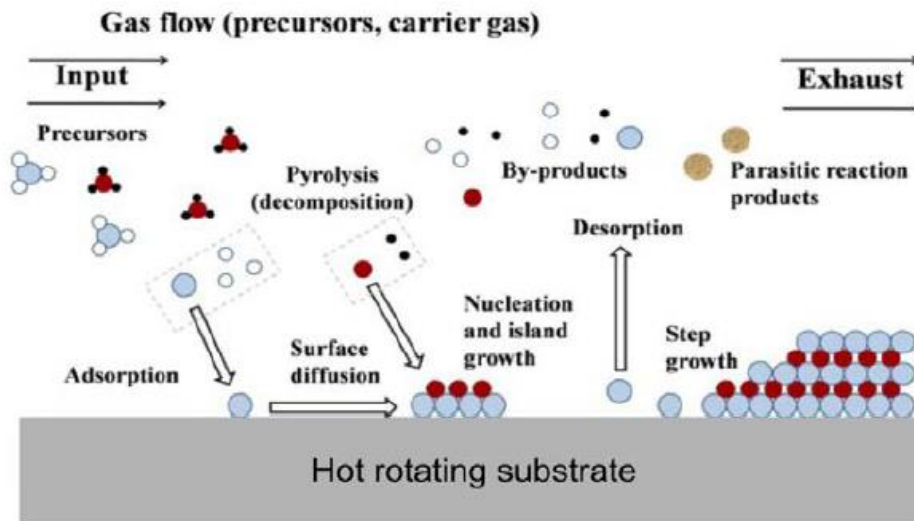
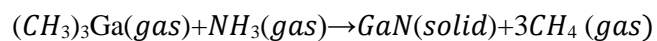


Figure 2- 2: Schematic of physical mechanisms operating during MOVPE growth.[1]

MOVPE growth relies on the transport and pyrolysis of precursors, as presented in the scheme of **Figure 2- 2**. In the case of GaN growth, the OM compounds, TMGa, and the ammonia gas are transported toward the heated growth chamber by the carrier gas. Pyrolysis then occurs, which is the decomposition of OM compounds into their constituent atoms (or radicals) at high temperatures. The desired atoms then diffuse towards the surface of the substrate, where they can through physi- or chemisorption be adsorbed and react, nucleating GaN to form islands, diffuse, or/and be desorbed depending on the chosen growth conditions. The general reaction can thus be summarized to:



The by-products (residues) of the chemical reactions are desorbed and evacuated by the carrier gas.

The growth rate and quality of the III-nitride epitaxial layers depend mainly on five parameters: temperature, pressure, III/V ratio, the absolute precursors' flow rate, and the carrier gas. The former parameter enables to define different growth regimes that impact the growth rate as follows:

- **Low T:** The growth rate is governed by the chemical reaction rate according to the Arrhenius law:

$$R = Ae^{\left(\frac{E_a}{kT}\right)}$$

Where R is the chemical reaction rate, A is the pre-exponential factor, E_a represents the activation energy of the slowest process of all those represented in **Figure 2- 2**, k is the Boltzmann constant and T is the temperature measured in kelvin.

Hence, this regime is limited by the kinetic reactions.

- **Intermediate T:** The growth rate is T-independent and the regime is referred to as “mass transfer”. The normal range of the T for GaN growth in this regime is between 800°C and 1200°C [1]. In this regime, the growth rate is higher than the one at lower temperatures.
- **High T:** The growth rate is mainly limited by surface reactions such as desorption, evaporation, and dissociation of the species from the surface. Therefore, the growth rate decreases during this regime compared to the one achieved in the “mass transfer” regime.

II.2.c Selective area growth principle

In this work, III-nitride growth is performed on textured SOI substrates. The strategy employed is similar to selective area growth (SAG), which relies on the deposition of a dielectric mask that covers the substrate’s surface except on the areas where localized growth is expected to occur. The mask in this case should be heat tolerant, inert to the carrier gas and precursors, and have a low sticking coefficient, to avoid any nucleation in areas besides those where the substrate is exposed. Otherwise, parasitic growth will occur and will perturb the growth of homogenous GaN films.[2] SiO₂ and SiN are the most commonly used dielectric masks; in this PhD, SiO₂ will be used in the fabrication of textured SOI substrates.

Besides the dielectric mask deposition, growth conditions play an important role in controlling the selective growth in the substrate-exposed regions. During SAG, the growth rate on the exposed growth area is impacted by the precursors attaining the zone directly from the vapor phase as well as the contribution from adatoms diffusion on the surface. Ideally, the species reaching the dielectric mask will migrate laterally towards the substrate-exposed regions and will contribute to the growth rate thereon, or will desorb.

Furthermore, once the GaN grains begin to grow from the exposed substrate regions, they will acquire a form, and morphology, dictated by the growth conditions, which determine the growth rate along each particular growth direction. Hiramatsu *et al.* investigated the selective area growth of GaN stripes aligned along various orientations [3]. **Figure 2- 3.a** shows the impact of growth conditions (e.g. temperature and pressure) on the growth of $[11\bar{2}0]$ aligned stripes, which will be the orientation of the semipolar GaN stripes grown on textured SOI. In that case, although the change in growth conditions will change the relative growth rate along crystallographic orientations, it has little impact on the shape of the $[11\bar{2}0]$ aligned stripes, given that highly-stable $\{1\bar{1}01\}$ planes rapidly form, as shown in **Figure 2- 3.a** and b. The situation is different for $[1\bar{1}00]$ aligned GaN stripes, where a change in temperature and pressure will drastically impact the shape and the formation of different crystallographic planes, as schematically presented in **Figure 2- 3.c**. The stability of each crystallographic surface depends mainly on its surface energy and the stability of surface atoms thereon, which can be enhanced or diminished through varying growth conditions, which will govern *in fine* the morphological changes [3]

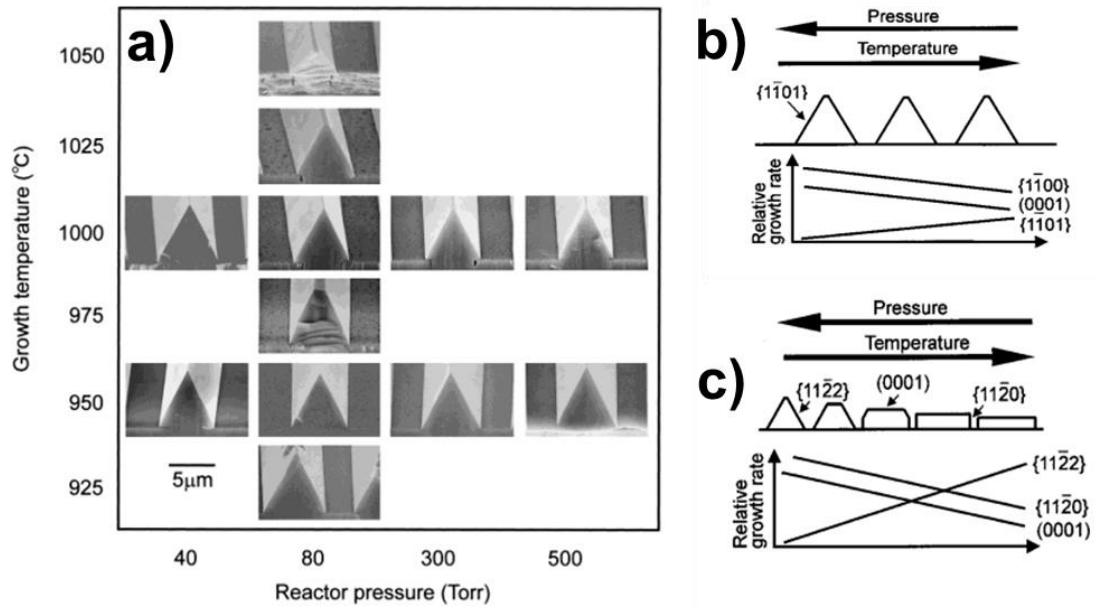


Figure 2- 3: a) Morphological changes of ELO GaN with [11 $\bar{2}$ 0] oriented stripes, for different reactor pressures and growth temperatures. Model of the morphological change in ELO GaN for b) [11 $\bar{2}$ 0] oriented and c) [1 $\bar{1}$ 00] –oriented stripes, for different reactor pressures and growth temperatures.[3]

The motivation behind the use of SAG is to improve the structural quality of GaN. The schematic in **Figure 2- 4** presents two approaches to reduce the threading dislocation density in GaN layers thanks to SAG [4]. In Model A threading dislocations (created at the substrate/GaN interface or coming from the underlying layer) will propagate along the vertical c -direction through the mask opening, resulting in areas of poor crystal quality over the mask opening and high quality over the dielectric mask. Note that the schematic omits the generation of dislocations at the grain boundary of stripes after coalescence. In Model B, growth conditions are changed to form inclined planes, where threading dislocations will bend laterally and potentially annihilate with bent dislocations coming from neighboring stripes. This will result in high-quality material in the mask opening and poor-quality material at the coalescence boundary where dislocations can propagate vertically or can be generated.

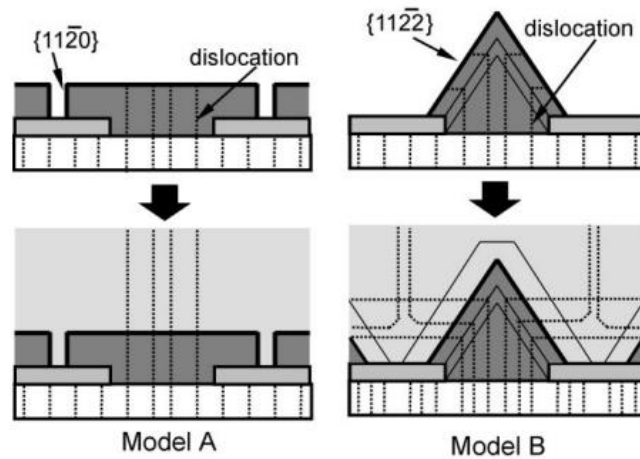


Figure 2- 4: Growth models of FACELO (Facet Controlled ELO) for two different types of models, A and B. [4]

SAG can be performed on planar substrates, as presented previously, or on textured substrates where growth along $[0001]$ direction is intended to take place on inclined facets to recover the required crystallographic orientation, which is the case for the SOI textured substrates of this Ph.D. Since in this case, the c -direction won't be perpendicular to the substrate surface, we can potentially obtain a semipolar or nonpolar GaN surface. Tendille *et al.* exploited textured r -plane sapphire substrate where (0001) c -plane sapphire facets were revealed through patterning and wet etching, as presented in **Figure 2- 5**. [5] Following an initial nucleation step to form $[1\bar{1}00]$ aligned GaN stripes, growth conditions were changed in order to promote growth along the c -direction before changing the growth conditions a third time in order to promote coalescence. In the case of semipolar and non-polar layers obtained with this approach, an additional challenge consists in filtering basal stacking faults and threading dislocations. Indeed, as already presented in **Chapter I**, BSFs will form along the $-c$ growth direction, which will necessarily happen whenever the c -direction is not perpendicular to the substrate surface. Thanks to the three-step growth approach developed by Tendille *et al.* they managed to reduce the propagation of BSFs below 30cm^{-1} and TDs down to $5.1 \times 10^7 \text{cm}^{-2}$. [5]

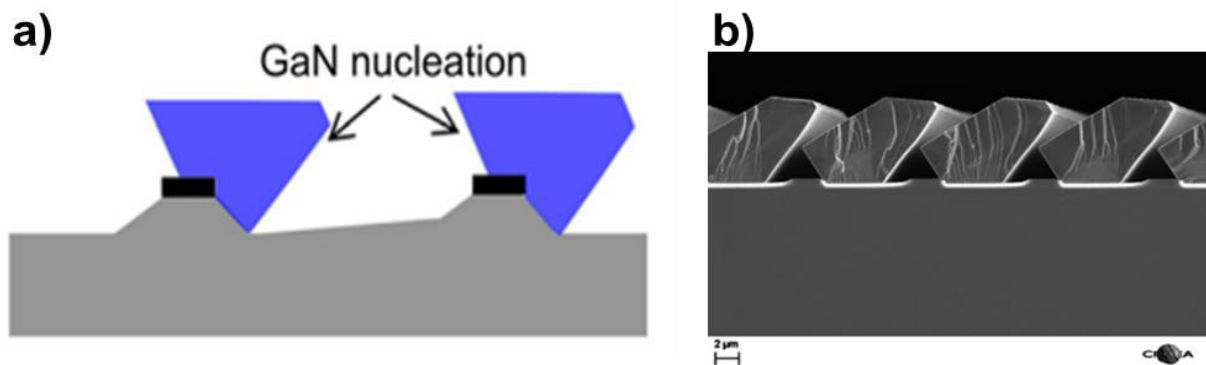


Figure 2- 5: a) Schematic representation of selective GaN growth on patterned r -sapphire and b) SEM image of the corresponding growth. [5]

Sapphire substrates are limited in size whatever the orientation exploited. Silicon however can reach 12 inches, which is thus more suitable for cost reduction and mass production. As such, the SAG approach on textured Si substrates has also been investigated with all the challenges that it involves (meltback etching and cracks) by Khoury *et al.* [6] as previously mentioned in **Chapter I**. Their

approach has been then transferred to SOI substrates by Mantach *et al.*[7] in order to further mitigate the generation and propagation of dislocations. This approach has been further exploited during this Ph.D. in order to move a step further in the development and fabricated microLEDs thereon.

II.3 Patterning Process

The substrate patterning is performed similarly to what Mantach *et al.* [7] previously reported. As a first step of this PhD, the aim was to reproduce their work. To do so, we used at first the same SOI substrates having the top layer of Si (001)6° off-axis, which were directly available at the start of the PhD. Note that the fabrication of new SOI wafers with the right crystallographic orientation of the Si(001) (7° angle) was only launched towards the end of the PhD. The full process of the SOI substrate texturing is described in **Figure 3- 1.a**, where an SiO₂ Buffered Oxide (BOX) of 500nm thickness is sandwiched between two Si layers. The top Si layer is 150nm thick and covered by a protection layer of SiO₂ of 1μm.

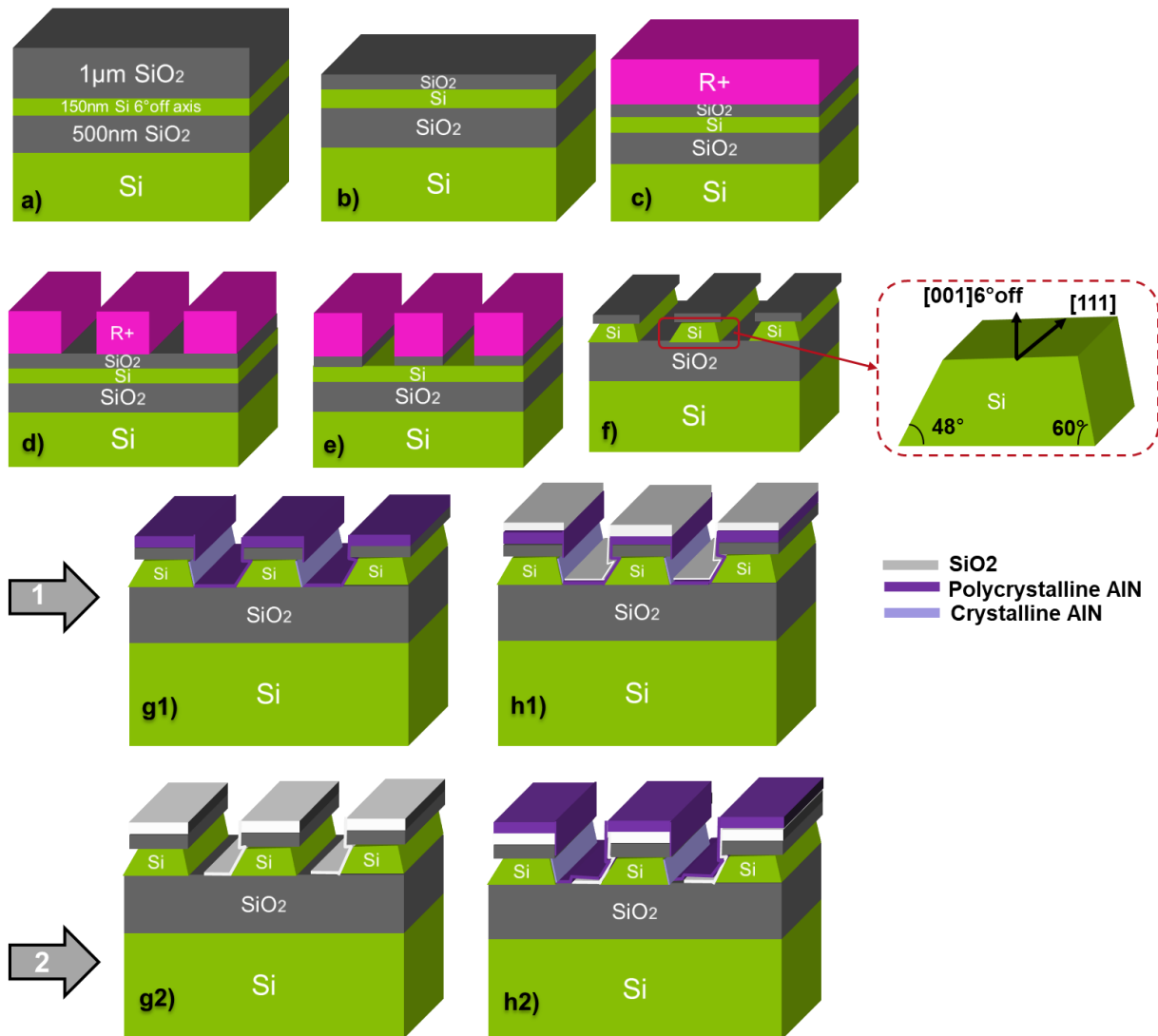


Figure 3- 1: Schematic of the different steps of the regular SOI substrate patterning.

The patterning of the substrate has been done using several steps as presented in the schematic of **Figure 3- 1**, which will be described in the following paragraph for two different methods:

II.3.a First method: Regular-SOI with thin SiO₂ mask

Here we present a list of the different patterning steps done on the substrate to accomplish a clean structured surface. Note that the recipe details are presented in the table in **Appendix A**.

- 1) Cleaning the substrate with solvents (Acetone, isopropanol, and ethanol) and 'Caro' (a mixture of sulfuric acid and hydrogen peroxide) to remove particle contamination.
- 2) A buffered oxide etch (BOE) cleaning then takes place to remove the entire SiO₂ protection top layer.
- 3) Deposition of 50nm of SiO₂ thin mask deposition on Si using the ion beam sputtering (IBS) all over the surface of the sample (**Figure 3- 1.b**).
- 4) Positive resist deposition (**Figure 3- 1.c**) followed by photolithography (**Figure 3- 1.d**) to pattern parallel trenches along the Si [110] axis with a periodicity of 5 μm (2.5μm for both ridges and trenches).
- 5) Dry etching of the SiO₂ then takes place using inductively coupled plasma (ICP) (**Figure 3- 1.e**). Resist residues were observed after plasma O₂ resist stripping and solvent cleaning, by acetone at 50°C followed by a quick rinse by the acetone pressure gun (**Figure 3- 2.a**). Therefore, to ensure the total stripping of the resist, samples were dipped in the Caro solution for 4min, which resulted in a clean resist-free surface (**Figure 3- 2.b**).

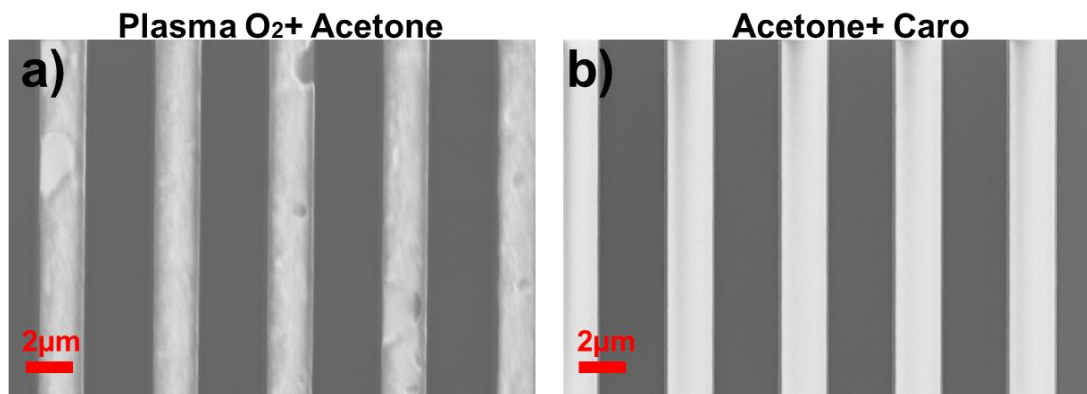


Figure 3- 2: SEM images post ICP etching and resist stripping by a) Plasma O₂ and Acetone highlighting the presence of resist residues unlike in b) after Acetone and Caro solution.

- 6) A short cleaning of BOE to ensure the removal of native oxide before starting the wet etching of Si using potassium hydroxide (KOH). The KOH is used to reveal the two facets of Si, (111) and $\overline{(111)}$, having two different inclinations with respect to the BOX, 60° and 48° respectively (**Figure 3- 1.f**).
- 7) Another cleaning of organic materials and particles is done using hydrochloric acid (HCl) or Caro.

It is important to note that after step 7, in this PhD two different approaches were introduced to finalize the substrate structuring and render it ready for the template growth. Initially, following Mantach *et al.* [7], an AlN growth is performed on the Si (111) facets right after step 7 (**Figure 3- 1.g1**). In this approach, after the first seven processing steps, the samples are packaged in LETI and sent to CRHEA, where AlN growth is performed, and samples are then shipped back to LETI to conduct the last two steps of the patterning process:

- 8) Coating the entire surface with 17nm of SiO₂ deposition using the inclined deposition in IBS. The orientation of the sample with respect to the beam enables to cover the whole surface except for the AlN(0001)/Si (111) facets, where GaN growth will occur (**Figure 3- 1.h1**).
- 9) Finally, a BOE cleaning is employed to remove any unwanted oxide that will block the GaN growth.

However, this approach is relatively time-consuming, as it involves processing (steps 1 to 7), growth (AlN), processing (steps 8 and 9), and finally GaN growth. The fact that processing (in LETI) and growth (in CRHEA) are not taking place in the same location adds to the complexity and required time. As such, following GaN growth initial trials, the process has been modified so that the 9 steps are performed simultaneously in LETI. After the inclined SiO₂ deposition (**Figure 3- 1.g2**) and BOE cleaning, the samples are packaged and sent to CRHEA for AlN deposition (**Figure 3- 1.h2**) resulting in one processing and one growth campaign instead of two. **Figure 3- 3.a** presents the cross-section SEM image of the second approach where the inclined SiO₂ is deposited as a last patterning step before AlN growth. The first approach is depicted in **Figure 3- 3.b** showing the inclined deposition after AlN growth. AlN nucleates everywhere on the sample, resulting in crystalline AlN on the Si facets and polycrystalline AlN on the SiO₂ surface. The impact of having the SiO₂ deposited before or after the AlN will be presented later, in section **II.4.c**.

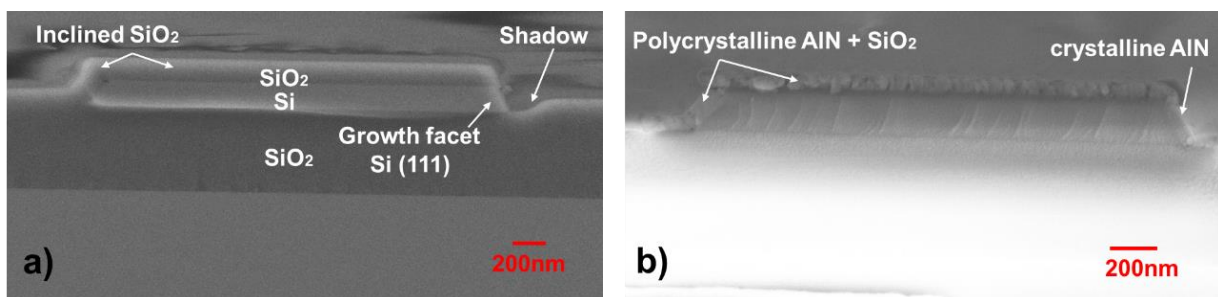


Figure 3- 3: Cross-section SEM images of the inclined SiO₂ deposition a) before AlN growth (second approach) and b) after AlN growth (first approach).

II.3.b Second method: ART-SOI

Before describing the effects of the patterned substrates on the growth of coalesced GaN templates, let us describe the preparation of the textured substrates for the ART approach. Most of the

patterning steps are similar to those presented in the previous section. The modifications made to prepare textured substrates adapted for ART concerns 5 steps:

- Removal of SiO₂ protection layer (step 1):
Instead of removing completely the protective SiO₂ layer on top of the SOI substrate, for ART the etching time of the first BOE is reduced to keep an SiO₂ layer thickness on top of SOI in the order of 600 nm, which was verified using an ellipsometer. This SiO₂ thickness is chosen based on the work done by Mantach *et al.* [8], as it should be thick enough to block the propagation of the bent dislocations as presented in **Chapter I**. Therefore, there is no need to deposit the first SiO₂ layer using the IBS, as in the first approach method.
- The ICP etching of the “thicker” SiO₂ layer (step 5):
The etching time was tuned in order to achieve well-defined ridges. Although the etching recipe is similar to the one used in regular SOI for SiO₂ etching, the quality of the ridges was improved by reducing the time from 250sec to 150sec as observed in **Figure 3- 4.a** and **b**, respectively. The resist was burnt for longer etching duration times, leading to slight etching of the top SiO₂ mask on the ridges, as indicated by the black spots of **Figure 3- 4.a**. This was solved by reducing the etching time to 150sec, for which the SiO₂ was completely etched between the ridges reaching the Si, as required while maintaining good SiO₂ quality mask on the ridges.

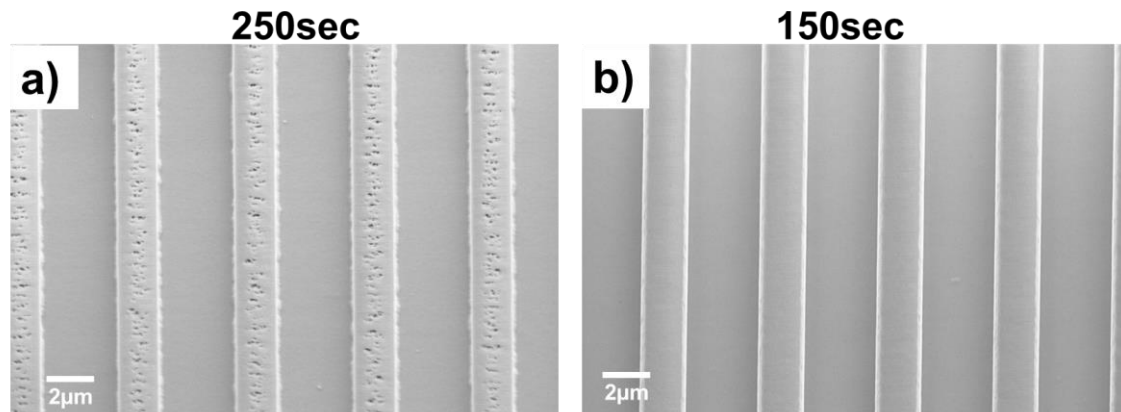


Figure 3- 4: Top view SEM image after a) 250sec and b) 150sec of dry etching and resist removal.

- KOH etching of the Si facets (step 6):

The beaker containing the KOH solution is typically in a water bath maintained at 37°C. The average etching time of this step was around 2 minutes and 30 seconds for all the regular and ART SOI samples. When the Si is fully etched, a different contrast is visually observed on the sample. However, in some cases, the etching is not fully achieved as seen in the cross-section SEM in **Figure 3- 5.a**, compared to a fully etched Si in **Figure 3- 5.b**. This can be due to either oxide contamination or the remaining SiO₂ etching of the previous ICP etching step, which was not entirely etched leading to SiO₂ residues blocking the Si layer even after the BOE. It can be further

due to inaccurate temperature or other environmental conditions impacting the etching rate of the KOH. Another possible reason is the inhomogeneous thicknesses of the Si(001) measured initially after SOI wafers fabrication. One easy way to make sure that the Si is fully etched was to verify the change of contrast of the sample, as seen in the example presented in **Figure 3- 5.c**. When two different contrasts are observed after the average etching time, as seen by the red and yellow squares, it means that Si etching was not completed over the entire surface.

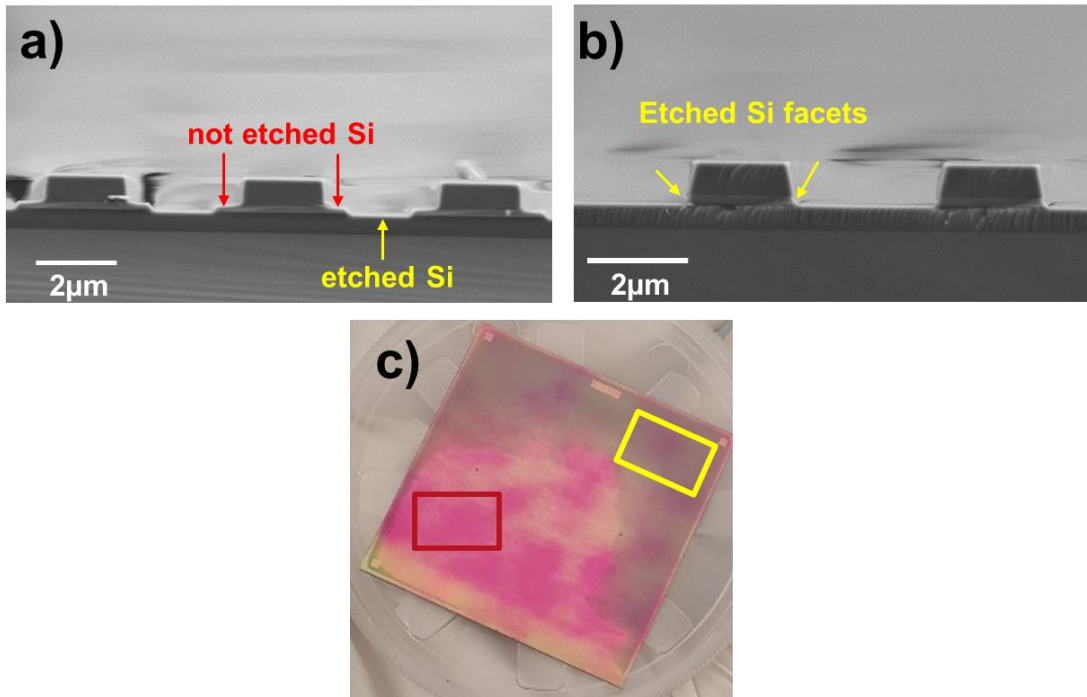


Figure 3- 5: Cross-section SEM images of two samples after KOH Si etching. a) Sample 1 presents the case where the KOH etching duration was not enough to etch the Si in between the ridges to form the required {111} facets. b) Sample 2 presents the fully etched Si facets indicated in yellow arrows. c) A visual example of an area where Si is not etched (red square) compared to a fully etched area (yellow square).

- The inclination angle of the IBS SiO₂ deposition (step 7):

The optimum inclination angle to cover only one of the two exposed Si facets depends on the thicknesses of both, the silicon and the SiO₂ mask. Therefore, with the ART approach, it was evident to tune the angle based on the same calculation made for the regular SOI approach. Following the scheme of **Figure 3- 6**, the expressions used to calculate the angle are as follows:

$$x = \frac{150}{\tan(60)} = 86.60 \text{ nm}$$

$$\text{Tan } a = \frac{x+50}{(150+600)} ; a = 10.32^\circ$$

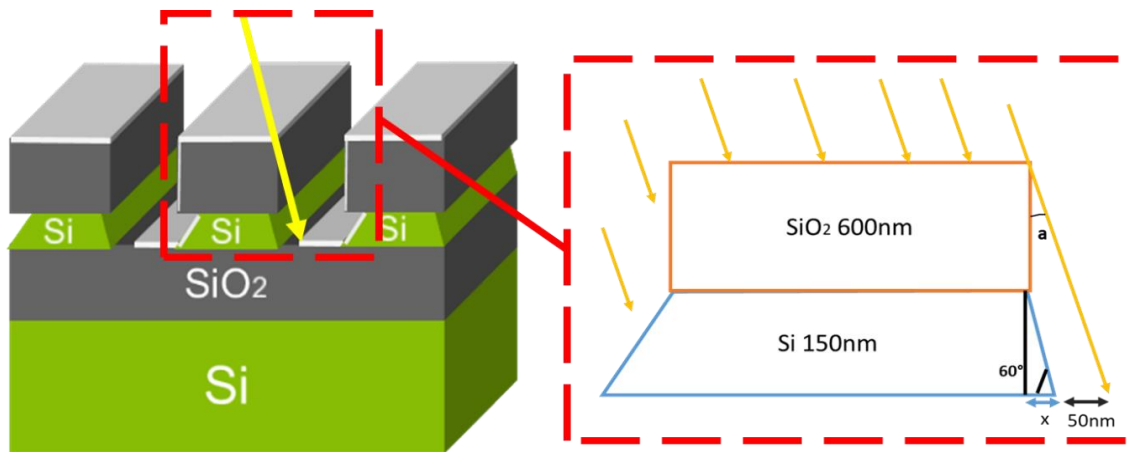


Figure 3- 6: Schematic of the ART-SOI substrate patterning after the inclined SiO₂ deposition. The yellow arrows correspond to the angle of deposition of the IBS.

The 50nm gap was chosen randomly as a minimum distance the deposited SiO₂ should be to not cover the Si facet.

- BOE etching post-inclined SiO₂ deposition:

This step is needed before the growth of GaN in order to remove the oxide on the (111) Si growth facet. The BOE etching rate was initially optimized for removing the SiO₂ protection layer deposited by PECVD. However, the different SiO₂ properties depending on the fabrication technique, PECVD, and by IBS, lead to different BOE etching rates. Therefore, another study was conducted for the last BOE etching step. **Figure 3- 7.a** and **b** show the inclined SiO₂ IBS deposition, followed by the BOE cleaning, respectively. It was observed that a 3sec BOE etch was enough to etch all the SiO₂ deposited on top of the ridge and on the BOX (red arrows in **Figure 3- 7.b**). However, the SiO₂ deposited on inclined planes (yellow arrow in **Figure 3- 7.b**) shows a very different (much slower) etch rate. Therefore, the BOE was then replaced by an HF 1% solution for 7sec to prevent the complete removal of the SiO₂ deposited.

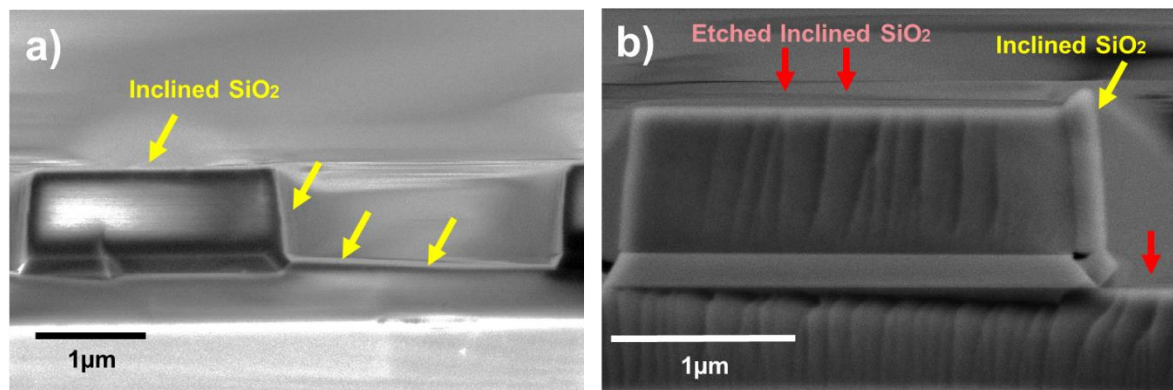


Figure 3- 7: Cross-sectional SEM images of the sample after a) inclined SiO₂ deposition (yellow arrows) followed by BOE etching in b).

Note that for ART-SOI, the AlN deposition was systematically made after the end of the processing and not as an intermediate step as it was for some regular SOI.

Having all processing steps accomplished, III-nitride selective growth on the (111) Si facets is the next challenge in this thesis. As already mentioned the first method, which will be referred to as 'regular

SOI', will be studied first to verify all growth conditions, before transferring them onto ART-SOI substrates.

II.4 Regular SOI Template Growth:

The precursors used during the template growth are trimethylaluminum (TMAI), trimethylgallium (TMGa), and ammonia (NH_3). **Figure 4- 1.a1-b1** illustrate the stages of GaN growth performed on a sample on which AlN deposition, of around 50 nm, was made prior to SiO_2 IBS deposition (**Figure 3- 1.g2-h2**). The AlN layer is commonly used to prevent meltback etching by isolating the Si surface from the Ga atoms. GaN growth is then carried out in two steps. In step one, GaN is grown selectively on AlN/Si (111) to create well-aligned GaN stripes (**Figure 4- 1.a1**). In step two, GaN coalescence is initiated in order to obtain a 2D layer (**Figure 4- 1.b1**).

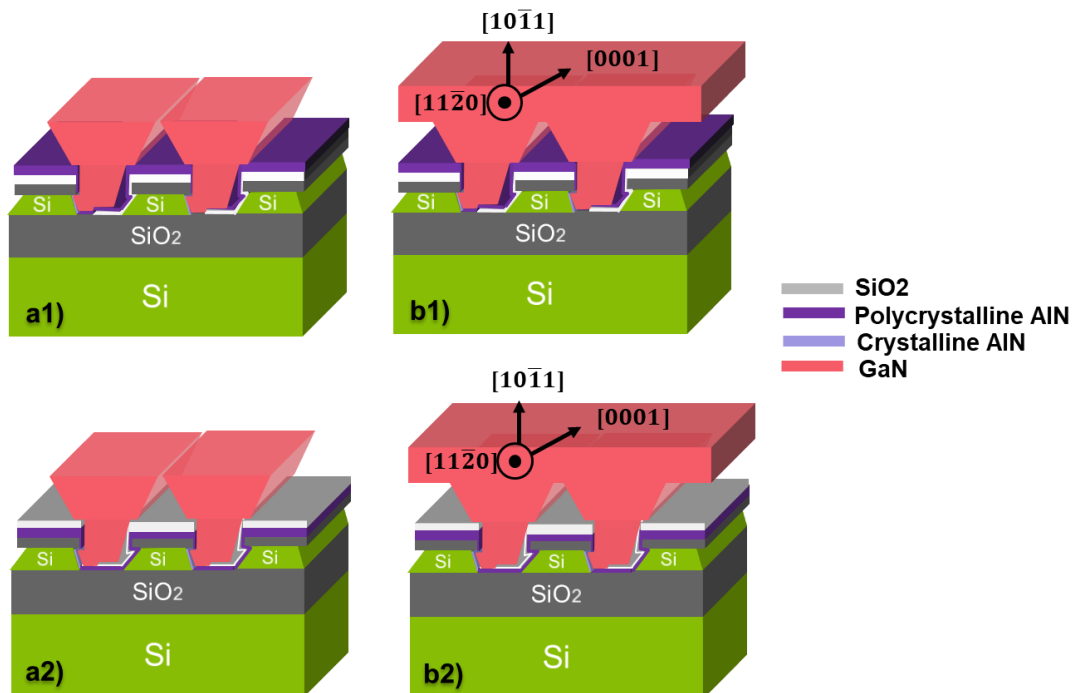


Figure 4- 1: Schematic of the different steps of III-nitride MOVPE growth.

Figure 4- 1.a2-b2 show the two-step GaN growth on the approach of **Figure 3- 1.g1-h1**, where AlN is grown before the inclined SiO_2 deposition. This approach will be mainly used in the following sub-sections. However, as mentioned in the patterning section, the impact of both approaches on GaN nucleation will be studied in section **II.4.c**.

The growth conditions of step 1 were first optimized in order to create relatively uniform GaN stripes without parasitic growth. GaN coalescence is subsequently performed on various test samples in order to see the impact of step 1 growth conditions on the coalescence and on the appearance of meltback etching.

Growth parameters	Stripes	Coalescence
NH₃ (mol/min)	0.156	0.067
TMGa (μmol/min)	84.450	84.450
Pressure (Torr)	<i>100 – 300 -500</i>	100
Duration (min)	<i>10 – 60 – 75</i>	60
Temperature (°C)	<i>1160 – 1090 – 1050</i>	<i>1160-1090</i>

Table 4- 1: List of parameters optimized (in red) and those kept constant throughout the optimization stage (in black).

The growth parameters are presented in **Table 4- 1**, indicating the fixed conditions and the ‘variable’ conditions used to study their impact on the GaN stripes and coalescence which will be elaborated in the following paragraphs.

II.4.a GaN stripes:

II.4.a.i Impact of pressure

To understand the effect of reactor pressure on the nucleation step, i.e. before the formation of homogenous GaN stripes, we characterized its influence on SOI substrates in which the SiO₂ deposition was carried out on the wrong Si(111) facet; this enabled us to address the effect of this parameter while not sacrificing adapted textured substrates.

The growth of GaN stripes is performed at three different pressures at a set temperature of 1160°C (real temperature around 1000-1050°C) under H₂ for 10 min. At 100 Torr, **Figure 4- 2.a1** and **a2** show the formation of GaN stripes on Si(111) with additional parasitic growth on the SiO₂, on top of both the stripes and the BOX. For such conditions, GaN nucleates not only on the crystalline AlN/Si (111) facets but everywhere. For 300 Torr, GaN is grown selectively on the crystalline AlN/Si (111), facets without any parasitic growth on the SiO₂, as observed in the scanning electron microscopy (SEM) images of **Figure 4- 2.b1** and **b2**. However, in these conditions, non-continuous stripes are observed, with the presence of voids in some areas, which points out that coalescence along $[11\bar{2}0]$ is not optimum in these conditions. At 500Torr, **Figure 4- 2. c1** and **c2** indicate random nucleation of GaN islands on all surfaces, on the crystalline AlN/Si (111) facets and the SiO₂.

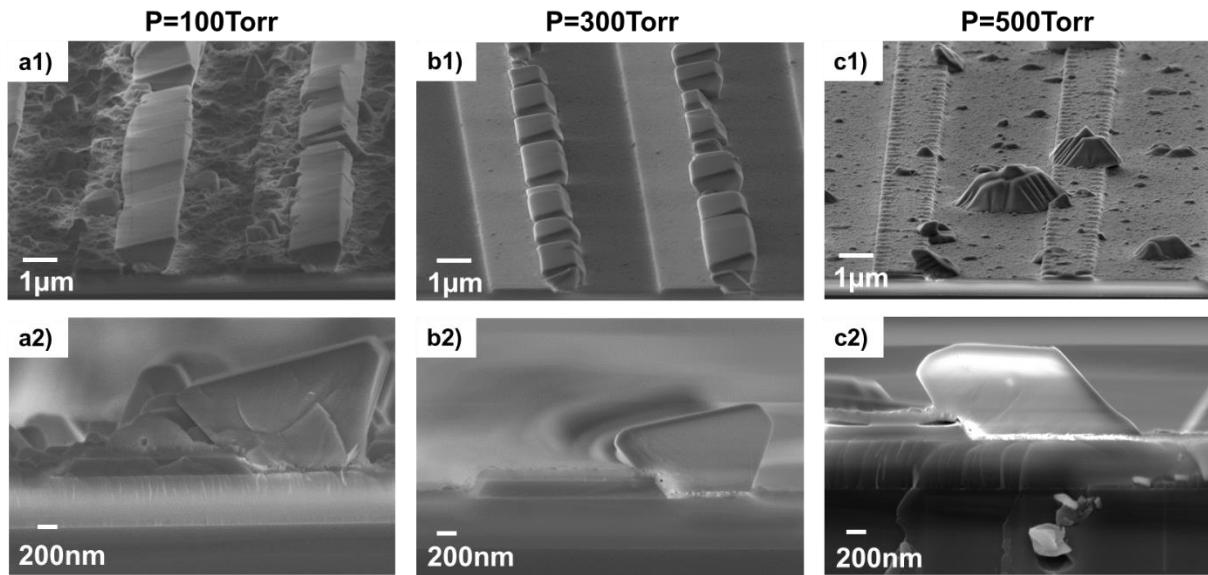


Figure 4- 2: Tilted and cross-section SEM images of three samples grown on the wrong Si facet at a1-a2) 100Torr, b1-b2) 300Torr, and c1-c2) 500Torr respectively.

We repeated this experiment on samples having the right crystallographic orientation as depicted in **Figure 4- 3**. In the tilted and cross-section SEM images, **Figure 4- 3.a1** and **a2** respectively, it is confirmed that by using 300 Torr, stripes were grown selectively on the crystalline AlN/Si (111) facets. For 1h growth, coalescence along $[1\bar{1}\bar{2}0]$ is almost complete, leading to the formation of continuous and well-defined stripes. At a larger scale, small variations in the width of some stripes, as well as non-continuous stripes (uncoalesced areas along $[11\bar{2}0]$), can be observed. **Figure 4- 3.b1** and **b2** confirm the parasitic growth nucleates on the SiO_2 at lower pressure. Therefore, the pressure will be fixed at 300Torr for step 1 for the rest of the thesis work.

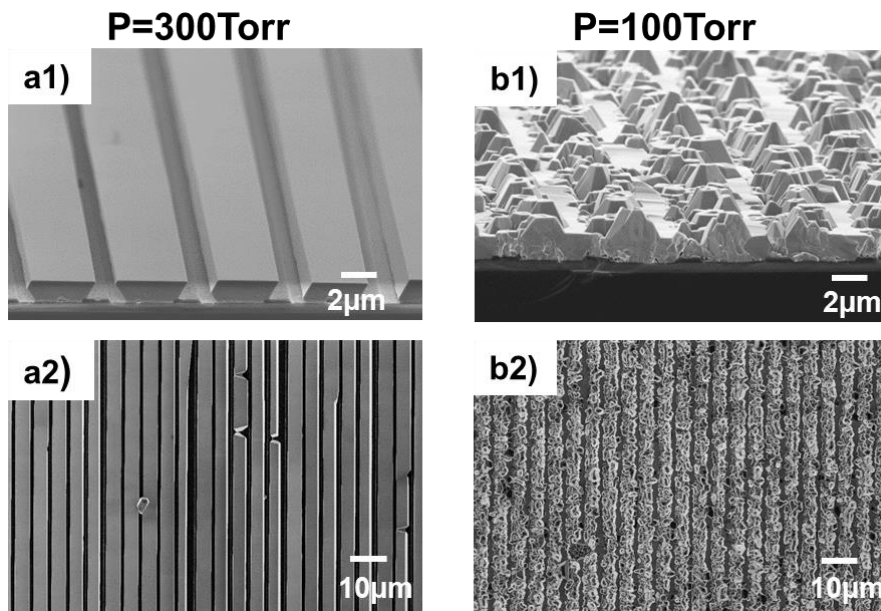


Figure 4- 3: Tilted and top-view SEM images of two samples grown at $T=1160^\circ\text{C}$, at a1-a2) 300Torr and b1-b2) 100 Torr respectively.

It is interesting to compare these results with the one presented just above in **Figure 2-3.a**. Indeed, in the case of the SAG of GaN stripes aligned along $[11\bar{2}0]$, there is almost no impact of the pressure on the SAG or on the formation of parasitic growth. In our case, the window for which pressure seems to lead to selective growth of GaN without parasitic growth is reduced. This could be explained by the inclined deposition of the SiO_2 mask, which might not be favorable for adatom to diffuse among a broad range of pressure.

II.4.a.ii Impact of the temperature

In order to further improve the width uniformity of the stripes, GaN growth was performed at different temperatures.

Figure 4- 4.a,b and c,d show the SEM images of the 1h GaN stripe growth at 1090°C and 1050°C set temperatures, respectively. A decrease to 1090°C seems to improve the continuity of the stripes along the $[11\bar{2}0]$, while still having some non-uniformities in the width of the stripes. Few parasitic growths can be also observed on the SiO_2 mask. A further decrease to 1050°C clearly improves the continuity and uniformity of the stripes, with less variation in width. However, a major drawback of using lower growth temperature is the presence of significant parasitic growth on the SiO_2 .

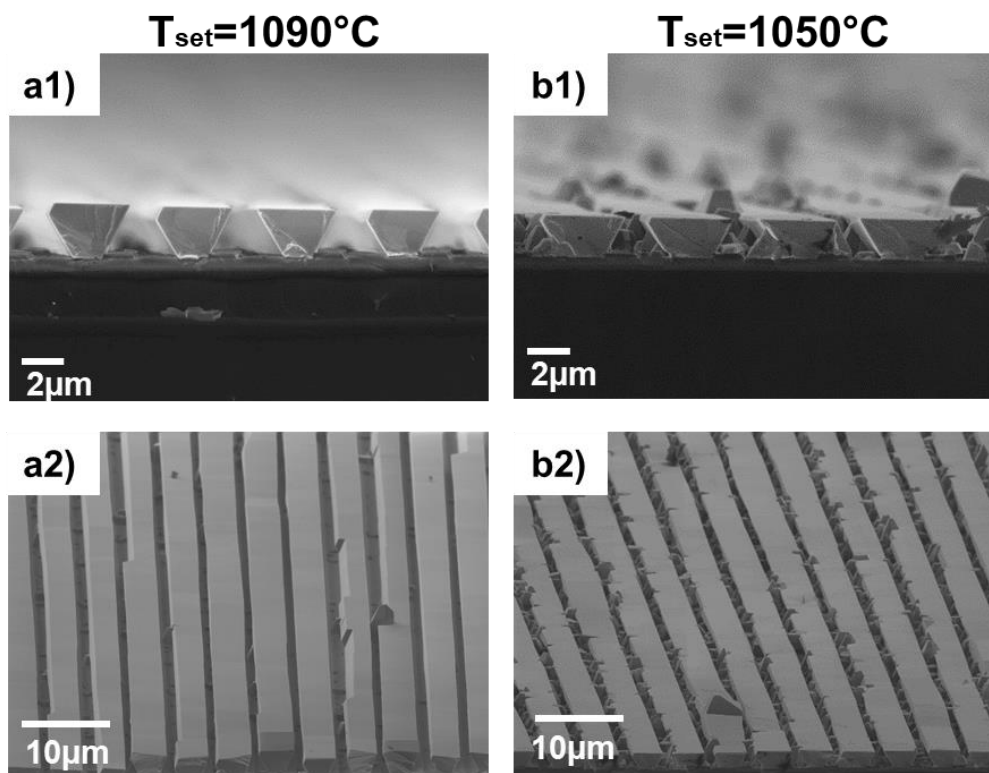


Figure 4- 4: Cross-section and tilted SEM images of two samples having a1-a2) 1090°C and b1-b2) 1050°C as set temperatures respectively.

Again, if we compare these results with the ones presented in **Figure 2-3**, it seems that the window for which the temperature leads to selective growth of GaN without parasitic growth is reduced on these textured substrates.

II.4.a.iii Impact of the stripe's growth time

Using 300Torr for the reactor pressure and 1090°C for stripe growth temperature, the growth time of step 1 was tuned in order to achieve closed-packed stripes before modifying the growth conditions

for initiating coalescence. Three different times are presented in **Figure 4- 5**. We observed an early stripe formation after 10min of growth, as seen in **Figure 4- 5. a**. Closer stripes were accomplished after 60min of growth as presented in **Figure 4- 5.b**. However, it is not until reaching 75min of stripe growth that we observed the closest stripe formation before reaching coalescence as depicted in **Figure 4- 5.c**. We verified that increasing the growth time did not degrade the quality of the stripes, but contributed to enlarging them, as we need for coalescence.

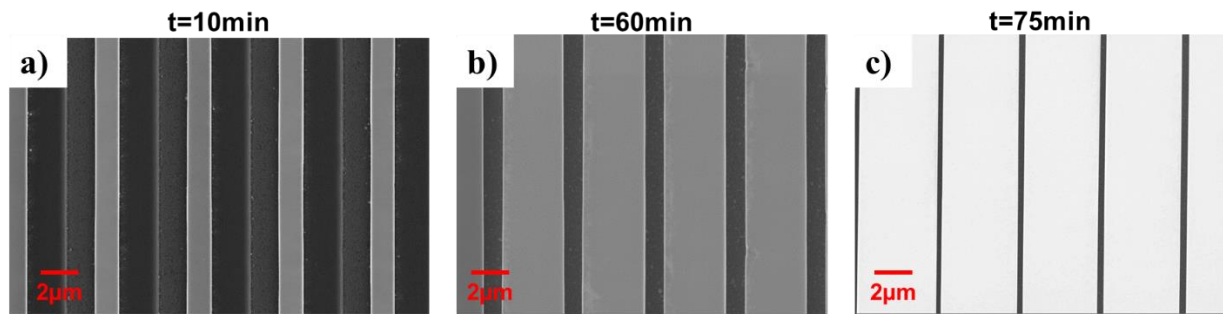


Figure 4- 5: Top view SEM images of step 1 growth after a) 10min, b) 60min and c) 75min.

II.4.b GaN coalescence

II.4.b.i Impact of the pressure

The coalescence has been performed on GaN stripes grown at 300 Torr at 1160°C (**Figure 4- 3.a1-a2**). Coalescence is favored by enhancing the growth rate along the c-direction through a decrease of both the pressure, which is reduced to 100 Torr, and the V/III ratio, which enhances the appearance of a $(10\bar{1}1)$ GaN 2D layer.

Figure 4- 6.a and **b** display a cross-section and tilted SEM image after 1h growth. The change in growth conditions enables the stripes to coalesce after 1h. However, a large area with meltback etching and parasitic growth can be observed at the surface after 1h of growth. We know that the meltback etching is induced by the reaction between Ga and Si. The growth conditions that are changed to reach coalescence, contribute to increasing the relative quantity of Ga available to react with Si. This is because the concentration of Ga is kept constant, while the concentration of NH_3 is reduced. Additionally, the reduction in pressure enables larger diffusion lengths for the adatoms, thus favoring the Ga atoms reaching the bare silicon surface below. The thickness of the AlN and SiO_2 deposited layers could be insufficient to prevent this direct contact of Ga with Si.

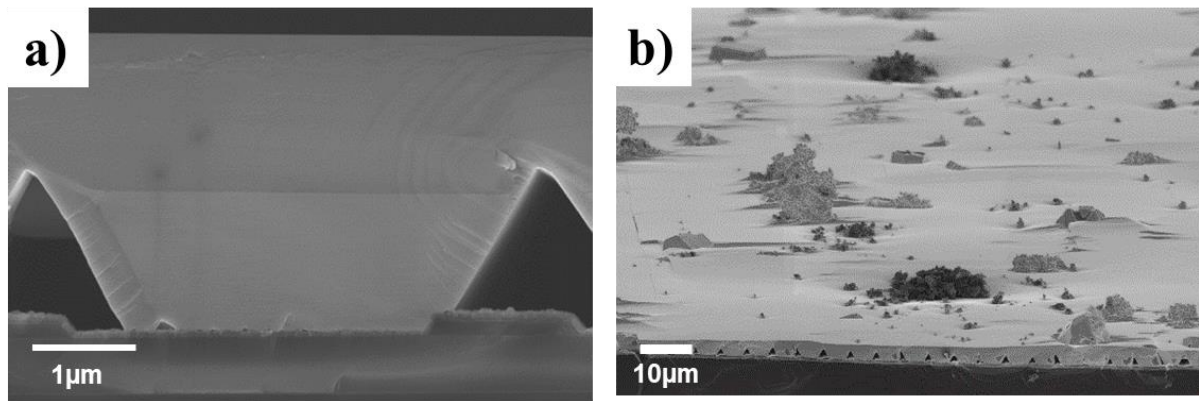


Figure 4- 6: a) A cross-section SEM image with its corresponding tilted SEM image in b) after 1h of GaN coalescence.

As a result, the impact of AlN and SiO₂ thicknesses on the formation of meltback etching has been investigated, and the results will be presented in the paragraph hereafter.

II.4.b.ii Impact of AlN and SiO₂ mask thicknesses

The growth of the GaN coalesced layer has been carried out using the same growth conditions as presented previously (1h of step 1 at 300 Torr at 1160°C) on two samples:

- i. 17nm SiO₂ on 50nm of AlN
- ii. 17nm SiO₂ on 100nm of AlN

Figure 4- 7. a, b, and c, d compare GaN growth on two different thicknesses of AlN (i and ii) but there is no significant reduction of meltback etching for the thicker AlN layer. Moreover, while coalescence is achieved for both thicknesses of AlN, surface morphology for the thicker AlN layer seems to be more disrupted.

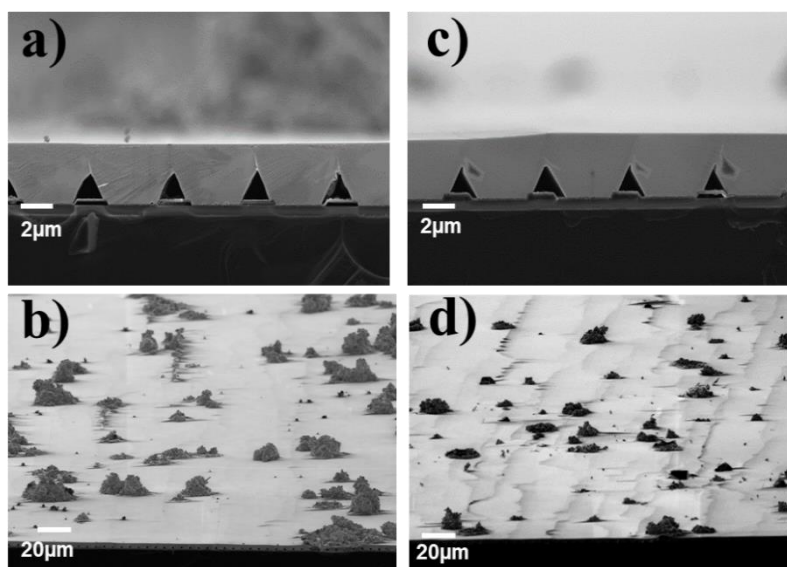


Figure 4- 7: The cross-section and tilted SEM images of GaN coalescence growth for two samples having 17nm SiO₂ and 50 nm AlN for a) and b), 17nm SiO₂ and 100nm AlN for c) and d).

As the AlN thickness, within the studied range, did not impact the meltback etching appearance, we decided to increase the thickness of the inclined SiO₂ deposited by IBS. In addition, because the 17 nm SiO₂ is deposited on rough and grainy polycrystalline AlN, it is suspected that the thickness may not be thick enough to fully cover the AlN layer below. This is because the SiO₂ deposition is followed by a BOE cleaning which may remove some of the SiO₂. Therefore, GaN coalescence was performed on a thicker SiO₂ mask (100nm) keeping the AlN 50nm thick.



Figure 4- 8: A tilted SEM image after 1h of GaN coalescence growth for a sample having 100nm SiO₂ thickness and 50nm AlN.

A decrease in meltback etching is observed in **Figure 4- 8** after coalescence in comparison to the samples having a thinner mask (**Figure 4- 7**). This suggests that a thicker SiO₂ can contribute to decreasing the probability of Ga attaining the Si substrate.

II.4.b.iii Impact of coalescence temperature

Figure 4- 9.a and **b** show 1h GaN coalescence growth performed at 1090°C on the two samples of subsection **II.4.a.ii**, where step 1 temperature was decreased. For the first sample, where stripes were grown at 1090°C, coalescence is achieved with a significant reduction in meltback etching at the GaN surface. For the second sample, where stripes were grown at 1050°C, coalescence is achieved but with a surface morphology highly impacted by the parasitic growth nucleated in between the stripes during step 1. Therefore, the temperature of step 1 is critical and needs to be controlled to avoid the formation of meltback etching after coalescence.

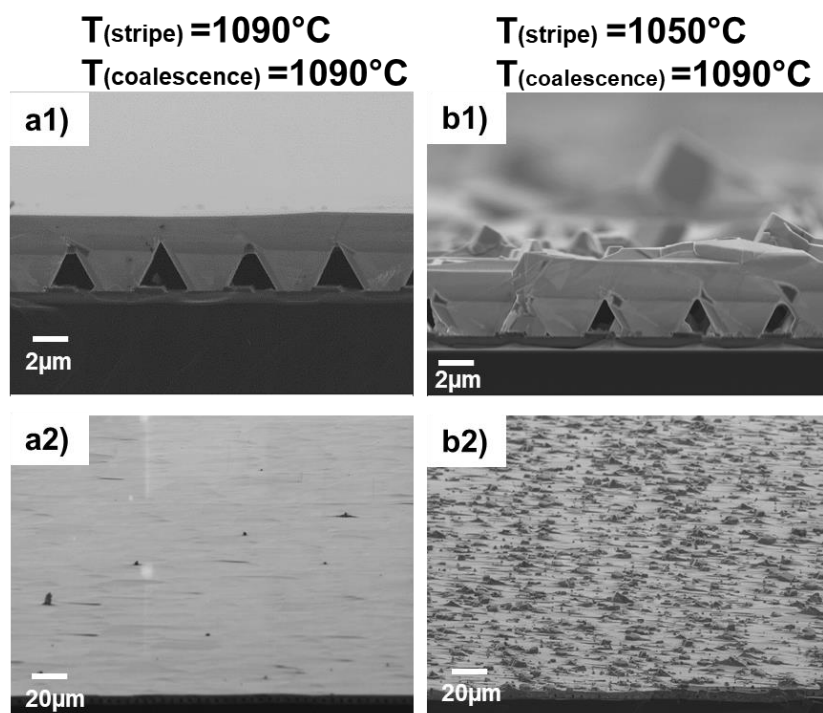


Figure 4- 9: Cross-section and tilted SEM images of GaN coalescence done at 1090°C set temperature on two samples with different growth T conditions of the stripes. a1-a2) present the sample where stripes growth was done at 1090°C and b1-b2) the sample where pyramids were grown at 1050°C.

II.4.c Impact of the AlN/SiO₂ and SiO₂/AlN approaches on GaN growth

All the results obtained so far were on regular SOI substrates that have been patterned and then coated with AlN before the inclined SiO₂ deposition, as described in section II.3. However, as this method is time-consuming, we decided to investigate the growth of GaN on both kinds of templates, referred in the following as AlN on SiO₂ (AlN/SiO₂) and SiO₂ on AlN (SiO₂/AlN).

Figure 4- 10. a-b and d-e, show the formation of stripes and the coalescence of the AlN/SiO₂ and SiO₂/AlN respectively. For 300Torr pressure and 1090°C growth temperature, the formation of GaN stripes on AlN/SiO₂ proved better uniformity and continuity compared to the growth on SiO₂/AlN. This could be due to the presence of SiO₂ residues on the growth facets when deposited after the AlN, despite the last BOE cleaning, preventing thereby the GaN nucleation in some areas. Consequently, the coalescence was fully accomplished along the surface of the former sample compared to the latter one, which has uncoalesced stripes indicated by the orange arrows of **Figure 4- 10.** e. Green arrows present cracks that formed perpendicular to the stripes, which are present for both samples.

Atomic force microscopy (AFM) measurements were also performed on these two samples which confirmed that the surface roughness of AlN/SiO₂ is 5nm root mean square (RMS), compared to 16nm for SiO₂/AlN, as shown in **Figure 4- 10.** c and f, respectively.

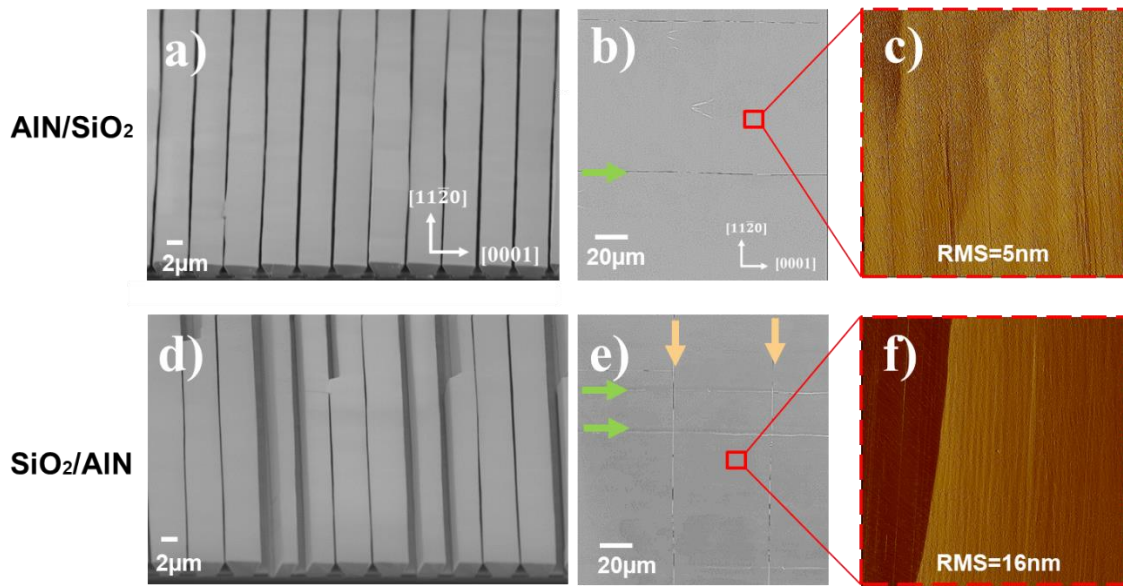


Figure 4- 10: AlN /SiO₂ deposition investigation shown in a-c) whereas SiO₂/AlN results are shown in d-f). Tilted SEM images of step 1 in a) and d) with their corresponding top view SEM images after 1h of coalescence in b) and e). Green arrows indicate the crack observed whereas orange arrows indicate uncoalesced stripes. AFM measurements on a 10x10µm² area of b) and d) samples present in c) and f) respectively.

II.4.d Growth parameter summary

A summary of the optimized growth conditions for both steps is listed in **Table 4- 2**, showing in red the parameters whose effects have been addressed. Based on these growth conditions, we will try to adapt them to the growth of templates with a reduced defect density, which requires an ART-SOI approach.

Growth parameters	Stripes	Coalescence
NH ₃ (mol/min)	0.156	0.067
TMGa (µmol/min)	84.450	84.450
Temperature (°C)	1090	1090
Pressure (Torr)	300	100
Duration (min)	75	60

Table 4- 2: Summary of the chosen growth conditions.

II.5 ART-SOI Template Growth:

In this section, we aimed to apply the same growth conditions listed in **Table 4- 2** on ART-SOI substrates. The objective of using ART is to reduce the threading dislocation density, as proven by Mantach *et al.*[8] Therefore, the initial SiO₂ mask is selected to be around 600nm thick, which is in principle [8] thick enough to block any TD propagating towards the surface and nucleated at the GaN/AlN-SI interface. After patterning the substrates following the procedure listed in **II.3.b**, AlN and GaN growth was carried out based on the growth conditions indicated in **Table 4- 2**.

II.5.a GaN Stripes

Figure 5- 1 displays the GaN stripes after step 1. **Figure 5- 1.a** highlights the selective growth of 2 μm GaN on the AlN on Si (111). No GaN is grown on the 600 nm thick SiO_2 , while GaN stripe growth continues over the SiO_2 BOX. The angle between the top pyramid and the substrate is found to be 1.2° . **Figure 5- 1.b** shows the relatively good continuity and uniformity of the stripes after step 1. The growth time is tuned in order to achieve closed-packed stripes before modifying the growth conditions for initiating coalescence. This has been found to further mitigate meltback etching. Note that scarce non-uniformities in the width of the stripes can be observed, resulting in two stripes being partially coalesced, as displayed in **Figure 5- 1.c**. In that case, we observe the early formation of triangular features, so-called *chevrons* [9].

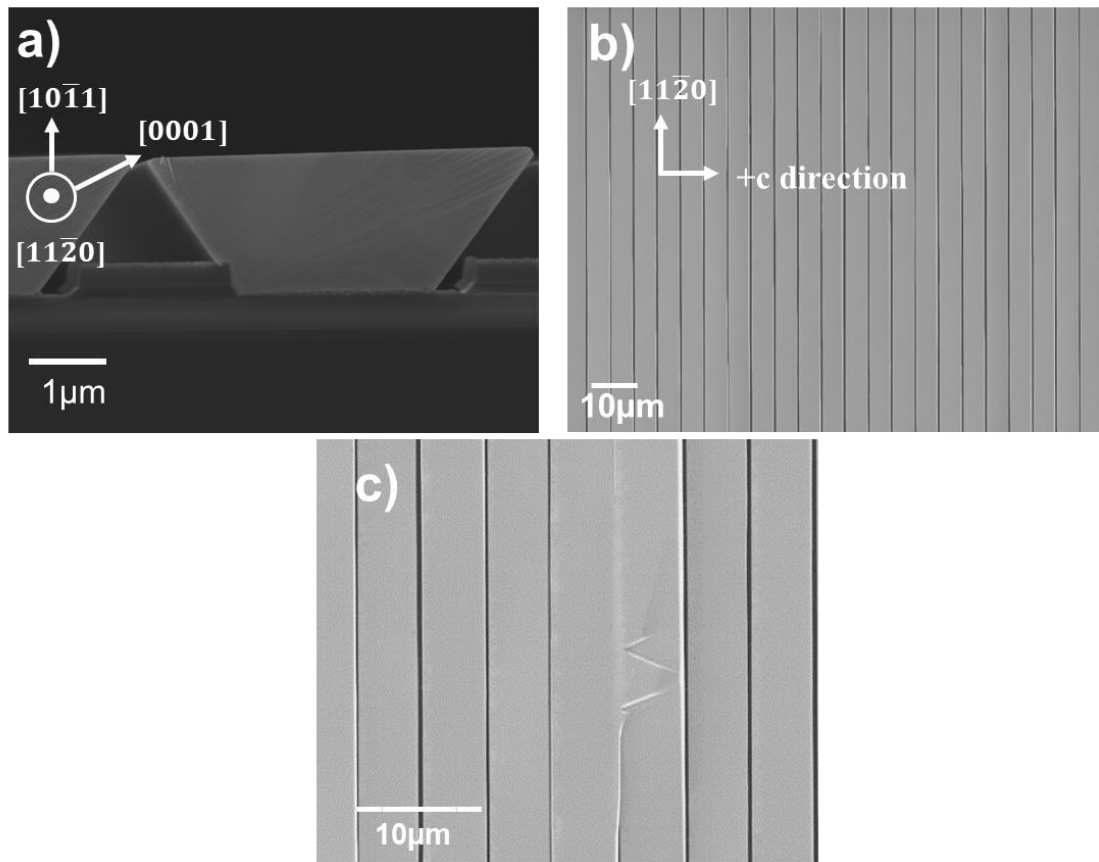


Figure 5- 1: a) Cross section and b,c) plan view SEM images of selectively grown GaN stripes on AlN/Si (111).

The formation of *chevrons* seems to be related to an imperfect coalescence, where a stripe climbs over a neighboring one due to small height differences between neighboring stripes, which agrees with other reports on different GaN orientations.[10] Additional fluctuations in height along one stripe, and/or localized morphological defects, could explain why these *chevrons* appear on isolated regions and not along the whole coalesced length. Note that these features were also observed on the regular SOI substrates. More characterization will be presented in the next chapter to understand their formation and their impact on InGaN QW growth.

II.5.b GaN Coalescence

In step two, GaN coalescence was initiated similarly to the regular SOI in order to obtain a 2D layer. However, as *n*-GaN doped buffer layer will be necessary for subsequent μ LEDs processing, we compared three coalescence strategies: 1) an undoped GaN coalescence, as previously used, 2) an *n*-doped GaN coalescence using silane (SiH_4), and 3) a half undoped/half *n*-doped GaN coalescence layer. The growth conditions of each strategy are detailed in **Table 5- 1**.

Samples	a	b	c
Growth	60min undoped GaN coalescence	60min <i>n</i> -doped GaN coalescence	30min undoped+ 30min <i>n</i> -doped GaN coalescence
Growth conditions	1120°C,100 Torr, 0.067 mol/min NH_3 , 84.450 $\mu\text{mol}/\text{min}$ TMGa, 60min	1160°C,100 Torr, 0.312 mol/min NH_3 , 144.771 $\mu\text{mol}/\text{min}$ TMGa, 133.9 $\mu\text{mol}/\text{min}$ SiH_4 , 60min	1140°C,100 Torr, , 0.067 mol/min NH_3 , , 84.450 $\mu\text{mol}/\text{min}$ TMGa, 30min + 1160°C,100 Torr, 0.312 mol/min NH_3 , 144.771 $\mu\text{mol}/\text{min}$ TMGa, 133.9 $\mu\text{mol}/\text{min}$ SiH_4 , 30min

Table 5- 1: Different growth conditions used for GaN coalescence.

The morphologies of these three GaN coalescence strategies are observed by tilted SEM and presented in **Figure 5- 2**. After 60 minutes and around 2 μm of undoped GaN coalescence, **Figure 5- 2.a** reveals a large density of *chevrons* at the surface. After 60 minutes of *n*-doped GaN coalescence, **Figure 5- 2.b** shows the presence of parasitic growth (highlighted in red) as well as uncoalesced stripes. The use of completely different growth conditions between undoped and *n*-doped GaN can explain these two types of features. Interestingly, 30 minutes of undoped GaN followed by 30 minutes of *n*-doped GaN, for a total thickness of around 2 μm , shows an improved surface morphology, with a lower density of *chevrons* (**Figure 5- 2.c**). Such improvement can be explained by a complete coalescence after 30 min of undoped GaN followed by *n*-doped GaN growth at a higher temperature, which enables to smoothing out of the surface. AFM was carried out on the last layer. **Figure 5- 2.d** displays a $10 \times 10 \mu\text{m}^2$ scan which reveals an RMS roughness of ~ 10 nm. Note that this roughness does not take into account the *chevron* features, which would increase further the measured roughness. Chiu et al. demonstrated a correlation between the formation of *chevrons* (or step-like structures) with the associated large roughness and the exact Si (001) substrate misorientation. They measured a GaN roughness of 5.9nm on a Si (001) with a 6.5° off axis compared to a 0.7 nm roughness on a 7° off axis when coalescing with undoped GaN.[11] Similarly, it was shown that $(10\bar{1}1)$ GaN surface with roughness below 1 nm can be obtained on $(11\bar{2}3)$ Al_2O_3 for which an angle of 61.22° is obtained with respect to *c*-plane sapphire, close to that of 61.96° between the $\{10\bar{1}1\}$ plane of GaN and the *c*-plane of GaN.[12], [13] This suggests that fine-tuning the initial Si (001) off-axis orientation can further improve the surface morphology of the GaN coalesced layer.

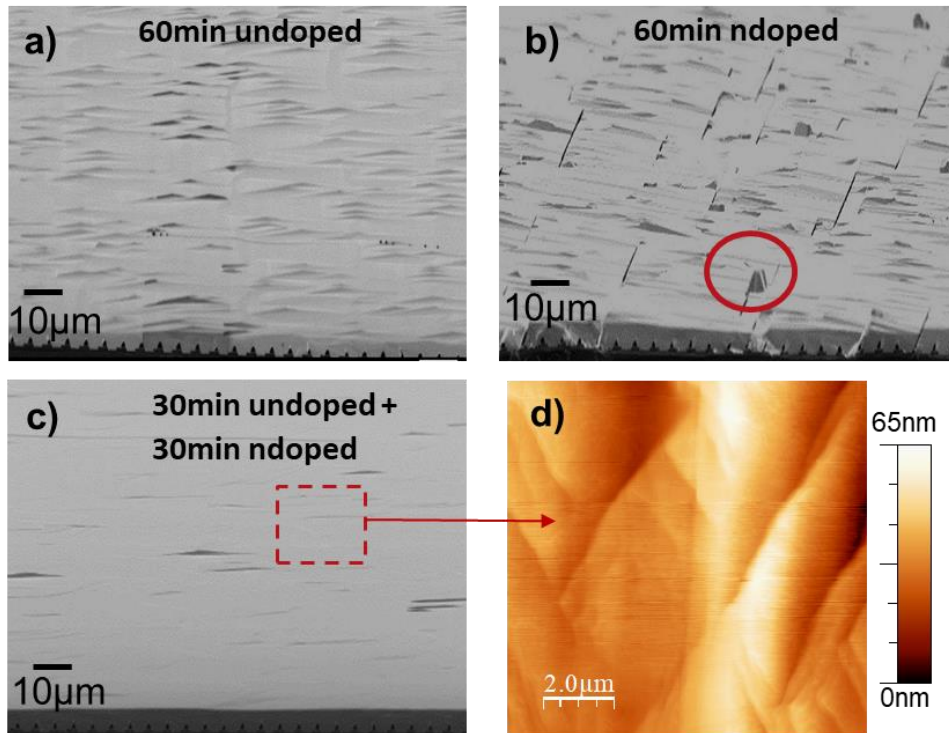


Figure 5- 2: Tilted SEM images of GaN coalesced layer after a) 60 min undoped, b) 60 min *n*-doped (red circle highlighting the parasitic growth), and c) 30 min undoped/30 min *n*-doped growth. d) 10x10 μm^2 AFM image of the sample in (c).

II.5.c Optical Characterization

We established in sections **II.5.a** and **b** the growth conditions for the template growth that will be used to grow MQWs and LED structures in **Chapter III**. As such, we will describe in this paragraph, the optical properties of the resulting templates, as they can contribute to giving a more accurate image of the crystalline quality.

Figure 5- 3 presents the room temperature photoluminescence (RT-PL) spectra recorded on the three GaN coalesced layers described in section **II.5.b**, using a frequency-doubled argon laser emitting at 244 nm.

The GaN near band edge (NBE) emission is observed at 360 nm, while the yellow band (YB) emission, often ascribed to point defects, is centered around 550 nm.[14] Intensities of the NBE increase with the increase of doping concentration due to the compensation of nonradiative transitions, which are stronger for undoped GaN.[15] The ratio between the NBE and the YB intensities is found to be larger for both SiH_4 doped samples compared to the undoped GaN, which can be further attributed to the substitution of Ga vacancies by Si dopants.[16] The half-undoped/half-doped GaN coalesced layer displays the best optical properties probably due to a combination of improved structural quality and the higher radiative recombination rate of the *n*-doped section.

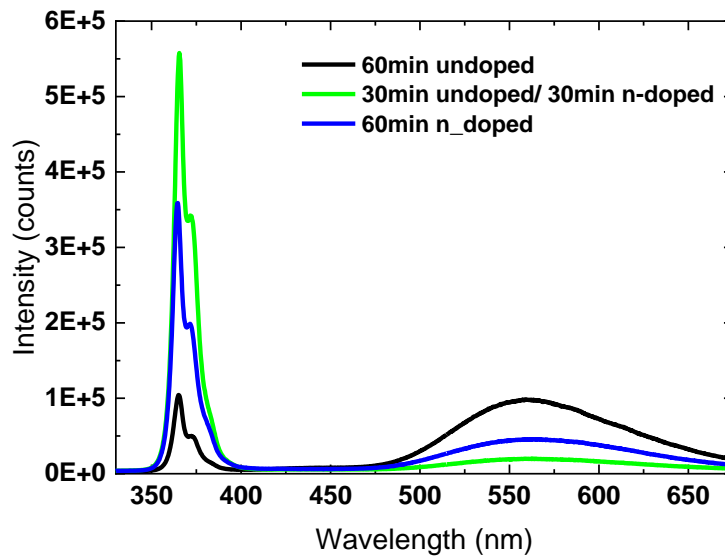


Figure 5- 3: RT PL spectra of the three GaN coalesced layers..

Cathodoluminescence (CL) was used at RT with an acceleration voltage of 10 KeV to investigate structural defects induced by the growth, as well as to assess their influence on the emission wavelength and intensity homogeneity on the half-undoped half-doped sample. Similar to the PL technique, CL will be further elaborated in **Chapter III**. RT CL integrated intensity map of the GaN NBE is illustrated in **Figure 5- 4.a**. It shows two distinguishable areas: one of large TD density, along the coalescence boundary of two consecutive stripes (red arrow), and a second region with a lower density of TDs in between coalescence boundaries (green arrow).

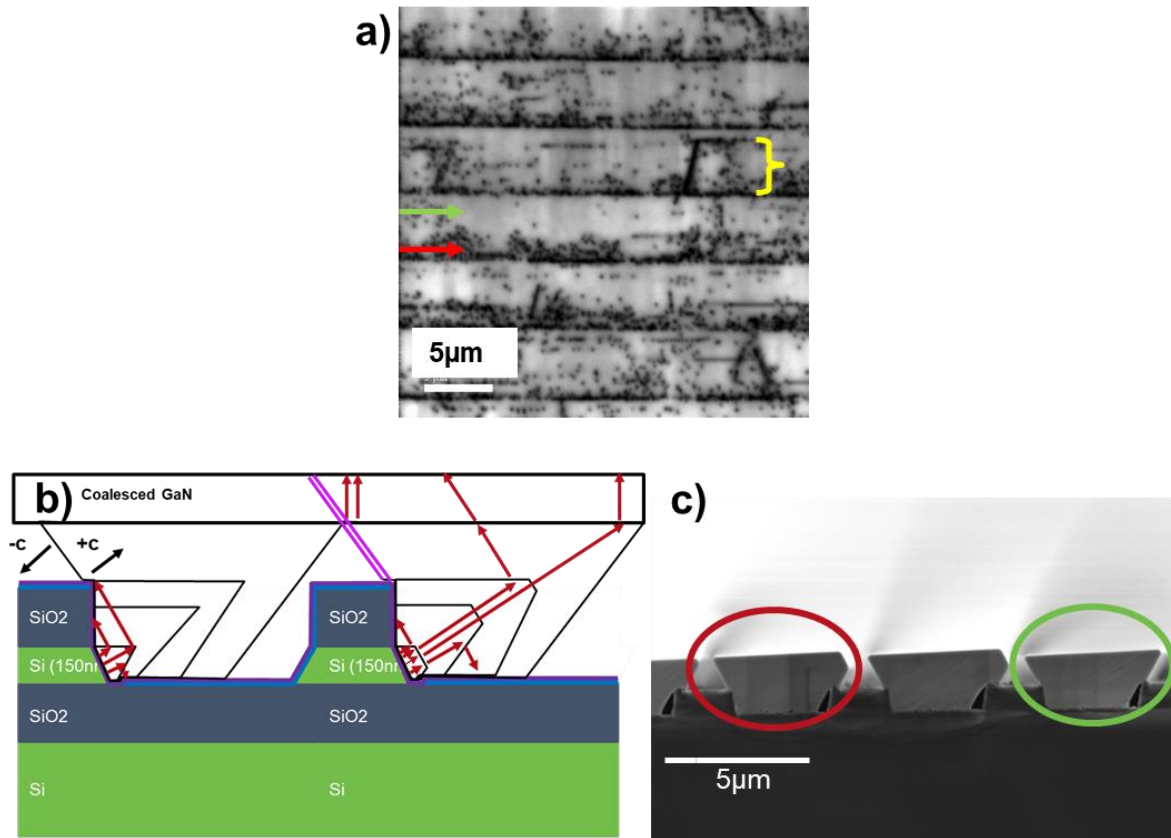


Figure 5- 4: a) RT CL NBE integrated intensity image indicating a high TD density with a red arrow and a low one with a green arrow. b) a schematic representing the propagation of TDs (red arrows) and the presence of BSFs (purple lines) at the coalescence boundary; in addition to showing the difference between complete and truncated pyramids resulting in the different dislocations blocking, and c) a 10° tilt cross-section SEM image of complete and truncated pyramids highlighted by green and red circles respectively.

The purpose of using a thick SiO_2 layer on top of the Si is to implement the ART strategy. However, one should note that for the ART to operate in the semipolar geometry, dislocations should bend laterally during early growth. Indeed, when TDs meet an inclined facet, they will bend at 90° (i.e. into the basal plane), as schematically depicted in *Figure 5- 4.b*. If the pyramidal GaN stripe is fully formed (i.e. its cross-section is a pyramid) in the early growth, as represented on the left side of *Figure 5- 4.b*, all dislocations will bend and will be trapped by the thick SiO_2 . On the contrary, if the pyramidal GaN stripe shows a truncated apex, as schematically shown in *Figure 5- 4.b* on the right side, TDs can propagate and bend at a later stage, with a reduced effect of the thick SiO_2 . *Figure 5- 4.c* shows a cross-section SEM of GaN stripes after step 1, where the formation of truncated (red circle) and fully formed (green circle) pyramidal GaN stripes can be observed. This seems to confirm the origin of the unexpected dislocation lines away from the coalescence areas (indicated by a yellow bracket in *Figure 5- 4.a*).

In order to tackle these problems and further reduce the dislocation density, the formation of GaN stripes in step 1 should be optimized in order to create only well-defined pyramids in the early growth stages.

To study the BSF formation during growth, we conducted cross-section CL images at a low temperature (8K). *Figure 5- 5.a* and *b* display a cross-section SEM image of the ART-SOI sample with

its corresponding monochromatic CL map acquired at 10keV, distinguishing the different GaN growth stages, each of which displays a particular optical response.

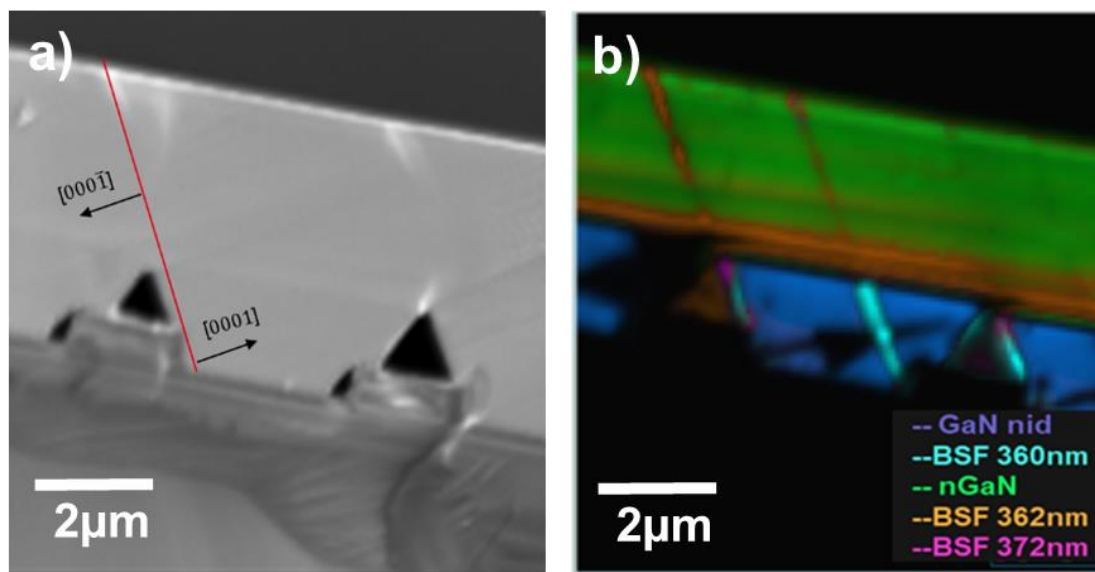


Figure 5- 5: Cross-section SEM image having a red line highlighting the c plane and black arrows indicating +c or -c orientations. b) a corresponding monochromatic CL mapping showing the different GaN layers emitting at different wavelengths.

We can observe the formation of 3 types of BSFs in the $-c$ direction ($000\bar{1}$) as schematically displayed in **Figure 5- 5.b** (purple lines), due to the slow GaN growth that induces impurities along this direction. As mentioned in **Chapter I**, the first type I1 emits at the lowest wavelength at 360nm, the second one I2 at 362nm, and finally E at 372nm. Note that although not investigated, the BSF density should be similar to the one observed by Mantach *et al.* for ART-SOI substrates ($\approx 10^4 \text{ cm}^{-1}$) [8].

II.6 Conclusion

We report the growth and characterization of $(10\bar{1}1)$ semipolar GaN templates on patterned $(001)\text{Si}$ 6° off-axis SOI substrates, implementing both the regular and ART techniques. The patterning process flow was initially adapted based on the results obtained by Mantach *et al.* After reproducing their work, we managed to improve the quality of the patterning which helped us improve the quality of the template growth in the following step. Despite the results achieved by Mantach *et al.* on the template growth, we still encountered several issues while adapting their conditions that led us to develop and improve the growth. This development was successfully achieved during the first growth campaigns on regular SOI substrates, where we optimized various growth parameters.

After the first growth step, we achieved uniform and continuous GaN stripes despite the local height difference among some neighboring stripes, which led to the formation of *chevron* features. Additionally, by depositing the inclined SiO_2 layer before AlN growth, and by switching from regular SOI to ART-SOI, we managed to achieve a GaN surface free of meltback etching after coalescence. Combining undoped and Si-doped GaN for 2D coalescence, we obtained $(10\bar{1}1)$ GaN templates on ART-SOI with good enough structural and optical quality and a relatively low surface roughness. Despite the efforts made, we assume that to further improve the surface morphology of the GaN template, $\text{Si}(001)7^\circ$ off-axis instead of 6° should be better adapted for this semipolar orientation, as

mentioned in **Chapter I**. Therefore, SOI wafers with Si(001)7° off were fabricated during the last months of this PhD, on which I have not had the time to conduct GaN growth yet.

II.7 References

- [1] S. Alam, « High Indium Concentration InGaN Multi-Quantum-Well-Based Blue-Green Light-Emitting Diodes Grown on InGaN ``Semi-Bulk'' Buffer ».
- [2] X. Yuan *et al.*, « Selective area epitaxy of III–V nanostructure arrays and networks: Growth, applications, and future directions », *Appl. Phys. Rev.*, vol. 8, n° 2, p. 021302, juin 2021, doi: 10.1063/5.0044706.
- [3] K. Hiramatsu, K. Nishiyama, A. Motogaito, H. Miyake, Y. Iyechika, et T. Maeda, « Recent Progress in Selective Area Growth and Epitaxial Lateral Overgrowth of III-Nitrides: Effects of Reactor Pressure in MOVPE Growth », *Phys. Status Solidi A*, vol. 176, n° 1, p. 535-543, nov. 1999, doi: 10.1002/(SICI)1521-396X(199911)176:1<535::AID-PSSA535>3.0.CO;2-I.
- [4] K. Hiramatsu, « Fabrication and characterization of low defect density GaN using facet-controlled epitaxial lateral overgrowth (FACELO) ».
- [5] F. Tendille, P. De Mierry, P. Vennéguès, S. Chenot, et M. Teisseire, « Defect reduction method in (11-22) semipolar GaN grown on patterned sapphire substrate by MOCVD: Toward heteroepitaxial semipolar GaN free of basal stacking faults », *J. Cryst. Growth*, vol. 404, p. 177-183, oct. 2014, doi: 10.1016/j.jcrysgro.2014.07.020.
- [6] M. Khoury, « Metal Organic Vapor Phase Epitaxy of Semipolar GaN on Patterned Silicon Substrates », l'UNIVERSITE de Nice-Sophia Antipolis.
- [7] R. Mantach *et al.*, « Semipolar (10-11) GaN growth on silicon-on-insulator substrates: Defect reduction and meltback etching suppression », *J. Appl. Phys.*, vol. 125, n° 3, p. 035703, janv. 2019, doi: 10.1063/1.5067375.
- [8] R. Mantach, P. Vennéguès, J. Zuniga-Perez, P. De Mierry, M. Portail, et G. Feuillet, « Freestanding-quality dislocation density in semipolar GaN epilayers grown on SOI: aspect ratio trapping », *Appl. Phys. Express*, vol. 13, n° 11, p. 115504, nov. 2020, doi: 10.35848/1882-0786/abc1cd.
- [9] C. Brasser *et al.*, « Cathodoluminescence studies of chevron features in semi-polar (112⁻2) InGaN/GaN multiple quantum well structures », *J. Appl. Phys.*, vol. 123, n° 17, p. 174502, mai 2018, doi: 10.1063/1.5021883.
- [10] M. Caliebe *et al.*, « Growth and coalescence studies of oriented GaN on pre-structured sapphire substrates using marker layers », *Phys. Status Solidi B*, vol. 253, n° 1, p. 46-53, 2016, doi: 10.1002/pssb.201552266.
- [11] C.-H. Chiu *et al.*, « Optical properties of (11⁻01) semi-polar InGaN/GaN multiple quantum wells grown on patterned silicon substrates », *J. Cryst. Growth*, vol. 318, n° 1, p. 500-504, mars 2011, doi: 10.1016/j.jcrysgro.2010.10.054.
- [12] S. Schwaiger *et al.*, « Planar semipolar (101⁻1) GaN on (112⁻3) sapphire », *Appl. Phys. Lett.*, vol. 96, n° 23, p. 231905, juin 2010, doi: 10.1063/1.3442484.
- [13] M. Takami, A. Kurisu, Y. Abe, N. Okada, et K. Tadatomo, « Growth of semipolar 10⁻1 GaN from c-plane-like sapphire sidewall of patterned n-plane sapphire substrate », *Phys. Status Solidi C*, vol. 8, n° 7-8, p. 2101-2103, 2011, doi: 10.1002/pssc.201001095.
- [14] J. Neugebauer et C. G. Van de Walle, « Gallium vacancies and the yellow luminescence in GaN », *Appl. Phys. Lett.*, vol. 69, n° 4, p. 503-505, juill. 1996, doi: 10.1063/1.117767.
- [15] E. F. Schubert, I. D. Goepfert, W. Grieshaber, et J. M. Redwing, « Optical properties of Si-doped GaN », *Appl. Phys. Lett.*, vol. 71, n° 7, p. 921-923, août 1997, doi: 10.1063/1.119689.
- [16] F. Qian, G. Xin, Z. Xiao-Ju, et H. Yue, « Photoluminescence characteristics of GaN:Si », *Chin. Phys.*, vol. 14, n° 10, p. 2133-2136, oct. 2005, doi: 10.1088/1009-1963/14/10/035.

Chapter III

III.1 Introduction

Chapter II described the development and optimization of a GaN template. This chapter focuses on growing an LED structure. To achieve good epitaxial quality LEDs, we first investigated the growth of multi-quantum well (MQW) structures on two MOVPE reactors at CRHEA. We begin by presenting the main characterization techniques used to study both MQW and LED structures. We then explore the MQW growth parameters and perform structural and optical characterization to correlate the impact of structural defects on the optical quality of the MQWs and to compare the results obtained with the two reactors. Finally, we detail and characterize the growth of the LED structures to prepare for the μ LED fabrication described in the next chapter.

III.2 Characterization techniques

III.2.a Cathodo-Luminescence (CL)

When a crystalline structure is bombarded with electrons from an electron gun in a scanning electron microscope (SEM), the electrons in the valence band acquire enough energy to jump to the conduction band, creating electron-hole pairs. Each incident electron carrying a few keV will release its energy in the material through a large number of interactions, each of which creates an electron-hole pair. This volume of interaction where electron-hole pairs are created, depends on the acceleration voltage of the incident electrons and limits the resolution of the technique.

The created electron-hole pairs can recombine by emitting photons with a characteristic wavelength that corresponds to the energy of the material's bandgap. They can also be temporarily trapped at energy levels introduced into the bandgap by defects in the crystalline structure. When these electrons are released from these traps, they emit photons with a wavelength that depends on the energy of the level introduced by the defects in the material's bandgap.

The cathodoluminescence (CL) technique has several advantages over photoluminescence. First, CL can obtain depth-resolved information by modulating the electron acceleration voltage, which changes the volume of interaction. Second, CL has a better lateral resolution, which is only limited by the volume of interaction of the electron and the diffusion length of the electron-hole pairs (the size of the electron beam itself is <10 nm). In comparison, the resolution of PL/ μ PL techniques is limited by the wavelength of emission.

By taking advantage of the high spatial resolution that CL provides, acquiring spectra and analyzing their peak positions can be highly effective for locally studying material strain states, doping, and impurities. Additionally, the CL images can be correlated with regular SEM images.

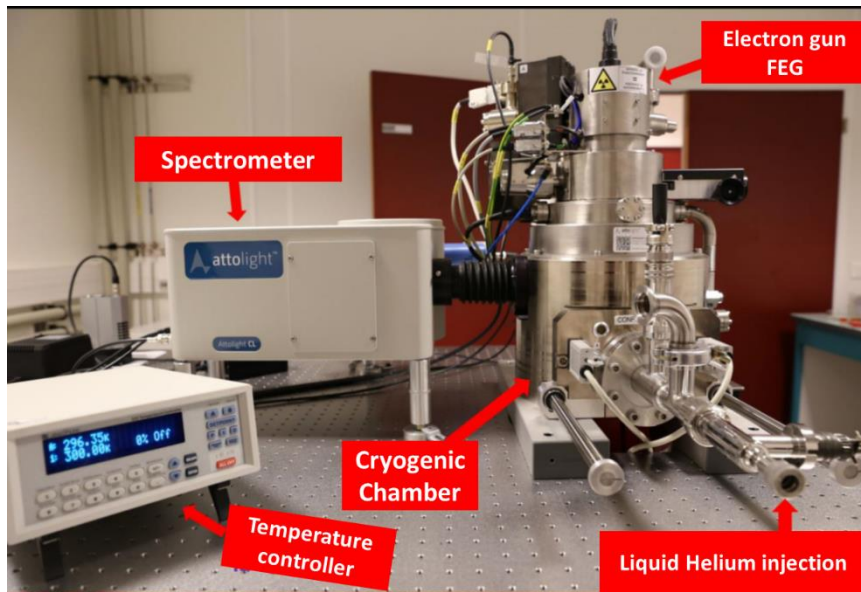


Figure 2-1: Cathodoluminescence setup.

The CL used in our study is Attolight equipment. Its SEM is equipped with a field emission gun (FEG) that allows for an acceleration voltage between 3 and 10 keV for a probe size below 3 nm. It is also possible on this equipment to perform measurements at temperatures down to 5 K, which is beneficial in our case to study the basal stacking faults (BSF), which are optically active only at low temperatures.

III.2.b Transmission Electron Microscopy (TEM)

Transmission electron microscopy (TEM) is an imaging tool that is based on the interaction of an electron beam at high voltages during its transmission through a specimen. The specimen is usually prepared by focused ion beam (FIB) milling to create a thin slice, called a lamella, where the area of interest is located. The basic setup of a TEM consists of the components of the schematic of **Figure 2-2**. An electron gun produces a beam of electrons that is focused by a condenser lens onto the specimen. An objective lens then focuses the beam after it has passed through the specimen and interacted with the atomic structure, to create the transmission image observed on the screen. In addition to these components, TEM has other components that are used to control the electron beam and to improve the resulting image mode such as the apertures presented in **Figure 2-2**. Either a dark-field image is formed by positioning the aperture to pass only one diffracted electron beam; or a bright field by positioning the aperture to pass only the transmitted electrons. This measurement is operated under a vacuum environment to prevent the scattering of the electron beam and the specimen contamination.

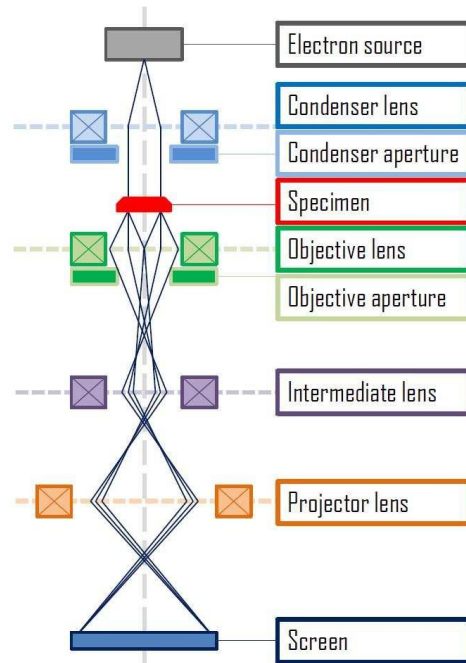


Figure 2-2: TEM setup [1].

In our work, we focused on using the scanning TEM (STEM) which consists of a focused electron beam on the specimen that scans its surface to acquire the images. STEM allows scanning at a very small scale, where atoms can be distinguished. In our case, it is aberration-corrected with a resolution between 0.7 and 1.1Å for acceleration voltages of 60 to 200 KeV, respectively. STEM can be coupled with various analytical techniques to obtain the needed information, such as high-angle annular dark-field (HAADF) imaging to analyze the electrons diffused at large angles by Rutherford scattering. This diffusion is a function of the scattered atom's atomic number (Z), which enables high precision at the atomic scale. Additionally, energy-dispersive X-ray spectroscopy (EDX) is highly used as a detector to analyze the elemental composition of the sample.

III.2.c Photo-Luminescence (PL)

In photoluminescence (PL), we use light excitation to generate electron-hole pairs in the semiconductor heterostructure, whose initial energy depends on the excitation wavelength. After thermalization, the electron-hole pair reaches a minimum of potential energy, such as a quantum well, a defect, or simply the band edge of the semiconductor. We use PL to obtain information on the quantum well (QW) composition and thickness and the defects. During my PhD, I used three types of PL setups: a macro-PL, a micro-PL, and a PL imaging setup. The three setups are detailed below:

III.2.c.i. Macro-PL

Two macro-PL setups were used during this PhD. At CRHEA, the setup used a frequency-doubled argon laser emitting at 244 nm on the sample. The photon energy being larger than the bandgap of GaN, electron-hole pairs were generated in the bulk GaN. This had two consequences: first, the carriers could

thermalize to GaN shallow or deep defects or to InGaN QWs. The PL spectra then included all the contributions of bulk GaN, QWs, and yellow band luminescence. Second, as the laser was absorbed in bulk GaN, its intensity decreased with depth, and it could be difficult to control the excitation of deep quantum wells.

At LETI, a macro-PL setup was also used to perform temperature-dependent PL measurements. The setup was quite similar, except that the sample was mounted in a cryostat and the laser was 375 nm with a spot size of 40 μm . The goal here was to compare room and low-temperature PL on the QWs at various excitation powers to estimate their internal quantum efficiency (IQE) at room temperature (assuming that IQE is 100% at low temperature).

III.2.c.ii. Confocal micro-PL (WITEC)

In our study, we used the WITEC bench for confocal micro-photoluminescence (μPL) measurements. μPL is a technique that relies on focusing the excitation laser onto the sample with a microscope objective. The emitted light is collected by the same objective and then transmitted to a spectrometer via a collection fiber. The use of a fiber is what makes the collection confocal, as only the PL emitted in a small volume is collected ($\sim\mu\text{m}^3$). The entire setup is shown in **Figure 2-3**. When using a 405-nm laser, the quantum wells (QWs) are excited resonantly, meaning that the energy of the excitation light is sufficient to create charge carriers in the QWs but not in the surrounding GaN material. The setup allows to perform mappings by recording a spectrum at each excitation spot. We end up with hyperspectral images- that give us information about intensity and wavelength distribution.

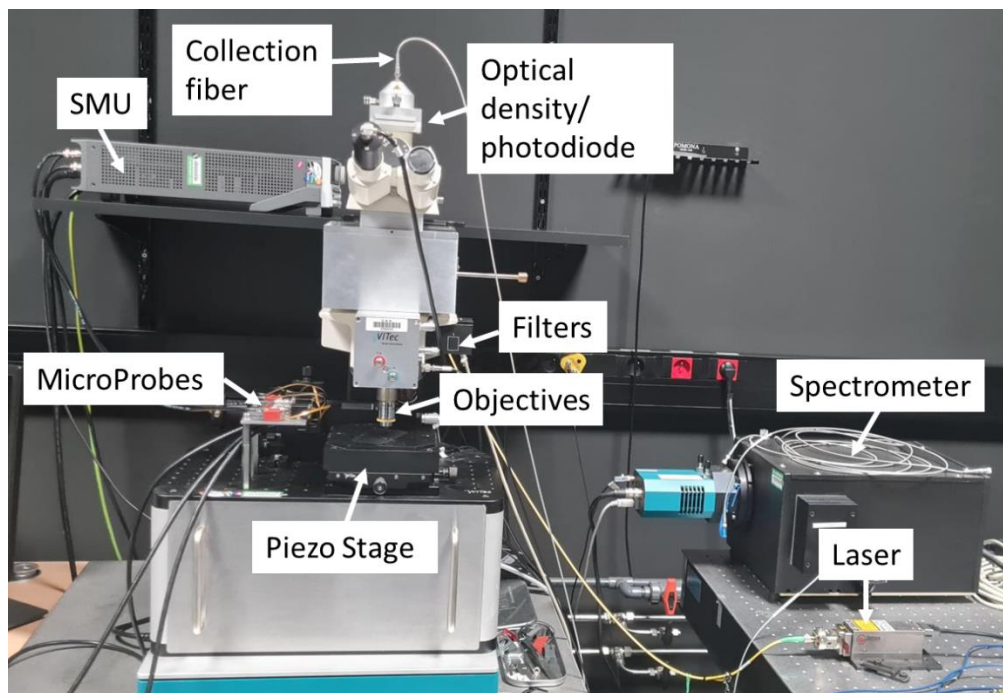


Figure 2-3: μPL and μEL setup.

In addition, this bench was modified to conduct micro-electroluminescence (μ EL) measurements to study LEDs, which will be presented in **Chapter V**. Instead of using a laser, LED pads are contacted with robot microprobes to polarize the devices (**Figure 2-3**). A single SMU with two channels can be used to perform I-V-L measurements. In this case, the photons emitted by the μ LEDs are collected through the objective and detected by a photodiode placed at the top of the optical column. The EL can also be collected with the optical fiber, in a confocal way, and analyzed by the spectrometer.

III.2.c.iii. Zeiss PL imaging setup

Finally, we used a Zeiss PL imaging setup, also called an epifluorescence microscope in biology, to excite and image the PL over a large area of the sample. The setup is based on a cube containing an optical filter to select the range of excitation wavelengths from a white light source, a dichroic mirror, and a PL filter that lets only the wavelengths of interest pass through. This setup allows us to image the PL distribution with a high-quality color camera. We also have the possibility to focus a 405-nm laser on the sample and image the PL with the same camera, as we will see in the red MQW study in section **III.3.e.ii**.

III.2.d Time Resolved Photo-Luminescence (TRPL)

With this technique, we aim to measure the lifetime of the electron-hole pair before recombination. At LETI, the TRPL setup uses a 376nm pulsed laser with a pulse duration smaller than 40ps and is used at a repetition rate of 5MHz (200ns period). The decay curve is constructed as the histogram of the time delay between pulsed excitation and PL photon arrival on the SPAD detector. From this decay curve, it is possible to estimate the carrier lifetime (τ) by fitting it with a mono-exponential function [2]:

$$I(t) = I_0 * e^{-\frac{t}{\tau}}$$

Where the carrier lifetime τ is expressed with two components, a radiative time (τ_{rad}) and a non-radiative time (τ_{nonrad}):

$$\frac{1}{\tau} = \frac{1}{\tau_{rad}} + \frac{1}{\tau_{nonrad}}$$

However, InGaN QW rarely exhibits mono-exponential decay. First because in a quantum well the decay time will depend on the carrier density as can be seen in the framework of an ideal ABC model [3]:

$$\frac{1}{\tau} = A + 2Bn + 3Cn^2$$

In a decay time experiment n changes with time, so τ as well. In addition, we should take into consideration the electric field screening, and band filling at high carrier densities and the potential

fluctuation in the InGaN QW. It is then difficult to model this complex decay and can just extract a characteristic time τ .

III.2.e Optical Differential Lifetime Measurement (ODL)

The main aim of this technique is to measure a decay time at a given carrier density within the active region. It is called the optical differential lifetime (ODL) measurement because the PL is excited with a continuous laser with the addition of a small-signal modulation. The time delay of the optical response to the small-signal excitation leads to the recombination lifetime. In addition, when the period of the small modulation gets close to the PL decay time, the S21 amplitude decreases.[4]

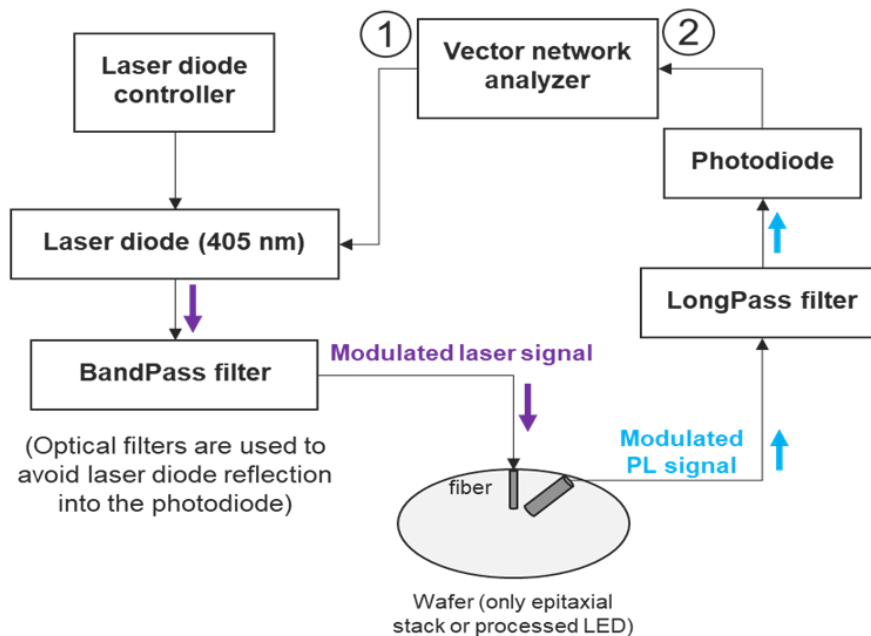


Figure 2-4: The schematic of the PL-RF setup (credits P.Le Maitre).

This experiment was mounted at the laboratory of CEA-LETI and is described in the schematic of **Figure 2-4**. The ODL experiment setup includes key components such as a laser diode controller that sends a direct current (DC) to a laser diode that excites the sample at 405nm. The sample can be in our case either an LED or MQW epistructure. In addition to the DC, a radio-frequency (RF) small signal is also added by the vector network analyzer (VNA) to the laser diode for frequency (f) modulation. This results in sine oscillations of the optical power response of the sample. By increasing the frequencies (f), we monitor the LED optical response until it decreases to half of its initial reference DC value (modulation bandwidth at 3dB) to calculate the carrier lifetime following this equation [5]:

$$\frac{\sqrt{3}}{\tau} = 2\pi f_{3dB}$$

III.3 Multi-Quantum Well (MQW) Growth

The multi-quantum well (MQW) epitaxial structure was initially grown in the TS reactor based on previous work on semipolar GaN done at CRHEA. The growth of this step was first developed in the TS reactor before switching to the Aixtron reactor. A similar growth recipe was used on both reactors, except for the temperature, which needed to be tuned. This section will first discuss the growth results obtained on the TS reactor. We will then focus on the results from the Aixtron reactor, comparing them to the TS results.

III.3.a MQW structure

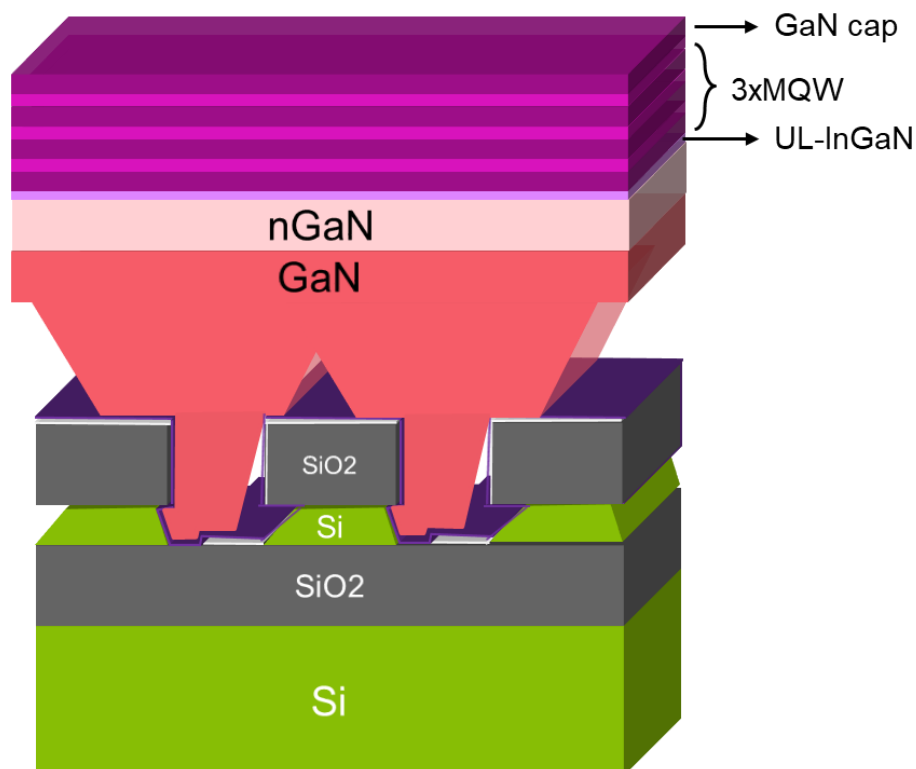


Figure 3-1: The different layers of the MQW structure.

The structure used in this work is described in **Figure 3-1** and consists of growing on top of the previously developed GaN coalesced layer:

1) An InGaN underlayer (UL) has a lower indium composition compared to the MQWs. This UL aims to trap the point defects that act as nonradiative recombination centers as explained in **Chapter I**. In addition, one of the advantages of semipolar GaN is the possibility of stress relaxation by dislocation gliding along the basal (0001) plane when growing an InGaN underlayer. This creates the misfit dislocations at the InGaN/GaN interface as explained by Romanov et al.[6] Consequently, this relaxed UL will help us incorporate more indium in the MQWs.

2) Three InGaN/GaN quantum wells with various growth temperatures. By decreasing the MQW's temperature, the composition and thickness of the InGaN QWs will be varied, and thus longer

emission wavelength will be obtained. Indium incorporation is sensitive to growth temperature because of In evaporation from the surface at higher temperatures during growth, hence the higher In composition while decreasing the MQW temperatures

3) A GaN cap layer having the same set temperature growth and duration as the GaN quantum barriers.

All the investigation of MQW growth was performed on 600nm SiO₂ ART thickness. The set temperatures used for the above-mentioned layers are described in **Table 3-1** below for both reactors.

Table 3-1: Growth set temperatures used for each grown layer for the TS and Aixtron MOVPE reactors.

Layers	TS Temperature (°C)	Aixtron Temperature (°C)
InGaN UL	980-960-940	980-940-900-880
InGaN QWs	840-820-800	860-820-760-710
GaN QB and cap	980-960-940	980-940-900-880

The growth recipes for both reactors were based on similar projects done at CRHEA on semipolar orientations. We were interested in modifying the recipes to achieve different wavelength emissions, which required adjusting the temperature of the MQWs. However, we did not have enough time to study the different layers and develop further growth.

III.3.b Characterization of MQW grown on the TS

III.3.b.i. Structural Characterization

SEM images in **Figure 3-2. a, b, and c** display similar surface features after MQW growth on TS, irrespective of the MQW growth temperature (from 840 to 800 °C). The surface reveals the complete absence of cracks, some undulations along the +c direction, and the presence of chevrons. The surface roughness was investigated on the sample grown at 800°C and revealed a 1.5nm RMS on a 2x2µm² area with no undulations as presented in **Figure 3-2.d**. The formation and presence of chevrons have already been discussed earlier in **Chapter II**. However, it is worth mentioning that the evolution of their dimensions could be further impacted by the lower growth temperature used for the QWs and the GaN barrier/cap. Meanwhile, the emergence of well-defined undulations could have two potential explanations. The first could be related to anisotropic surface diffusion between the [10 $\bar{1}$ 1] direction and the +c-direction, which has already been reported for different directions in (11 $\bar{2}$ 0) GaN layers grown on (11 $\bar{2}$ 0) bulk GaN substrates [7]. A lower growth temperature, used for the QWs and the GaN barrier/cap, could then further enhance the anisotropic surface diffusion between the two directions and trigger the formation of periodic undulations. A second explanation could be the initial imperfect coalescence, triggering periodic undulations after GaN coalescence, which would be then further exacerbated at lower temperatures. Note that the periodicity of the aforementioned undulations seems to vary between the samples but is always larger than the initial 5 µm period of the patterned stripes.

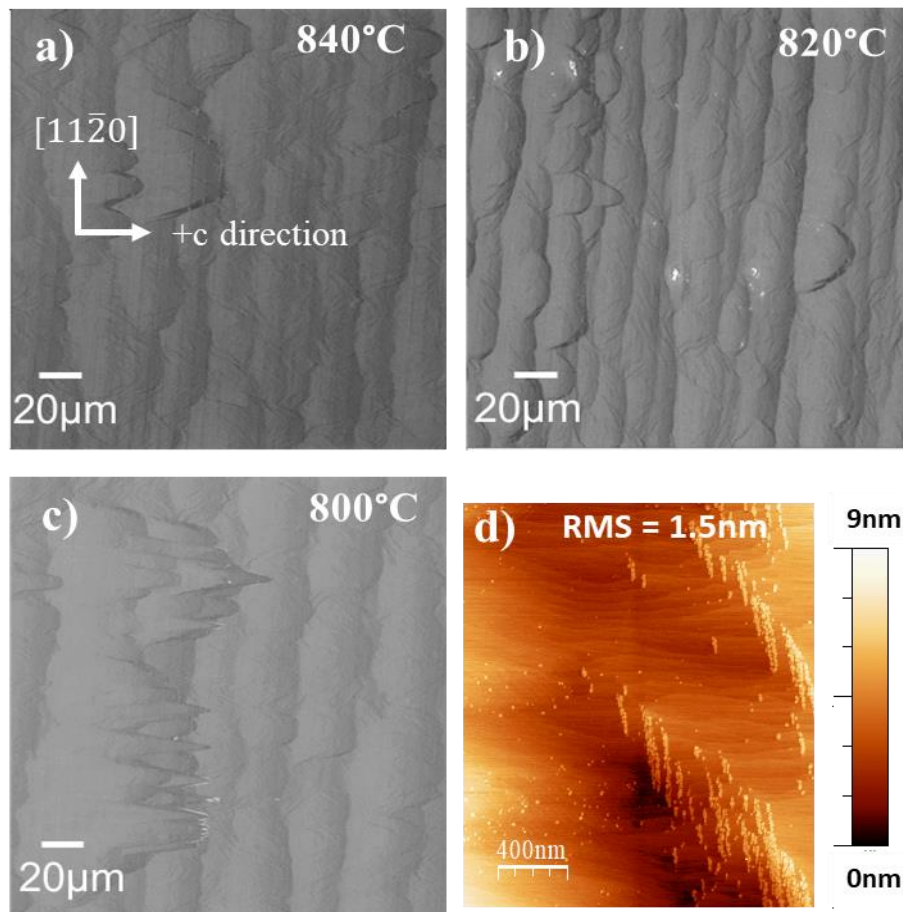


Figure 3-2: Top view SEM images of three MQW grown at a) 840°C, b) 820°C and c) 800°C. d) $2 \times 2 \mu\text{m}^2$ AFM image of sample c).

III.3.b.ii. PL

Figure 3-3.a shows the RT macro PL spectra of the three different MQWs grown at different temperatures conducted at CRHEA. It clearly shows that when decreasing the temperature from 840 to 800 °C, the InGaN emission redshifts from 430 to 490 nm. PL images are acquired on the Zeiss microscope on these three MQWs as depicted in **Figure 3-3.b-d** to confirm the emission wavelength shifting from purple to green as we decrease the temperature. In addition, we only observe a slight decrease in intensity with the temperature, which might be ascribed to the quality degradation when incorporating more indium.[8] However, we need to be careful with absolute PL intensity comparison, as light extraction can vary from one sample to another. For instance, due to a possible small change of density of large defects like chevrons or light scattering along the stripes due to the void between two consecutive stripes as seen in **Figure 3-1**. Few chevrons are observed on the PL microscopy images showing a different emission. Their behavior will be further investigated locally in section **III.3.b.iv**.

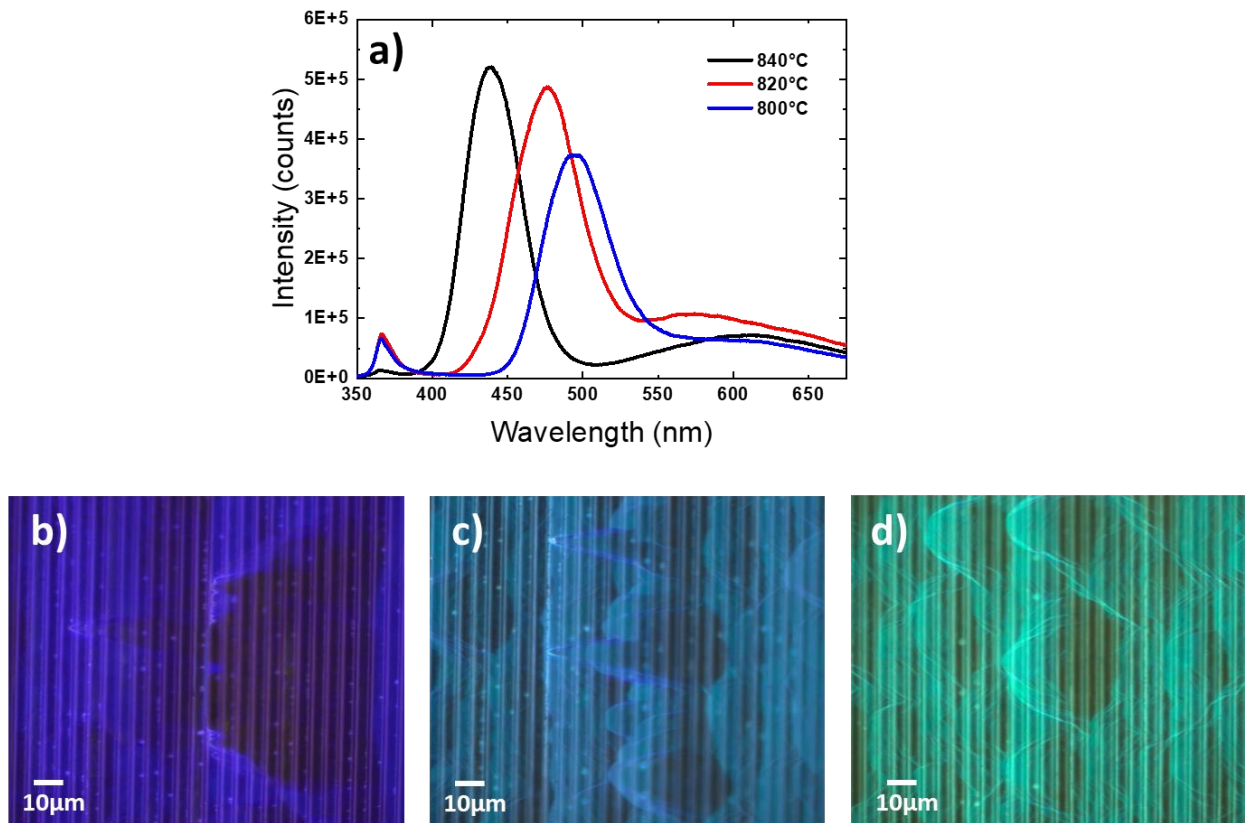


Figure 3-3: a) RT PL spectra of the three samples having MQW grown at 840°C (black), 820°C (red), and 800°C (blue) with their corresponding PL microscopy images in b-d) respectively.

III.3.b.iii. TEM

Figure 3-4 displays an STEM image at two areas of the MQW sample grown at 820°C emitting around 470nm. Non-uniformities of the QW thicknesses were clearly observed in both areas of the sample where the thicknesses were random. The reason behind this growth behavior is still unresolved as it can be due to the surface morphology and/or the growth temperature impacting the surface diffusion of the species. However, as the two investigated areas are close to each other, it is unlikely that the growth temperature is the reason behind this nonuniformity. As for the surface morphology, this will be further studied when using the second reactor in section III.3.d. The impact of this MQW nonuniformity on the wavelength shifting will be discussed in **Chapter V** after the μ LED fabrication.

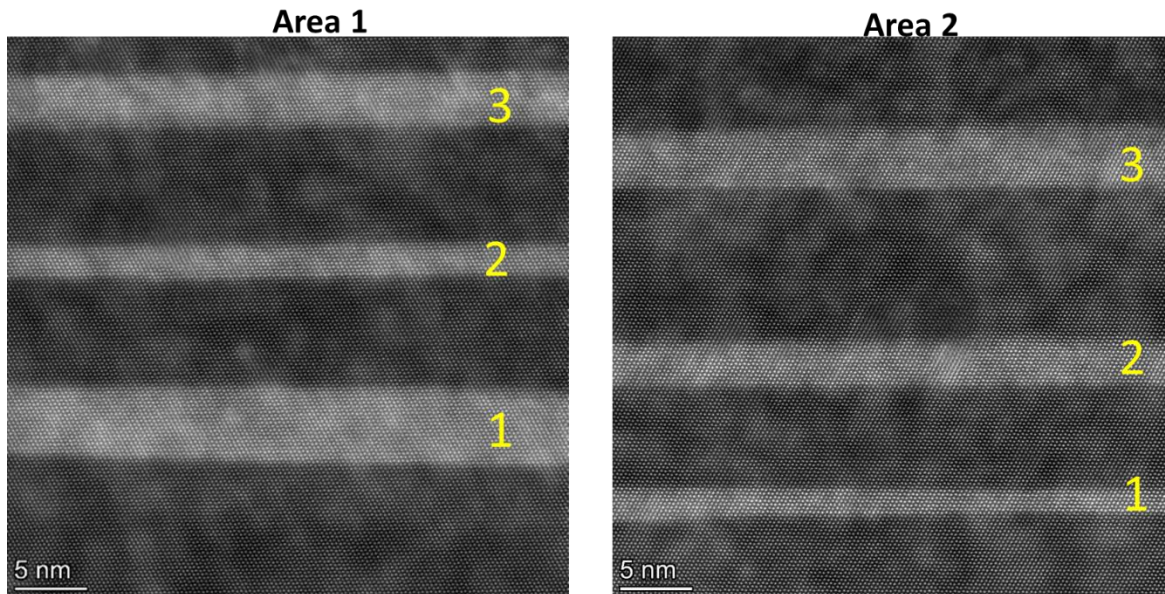


Figure 3-4: High-resolution STEM image of the MQW sample grown at 820°C showing a variation of thicknesses of the 3 QWs for two different areas.

III.3.b.iv. CL

The map of the wavelength peak position in **Figure 3-5.a** indicates a relatively low wavelength dispersion of 485 ± 10 nm on the flat area surrounding the chevron and on its top. The arms of the chevron are instead dominated by a lower wavelength emission at 455 ± 15 nm. This could be due either to a lower In incorporation or to a variation of the well widths along the different GaN plane orientations on the chevron arms. The FWHM map of the QW emission indicates a broadening in the order of 50 ± 5 nm, which becomes narrower within the chevrons arms (**Figure 3-5.b**). Both results highlight the chevron's impact on the resulted in QW wavelength emission and FWHM, which was also observed by Brassler *et al.*[9]

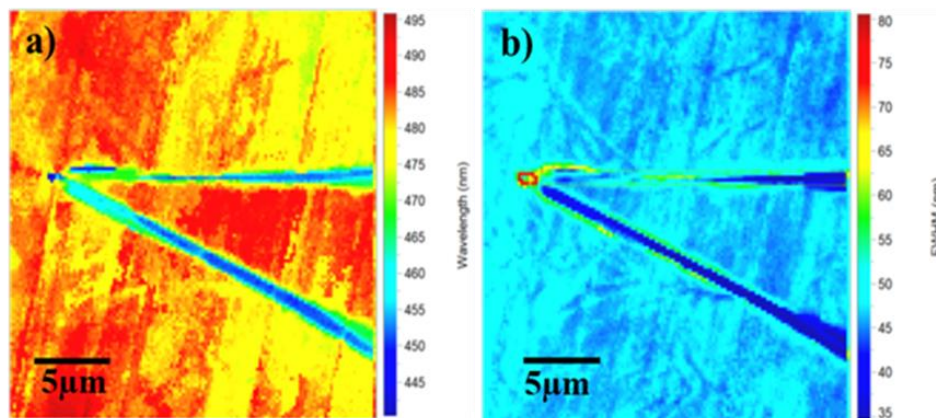


Figure 3-5: RT CL map of the (a) wavelength peak position and (b) FWHM of the QW emission for the sample grown at 800°C.

III.3.c TS and Aixtron reactor comparison

Electrochemical capacitance–voltage (ECV) measurement has been performed on two blue quantum well samples grown on the TS and the Aixtron reactors to identify and compare the active n-dopant concentrations. The Aixtron sample presented a better concentration of $1.1 \times 10^{20} \text{ cm}^{-3}$ compared to

$1 \times 10^{19} \text{ cm}^{-3}$ of the one grown in TS as observed in **Figure 3-6**. These results convinced us to focus on growing all the MQW and LED structures on the Aixtron reactor which will be characterized in the following sections.

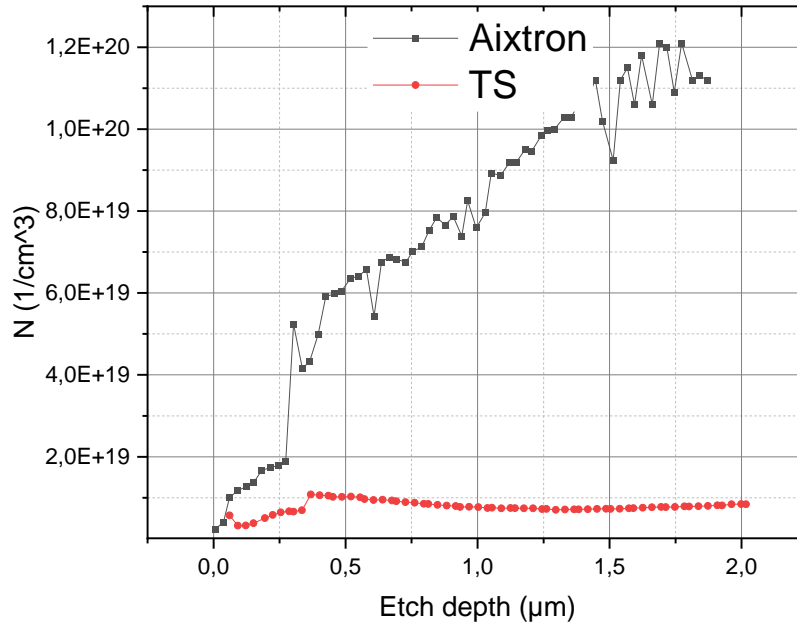


Figure 3-6: ECV measurements of active n-dopant concentrations on a sample grown on the TS (red) and a sample grown on the Aixtron (black).

III.3.d Characterization of MQW grown on the Aixtron

III.3.d.i. TEM

As seen previously, the samples grown on the TS reactor presented a non-uniformity in the MQW thicknesses. Therefore, the same experiment was conducted on one of the samples grown on the Aixtron reactor to verify the MQW thicknesses. **Figure 3-7** shows a STEM image of the three MQWs having similar thicknesses ($\sim 2 \text{ nm}$) and a thick UL of $\sim 6 \text{ nm}$ close to the first grown QW. Contrary to what was observed on the TS samples, the QW thicknesses of this batch are repeated in several areas and on different samples despite the similar surface morphology obtained in both reactors. Qualitatively, we observed a lower [In] concentration in the UL compared to the three MQWs, but the calculation of the In composition will be presented in **Chapter V**.

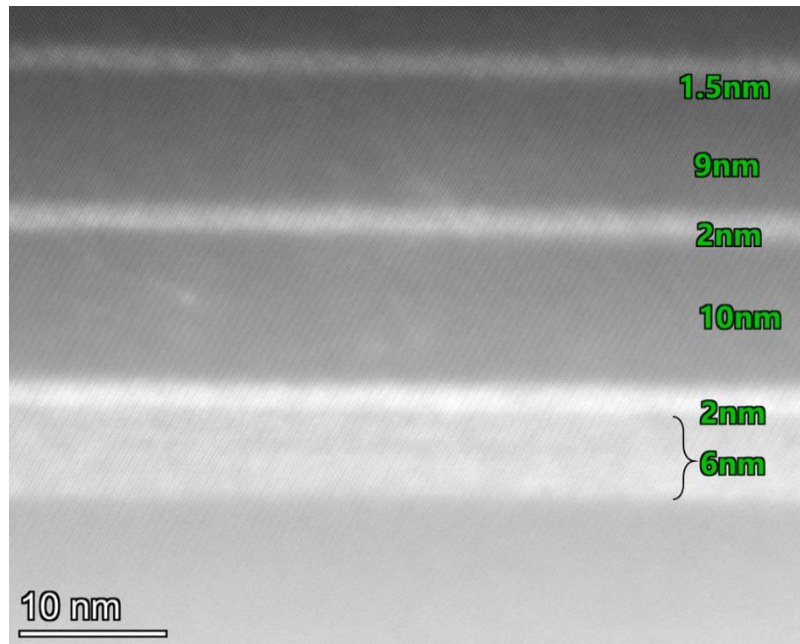


Figure 3-7: High-resolution STEM image of the MQW sample showing uniform MQWs thicknesses while growing the UL InGaN directly before the first QW.

III.3.d.ii. PL

As presented in **Table 3-1**, four different MQW set temperatures were adjusted to reach an emission wavelength going from turquoise to red. **Figure 3-8.a** shows the RT macro-PL of a GaN template as a reference and the 4 MQW samples. As previously seen on the TS MQW samples, the emission wavelength redshifts with the decrease in growth temperatures. Although we aimed to reach red at 710°C, the wavelength ended up in the yellow band region with an emission at 558nm. Further investigation on this sample will be presented later in this chapter. PL microscopy was then performed on the turquoise, green, and orange samples to study the emission uniformity on the surface as presented in **Figure 3-8.b-d**, respectively. A change in PL intensity is observed orthogonally to the stripes in specific areas of the samples that we tentatively attributed to the undulations along the same directions. Knowing that the morphology of these samples was similar to the surface morphology observed by SEM on the TS samples.

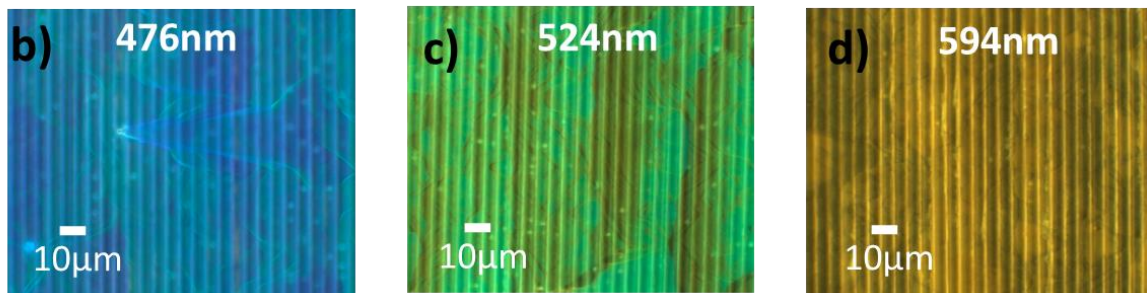
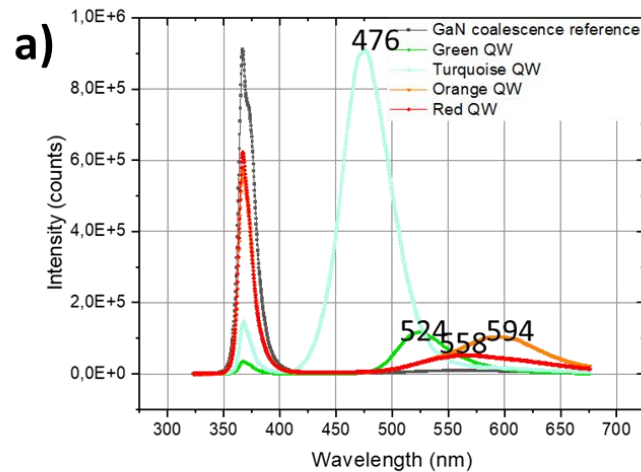


Figure 3-8: a) RT PL of a reference GaN template and the four MQW samples (turquoise to red) grown at 860-710 °C. b-d) PL microscopy images of the turquoise, green, and orange samples, respectively.

III.3.d.iii. Low Temperature PL (LT PL)

One of the advantages of using semipolar GaN is the wavelength stability obtained when the carrier density changes. This is related to the low internal field present along these crystallographic orientations. Therefore, we conducted a LT-PL on the three MQW samples to test their qualities. To do this experiment, we needed a power-dependent LT-PL that allowed us to also verify the wavelength shift. **Figure 3-9.a** presents the LT-PL spectra of the turquoise sample obtained when changing the laser power from 1.7×10^{-6} W to 3.5×10^{-2} W. A stable wavelength is indeed observed which is consistent with the literature results[10]. For polar GaN, a blueshift normally occurs when increasing the excitation power due to the electric field screening [11] as explained in **Chapter I**. To assess the quality of the MQW, we aimed to estimate the IQE by performing RT and LT-PL. The normalized PL efficiencies at 13K and 290K for the turquoise sample are given in **Figure 3-9.b**. The efficiency for both temperatures of this sample remains roughly stable throughout the power variation with a maximum IQE measured to be 46%. The reason behind this maximum value could be due to the dislocations and surface defects present along the surface.

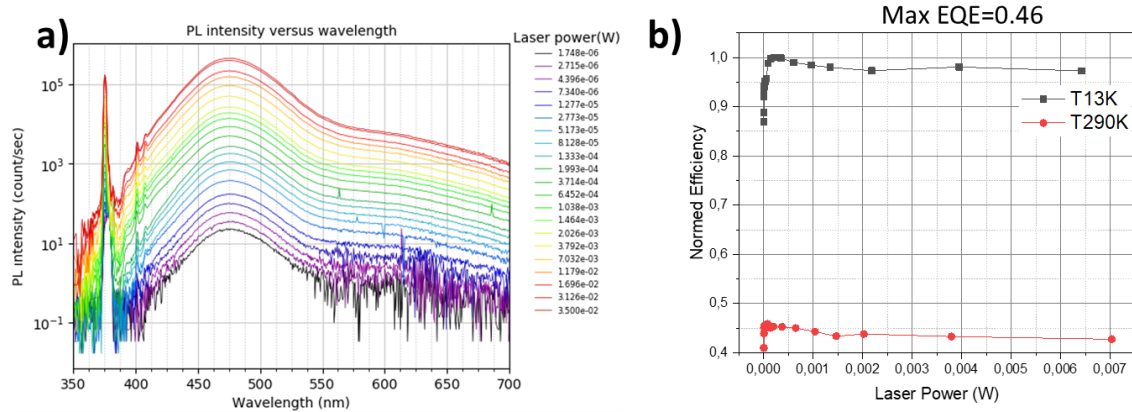


Figure 3-9: a) LT-PL intensity spectra and b) Normalized PL efficiency of the turquoise MQW.

III.3.d.iv. Time-Resolved PL (TRPL)

To have more insights into the recombination rate within the MQW, time-resolved photoluminescence measurements were conducted at low and room temperature on the 3 MQW samples. **Figure 3-10** presents the TRPL results obtained at the median wavelength for each sample that we will compare qualitatively due to the complexity of the calculation.

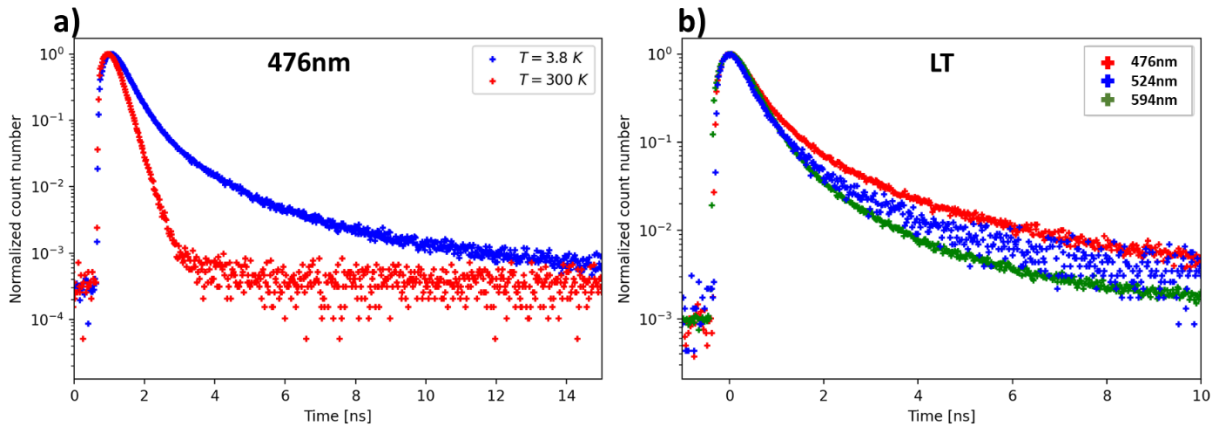


Figure 3-10: TRPL measurement on the three MQWs samples. a) A comparison of the turquoise MQW at RT and LT. LT-TRPL measurements on the green and orange MQW samples in b and c) respectively.

Figure 3-10.a shows a faster decay at RT compared to the LT-TRPL for the turquoise sample due to the contribution of non-radiative recombinations typically attributed to the defects.[12] Focusing on the radiative recombination rate, which is dominant at low temperatures, **Figure 3-10.b** presents the plotted decay curve of the turquoise (red curve), green(blue curve), and orange(green curve) MQW samples showing a fast and similar decay. Contrary to polar InGaN QWs, when changing the indium composition, semipolar InGaN QWs presented no significant difference in the decay time which is consistent with a low internal field.

It is important to insist that these decay curves are dependent on the carrier concentration (hence the excitation power) as explained earlier in the framework of the ABC model in **III.2.d**. This explains the fast decay at $t=0$ when the MQWs are filled with a high density of carriers and then slower recombination over time. Here the important point is to assume that the 376nm laser excites the MQW in the same way which allows us to compare them. However, due to the complexity of this technique, we complemented these results with optical differential lifetime (ODL) measurements. Using the latter technique enables control the number of carriers for a given decay time.

III.3.d.v. Optical Differential Lifetime (ODL)

We compared the frequency response of the semipolar green MQW sample to that of two polar samples with single QWs of different thicknesses, as presented in the plot of **Figure 3-11**. The first polar sample has 1.5nm thick QWs that emit at 430nm whereas the second sample has a thicker one of 2.5nm that emits at 450nm. The semipolar MQWs thicknesses are around 2nm. In **Figure 3-11**, the optical transmission power represents the PL response to the small signal modulation used in ODL. A decrease in the power transmission means that the recombination process is not fast enough to properly respond to the modulation frequency. We can see that at the same excitation power (so similar carrier concentrations), we observed a decrease in the optical transmission power at a lower frequency for both polar QW samples compared to the green MQW of the semipolar. With an even higher Indium composition and similar QW thicknesses, semipolar presented a better performance. This is an important result that confirms the potential of semipolar MQWs for the μ displays (that need fast emitters for PWM dimming and high frame rate) as well as for VLC applications which is a growing activity in our laboratory. However, we have to keep in mind that this technique is conducted at room temperature and with a rather low excitation power density. It means that the SRH non-radiative recombination could contribute to the faster response of the semipolar sample compared to a more matured epitaxial quality such as the polar ones. Therefore, to confirm this outcome, we repeated similar measurements after the μ LED fabrications in **Chapter V** with an electrical injection of the carriers and we could confirm the same trend compared to the c-plane even at high current density when SRH non-radiative recombination is less important.

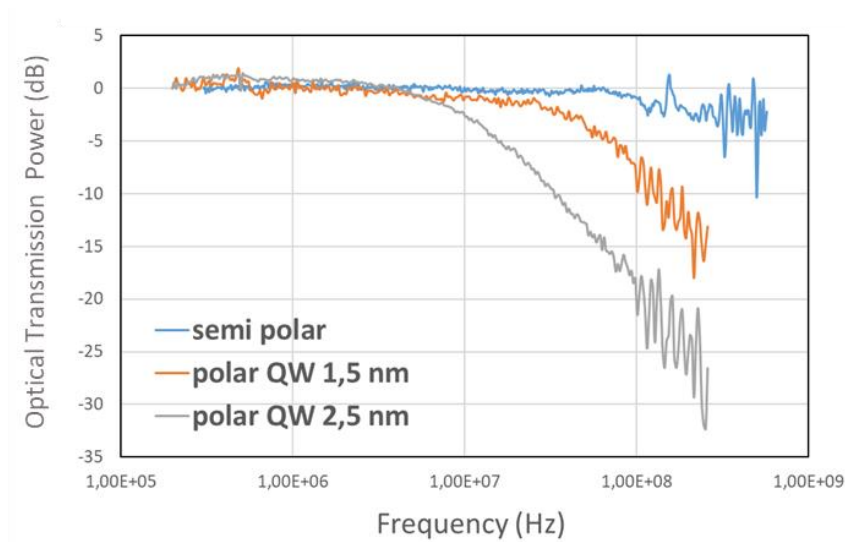


Figure 3-11: ODL on two polar GaN samples grown on different QW thicknesses compared to a green semipolar QW sample.

III.3.d.vi. Cathodoluminescence (CL)

Room temperature CL was used on a blue LED structure emitting at 460nm to quantify the dislocation density across the surface.

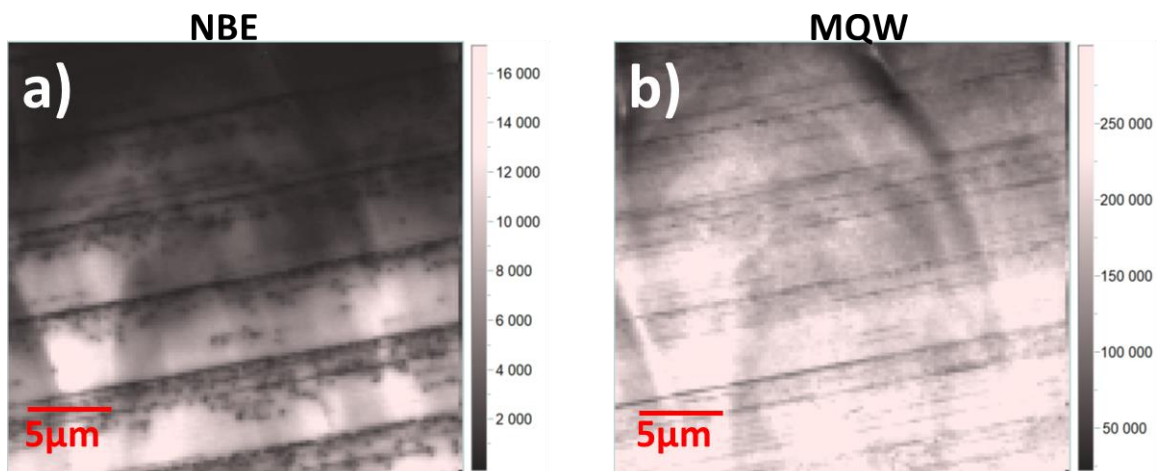


Figure 3-12: Integrated plan-view CL intensity imaging measured at RT of the blue LED epi structure (electrons acceleration voltage: 5KV) of the a) GaN NBE at 360nm and b) InGaN/GaN MQWs at 460.

Figure 3-12.a and **b** show the plan-view integrated CL intensity images of the GaN NBE and MQWs emission, respectively. Both are measured using the same acceleration voltage of 5KV enabling the electron beam to reach the nGaN layer. The black spots observed in **Figure 3-12.a** are the TDs as previously seen in **Chapter II** at the template level. The aim of comparing the NBE with the MQWs peak is to check if the TD density is increasing with the additional layers grown at different temperatures. **Figure 3-12.b** shows black lines (misfit dislocations) almost replacing the high TDs areas present in **Figure 3-12.a**. This behavior is commonly observed for dislocation in semipolar orientations when MQWs are relaxed [6], [13] as elaborated in **Chapter I** and in section **III.3.a** of this chapter.

III.3.e Red MQW characterization

The macro-PL results of **Figure 3-8.a** done at CRHEA, show that InGaN/GaN growth at 710°C resulted in a yellow band emission. As mentioned in section **III.2.c.i**, the use of a 244nm laser excites the GaN, the yellow band emission as well as the QWs. Therefore, in order to understand the MQW emission of this sample, more localized characterizations were conducted using a 405nm laser.

III.3.e.i. μ PL

μ PL is complementary to the PL measurements in terms of optical quality, but instead of integrating a large region, μ PL enables the excitation of specific localized areas using a 100x Olympus microscope objective (NA=0.95) with a spot size of roughly 300nm close to the diffraction limit. In our case, this will provide us with more spatial information on the wavelength shifting regarding the chevrons, the stripes, and the defective areas.

We first used this technique to study the wavelength shifting with respect to a set of laser power as a confirmation of the power-dependent LT macro-PL previously conducted on the turquoise MQW sample.

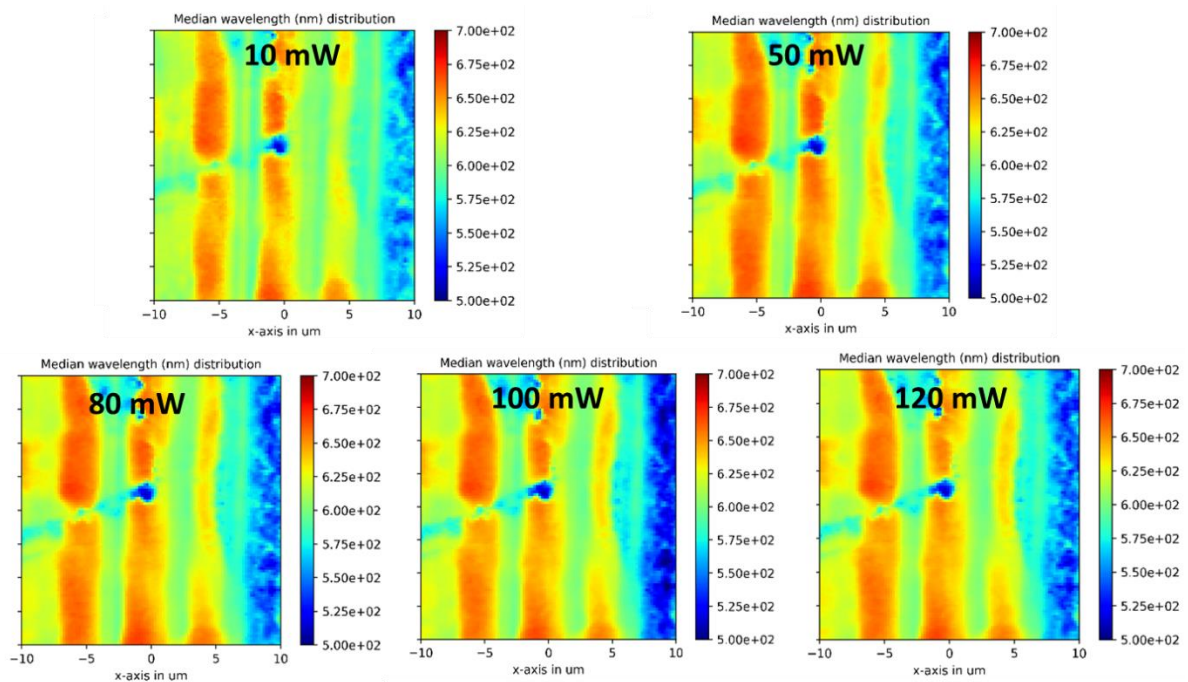


Figure 3-13: μ PL mapping of the red MQW for a set of optical laser power.

Figure 3-13 displays the μ PL mapping of the various excitation power used (10 to 120mW). Three observations can be deduced from this result; the first one is the three different emission areas following the stripes direction. The second one is the wavelength stability while varying the excitation power. The last observation is the red emission around 650nm. However, due to the very low intensity compared to the yellow band, when using a larger spot size as in macro-PL, the average wavelength is dominated by the yellow band emission.

The WITEC is a confocal microPL setup that can perform mapping over small areas but it is not adapted to explore rapidly the whole sample. For that reason, a PL microscope will be used in order

to locate the positions of the three different emission areas observed in **Figure 3-13** compared to the surface defects, undulations, and the coalescence lines.

III.3.e.ii. PL microscopy

We used the PL microscope for its high-quality color camera, the ability to use a focused laser source similar to the one used on the WITEC, and the motorized stage that made exploring the sample easier. This allowed us to distinguish the variation of wavelength emission by scanning along the sample surface and to locate the different emission areas previously observed by μ PL. As shown in **Figure 3-14.a**, we decided to investigate a defect-free area emission (red, blue, and purple circles ascribed to **Figure 3-14.b,c** and **f**) as well as the impact of the undulations on the wavelength (yellow and green circles ascribed to **Figure 3-14.d** and **e**). By comparing the μ PL results obtained, we can clearly distinguish that the emission around 650nm is attributed to the area in between the coalescence lines, shown in **Figure 3-14.b**, whereas the coalescence lines are emitting in orange as seen in **Figure 3-14.f**. The highest dislocation density is along the coalescence lines as seen by the CL which might explain the blueshifting compared to a defect-free area emitting in red. However, once closer to the undulations, the wavelength strongly blueshifts as observed in **Figure 3-14.c-e**. This result was repetitive along the entire surface of this sample. This strong blueshift can be attributed to the different semipolar orientations along this undulation leading to a different In incorporation. Or the undulations might be causing variation in the MQW thicknesses. However, this was not observed on the other three MQW samples (turquoise, green, and orange), hence the reason behind this strong blueshift along the undulations is still unknown. Further local characterization of chevrons and undulations will be presented in the following section.

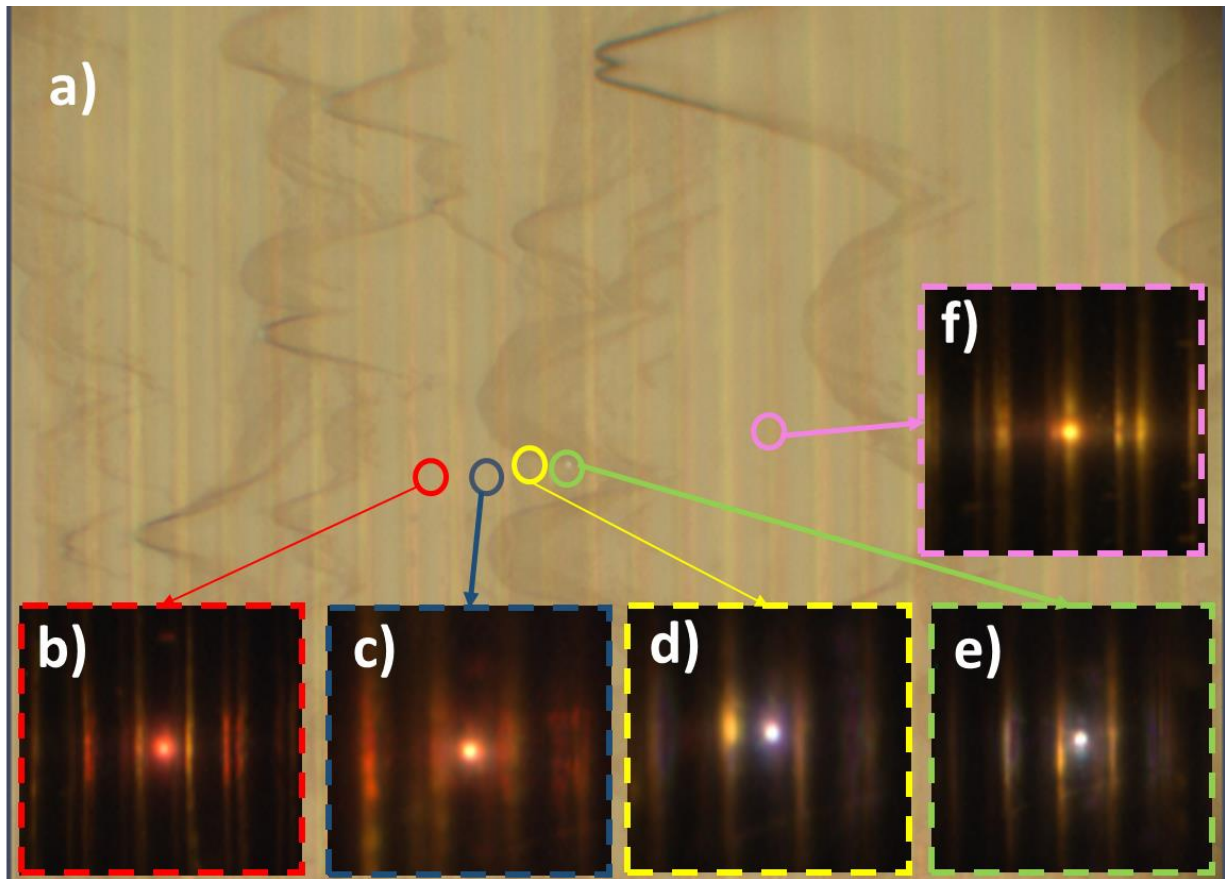


Figure 3-14: a) Optical microscope (OM) image indicating the studied areas by circles. The color of the PL emission of each area is presented in b-f).

III.3.e.iii. TEM

TEM measurements were done on the same sample to have more understanding on the indium incorporation that might lead us to confirm the MQW red emission.

We can see the three QW being brighter than the GaN bulk and QBs due to the In concentrations in **Figure 3-15.a**. The InGaN underlayer is also present right before the first grown QW. One can distinguish two threading dislocations, indicated by the red arrows, reaching the MQWs from the GaN template. Contrary to the turquoise MQW observed by STEM in **Figure 3-7**, a high density of dislocations is formed at the MQWs level indicating their relaxation. Typically, with the increase of the In concentration, the lattice mismatch between the QW and barrier increases, and hence, more TDs are generated to relax the strained MQW.[14] The high density of dislocation observed in this sample might explain the low red PL intensity and domination of the yellow band intensity instead. **Figure 3-15.b** shows a closer view of the UL and first QW. We can see that dislocations are formed at the MQWs level, meaning that the UL is still strained. Mantach *et al.*[15] observed partial relaxation of the UL starting at a thickness of 10 nm for the same semipolar orientation. Therefore, in our case, the UL is 6nm which is less than the critical thickness for relaxation. Additionally, the growth temperature of the underlayer was varied according to the MQW temperatures used. In order to study the impact of this layer, the growth parameters should be fixed for the different MQW temperatures.

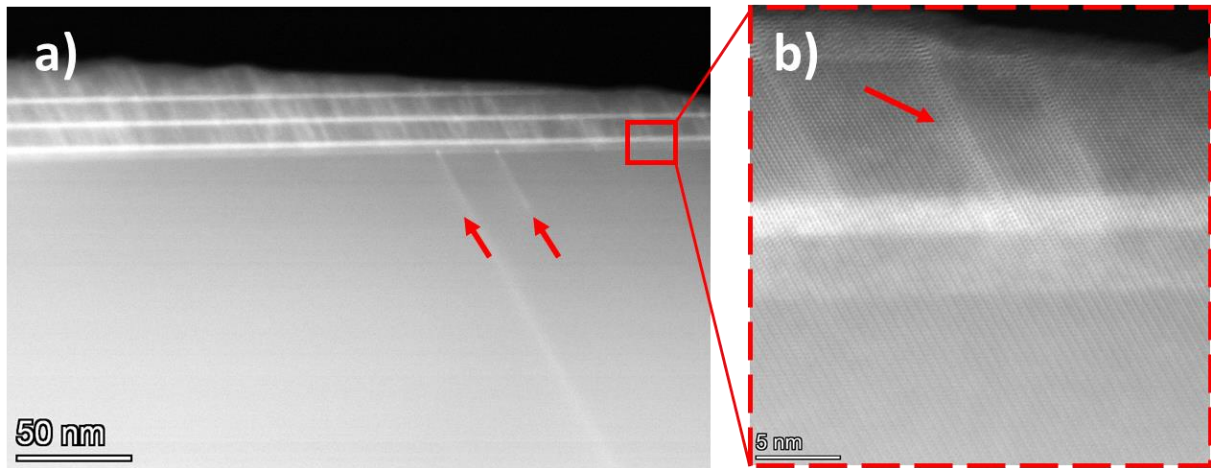


Figure 3-15: a) STEM on the three MQWs showing the high density of TDs starting from the growth of the first QW as confirmed in b).

Due to the relaxed MQWs, we weren't able to have an accurate calculation of the In concentrations using a method that relies on strain-induced deformation. Therefore, we used the EDX to realize chemical maps and chemical analyses. The STEM-HAADF image of **Figure 3-16.a** shows distinctively the 3 InGaN/GaN MQWs and barriers with the InGaN UL. **Figure 3-16.b** shows EDX chemical Ga and In maps from the region seen in **Figure 3-16.a**.

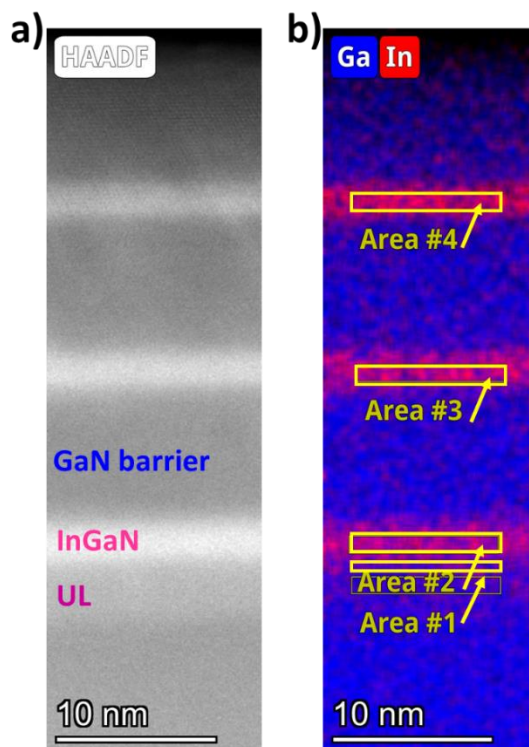


Figure 3-16: a) High-resolution HAADF image showing the 3 InGaN MQWS, GaN barriers, and the InGaN UL. b) EDX elemental map for the spatial distribution of Ga and In atoms of a).

The In and Ga compositions of the different areas mentioned in the EDX map and their error range of **Figure 3-16.b** are presented in **Table 3-2** below:

	% Ga	% In	error % Ga	error % In
Area #1	93.96	6.04	0.77	0.77

Area #2	76.35	23.65	2.44	2.43
Area #3	75.25	24.75	2.52	2.52
Area #4	69.38	30.62	2.87	2.87

Table 3-2: In and Ga composition percentage as measured by EDX.

As expected from the contrast of the STEM images, the InGaN UL has a low In concentration compared to the MQW. The percentage of In differs from one QW to another noting the highest concentration is observed in the last grown QW (area 4) reaching 30%.

It is evident that we lack some characterization data, but these results are still encouraging for this sample and support our goal of reaching red emission with semipolar orientation.

III.4 LED Growth :

III.4.a LED structure

After achieving good growth results out of the MQWs samples grown on the Aixtron in terms of morphology, wavelength, and n-dopant concentrations, we moved to the following step, which is growing an LED structure on a 600nm ART-SOI sample as described in **Figure 4-1** below:

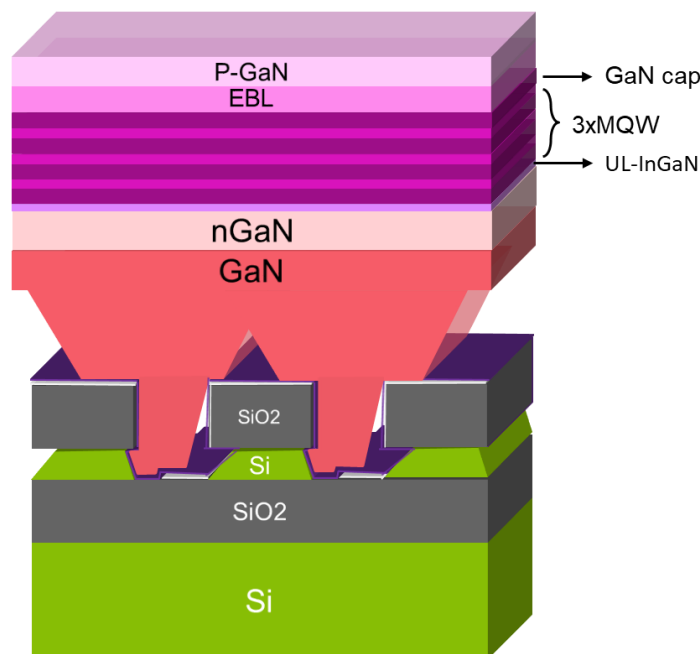


Figure 4-1 : The different layers of the LED structure.

Initially, the development of the LED structure is accomplished on the TS reactor before switching to the Aixtron. The MQWs were chosen to be emitting in the blue for the TS and two samples for the Aixtron one for blue and the other for green emission. The MQWs growth temperature used for these three samples is listed in **Table 4-1**. The temperatures are chosen based on the previous experiments conducted on the MQW grown on the TS and Aixtron reactors. An additional EBL layer of undoped and p-doped AlGaIn was grown on top of the MQW, followed by a pGaIn layer at roughly the same temperature for the T as listed in the table below.

Layers	TS Temperature (°C)	Aixtron Temperature (°C)	
InGaIn/GaIn	820/960	870/990	810/930

GaN cap	960	990	930
AlGaIn+pAlGaIn (EBL)	1140	1195	
p-GaN	1140	1185	
Annealing	900	930	

Table 4-1: Growth temperature of the LED structure layers for both reactors.

III.4.b LED characterization

III.4.b.i. TS sample

Plan-view SEM image and AFM measurements of the blue LED sample shown in Figure 4-2.a, b, respectively, indicate a similar surface morphology to the one of the MQW structure grown on the TS in terms of undulations, but with a slight increase of the surface roughness (~ 5 nm).

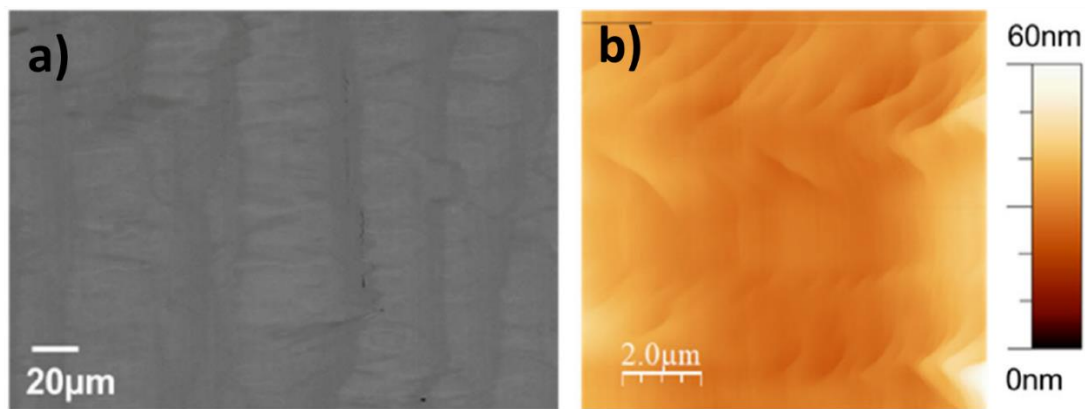


Figure 4-2 : a) a top view SEM image and b) a $10 \times 10 \mu\text{m}^2$ AFM image of an LED sample.

Figure 4-3.a,b shows μPL intensity and wavelength maps of the blue LED structure, respectively. Despite the undulations and chevrons, the intensity was homogenous along the surface and a uniform emission wavelength was observed around 450 nm. The emission wavelength blue shifts between MQWs and LED structure (around 25 nm) for the same MQW growth temperature might be attributed to the indium interdiffusion occurring in the MQWs when subsequent layers are grown at a higher temperature.

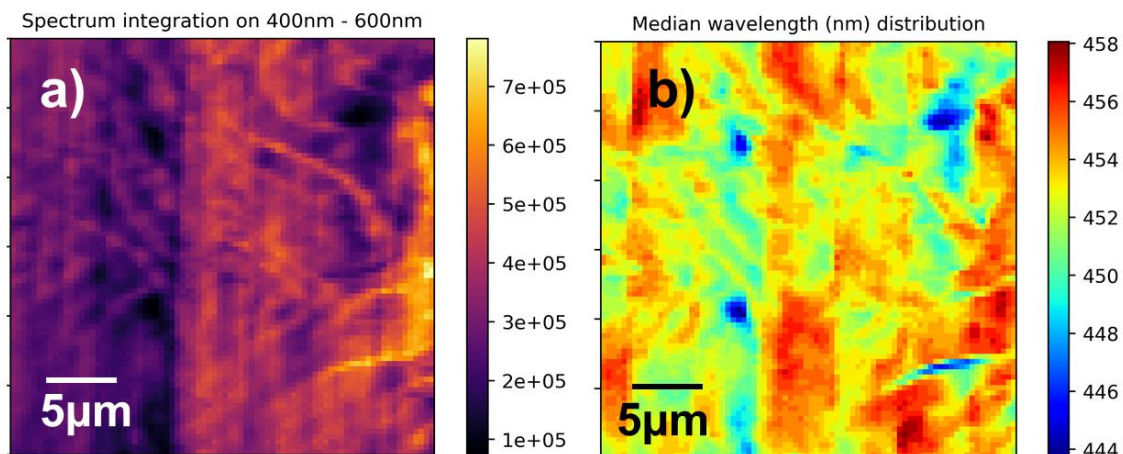


Figure 4-3 : a) μ PL intensity mapping and b) wavelength mapping for the same area of the blue LED sample.

III.4.b.ii. Aixtron sample

For the Aixtron reactor, we tried to obtain blue and green LED epi structures by using the conditions previously mentioned in **Table 4-1**. Although not mentioned in this paragraph, the surface morphology of the blue LED was found to be similar to the TS LED sample. However, the green LED has a higher density of undulations and chevrons whose impact will be observed hereafter. **Figure 4-4.a** presents the RT macro PL conducted at CRHEA of both samples emitting indeed in blue (460nm) and green (533nm). This is also confirmed by the PL microscopy in **Figure 4-4.b** and **c** both the blue and green LED, respectively. However, it is clear that the epitaxial structure quality of the blue sample is more uniform and presents fewer cracks compared to the green sample where cracks can be observed regularly. In addition, emission intensity is very low in various areas along the stripes which is also seen in the MQW PL microscopy of **Figure 3-8**, where these areas become more important with the increase of In concentration. The reason behind their formation, their periodicity, and their impacts are yet to be understood. We suspect that the high growth temperature of the EBL and p-GaN might have damaged the MQWs of the green LED more than the blue one due to the higher In composition MQWs. One possible solution is to try different p-GaN temperatures to verify if similar emission behavior will be obtained.

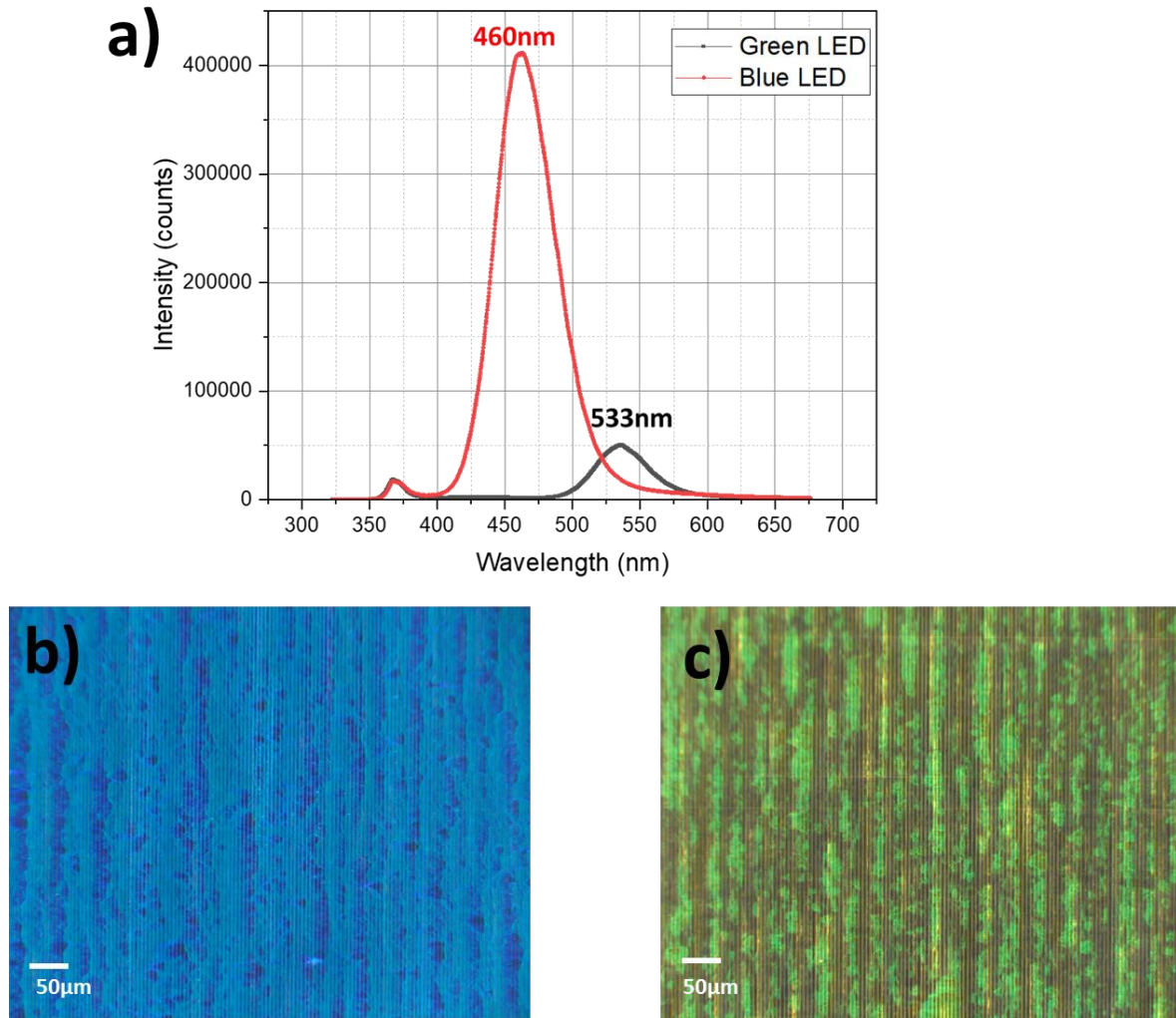


Figure 4-4: a) RT PL of blue and green LED epi structure with their corresponding PL microscopy images in b and c) respectively.

III.5 Conclusion

A comparison of two growth reactors has been performed on two MQW growth batches. Both reactors presented a similar surface morphology as the GaN template in terms of undulations, no meltback etching and low roughness. A change in the MQWs temperature shows a clear shift toward longer wavelengths for both reactors. However, using the Aixtron reactor helped achieve a higher active n-dopant concentrations and a better MQW thickness uniformity as observed by TEM. Optical characterizations were conducted on different MQWs samples to study their quality. Semipolar samples proved to have a decent IQE, wavelength stability when changing the excitation power, and a faster recombination response compared to the polar GaN. These results were consistent with the low internal electric field present in semipolar orientations. More localized characterization was done on a red MQW sample to confirm a red emission around 650nm. CL highlighted the effect of the chevron morphology on the wavelength emission.

Finally, a semipolar LED structure was achieved with a similar surface morphology as the MQW structures and a uniform wavelength emission for both reactors. These results constitute a

demonstration of all necessary building blocks to fabricate a semipolar LED epi structure that will be key in the near future for the realization of semipolar μ LEDs.

III.6 References

- [1] N. Abrikossova, *Investigation of nanoparticle-cell interactions for the development of next generation of biocompatible MRI contrast agents*, vol. 1961. in Linköping Studies in Science and Technology. Dissertations, vol. 1961. Linköping: Linköping University Electronic Press, 2018. doi: 10.3384/diss.diva-152347.
- [2] A. David, N. G. Young, C. Lund, et M. D. Craven, « Review—The Physics of Recombinations in III-Nitride Emitters », *ECS J. Solid State Sci. Technol.*, vol. 9, n° 1, p. 016021, janv. 2020, doi: 10.1149/2.0372001JSS.
- [3] Y.-M. HUANG, « High-efficiency InGaN red micro-LEDs for visible light communication ».
- [4] A. David, N. G. Young, C. A. Hurni, et M. D. Craven, « All-optical measurements of carrier dynamics in bulk-GaN LEDs: Beyond the ABC approximation », *Appl. Phys. Lett.*, vol. 110, n° 25, p. 253504, juin 2017, doi: 10.1063/1.4986908.
- [5] R. Wan, L. Wang, J. Huang, X. Yi, H.-C. Kuo, et J. Li, « Improving the Modulation Bandwidth of GaN-Based Light-Emitting Diodes for High-Speed Visible Light Communication: Countermeasures and Challenges », *Adv. Photonics Res.*, vol. 2, n° 12, p. 2100093, 2021, doi: 10.1002/adpr.202100093.
- [6] A. E. Romanov *et al.*, « Basal plane misfit dislocations and stress relaxation in III-nitride semipolar heteroepitaxy », *J. Appl. Phys.*, vol. 109, n° 10, p. 103522, mai 2011, doi: 10.1063/1.3590141.
- [7] K. Hiramatsu, K. Nishiyama, A. Motogaito, H. Miyake, Y. Iyechika, et T. Maeda, « Recent Progress in Selective Area Growth and Epitaxial Lateral Overgrowth of III-Nitrides: Effects of Reactor Pressure in MOVPE Growth », *Phys. Status Solidi A*, vol. 176, n° 1, p. 535-543, nov. 1999, doi: 10.1002/(SICI)1521-396X(199911)176:1<535::AID-PSSA535>3.0.CO;2-I.
- [8] S. T. Pendlebury, P. J. Parbrook, D. J. Mowbray, D. A. Wood, et K. B. Lee, « InGaN/GaN quantum wells with low growth temperature GaN cap layers », *J. Cryst. Growth*, vol. 307, n° 2, p. 363-366, sept. 2007, doi: 10.1016/j.jcrysgro.2007.07.018.
- [9] C. Brasser *et al.*, « Cathodoluminescence studies of chevron features in semi-polar (112̄2) InGaN/GaN multiple quantum well structures », *J. Appl. Phys.*, vol. 123, n° 17, p. 174502, mai 2018, doi: 10.1063/1.5021883.
- [10] M. Monavarian, A. Rashidi, et D. Feezell, « A Decade of Nonpolar and Semipolar III-Nitrides: A Review of Successes and Challenges », *Phys. Status Solidi A*, p. 1800628, déc. 2018, doi: 10.1002/pssa.201800628.
- [11] G. Morello, « Intrinsic optical nonlinearity in colloidal seeded grown CdSe/CdS nanostructures: Photoinduced screening of the internal electric field ».
- [12] C.-H. Chiu *et al.*, « Optical properties of (11̄01) semi-polar InGaN/GaN multiple quantum wells grown on patterned silicon substrates », *J. Cryst. Growth*, vol. 318, n° 1, p. 500-504, mars 2011, doi: 10.1016/j.jcrysgro.2010.10.054.
- [13] J. Bruckbauer, « Luminescence behavior of semipolar (10-11) InGaN/GaN “bow-tie” structures on patterned Si substrates ».
- [14] Y. Meng *et al.*, « Red Emission of InGaN/GaN Multiple-Quantum-Well Light-Emitting Diode Structures with Indium-Rich Clusters », *Phys. Status Solidi A*, vol. 215, n° 23, p. 1800455, déc. 2018, doi: 10.1002/pssa.201800455.
- [15] R. Mantach, « Croissance de pseudo-substrats GaN semi polaire (10-11) sur silicium sur isolant (SOI) », Université Côte d'Azur.

Chapter IV

IV.1 Introduction

The objective of this chapter is to present the development and progress made in device fabrication throughout this thesis. I will start by presenting an overview of the device fabrication, outlining the key steps of the process flow. Subsequently, I will introduce the lithography mask set specifically designed to contain all the required devices for this thesis. Detailed explanations of the different process steps will follow, accompanied by a discussion of the challenges encountered and the optimization approaches employed to achieve semipolar GaN-based μ LEDs. In order to validate the functionality of the process, c-plane GaN samples were also processed. Finally, devices made on both GaN orientations will be characterized as the concluding step of this chapter.

IV.2 An overview of the process steps involved in the device fabrication

The device fabrication process is conducted within the PFP cleanroom facility of CEA-LETI. It involves several key steps such as lithography, deposition, etching, and liftoff. Lithography involves defined patterns through photo exposure using a dedicated mask with the corresponding photoresist polarity. Each mask contains patterns corresponding to different process steps for complete device fabrication, along with alignment marks to facilitate sequential mask alignment. The polarity of each mask refers to the contrast of the patterns, which can be chromium (black) or quartz (transparent). This polarity and the following process steps, such as etching or liftoff approaches, determine whether to use a negative or a positive tone photoresist to transfer the patterns. The schematic of **Figure 2- 1** illustrates the basic steps of lithography using both positive (**Figure 2- 1.a1-d1**) and negative resist (**Figure 2- 1.a2-d2**) exploited for etching and liftoff processes, respectively.

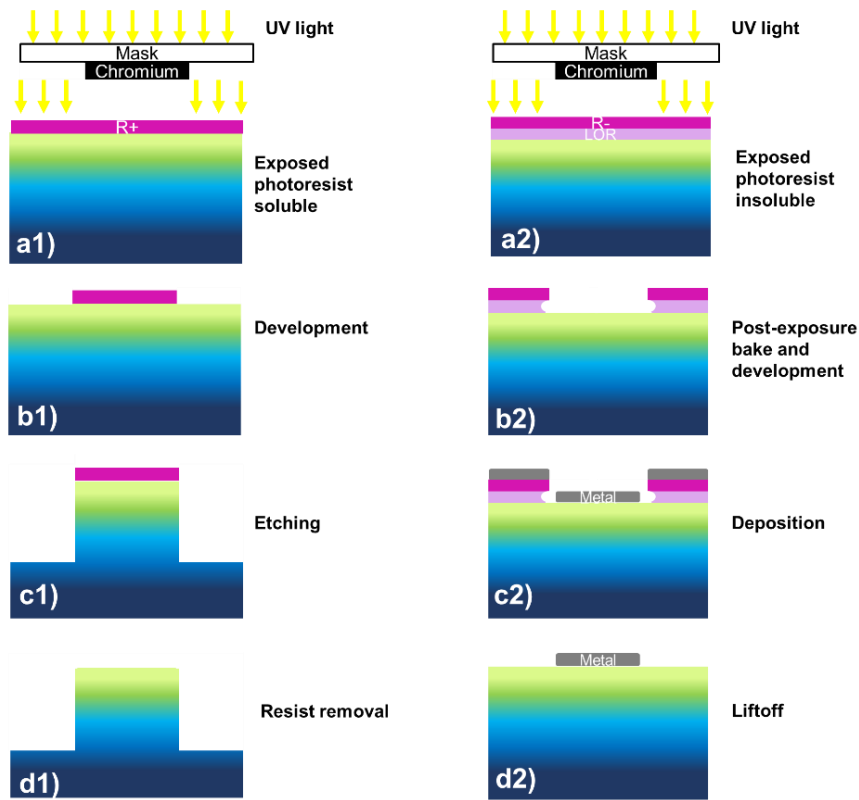


Figure 2- 1: Schematic representation of the different steps of photolithography exposure on positive resist in 1) and negative resist in 2) exploited for etching and liftoff respectively.

In order to etch the material with a specific design, a mask needs to be created first. To do so, a positive resist is deposited onto a substrate using spin-coating techniques. The thickness of the resist can be controlled by varying the spin speed and duration. Subsequent UV exposure induces a chemical transformation in the resist, making it soluble (**Figure 2- 1.b1**) in the developer solution. The open areas are etched via physical or chemical means to transfer the pattern from the mask to the underlying layer (**Figure 2- 1.c1**). Finally, the remaining resist is removed using solvents in a process known as resist stripping (**Figure 2- 1.d1**).

In the liftoff process, the substrate is first coated by a liftoff resist (LOR), then by a negative resist as a second step. The LOR layer serves as an undercut underlayer to achieve an easier lift-off. In this case, the resist exposed under UV is insoluble in the developer (**Figure 2- 1.b2**). Note that it is also necessary to bake the substrate before the development of the negative resist (nLOF 2000series), known as a post-exposure bake (PEB), to make the resist thermally stable. Next, a layer of metal is deposited over the entire surface (**Figure 2- 1.c2**), which is subsequently lifted off by immersing the sample in solvents that dissolve both the negative and LOR resists (**Figure 2- 1.d2**).

Based on these two aforementioned approaches, we created a set of 8 lithography masks each consisting of a single level of the process flow. Each of these levels includes the desired patterns that lead to the device's fabrication. Note that the first level named TRENCH is the lithography level done while patterning the SOI substrate to create the trenches just before growth as explained in **Chapter II**. The second level named MARKS, aims at creating metal alignment marks for better contrast while aligning the following levels. The 6 others are used during the LED process flow described in **Figure 2-2**.

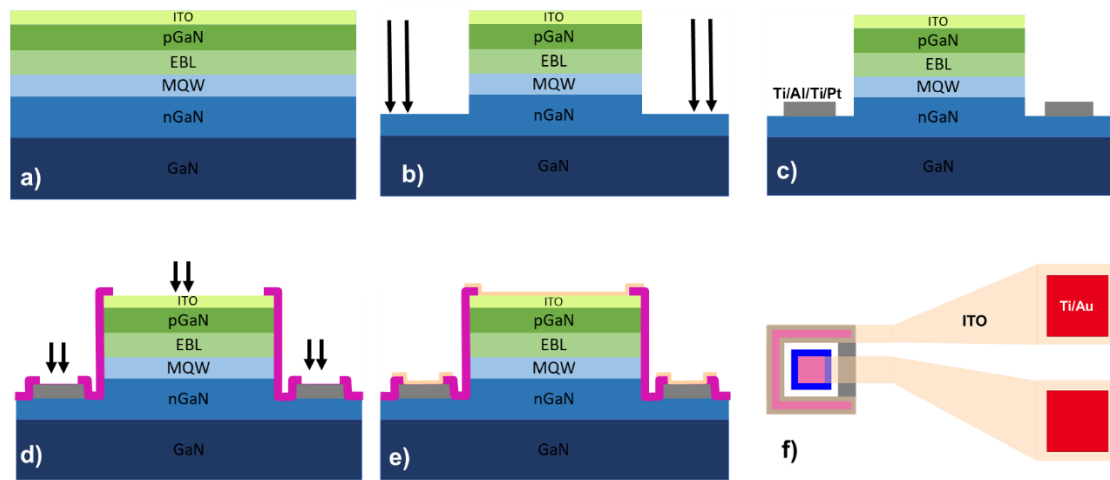


Figure 2-2: A cross-section schematic representing the different steps of the process flow. a) Deposition of ITO as a p-contact, b) ITO+mesa etching by dry etching (MESA level), c) n-contact deposition by liftoff (CTN level), d) SiO₂ insulation and vias opening (ISOL level), e) ITO as current spreading and electrical wiring by liftoff (PAD level). Finally a top view schematic of the f) Metal pads deposition by liftoff (TEST level).

Figure 2-2 is a summary of the main process steps to realize self-aligned micro-LEDs (μ LEDs). Going through each step in detail below:

Figure 2-2.a illustrates the deposition of a layer of ITO onto the LED epi-structure as the p-contact. This helps to prevent any degradation of the sensitive surface of p-GaN.

Figure 2-2.b describes the MESA level where a dry etching process is employed to create a mesa structure, etching both the p-contact and the epi-structure down to the n-GaN. This level ensures precise alignment between the p-contact and mesa structure.

(Note: The CTP level is not shown in the schematic, but it is used to define the p-TLM and p-vdP structures through wet etching. However, it does not directly impact the LED devices.)

Figure 2-2.c is associated with the CTN level, where a metallic n-contact stack of Ti/Al/Ti/Pt is deposited by physical vapor deposition (PVD) and patterned through lithography and liftoff techniques.

Figure 2-2.d presents the ISOL level which initially needs an SiO₂ passivation layer deposited using plasma-enhanced chemical vapor deposition (PECVD) covering the entire surface. This layer is then selectively etched on top of the contacts via the ISOL level.

Figure 2-2.e depicts the PAD level that consists of depositing a thick ITO layer to be then patterned and lifted off. This layer served as a current spreading grid on the top of the LED and as electrical wiring.

Figure 2-2.f shows a top view of the TEST level as the final process step where metallic pads (indicated by red squares) are deposited using PVD on the ITO previously deposited. These pads will be utilized for electrical probe testing purposes.

Various types of devices are fabricated using this process flow including single LEDs with different configurations, an operational LED in a matrix environment, RF LEDs, and electrical test devices. The aim of each device will be elaborated in the upcoming paragraphs.

It is worth mentioning that in this chapter, a polar GaN sample alongside the semipolar one, will be utilized for two purposes: firstly, for the development of the process flow, and secondly, as a reference for comparison between semipolar and polar GaN LEDs.

The LED epi-structure of this reference sample is grown using an MOCVD at the CEA-LETI. The various layers of the structure are outlined in the **Table 2-1** below:

Layer	Thickness
p^{++} -GaN cap	40nm
p -GaN	200nm
p -Al _{0.15} Ga _{0.85} N (EBL)	200nm
GaN (final barrier)	40nm
5x GaN (barrier)	8nm
5x InGaN (QW)	2.5nm
n -GaN	1.1 μ m
600nm GaN nid	600nm
Al _{0.25} Ga _{0.75} N	1 μ m
Al _{0.5} Ga _{0.5} N	500nm
Al _{0.75} Ga _{0.25} N	300nm
AlN	350nm
Si (111)	1mm

Table 2-1: c-plane GaN on silicon substrate LED epi-structure.

IV.3 Mask set fabrication

In order to fabricate the devices, a set of masks is prepared according to the thesis's goal which is fabricating μ LEDs and studying their performances.

IV.3.a Mask Description

Figure 3-1 presents the map of the devices which will be discussed next. It contains LEDs but also test structures to study the contacts.

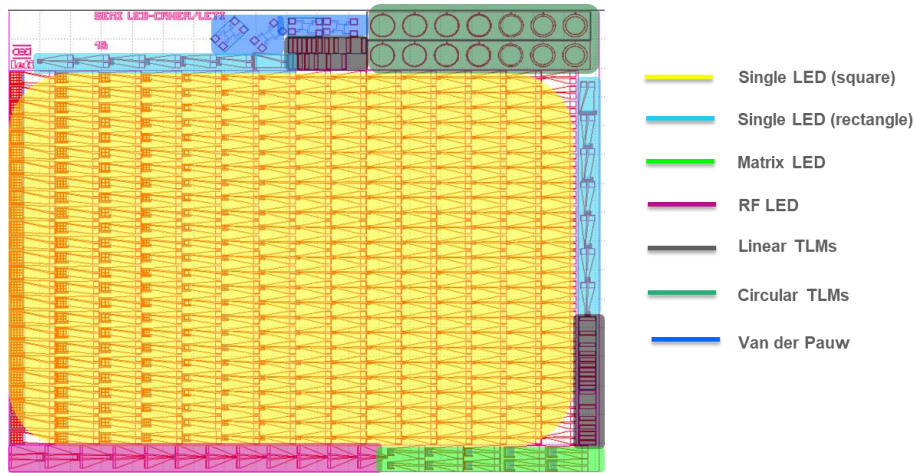


Figure 3-1: A field of the mask showing the spatial organization of the different devices.

- Square single LED

First, as we know that, in c-plane, the performance of μ LEDs degrades as their size decreases [1] we have planned to make LEDs of 15 different sizes, to study the impact of the size in our semi-polar orientation (see **Table 3-1**). As already explained in **Chapter I**, we would expect that the faster recombination time limits the carrier diffusion to the sidewalls and hence non-radiative recombination. In addition, as seen in **Chapters II** and **III**, dislocations and BSFs will be present at least at the coalescence between stripes, one question we anticipated was their impact on the μ LED performance. For that reason, the 15 different LEDs as listed in **Table 3-1** were shifted by step of $0.2\mu\text{m}$ over 15 lines (**Figure 3-2**).

LED Dimensions (μm)	200	150	125	100	80	50	30	15	10	9	8	7	6	5	4

Table 3-1:A list of all the square single LED sizes.

As a result, the $0.2\mu\text{m}$ shift should enable to position of the $4\mu\text{m}$ μ LEDs in a defect-free area as highlighted by the blue square in **Figure 3-2**. For large LEDs, it should not make any difference as several defective lines are present.

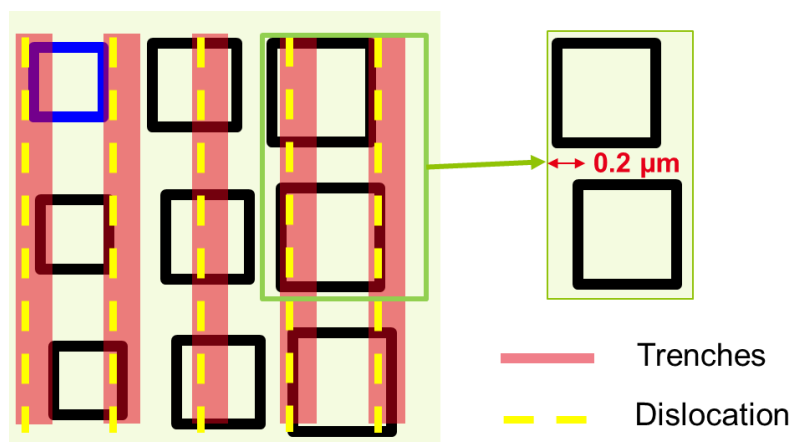


Figure 3-2: Square μ LEDs, having a $0.2\mu\text{m}$ shift vertically, aligned at different positions with respect to the defects highlighted in yellow lines.

- Rectangular single LED

Rectangular single LEDs are similar to the square LEDs in terms of fabrication. However, these LEDs are used in two sets, perpendicular and parallel to the trenches having a constant surface/perimeter ratio equal to 7.5 as depicted in **Figure 3-3.a** and **b**. They aim to study the impact of the propagation of the defects on the vertical and horizontal facets while keeping almost the same density of dislocations (presented in yellow).

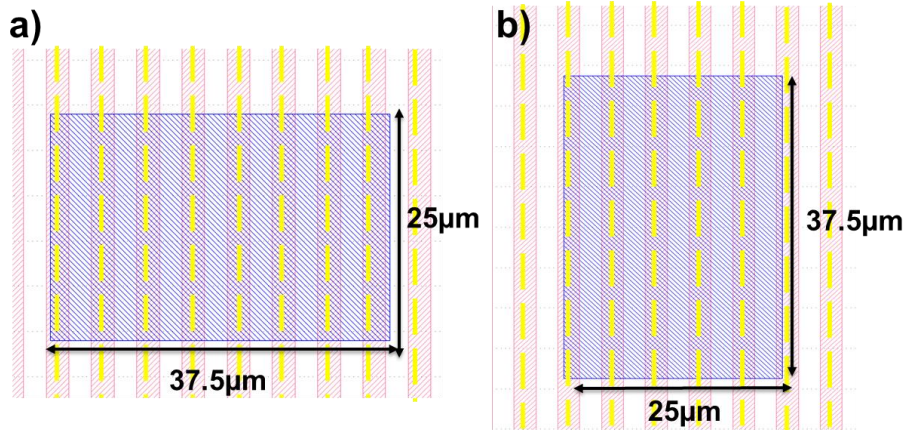


Figure 3-3: A mesa GDS drawing of a horizontal rectangular LED being a) perpendicular to the trenches and b) parallel to the trenches. Coalescence lines inducing dislocations are indicated in yellow.

The different rectangular LED sizes are presented in **Table 3-2**:

LED Dimensions (μm)	30x30	25x37.5	20x60	19x71.25	18x90	17x127.5	16x240
---------------------	-------	---------	-------	----------	-------	----------	--------

Table 3-2: A list of all the rectangular single LED sizes.

- RF LED

The reduced QCSE in semipolar GaN orientations compared to their c-plane counterparts, leads to a larger wave function overlap and a faster carrier recombination [2]. Therefore, it seems interesting to investigate the modulation bandwidths of these devices fabricated on both semipolar and c-plane GaN samples for comparison, as visible light communication (VLC) and LED-based RF communication are becoming of interest in our lab. We have then designed specific devices for that purpose (so-called radio frequency (RF) devices) on the mask set. They are single LEDs having specific RF pads as shown in **Figure 3-4** and will be used to test the first 12 LED sizes listed in **Table 3-3**.

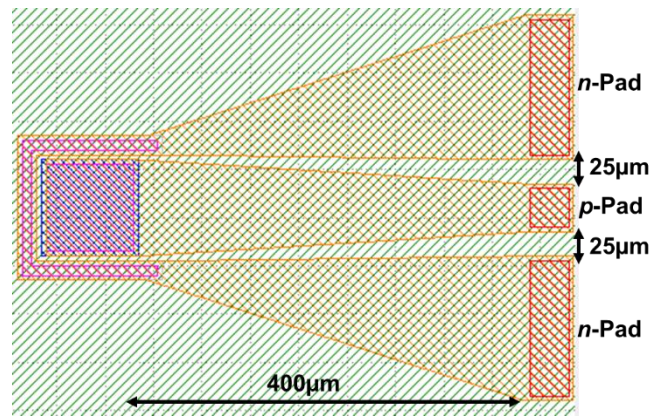


Figure 3-4: RF LED with specific n and p-PADs.

LED Dimensions (μm)	4	5	6	7	8	9	10	15	30	50	80	100
---------------------	---	---	---	---	---	---	----	----	----	----	----	-----

Table 3-3: A list of all the RF LED sizes.

The dimensions of the pads are chosen based on the RF probes used on the semi-automatic prober. The dimensions of *n* and *p*-pads are $150 \times 50 \mu\text{m}^2$ and $50 \times 50 \mu\text{m}^2$ respectively separated by $25 \mu\text{m}$ each. The distance between the pads and the mesa is $400 \mu\text{m}$ to let enough space between the probes and the collection of optical fiber. This distance remains constant, ensuring consistent measurements on a prober without requiring adjustments.

- LED Matrix

The final objective of this mask set is to fabricate a μLED array for $\mu\text{display}$ applications. Thus, having one operational μLED in a matrix environment will be a first step before addressing all the μLEDs to be able to study the efficiency and leakage induced by the process in this environment. The LED matrix is composed of 11×11 pixels having only one active LED located in the middle, where an opening over the *p*-contact occurs and therefore is the only LED connected to the pads. Different matrices are present on this mask having different sizes and pixel spacing as listed in **Table 3-4** below and shown as a GDS drawing in **Figure 3-5**:

MESA dimension	Column	Trench size
$4 \times 4 \mu\text{m}^2$	A	$3 \mu\text{m}$
$5 \times 5 \mu\text{m}^2$	B	$3 \mu\text{m}$
	C	$5 \mu\text{m}$
$10 \times 10 \mu\text{m}^2$	D	$3 \mu\text{m}$

Table 3-4: The different LED sizes and spacing used for the LED matrices.

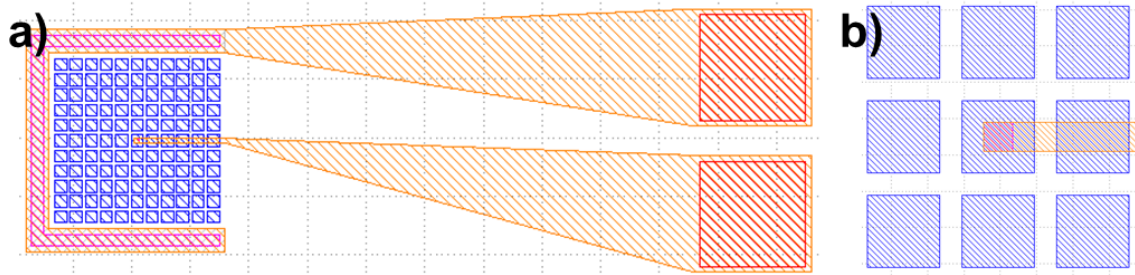


Figure 3-5: a) a GDS drawing of a $10 \times 10 \mu\text{m}^2$ LED matrix composed of 11×11 pixels having one operational highlighted in b).

It is worth noting that the ultimate microLED size, $4 \mu\text{m}$, is quite aggressive and challenging, but corresponds to state-of-art microdisplays developed for AR/MR applications.

- TLMs

Linear transmission line models (L-TLMs) are used to measure the sheet and contact resistances (as long as the contact resistance is ohmic). The theory of the linear TLM is explained in more detail in section IV.5.a.i. The main idea is to separate the resistance coming from a sheet of semiconductor itself (sheet resistance) from the resistance coming from the metal-semiconductor interface (contact resistance). The sheet resistance depends mainly on the doping level of the layer whereas the contact resistance depends on the nature of the metal used for contact, the quality of the interface (oxidation), the surface doping of the semi-conductor, etc... Owing to the poor conductivity of p-doped GaN, it is particularly difficult to get a good ohmic contact as further elaborated in **Chapter I**. Linear and circular TLMs are present on this mask set as shown in **Figure 3-6**. Besides the motivation of knowing the quality of our n and p contact on our LEDs, we have designed the TLM in two orientations, parallel and perpendicular to the trenches to study a possible impact of the BSFs on the sheet resistance or at least a possible impact of the non-symmetrical crystallography.

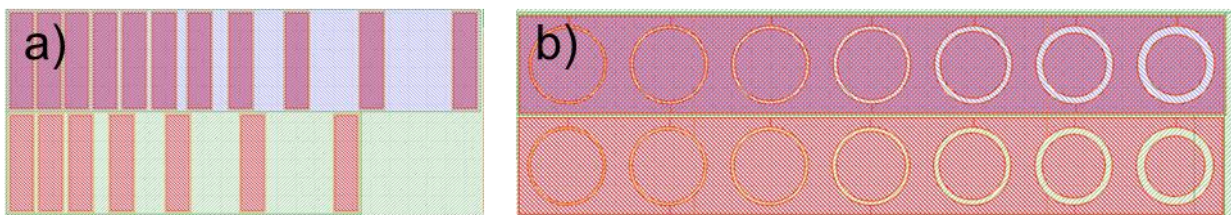


Figure 3-6: A GDS drawing of a) linear and b) circular p-TLMs on the top and n-TLMs on the bottom.

Linear p and n-TLMs are rectangular mesas with contact pads of $70 \times 270 \mu\text{m}$. Their spacing is detailed in **Table 3-5**. Note that more mesas are designed for p-TLM to target smaller gaps. This is specifically designed to get accurate values of the contact resistance due to the high sheet resistance of the p-GaN. This will be clearer in section IV.5.a.i when the TLM analysis will be explained.

Table 3-5 below lists the different TLM types with their corresponding pad gaps.

TLM	Gaps (μm)
Vertical p-TLM	3,4,6,8,10,25,40,80,130,180
Vertical n-TLM	8,10,40,80,130,180
Circular p/n-TLM	4,6,8,14,22,30,38

Table 3-5: Linear and circular TLM gaps for p and n-type.

- Van der Pauw

The van der Pauw (vdP) method is a well-known technique to measure the semiconductor's electrical properties. It consists of applying a current and measuring the voltage obtained to deduce the sheet resistance. In addition, when applying a magnetic field, Hall effect characterization can be performed to obtain the carrier mobility and concentration of the doped layer. [3], [4] The difference between TLM and vdP measurements is that vdP requires a four-probe method, hence four contacts. The size and location of these contacts are necessary for measurement reliability and accuracy. Therefore, several geometrical shapes of the vdP contacts were studied such as disc, square, cross, and cloverleaf [5], [6]. Square and cloverleaf geometries proved a reduction in measurement errors compared to circular ones. [7]

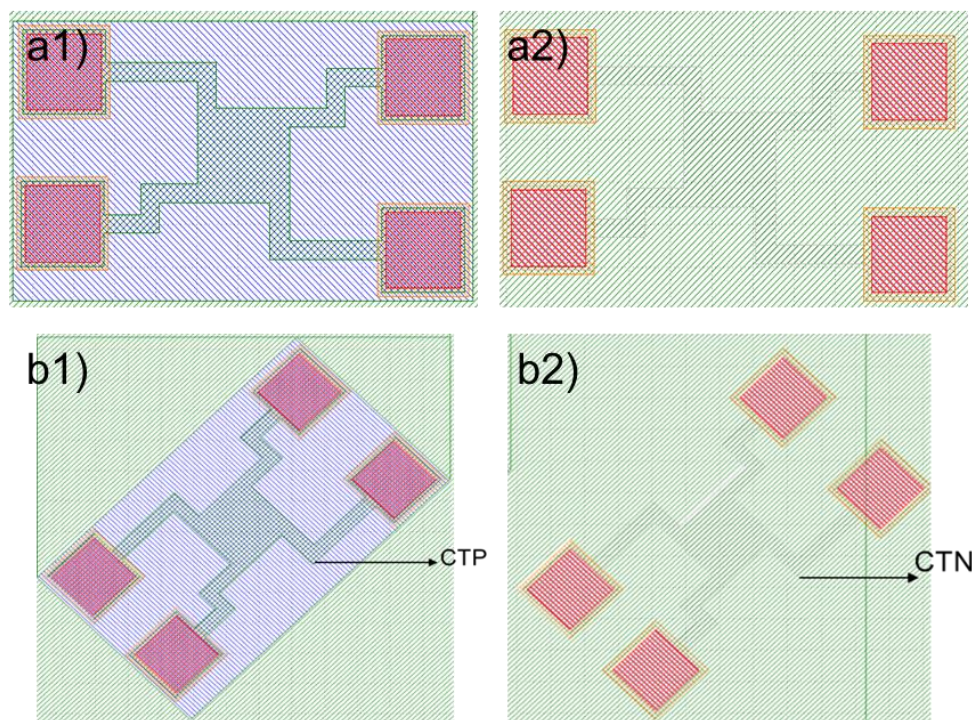


Figure 3-7: The two orientations a) 0 and b) 45° of van der Pauw devices of type p on the left and type n on the right.

The geometry of the vdP devices and the dimensions used in this work are chosen based on previous similar work by the laboratory team. vdP devices have two angles as presented in **Figure 3-7** a and b for 0° and 45° simultaneously for both doping types for similar reasons as the TLM study.

Given the time we had, we were unable to conduct measurements on these particular devices, and thus, we could not assess their characteristics.

IV.3.b Alignment

The alignment of the several levels with one another will be done using automatic fine alignment (AFA) marks of 0.1 μ m. They will be present and repeated over 2 columns on each side of the sample separated by a distance of 20mm as seen in **Figure 3-8**.a and b marked by (1). In addition, other alignment marks are present on the mask marked by (2) and (3) in **Figure 3-8**.a with their corresponding drawing in **Figure 3-8**.c and d. The marks on the 36x36mm² sample are square-shaped

and located along the edges, with an additional mark in the top-middle position. These marks serve the purpose of aiding in the alignment of the TRENCH level.

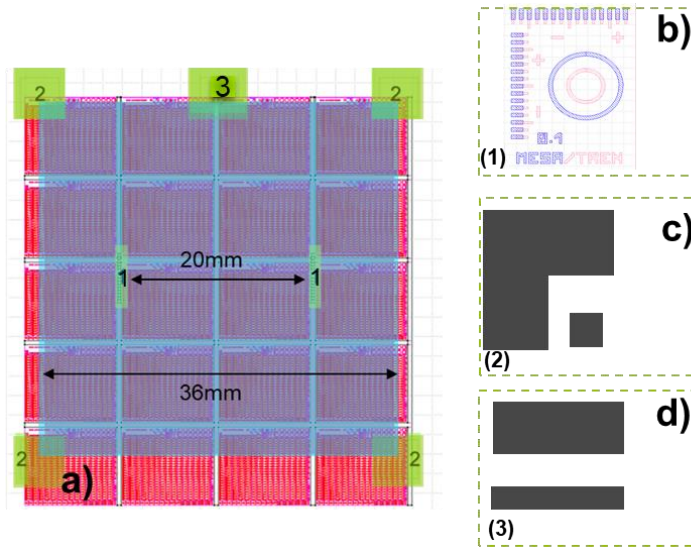


Figure 3-8: a) The mask containing 20 fields for samples having 36x36 mm². b) the alignment AFA marks annotated as (1) , c) the alignment marks annotated as (2), and d) the alignment marks annotated as (3).

As previously mentioned in **Chapter I**, the TRENCH level is used to pattern parallel trenches of 2.5µm width with a period of 5µm over the entire surface of the sample. To have accurate trenches parallel to the sample edges, the square alignment marks are used at each side of the sample to make sure the trenches are well aligned horizontally and vertically. The aim is to have the trenches parallel to the dicing of the wafer which follows the [112̄0] crystalline orientation. The top middle mark is to track the sample’s orientation for the following lithography steps of the substrate patterning and to easily recognize the orientation if cleaving or electrical measurements are required.

To reach an accurate alignment, **Table 3-6** lists the various possibilities of alignment levels for each lithography level mentioned previously in section **IV.2**.

Levels Aligned over	MARKS	MESA	CTP	CTN	ISOL	PAD	TEST
TRENCH	x	x					
MARKS		x	x	x	x	x	x
MESA			x	x	x	x	
CTP		x		x	x	x	
CTN					x	x	
ISOL						x	
PAD							x

Table 3-6: List of the different alignment possibilities present on the mask set for each level.

IV.4 Process steps description

IV.4.a P-GaN Activation

Right after the growth of an LED epi-structure, the p-dopant Mg is passivated by hydrogen making it inactive. Therefore, before any processing a first step of annealing is required to dissociate the hydrogen bonds (Mg-H) and activate the p-GaN top layer.

The first strategy was to perform the annealing directly in the growth reactor right after the growth for 1200 seconds at 930°C. This approach has proven effective for c-plane LEDs. However, after cleaning the sample and before processing, we could verify that the p-GaN was not activated by placing two probes in direct contact with the surface of p-GaN. We can see in **Figure 4-1** that the p-GaN layer is insulating.

Therefore, to activate the p-type, the semipolar samples are annealed under nitrogen (N₂) and oxygen (O₂) gases with a 19% N₂/O₂ ratio at 820°C, then the temperature cools down to 700°C under N₂. Previous studies showed that thermal annealing in an N₂/O₂ gas mixture improves the electrical properties of the p-GaN layer grown along the c-axis. The introduction of O₂ can promote the formation of the residual H dissociated from Mg-H complexes by N₂ into H₂O molecules on the surface and N₂ helps reduce N vacancies formation caused by surface oxidation.[8], [9] This activation recipe was developed by the laboratory and it is performed using a cold wall Jipelec rapid thermal annealing (RTA) equipment. RTA consists of a Silicon Carbide (SiC) susceptor, halogen lamps providing heat, a thermocouple, and a pyrometer to control the temperatures.

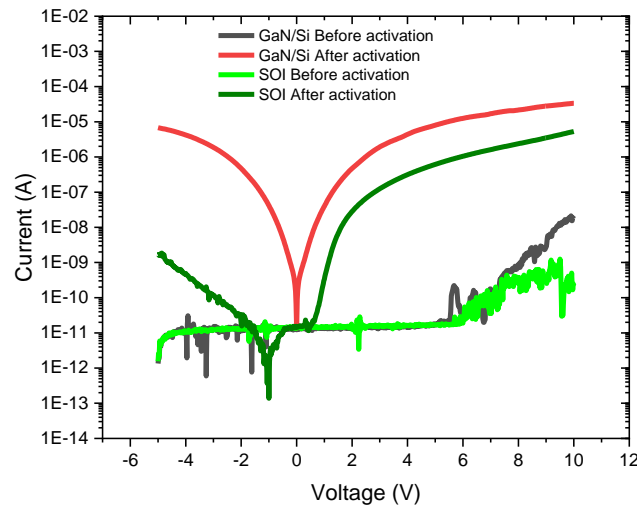


Figure 4-1: I-V measurements conducted on the LED ep-structures of the polar GaN/Si reference sample and semipolar SOI sample before and after p-GaN activation.

To verify that the recipe is also effective in activating the p-GaN grown along $[10\bar{1}1]$, I-V measurements are performed by probing directly the p-GaN of an LED epistucture of an SOI semipolar sample and for comparison on a polar GaN/Si reference sample. The I-V characteristics before and after activation are presented in **Figure 4-1**.

First, both samples reached a maximum current of 10^{-6} A and 10^{-5} A for semipolar and polar respectively after activation which is higher than 10^{-9} A and 10^{-8} A before activation. Second, the IV characteristics appear ohmic in the case of the polar sample and still slightly Schottky in the case of the semi-polar one but with a barrier lower than 1V. This confirms that the p -type dopant is activated for both samples. However, the observed asymmetry of the IV curve could be due to direct probing of the p -contact layer without proper p -metal contact.

IV.4.b MARKS

The first processing step consists in the realization of metallic alignment marks. Indeed, the strong surface roughness present on our semi-polar epilayers prevents a good sight of the AFA marks and hence, inaccurate alignment. Therefore, this step aims to pattern by lithography, AFA marks made out of metal for better contrast, to help align all the upcoming lithography levels. In order to do so, we perform a liftoff (previously explained in the section IV.2) with metal deposition by physical vapor deposition (PVD) sputtering. The metal stack is composed of Titanium (Ti), platinum (Pt), and gold (Au), with 10/300/100 nm of thicknesses respectively. The Ti is deposited as a first layer for better adherence, and the Pt/Au is chosen based on their ability to resist plasma etching and HCl wet etching which will be used later on in the process and will be discussed in the next paragraphs.

IV.4.c P-contact deposition

The next step is the realization of the p -contact. Just before its deposition, the samples are immersed in 37% pure hydrochloric acid solution for 10min at room temperature to remove any oxide layer [10]. Due to the difficulty of highly p -dope GaN, the contacts tend to have a high resistance and often a Schottky characteristic. Various stacks have been developed over the years and proposed in the literature to improve the electrical performance of the contact. The best p -contacts reported are: Pt, Ag, ITO, Ni/Au, etc. [11]. In this work, as we are working with an opaque substrate, where light will be extracted from the top surface. Thus, we chose ITO as a p -contact due to its good transparency in the visible range [12].

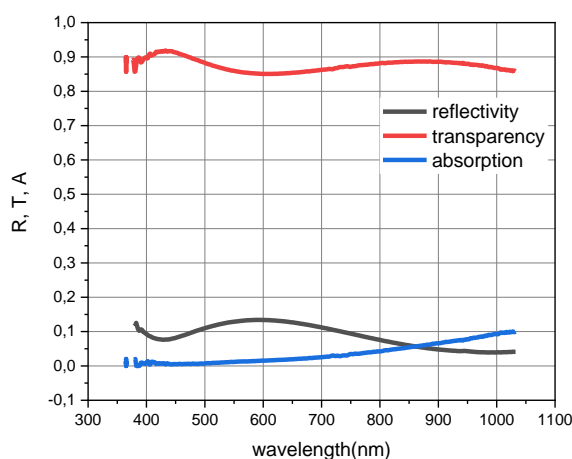


Figure 4-1: Graph representing the Reflectivity (R), the Transparency (T), and the Absorption (A) of the deposited 100nm ITO on a glass substrate with respect to the wavelength.

Hence, 100nm of ITO thin films are deposited by a PVD sputtering using a well-developed recipe by the laboratory team. The samples were then annealed by an RTA at 270°C under air conditions for

20min. The chosen annealing recipe for the same ITO deposition recipe was tested and resulted in 91% transparency at 450nm and 0.5% absorption as seen in **Figure 4-1**.

IV.4.d MESA

After ITO contact deposition, the ITO and the mesa etching take place using a single lithography level to have the contact well aligned on the mesa. The first step is the ITO etching by an ion beam etching (IBE), which is monitored by an in-situ secondary ion mass spectroscopy (SIMS). The graph presented in **Figure 4-2.a** depicts the evolution of the presence of different elements in the chamber as a function of the etching time. We can observe a reduction in the indium (In) concentration (blue curve) as the concentration of Ga increases (red curve). This trend persists after 4 minutes until a sharp drop (increase) is observed for In (Ga), indicating that the ITO layer above has been etched away, and the p-GaN layer has been reached.

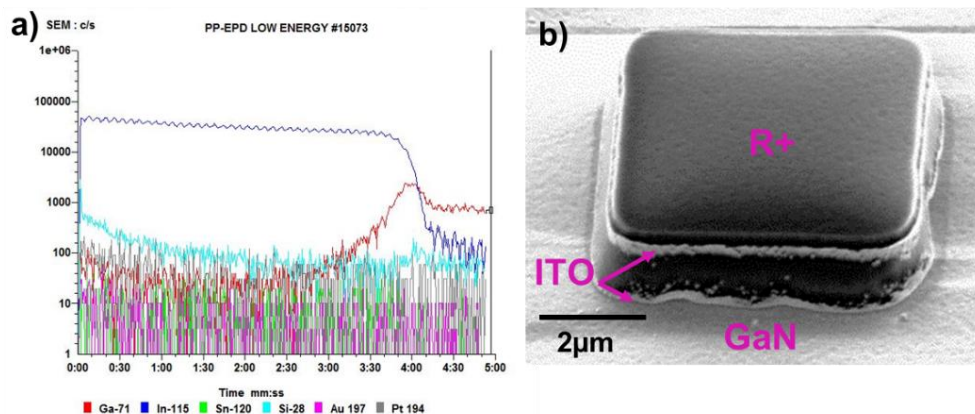


Figure 4-2: a) In-situ SIMS measurements of ITO etching by IBE. The dark blue curve represents the Indium concentration coming from ITO films and the red curve represents the Gallium from the p-GaN layer. b) An SEM image after IBE highlighting the ITO re-deposition on the resist (R+).

During Ion Beam Etching (IBE), Argon ions (Ar+) are directed at a sample to physically remove atoms from the surface. However, some of the etch by-products may re-deposit on the sidewalls due to various factors, including the incident angle [13], which can result in a p-n junction short circuit. Studies have shown that increasing the incident angle can reduce re-deposition, [14],[15] but it strongly depends on the etch rate and the material [16]. To address this issue, the laboratory team has developed an ITO etching recipe that balances the incident angle and rotational speed to minimize re-deposition. The etching was performed at a 20° incident angle and 10 rpm rotational speed, which still resulted in a thin re-deposited ITO layer, as shown in **Figure 4-2.b**. Further optimization is required to avoid any redeposition.

The second step involves etching the GaN layer in an Inductively Coupled Plasma (ICP) system, using chlorine-based chemistry. The goal is to etch down to the n-GaN layer in order to contact the n-side of the p-n junction. In our study, the n-GaN layer has a thickness of 1µm, the etch depth is set around 700nm and 600nm for polar and semipolar samples respectively. An end-point detection system is present in the ICP and enables real-time monitoring via interferometry with a laser beam emitting at 675nm reflected off the surface. The system detects the sinusoidal signal resulting from the interference between the top surface being etched and the layer underneath. The number of

oscillations can thus be exploited to extract the etched depth. The amplitude variation indicates a change in the refractive index of the former material that is fully etched and the start of the material underneath. For this process recipe, each oscillation is equal to 143nm of GaN etching ($675/2 \times 2.37$), hence, around 715 nm have been etched (5 oscillations) for the polar sample observed in **Figure 4-3.a**.

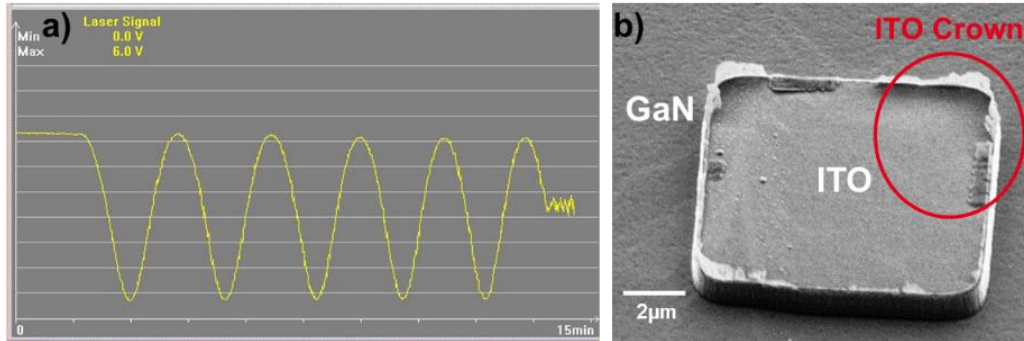


Figure 4-3: a) interferometric signal indicating the etch end of our polar GaN sample after 5 oscillations. b) SEM image of a mesa after etching indicating the remaining of an ITO ring on the LED borders.

Figure 4-3.b presents an SEM image of a μ LED mesa after IBE, ICP etching, and resist removal. The stripping has been done using several techniques including an ultrasound bath and an acetone pressure gun in order to force mechanically the removal of the re-deposited ITO layer. However, a thin ITO crown remained on the borders of the mesa as depicted in **Figure 4-3.b**. It is important to note that this crown could potentially create a short circuit between the p -GaN and n -GaN regions if it establishes an electrical bridge between the two regions.

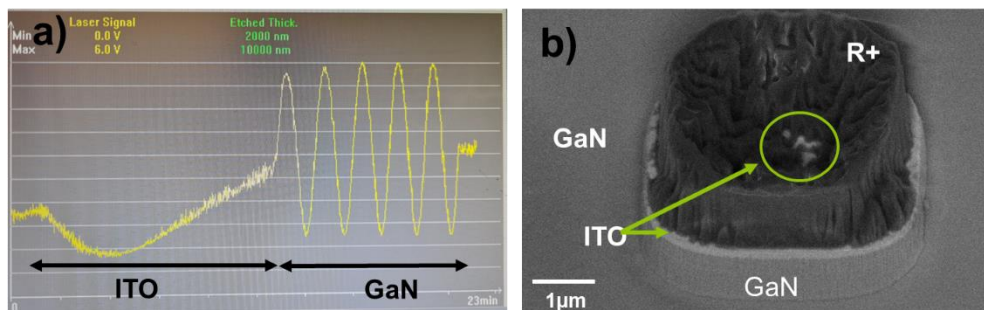


Figure 4-4: a) laser interferometric signal of two different materials (ITO then GaN) etched successively and b) an SEM image of the resulting burned resist and ITO exposure while MESA etching.

Another approach has been used for this lithography level by etching the ITO and the GaN epilayers successively in the same run of ICP etching and with the same process recipe as presented before.

Figure 4-4.a shows that the ITO etching takes around 15 min in this condition. Adding the GaN etching to it results in a resist being burned due to plasma overheating, as shown in **Figure 4-4.b**. In addition, a slight area of the ITO is exposed during the etching. It is important to notice that it is challenging to completely remove a burned resist. To ensure a resist-free surface, longer stripping steps duration such as plasma O_2 , immersion in acetone at high temperature, acetone pressure gun, and a longer rinsing in isopropanol and ethanol were adopted.

Both approaches appear to be capable of achieving the MESA level; however, additional process adjustments are necessary for both. Modifying the incident angle during etching may help prevent

re-deposition [15] in the first approach. The second one requires adapting the recipe for ITO etching or more extensive cooling of the chamber along the etching process to prevent the resist from burning. Nevertheless, we opted to proceed with the former approach for this level, which involves using IBE for ITO etching.

IV.4.e P-Contact (CTP)

This level does not affect the μ LED fabrication but is necessary to define the p-TLM and p-VdP devices necessary for characterizing the p-contact quality. This step aims to selectively etch the ITO contact. It led us to use HCl wet etching instead of dry etching methods used in the MESA level, to avoid degradation of its quality. In the MESA level, a mesa was etched around the p-type TLM and VdP devices, to force the current lines to remain only between the contact pads (see section IV.5.a.i for more details). To accomplish the CTP level, investigations on the etching duration have been conducted starting from 3min to 10min. As a result, 5min was suitable to remove the ITO while having a slight over-etching, as presented in the SEM image by the grainy ITO residues at the edges in **Figure 4-5.a**. The schematic in **Figure 4-5.b** describes the ITO grains formation under the resist when ITO is slightly over-etched. Over-etching is performed to ensure the complete removal of any residual ITO between the pads. The objective is to establish a clear pathway for the current flow through the p-GaN region only, minimizing any potential conductivity through the remaining ITO residues.

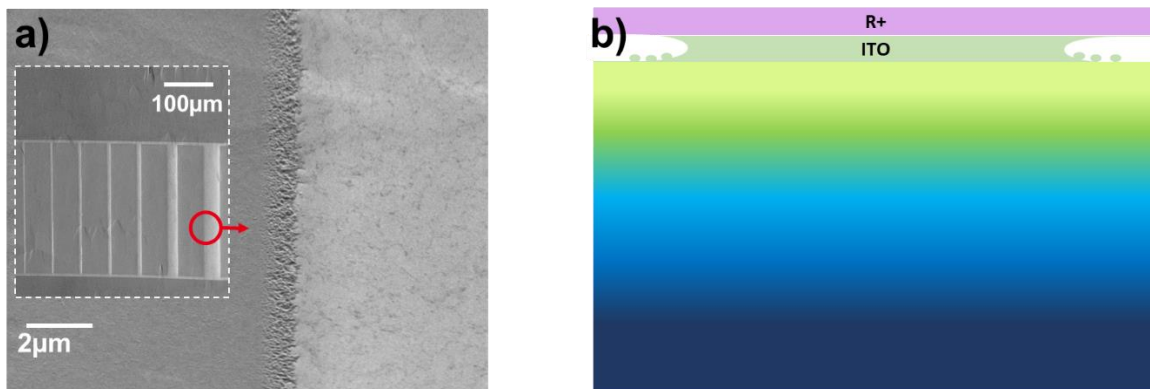


Figure 4-5: a) An SEM image of vertical TLM after 5min of HCl etching and resist stripping highlighting the slight ITO over etching leaving grainy residues as described schematically in b) before resist stripping.

It is important to notice that this over-etch can change the gaps between pads and will need to be measured if proper TLM analysis were to be performed. This correction would be particularly critical for small gaps.

IV.4.f N-Contact (CTN)

This level consists of depositing n -contacts all around the single LEDs as shown in **Figure 4-6.a** in order to improve current spreading, especially for large LED sizes. A Ti/Al/Ti/Pt (15/220/10/50 nm) metal stack is deposited similarly to what has been performed at the MARKS level using the electron beam evaporation followed by the liftoff approach. The thin Ti layer is deposited for better adherence to a thick Al layer. It can also improve the interfacial doping layer by forming a TiN layer when N atoms out-diffuses from GaN leaving nitrogen vacancies as GaN donors [17]. This provides the configuration needed for carrier injection by tunneling (Ohmic contact) [18], [19]. The Ti/Al metallization is a common metal contact used for GaN that proved a low resistivity and thermal

stability compared to Ti/Au, Cr/Al, and Cr/Al/Ni/Au [13,]. However, this alloy suffers from a strong tendency towards oxidation which can be prevented by the additional thin multilayer of Ti/Pt. Noting that after the metallization step, we suspect that the previously seen ITO crown collapsed. This phenomenon can be attributed to the spin coating used when depositing the resist. The ITO residues could have established bridging connections between the p and n -GaN regions, however, no short circuit was detected when electrical measurements were conducted, meaning that the ITO residues remained on top of the mesa (**Figure 4-6.b**). In addition, n -type vertical and circular TLMs pads and VdP are also defined using this level.

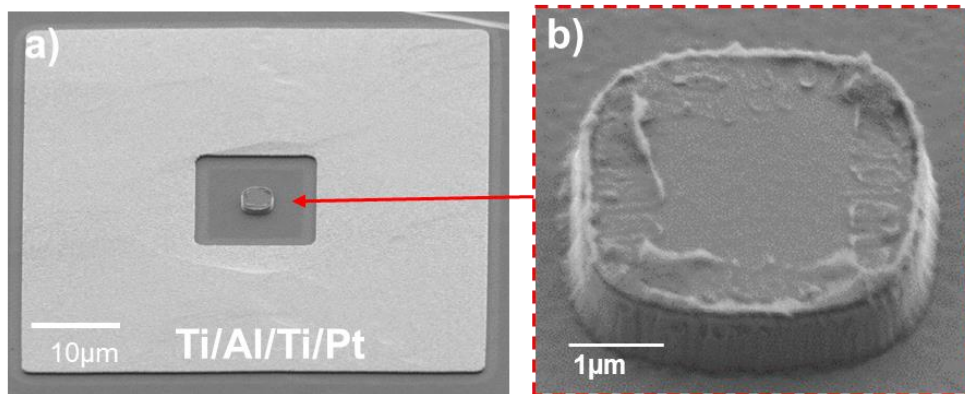


Figure 4-6: Top view SEM images of a) $4 \times 4 \mu\text{m}^2$ μLED after n -contact deposition and b) a highlight of the ITO residues on the LED center after electron beam evaporation.

IV.4.g ISOL

A critical step in LED fabrication is to prevent electrical shorts between the p and n contacts. It involves first depositing a dielectric layer, such as SiO_2 or silicon nitride (SiN_x), across the entire surface to guarantee good insulation. Secondly, it requires creating openings in the insulator on top of the n and p contacts to be able to establish electrical connections in the next step. Two different approaches were tested to insulate and open on top of the contacts:

- Encapsulation of the surface by a silicon dioxide-based negative resist (SiNR), a siloxane-based polymer that can play the role of a photo-resist and insulator. After deposition by spin coating, it is opened by lithography/development on top of the contacts, also referred to as vias openings (**Figure 4-7.a**). The development can be achieved by isopropanol, then the SiNR is cured at 180°C under a vacuum for 1h to harden it. This specific resist after curing has good mechanical and insulation properties.
- Deposition of SiO_2 on the entire surface by PECVD, followed by dry etching using an ICP to open the vias (**Figure 4-7.b**). This procedure is similar to the one described in **Chapter II** when we patterned the trenches.

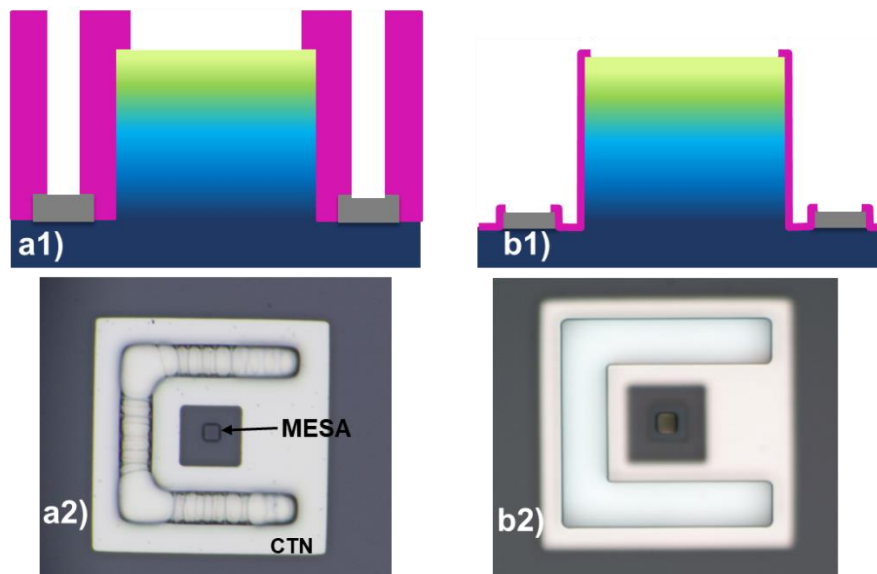


Figure 4-7: a) Cross-section schematic of an opening on top of the SiNR encapsulated surface with its corresponding optical microscopic image. b) Similar to a) for the SiO₂ deposition approach.

As mentioned in section IV.2, the tones of the resist are dependent on the chosen mask polarity and the process step. In this particular lithography level, both negative (for SiNR) and positive resists (for SiO₂) are needed. Therefore, to obtain the same results, two mask polarities need to be employed. For the SiNR, the chromium mask patterns were placed on top of the contacts, while the rest of the mask was clear, in order to open the vias. In contrast, the opposite configuration was used for the SiO₂ mask.

SiNR encapsulation provides the advantage of surface planarization and having a faster process flow, requiring only a single lithography exposure step. Yet, it requires adjustments in terms of lithography exposure doses and isopropanol development time for smaller patterns as seen in **Figure 4-7.a2**. Although the second approach is more time-consuming (deposition, lithography, and etching), it allows for achieving well-defined isolation and passivation regardless of the pattern size as seen in **Figure 4-7.b2**. Therefore, we chose the second approach as it will also provide a good sidewall passivation layer.

IV.4.h PAD (Electrical Wiring)

After the vias opening, the samples are loaded in the PVD chamber for 200nm of ITO deposition. The role of this level is to deposit the conductive lines that will bring the current from the metallic pads for electrical measurements to the *p* and *n-contact* openings. The deposition will also add a current spreading layer (or grid) on top of the *p*-contact. The choice of material for this layer is critical due to the need for an accurate alignment to prevent shadowing the top surface of the smallest sizes of LEDs. Therefore, the thick ITO layer covering the mesas, as presented in **Figure 4-8.a**, will not impact the light-emitting area of the LEDs, especially the ones with sizes <10μm due to their transparency. The scheme of **Figure 4-8.b** shows the current spreading by the red arrows, through the ITO deposition design of the smallest LED sizes presented in the SEM image.

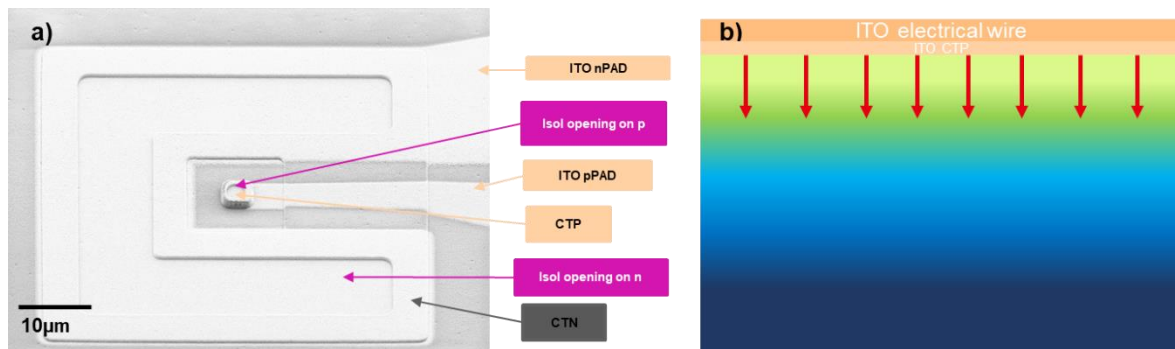


Figure 4-8: a) SEM images of the PAD level of an annotated $4 \times 4 \mu\text{m}^2$ LED and b) its corresponding cross-section scheme showing the role of the current spreading layer.

IV.4.i TEST

The final step involves depositing a metal stack of Ti/Au (20/250nm) as test pads for LED electrical measurements. This is achieved one more time by lithography, metal deposition by electron beam evaporation followed by lift-off. It creates metal pads on top of the ITO electrical wires, as indicated by the red arrows in **Figure 4-9**. The Ti/Au stack is a preferred choice for the excellent adhesion of Ti on GaN and the superior electrical conductivity of Au without any surface oxidation. Probing these pads will enable the electrical characterization of the LED directly on the wafer.

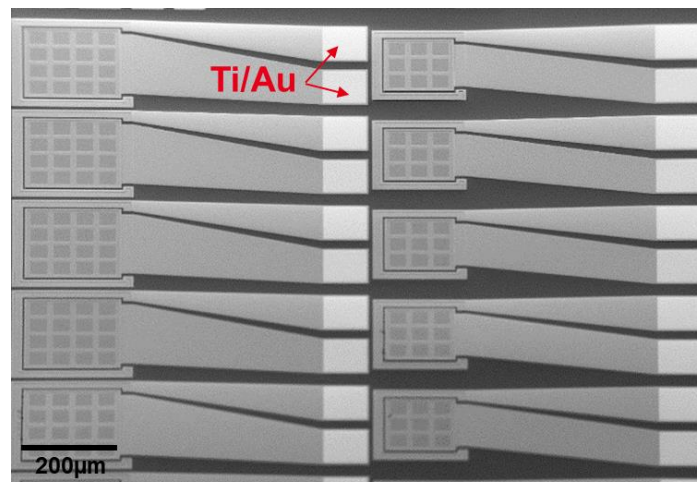


Figure 4-9: Top view SEM image after metallic pad deposition as indicated by the red arrows on the electrical wiring coming from the p-contact (bottom square) and the one from the n-contact (top square).

IV.5 Process verification

We investigate the electro-optical performances of polar and semipolar GaN LED devices fabricated using the process flow described above. The objective of these initial characterizations is to determine if further process optimization is required to enhance the LED performances. To achieve this, we conducted TLM measurements and obtained optoelectrical characteristics (current(I)-voltage(V)-optical power(L)) for both polar and semipolar orientations.

IV.5.a Linear TLM

In this section, we will explain the theory of L-TLMs by giving the mathematical formulas involved in this model to extract the desired characteristics. In addition, we will provide an analysis for both GaN orientations, exploring their properties using the TLMs fabricated by the previously described process flow.

IV.5.a.i Theory

A schematic diagram of the p and n -TLMs is presented in **Figure 5-10** a and b simultaneously. The same measurements are conducted for both TLMs. However, the difference is that on p -type, a rectangular mesa has been etched up to the n -GaN to force the current to flow only between the pads. This is complicated to achieve for n -TLMs on LED structures as it is hard to reach the substrate. As a result, the analysis of the obtained characteristics is not reliable as the calculations do not take into account the current flowing laterally. Therefore, the use of circular TLMs gives more accurate and reliable results since the current flows radially so the mesa etching is not needed in this case. Nevertheless, in this work, we will focus on the linear ones due to the possibility of studying the properties of both orientations, parallel and perpendicular to the trenches to verify whether the crystallographic orientation has an impact on the extracted electrical properties.

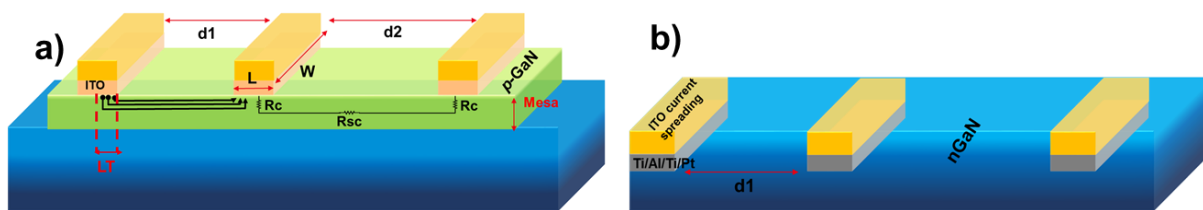


Figure 5-10: Schematic diagram of linear a) p-TLMs and b) n-TLMs.

To perform the measurements, two probes are placed each on two adjacent pads. The current is then driven through as indicated by the black arrows in **Figure 5-10.a**. The current flows through the least resistive path, hence, the transfer length L_T is the average distance of the carrier flowing through the contact.

The I-V between the two pads is measured for all the gaps (d_i) present for each TLM type. **Figure 5-11.a** presents the I-V characteristics measured for all the n-TLM gaps of the polar GaN LED. As the contact is not perfectly linear, we were not able to do the TLM analysis, particularly for the contact resistance. As a figure of merit, we decided to choose the maximum voltage (1V) where the curve becomes linear to estimate the sheet resistance. Therefore, the total resistance measured with respect to the same gaps is plotted in the graph of **Figure 5-11.b**. Although the transfer length and contact resistance are not accurate because the contact is not ohmic, we still expected to obtain information about the sheet resistance from the slope, which would also make the following calculations easier to explain.

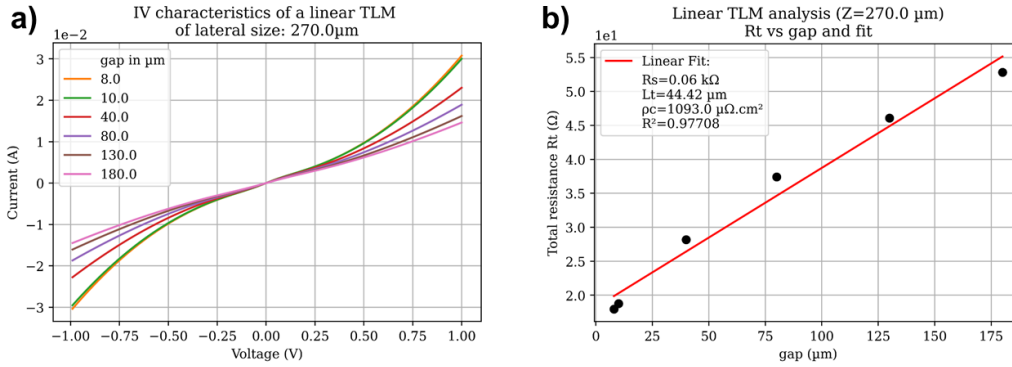


Figure 5-11: a) I-V characteristics of the different pad gaps and b) represents the total resistance as a function of the gaps at 1V of a linear n-TLM measured on the blue polar GaN LED sample.

This is plotted and calculated using a Python script that includes the following equations to determine the sheet and contact resistance, the specific contact resistivity, and the transfer length.

First, the total resistance between 2 pads can be calculated in the case of an ohmic contact as:

$$R_{tot} = 2R_c + R_{sc} \tag{IV.1}$$

Where R_c is the contact resistance and R_{sc} is the semiconductor resistance given by:

$$R_{sc} = \frac{\rho d}{tW} \tag{IV.2}$$

Where d is the gap between two pads, ρ is the semiconductor resistivity, W is the pad width, t is the mesa thickness and the sheet resistance R_s is given by:

$$R_s = \frac{\rho}{t} \tag{IV.3}$$

Using equations (IV.2) and (IV.3) in (IV.1) yields to

$$R_t = 2R_c + R_s \frac{d}{W}.$$

Reeves *et al.*[21] have shown a relationship between the contact resistance R_c and the specific contact resistivity ρ_c given by:

$$R_c = \frac{\rho_c}{LTW} \tag{IV.4}$$

Where

$$LT = \sqrt{\frac{\rho_c}{R_s}} \tag{IV.5}$$

Hence, the total resistance $R_{tot} = 2 \frac{R_s LT}{W} + R_s \frac{d}{W} = \frac{R_s}{W} (2LT + d)$.

This equation is considered a linear equation in slope-intercept form ($y=ax+b$),

where $y=R_{tot}$, $x=d$, $a=\frac{R_s}{W}$ and $b=2LT$.

Therefore, R_s can be calculated from the slope of the linear curve in **Figure 5-11.b**. L_T can be obtained from the intersection of the curve when $R_{tot}=0$. One can deduce the contact resistivity from equation (IV. 5)

At $d=0$, the value at the intersection with the y-axis is equal to $2R_c$.

IV.5.a.ii Semipolar GaN TLM analysis

We performed TLM analysis using the previously explained equations on the blue semipolar GaN LED. The I-V characteristics presented in **Figure 5-12** measured for all the n-TLM gaps exhibit a strong Schottky behavior. Similar to the polar sample analysis, the current flows relatively easier from one contact to another for small gaps compared to bigger gap sizes resulting in a lower resistance.

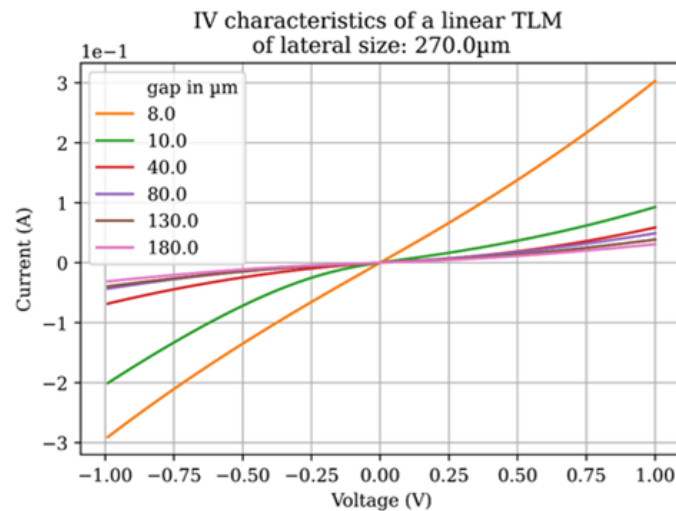


Figure 5-12: I-V characteristics of the different pad gaps of a linear n-TLM measured on the blue semipolar GaN LED sample.

However, this was not the case for all the TLMs present in the sample. In some cases, the I-V behavior was random for the different gap sizes. We attributed this phenomenon to diverse factors, including the influence of epitaxial defects such as surface cracks or chevrons, which have the potential to alter the current pathway.

Therefore, we focused on the smallest gap for both p -TLMs ($d=3\mu\text{m}$) and n -TLM ($d=8\mu\text{m}$) to compare semipolar and polar samples.

Figure 5-13 indicates a Schottky behavior for both samples on n and p -contacts. The p -type (**Figure 5-13.a**) presented a similar behavior for both orientations. Nonetheless, we observed a better n -TLM performance in semipolar samples compared to polar ones (**Figure 5-13.b**) which can be attributed to a better n -doping layer ($\sim 8E^{19}\text{cm}^{-3}$ and $4.5E^{18}\text{cm}^{-3}$ for semipolar and polar, respectively) that results in a higher conductivity and a lower sheet resistance.

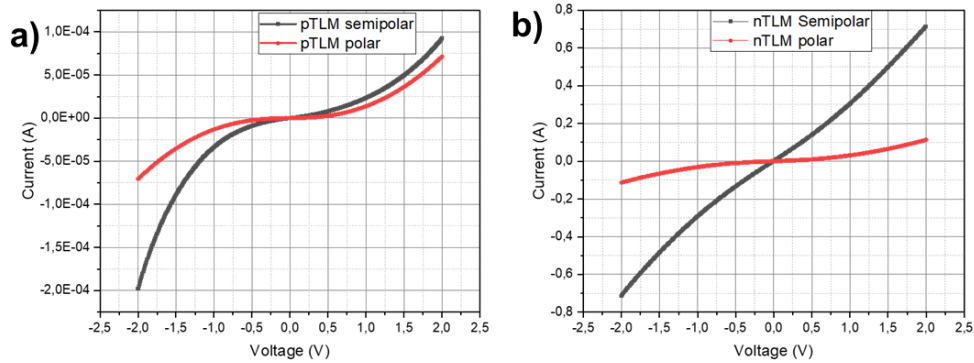


Figure 5-13: Graphs of the I-V measurements on a) p-TLM and b) n-TLM for polar and semipolar LED samples.

IV.5.b Optoelectrical Measurements on LEDs

In this section, we are going to present the first LED characterizations done on the semipolar and the polar samples using a semi-automatic prober. The objective is to verify if the process is functional and the problems that can be induced. Using a polar GaN sample as a reference will help distinguish whether the problems are epitaxy-related or process-related.

IV.5.b.i Semiautomatic Prober Description

The semi-automatic prober we have used is a FormFactor CM300. It was used to perform electroluminescence (EL) measurements at room temperature on all the LEDs present in the samples automatically. However, for this section, we are going to focus on two different LED sizes for polar and semipolar orientations just to inform us of the process quality. Further explanation and I-V-L characterization of the different LED configurations presented in section Error! Reference source not found. will be presented in **Chapter V**.

The LED sample is fixed on a 300mm round chuck, as depicted in **Figure 5-14**.

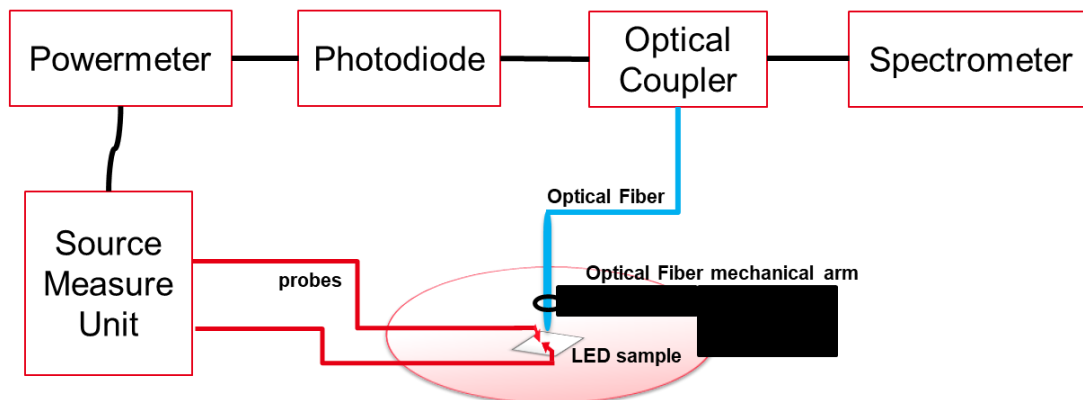


Figure 5-14: Experimental setup diagram of the semi-automatic prober for I-V-L measurements.

Two probes, connected to a source measure unit (SMU), are used to apply a voltage on the metal test pads of the μ LED and to measure the current. The light emitted by the μ LED is captured by a 200 μ m optical fiber positioned approximately 50-100 μ m above the μ LED. The fiber has a numerical aperture of NA=0.39, which enables the collection of the light in a cone angle of 22°. This fiber is mounted on a mechanical arm whose coarse and fine positioning is done by a stepper motor and a piezoelectric stage respectively, enabling automatic fiber alignment prior to each measurement to enhance light collection accuracy. The collected light is then split into two outputs. The first output is

connected to a spectrometer, enabling measurement of the spectrum at a given voltage. The second output is directed towards a photodiode read by a power meter. To automate the IVL measurements, the laboratory has developed a Python code that configures all the required parameters: die numbers, μ LED positions, applied voltage, compliance in current, etc.

IV.5.b.ii I-V-L Analysis

Optoelectrical characteristics of polar and semipolar GaN LEDs are plotted together in **Figure 5-15.a** and **b** with a voltage going from -5V to 10V. Two LED sizes are measured: a $100 \times 100 \mu\text{m}^2$, corresponding to one of the largest LEDs depicted by the blue curves, and a smaller $4 \times 4 \mu\text{m}^2$ size, represented by the magenta curves. The continuous lines illustrate the current, while the dashed lines depict the luminescence in relation to the voltage.

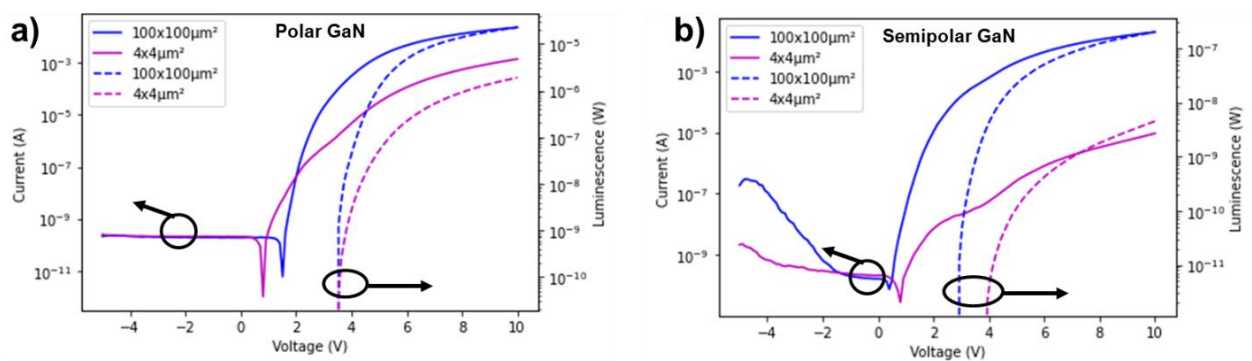


Figure 5-15: Graphs presenting the I-V-L characteristics of a) polar GaN and b) semipolar GaN LEDs with two different LED sizes: $4 \times 4 \mu\text{m}^2$ and $100 \times 100 \mu\text{m}^2$. The magenta curves represent the $4 \times 4 \mu\text{m}^2$, while the blue curves correspond to the $100 \times 100 \mu\text{m}^2$.

Both LED samples presented a good performance with the two LED sizes. In the I-V characteristics, the current shows an exponential increase below 2V. However, it is seen that during this range of voltages, no light is detected. The absence of light emission suggests that carriers injected into the device are predominantly undergoing nonradiative recombination. The turn-on voltage, as observed in the optical power curves, is around 3.5V for both polar sizes, 3 and 4V for the $100 \times 100 \mu\text{m}^2$ and the $4 \times 4 \mu\text{m}^2$ semipolar samples, respectively. At 10V for the $100 \times 100 \mu\text{m}^2$ LEDs, the power of polar GaN is two orders of magnitude higher than that of the semipolar sample which might be attributed to the more mature epitaxy for the polar sample. The region between 2V and 3.5V is considered to be associated with the SRH recombination zone. This is considered a great achievement for the first fabrication of $4 \times 4 \mu\text{m}^2$ μ LEDs made on semipolar GaN orientation. However, most of the devices present in the sample were leaky under reverse biased current. This region is related to the leakage current of the parallel resistance as the current flowing through the diode is considered neglected.[22]

The absence of leakage in the polar GaN LEDs confirms that the process flow is well-established for all LED sizes within the samples. The observed leakage in the semipolar samples can be attributed to the specific characteristics of the LED epi-structure. In the next chapter, investigations will be undertaken to thoroughly assess the influence of this epi-structure on the various LED configurations.

IV.6 Conclusion

In this chapter, we fabricated and characterized semipolar and polar GaN-based μ LEDs. These results serve as an initial demonstration of the viability of the developed process flow. Furthermore, we were able to achieve the first operational blue and green semipolar μ LEDs, successfully down to $4 \times 4 \mu\text{m}^2$.

The primary objective was to assess the need for further adjustments in the process hence, preliminary results on the contact quality using linear TLMs were done. It proved Schottky contacts on p and n -TLMs which were expected for the p -type. Better quality contact for the semipolar n -TLM compared to the polar ones due to the better doping quality.

Finally, a study involved conducting the first I-V-L measurements on both semipolar and polar GaN samples. The results demonstrated superior characteristics of the polar LEDs compared to their counterparts, which can be attributed to the LED epi-structure. However semipolar microLED as small as $4 \mu\text{m}$ could be operated. The observed differences could potentially arise from defects or variations in the surface morphology of the samples. To gain deeper insights, more comprehensive investigations into the performance of semipolar LEDs will be conducted in the subsequent chapter.

IV.7 References

- [1] F. Olivier, A. Daami, C. Licitra, et F. Templier, « Shockley-Read-Hall and Auger non-radiative recombination in GaN-based LEDs: A size effect study », *Appl. Phys. Lett.*, vol. 111, n° 2, p. 022104, juill. 2017, doi: 10.1063/1.4993741.
- [2] N. Poyiatzis, M. Athanasiou, J. Bai, Y. Gong, et T. Wang, « Monolithically integrated white light LEDs on (11–22) semi-polar GaN templates », *Sci. Rep.*, vol. 9, n° 1, Art. n° 1, févr. 2019, doi: 10.1038/s41598-018-37008-5.
- [3] X. Hu, L. Zhu, K. Diao, W. Liu, X. Deng, et H. Wang, « Electrostatic derivation for the van der Pauw formula and simulation using arbitrarily shaped resistive materials », *AIP Adv.*, vol. 12, n° 7, p. 075208, juill. 2022, doi: 10.1063/5.0081561.
- [4] M. Reveil, V. C. Sorg, E. R. Cheng, T. Ezzyat, P. Clancy, et M. O. Thompson, « Finite element and analytical solutions for van der Pauw and four-point probe correction factors when multiple non-ideal measurement conditions coexist », *Rev. Sci. Instrum.*, vol. 88, n° 9, p. 094704, sept. 2017, doi: 10.1063/1.5001830.
- [5] D. W. Koon, M. Heřmanová, et J. Náhlík, « Electrical conductance sensitivity functions for square and circular cloverleaf van der Pauw geometries », *Meas. Sci. Technol.*, vol. 26, n° 11, p. 115004, nov. 2015, doi: 10.1088/0957-0233/26/11/115004.
- [6] D. W. Koon, « Effect of contact size and placement, and of resistive inhomogeneities on van der Pauw measurements », *Rev. Sci. Instrum.*, vol. 60, n° 2, p. 271-274, févr. 1989, doi: 10.1063/1.1140422.
- [7] D. W. Koon, A. A. Bahl, et E. O. Duncan, « Measurement of contact placement errors in the van der Pauw technique », *Rev. Sci. Instrum.*, vol. 60, n° 2, p. 275-276, févr. 1989, doi: 10.1063/1.1140423.
- [8] B. A. Hull, S. E. Mohny, H. S. Venugopalan, et J. C. Ramer, « Influence of oxygen on the activation of *p*-type GaN », *Appl. Phys. Lett.*, vol. 76, n° 16, p. 2271-2273, avr. 2000, doi: 10.1063/1.126318.
- [9] W. Lu, D. Aplin, A. R. Clawson, et P. K. L. Yu, « Effects of the gas ambient in thermal activation of Mg-doped p-GaN on Hall effect and photoluminescence », *J. Vac. Sci. Technol. Vac. Surf. Films*, vol. 31, n° 1, p. 011502, janv. 2013, doi: 10.1116/1.4768174.
- [10] C. H. Chen *et al.*, « GaN metal-semiconductor-metal ultraviolet photodetectors with transparent indium-tin-oxide Schottky contacts », *IEEE Photonics Technol. Lett.*, vol. 13, n° 8, p. 848-850, août 2001, doi: 10.1109/68.935824.
- [11] Y. Liu, « Recent research on ohmic contacts on GaN-based materials », *IOP Conf. Ser. Mater. Sci. Eng.*, vol. 738, n° 1, p. 012007, janv. 2020, doi: 10.1088/1757-899X/738/1/012007.
- [12] D. W. Kim, Y. J. Sung, J. W. Park, et G. Y. Yeom, « A study of transparent indium tin oxide (ITO) contact to p-GaN », *Thin Solid Films*, vol. 398-399, p. 87-92, nov. 2001, doi: 10.1016/S0040-6090(01)01368-2.
- [13] M. Ji *et al.*, « Study on the effect of re-deposition induced by ion beam etching on MTJ performances », *AIP Adv.*, vol. 9, n° 8, p. 085317, août 2019, doi: 10.1063/1.5117312.
- [14] V. Ip *et al.*, « Ion Beam Patterning of High-Density STT-RAM Devices », *IEEE Trans. Magn.*, vol. 53, n° 2, p. 1-4, févr. 2017, doi: 10.1109/TMAG.2016.2603921.
- [15] A. Olivier *et al.*, « Indium Tin Oxide optical access for magnetic tunnel junctions in hybrid spintronic–photonic circuits », *Nanotechnology*, vol. 31, n° 42, p. 425302, oct. 2020, doi: 10.1088/1361-6528/ab9c56.
- [16] P. G. Glöersen, « Ion–beam etching », *J. Vac. Sci. Technol.*, vol. 12, n° 1, p. 28-35, janv. 1975, doi: 10.1116/1.568767.
- [17] S. Ruvimov *et al.*, « Microstructure of Ti/Al and Ti/Al/Ni/Au Ohmic contacts for *n*-GaN », *Appl. Phys. Lett.*, vol. 69, n° 11, p. 1556-1558, sept. 1996, doi: 10.1063/1.117060.
- [18] R. B. Chung, H.-T. Chen, C.-C. Pan, J.-S. Ha, S. P. DenBaars, et S. Nakamura, « The polarization field dependence of Ti/Al based Ohmic contacts on N-type semipolar GaN », *Appl. Phys. Lett.*, vol. 100, n° 9, p. 091104, févr. 2012, doi: 10.1063/1.3690878.
- [19] M. E. Lin, Z. Ma, F. Y. Huang, Z. F. Fan, L. H. Allen, et H. Morkoc, « Low resistance ohmic contacts on wide band-gap GaN ».

- [20] L. Dobos *et al.*, « Metal contacts to n-GaN », *Appl. Surf. Sci.*, vol. 253, n° 2, p. 655-661, nov. 2006, doi: 10.1016/j.apsusc.2005.12.167.
- [21] G. K. Reeves et H. B. Harrison, « Obtaining the specific contact resistance from transmission line model measurements », *IEEE Electron Device Lett.*, vol. 3, n° 5, p. 111-113, mai 1982, doi: 10.1109/EDL.1982.25502.
- [22] Y. Sun *et al.*, « Properties of GaN-based light-emitting diode thin film chips fabricated by laser lift-off and transferred to Cu », *Semicond. Sci. Technol.*, vol. 23, n° 12, p. 125022, déc. 2008, doi: 10.1088/0268-1242/23/12/125022.

Chapter V

V.1 μ LED Electro-optical measurements

Electro-optical characterization of fabricated μ LEDs is essential for understanding the main problems of the device and differentiating between those that arise during fabrication from those that arise during epitaxy. First I-V measurements on polar and semi-polar micro-LEDs were presented at the end of **Chapter IV**. The absence of leakage on the polar devices confirmed good control of the process. However, the majority of the semi-polar micro-LEDs were leaky. Therefore, in this chapter, we investigate the impact of the $(10\bar{1}1)$ epi-structure on various devices' performance and characteristics.

V.1.a $4 \times 4 \mu\text{m}^2$ μ LEDs

One of the most interesting results of this thesis is the demonstration of the first functional $4 \times 4 \mu\text{m}^2$ semipolar μ LED. Therefore, I dedicated first a study to compare the performance of these devices fabricated from samples grown on the TS and Aixtron growth reactors. To acquire the current-voltage-optical power, we used the semi-automatic prober CM300 already described in **Chapter IV** for I-V-L measurements.

V.1.a.i Aixtron reactor

We chose a $4 \times 4 \mu\text{m}^2$ μ LED that presents good electro-optical performance as observed in the I-V-L characteristics in **Figure 1-1.a**. The maximum of EQE calculated was 0.02% at a current density of $\sim 10 \text{A/cm}^2$ as seen in **Figure 1-1.b**. It is important to mention that the light collection in this prober is done with a $200 \mu\text{m}$ optical fiber in close contact with the μ LEDs. Because of the numerical aperture of the fiber, we can collect only the photons emitted at a 20° cone angle. We did a comparison between the light collected with this fiber and the light collected in sphere-like measurements on the same device and we found a factor of ~ 20 (that reveals other sources of losses in the collection path). The actual maximum EQE is then closer to 0.4%

The emission wavelength was also measured at current densities going from 5 to 200A/cm^2 showing a 7nm blue shift (**Figure 1-1.c** and **d**). Although this shift is still lower than what is usually observed in polar μ LED which is around 13nm at low J [1], we were surprised by this result as in **Chapter III** we observed no significant wavelength shift in the MQW PL spectra when the excitation power was increased. We expected similar behavior of the μ LEDs in electroluminescence. The reason behind this will be investigated in the following paragraphs.

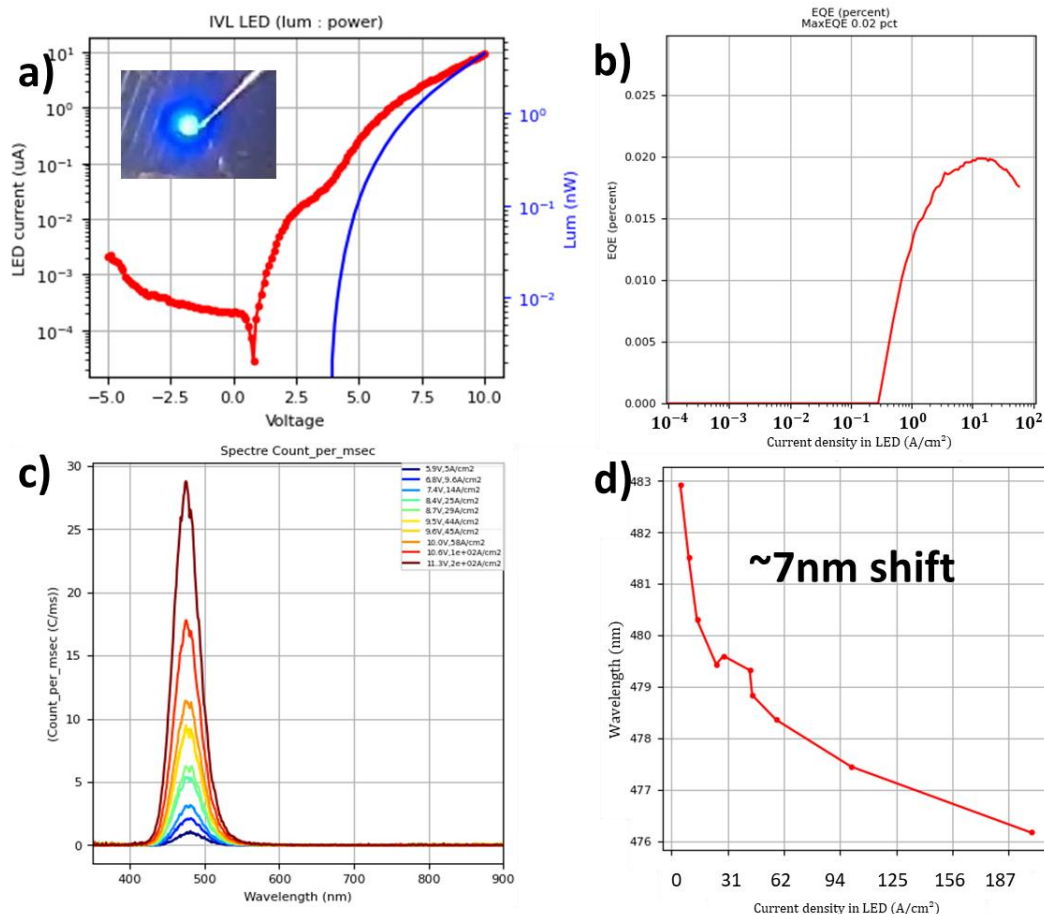


Figure 1-1: a) Current-voltage-optical power characteristics of a $4 \times 4 \mu\text{m}^2$ μ LED grown on the Aixtron. b) Corresponding EQE vs current density curve. c) Spectra acquired at different current densities and d) the median wavelength vs current density.

V.1.a.ii TS reactor

Similar I-V-L characteristics as those obtained on the Aixtron-grown samples were acquired on the samples grown on the TS reactor (**Figure 1-2.a**). They have the same surface morphology, in terms of undulations and chevron features, which plays an important role in these measurements. In addition, we reached a similar max EQE value but at $J_{\text{max}} = 10^3 \text{ A}/\text{cm}^2$, as presented in **Figure 1-2.b**. High J_{max} values for polar GaN LEDs are usually ascribed to SRH non-radiative recombination [2] and go in pairs with a decrease of the maximum EQE. However, in semipolar LEDs, due to the reduction of the internal electric field, the carriers recombine faster and the maximum EQE is expected to occur at higher J (for the same rate of SRH recombination). However, as we have previously seen, the sample grown on the Aixtron reactor reaches the maximum EQE at a lower J . The fact that we obtained similar maximum EQE for a different J_{max} could be caused by carrier localization in some areas of the QW. This would effectively reduce the surface of the active region underestimating the real current density and the carrier density in the emitting area. The latter reason was observed on most μ LEDs during the μ EL measurements.

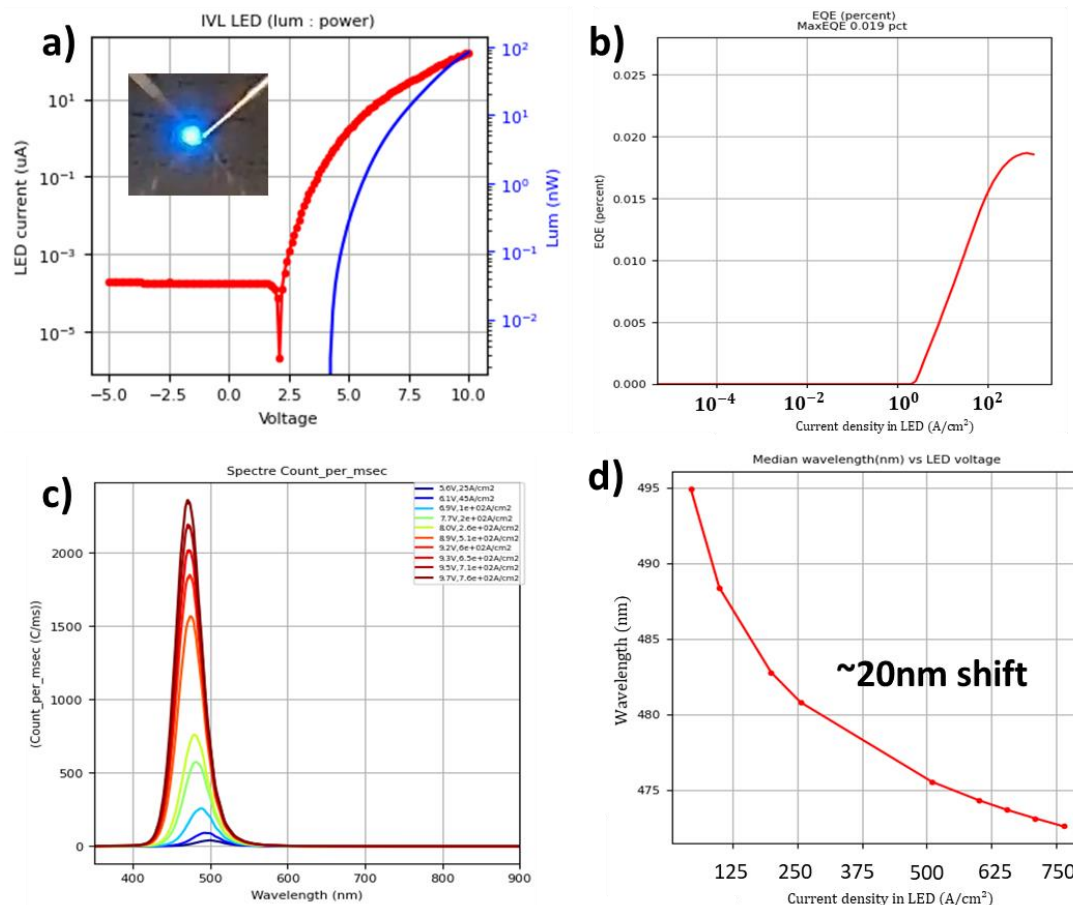


Figure 1-2: a) Current-voltage-optical power characteristics of a $4 \times 4 \mu\text{m}^2$ μ LED grown on the TS reactor. b) Corresponding EQE vs current density curve. c) Spectra acquired at different current densities and d) the median wavelength vs current density.

On this sample, the wavelength blue-shift is nearly three times larger than the shift observed on the Aixtron as seen in **Figure 1-2.c** and **d**. Reminding that in this sample, the thicknesses of the three MQWs varied randomly across the surface. This means that when the current is injected, the emission wavelength will depend on the thickness of the main QW that will emit photons.

We decided to focus on studying the Aixtron samples based on the lower wavelength shift and the uniform MQWs thicknesses observed by the different electro-optical characterizations.

V.1.b Coalescence lines impact on $4 \times 4 \mu\text{m}^2$ blue μ LED

The size of the $4 \times 4 \mu\text{m}^2$ μ LED was chosen to be able to fabricate μ LED in between the coalescence lines separated by a $5 \mu\text{m}$ distance. As previously seen, the coalescence lines are the location of the high dislocation densities. Therefore we could expect higher performance of the μ LEDs in between these lines. Also, being able to compare μ LED located in a defect-free area to μ LEDs overlapping the coalescence region would help us understand the impact of dislocations on the efficiency of the devices. It was for that reason, that the mask was designed to make μ LEDs progressively shift from one another so that they would occupy any position regarding the coalescence region. Despite the fact that our semi-polar μ LEDs were in majority leaky, we tried to make this comparison. Three $4 \times 4 \mu\text{m}^2$ μ LEDs were then selected based on their different positions with respect to the coalescence lines. The comparison of the performance between the μ LED located in between those lines and the two others is presented in **Figure 1-3**. The insets of **Figure 1-3.a** show the different positions of the

square μ LEDs, L9C15 being in between the parallel black lines of coalescence. The EQE with respect to the current density is plotted for the three samples that show a better efficiency of L9C15 (orange) compared to the other two. However, it is clear that the three EQEs are low ($<10^{-4}\%$ on CM300) compared to the best EQE obtained on this sample (0.02%) which can be attributed to the leakage and SRH. Indeed, the abrupt increase of EQE at low current density is typical from devices presenting some degrees of leakage. The IV characteristic also indicates probably a mix of non-radiative recombination and leakage. (**Figure 1-3.b**). We cannot conclude that this difference in performance is caused by the μ LED positions with respect to the coalescence lines. Due to the quality of the epitaxy, it may be random. We would need more statistics and less leakage on these $4 \times 4 \mu\text{m}^2$ to be able to conclude the impact of the dislocations on their performance.

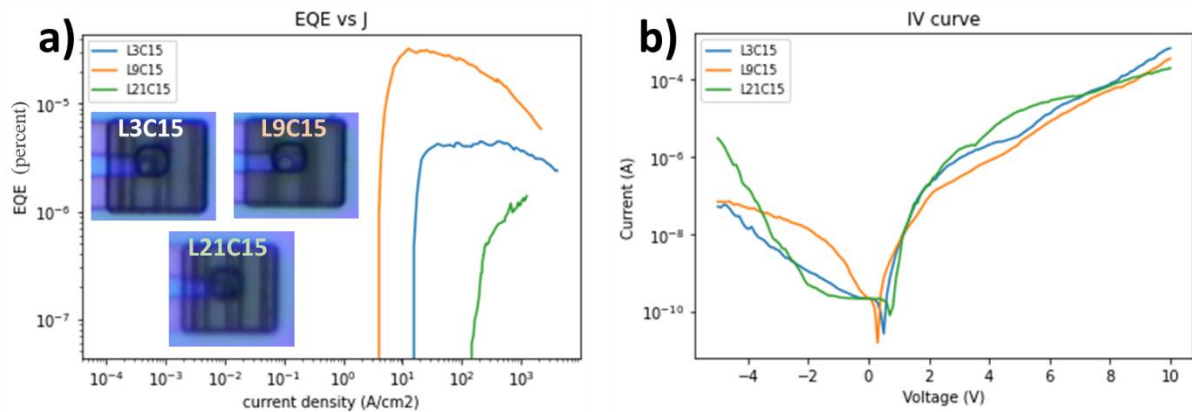


Figure 1-3: a) EQE vs J and b) I-V characteristics of the three $4 \times 4 \mu\text{m}^2$ μ LED devices located on different areas with respect to the coalescence lines, as described on the insets.

V.1.c Size-dependent characteristics of semi-polar μ LEDs

One of the studies we planned during the mask design, was the comparison of the electro-optical properties of the semi-polar μ LEDs as a function of their size. It is well known that in polar μ LEDs, the SRH coefficient A increases with decreasing μ LED size as described by Olivier et al. [3]. In semi-polar orientation, the reduction of the internal electric field is expected to decrease this size dependence. However as leakage is observed for most of the devices, we chose the best J-V characteristics to compare the different sizes with each other. **Figure 1-4.** presents the J-V characteristics for different LED sizes starting from 6×6 to $100 \times 100 \mu\text{m}^2$.

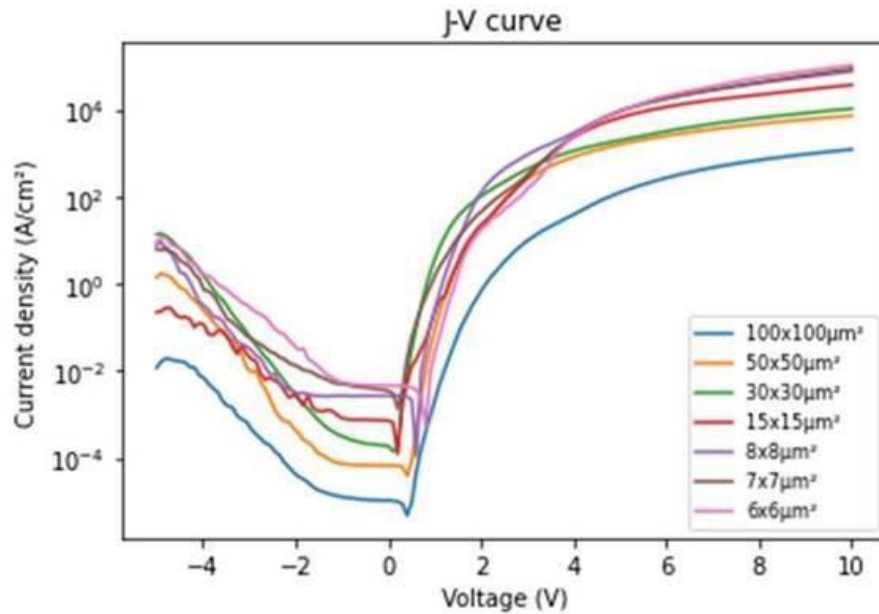


Figure 1-4: J-V characteristics of the different μ LED sizes from $6 \times 6 \mu\text{m}^2$ to $100 \times 100 \mu\text{m}^2$

Figure 1-4 shows that the current density decreases with the increase of the LED size which is due to the increase of the series resistance for the larger LED sizes that is probably related to the ITO access lines to the metallic pads. For the small LED, we observe quite clearly a first bump in current at a low voltage which is typical of SRH non-radiative recombination. At higher voltage (above 3-4V) the μ LED starts to light up. It is not clear that this bump is more pronounced than in larger LEDs as it is difficult to separate the two contributions. Besides, the non-uniform efficiency of our MQWs probably also introduces variations of SRH contribution that will mask their possible size dependence.

V.2 Study of the origin of the device leakage

V.2.a Micro-electroluminescence measurements

We described in **Chapter III** the possibility of using the WITEC setup to conduct confocal μ EL as well as μ PL measurements. This experimental technique is well suited to study the spatial distribution of the electroluminescence which is helpful to understand the composition of the emitted light and a possible non-uniform injection. We selected a $30 \times 30 \mu\text{m}^2$ μ LED grown on the Aixtron to perform sequential I-V characteristics up to 6V as presented in **Figure 2-1**. We noticed a clear degradation in the device's performance after each acquisition, with the leakage current increasing. The reason behind the leakage is investigated in this section for the same sample by different characterization techniques.

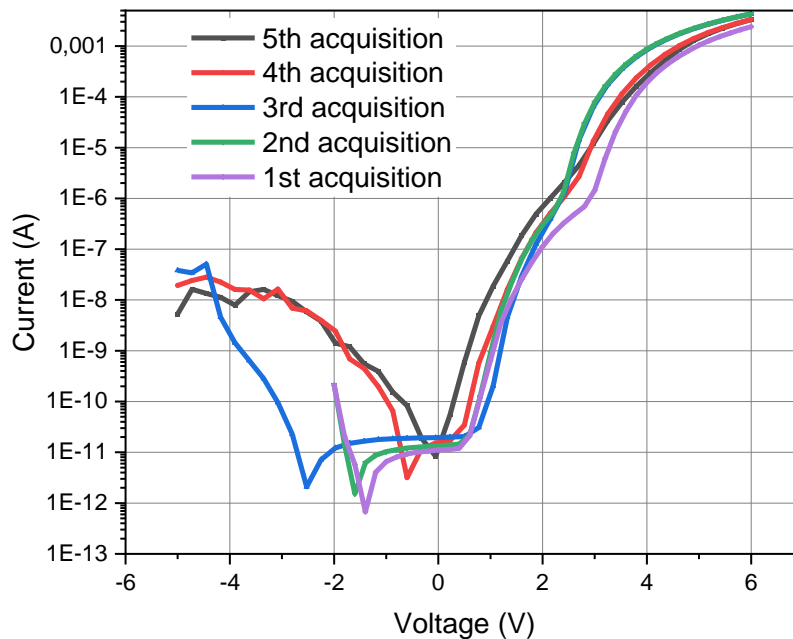


Figure 2-1: I-V characteristics of a $30 \times 30 \mu\text{m}^2$ μ LED showing a progressive increase of leakage current after five successive acquisitions up to 6V.

Then, we performed a mapping of the electroluminescence with the WITEC by applying 7V on the μ LED, and analyzing the emission wavelength with a spectrometer. First, we clearly saw on the optical microscope image of **Figure 2-2.a**, a local bright spot compared to the rest of the μ LED emission. The optical image has the advantage of being able to locate the emission with respect to the coalescence lines. μ EL integrated intensity mapping of **Figure 2-2.b** confirms the non-uniform emission as previously discussed in section **V.1.a.ii**. This non-uniformity can be caused by surface disruptions along the sample, such as undulations that seem to have a huge impact on the emission, as observed in the MQW characterizations of **Chapter III**. In addition, it points towards a higher injection in a local spot inducing a higher intensity. This spot may be at the origin of the leakage path detected in the I-V characteristics, where all injected carriers would initially flow. At higher voltage, the resistance of this path would allow the rest of the LED surface to light up. However, it is likely that after several I-V characteristics acquisition, this path could deteriorate and become leakier. As far as the blue shift is concerned, in polar GaN, an increase of carrier concentration in the QWs can explain a blue shift due to the screening of the internal electric field, but in our case, the MQW characterization revealed that the electric field was limited. Hence, it seems unlikely that the 40nm blue shift observed in **Figure 2-2.c** in the wavelength mapping, could be due to some residual internal field screening. It may be more related to a difference in the composition of the active region that could be at the origin of this local injection path. That is why μ PL was also conducted on the same sample to further understand the emission properties of this area.

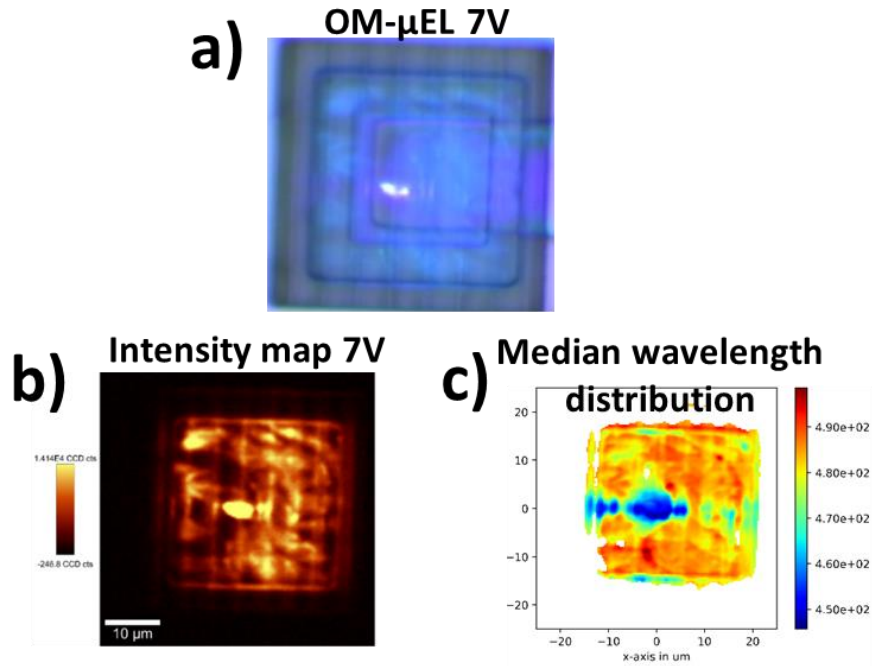


Figure 2-2: μ EL measurements on the $30 \times 30 \mu\text{LED}$. a) an optical microscopic image of the μLED at 7V with its corresponding μEL intensity mapping in b) and the median wavelength distribution map in c).

V.2.b Photoluminescence measurements

First, quantum well luminescence is studied on the WITEC μPL and the Zeiss PL microscope. The WITEC uses a 405 nm laser to resonantly excite the active region, as explained in **Chapter III**. We chose the same $30 \times 30 \mu\text{m}^2$ μLED to perform mappings of the μPL intensity and wavelength, as presented in **Figure 2-3.a** and b, respectively. The white circle on the intensity map of **Figure 2-3.a** indicates the area of the bright spot, which was located based on the dimensions in **Figure 2-2.b**. Non-uniform intensity is observed along the μLED , following the undulations present on the surface. The bright spot is located in an area emitting a low intensity. As such, the μPL mapping of the wavelength in **Figure 2-3.b** shows a wavelength blue shift on the dimmer areas observed in **Figure 2-3.a**. These results are similar to the characterization acquired before fabrication, which highlights the impact of the surface disruption on the wavelength emission. This is also consistent with the non-uniform EL measurements.

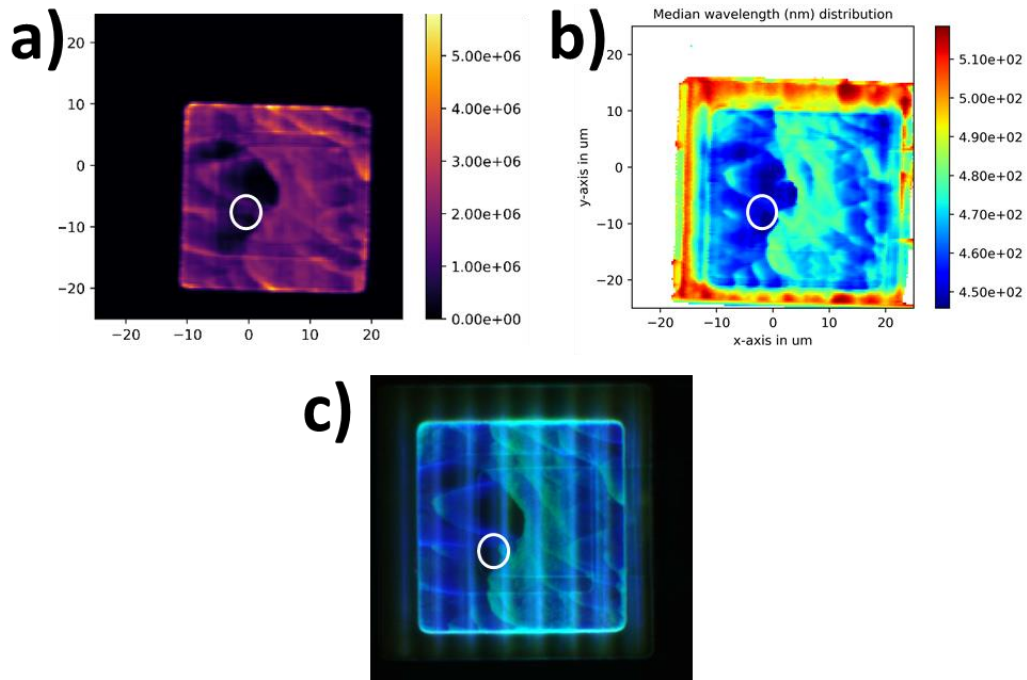


Figure 2-3: a) μ PL integrated intensity with a white circle indicating the bright spot of the $30 \times 30 \mu\text{m}^2$ μ LED also studied in μ EL, with its corresponding median wavelength map in b). c) PL microscopy image of the same μ LED.

PL microscopy of the same μ LED was conducted to confirm the result and make it more visible with the color camera. **Figure 2-3.c** indeed confirms the non-uniform wavelength emission along the undulations with no sight of special defects on the bright spot area. Therefore, we decided to do in-depth characterization by doing a TEM study on the leakage spot.

V.2.c Transmission electron microscopy

STEM measurements were conducted in the L2MD CEA-LETI laboratory on a different device of $100 \times 100 \mu\text{m}^2$ presenting the same type of μ EL bright spot as can be seen on the WITEC optical microscope (**Figure 2-4.a**). An SEM image in **Figure 2-4.b** shows the 250nm thick specimen that contains the defective area, during the FIB preparation.

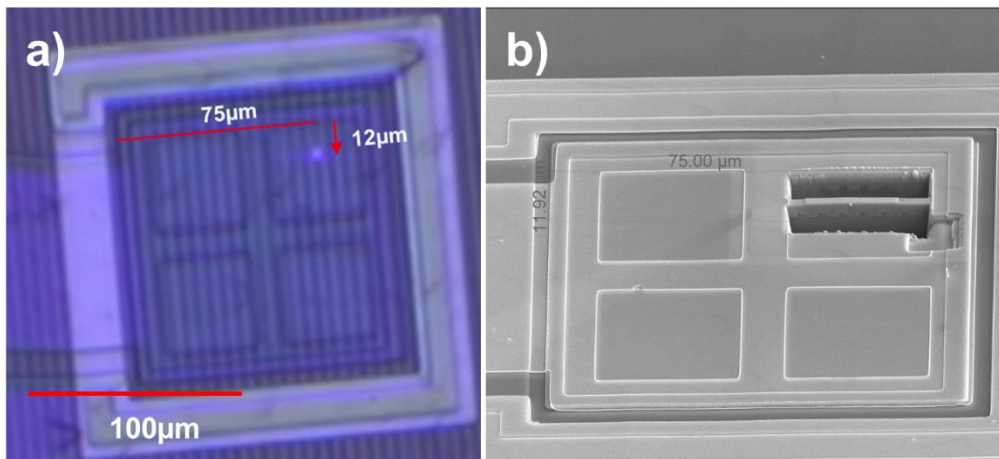


Figure 2-4: a) μ EL optical microscope image of the 100x100 μ m² under applied voltage that reveals the bright spot and allows its coordinates measurement. b) An SEM image of the FIB cut preparation on the same spot.

A cross-sectional HAADF-STEM image of the area of interest is depicted in **Figure 2-5**. Three different regions indicated in red squares were distinguished by the different MQW numbers. It appears that at the leakage spot, the typically grown three MQWs are reduced into a single QW layer. We suspect that in this area, the surface quality might have impacted the growth rate and the nucleation of the species leading to this growth behavior. Although the reason behind this growth perturbation is still not clear, it could explain the blue shift observed in μ PL and the μ EL measurements, as the QWs that light up are different in these regions.

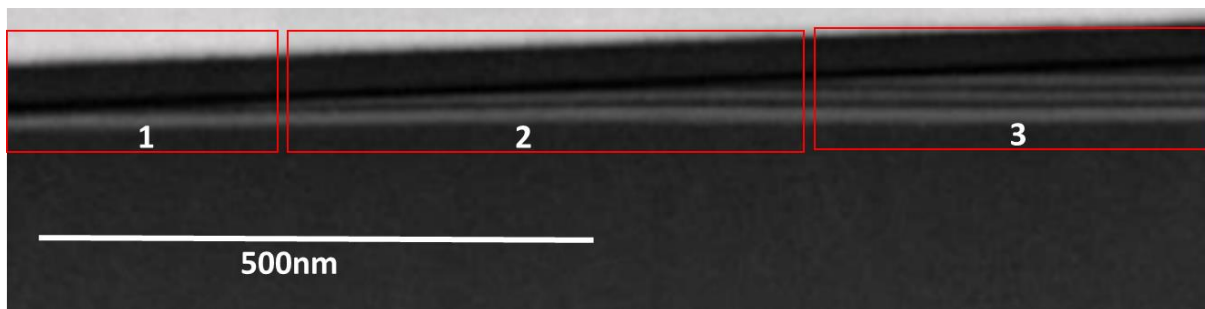


Figure 2-5: A cross-section HAADF-STEM image on the leakage spot showing an intersection of unexpected three MQW merging into a single QW.

V.3 Wavelength shift study

After studying the potential reason behind the leakage on the semi-polar μ LEDs, we wanted to investigate the wavelength shift observed in the EL measurements. Indeed, while studying our semi-polar MQW structures, we observed no significant change in the emission wavelength when power-dependent-PL was performed. In polar GaN, as explained earlier, the screening of the internal electric field by injected carriers in the QWs is the main reason behind this wavelength blue shift when increasing the current density. Therefore, we could have expected a similar blue shift in EL and PL when current and laser power are increased respectively, as only the carrier density in the QW matters with this explanation. In this section, we will be investigating the reason behind this shift by different characterization techniques.

V.3.a **Transmission electron microscopy**

The first important characterization to perform in order to understand the emission properties of the active region is a STEM analysis of semi-polar LED epi-structures to know more precisely the In composition and the thickness of the different QWs. We chose the same $100 \times 100 \mu\text{m}^2$ LED device of the blue sample of the Aixtron, previously characterized in section **V.2.c**. A cross-section STEM is presented in **Figure 3-1.a**, showing the InGaN underlayer and the three MQWs. A strain map was also performed to extract the lattice deformation within the UL and the three MQWs as depicted in **Figure 3-1.b**. A calculation has been conducted based on the extracted deformation of the lattice along the growth to obtain the Indium percentages within each layer. For more details on similar calculations, one can refer to Romanov *et al.* [4]

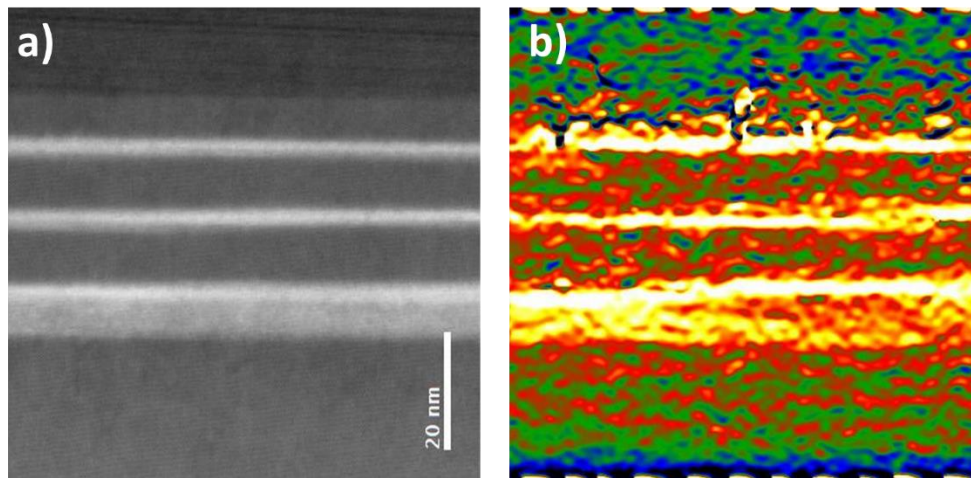


Figure 3-1: a) Cross-section STEM image of the three MQWs, the EBL, and p-GaN of the $100 \times 100 \mu\text{m}^2$ LED. b) The strain map of the UL and 3 MQWs is shown in a).

The strain-induced deformation as a function of the In percentage is plotted as a linear curve in **Figure 3-2**. The InGaN underlayer has $\sim 8\%$ In whereas the first, second, and third-grown QWs have $\sim 17\%$, 20% , and 15% respectively. The different indium concentrations within the MQWs might explain the wavelength shift if more than one QW lights up when carrier injection increases. Indeed, if contrary to c-plane LEDs, the high-composition QW lights up at a low injection current and the other QWs at a higher current, then we could expect a blue shift, unrelated to the screening of the internal field. To better understand the carrier injection changes with bias in the MQWs of our semi-polar structure, and in particular, to determine which of the three QWs will emit at low bias, we decided to run band structure simulations on this LED structure.

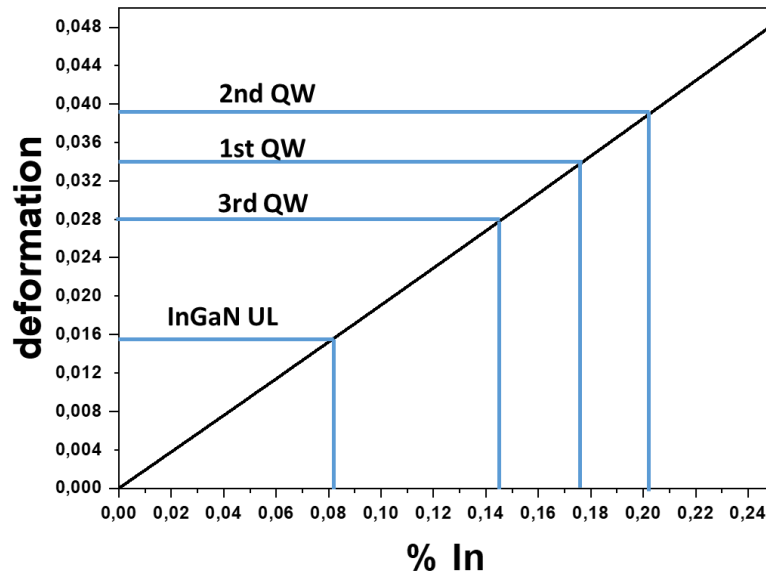


Figure 3-2: The strain-induced deformation function of the In percentages (credits to P.Vennéguès and P. De Mierry)

V.3.b SiLENSe Simulation

SiLENSe is a band structure simulation program of the STR company, particularly well-designed for nitride semiconductors. Based on the composition, doping, and thicknesses of an LED structure, the software can simulate the shape of the valence maxima and conduction band minima, the quasi-fermi levels, the electron and holes current, the carriers density, the internal electric field, the emitted spectrum, etc. We can also choose the right orientation of the substrate, $(10\bar{1}1)$ GaN in this case, to understand the behavior of the light emission with respect to the semipolar orientation.

Figure 3-3 presents the energy band diagram at a bias of 2.6V of the LED structure estimated by TEM and deformation calculation.

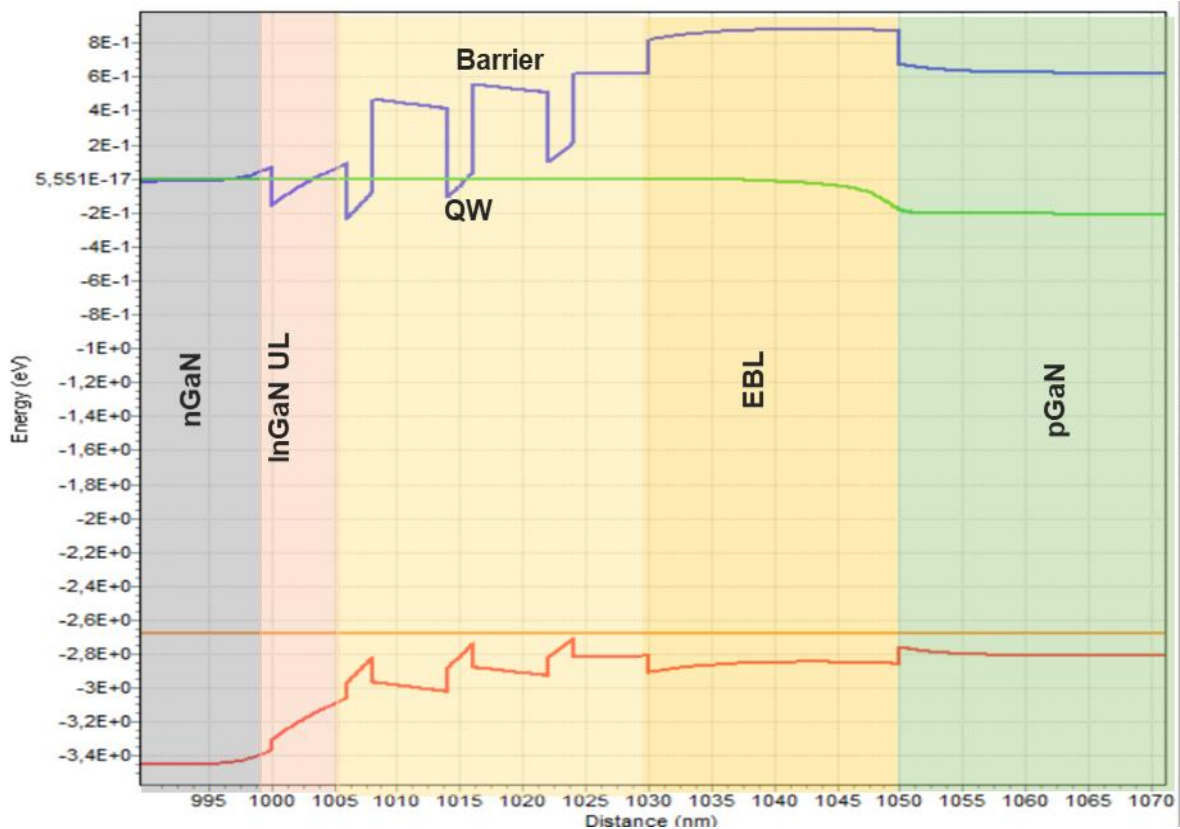


Figure 3-3: Energy band diagram of the simulated LED structure at 2.6V.

In SiLENSe, the contacts are considered ohmic, therefore the first detected photons were observed at 2.6V which is lower than in our μ LEDs emitting light at around 3V because of the imperfect contact. The current density with respect to the voltage and the wavelength variation with respect to the current density were then plotted for four different structures:

- An LED structure with MQW thicknesses of 2nm as measured by the TEM and In composition having the highest In concentration in the second grown QW (17%-20%-15%).
- A second LED structure with a similar In composition of 17% and thicknesses of 2nm for all QWs as a reference of the expected wavelength shift in a semi-polar LED.
- A third LED structure having similar In composition of 20% for the first two QWs, and 15% for the third one. The aim is to study the impact of the first QW on the wavelength emission.
- A fourth LED structure having similar In composition of 20% for the three MQWs to study the impact of the third QW on the wavelength emission compared to the third LED structure. In addition, the higher In composition normally causes more wavelength shift due to the internal field. Therefore, this structure will be compared to the second LED structure with lower [In].

Figure 3-4.a presents the J-V characteristics of all the structures showing similar injection properties for LED structures having similar In composition in the first QW. The range of current density simulated was the same as in our experimental results on the semi-automatic prober in section V.1.a.i. Figure 3-4.b shows the μ EL emission wavelength variation with respect to the current density. Around 12nm of wavelength blue shift is evident for all the trials with increasing the current density (J). When we compare the first with the third LED structure, the In composition of the first QW

increased by 3% while the second and third QWs remained constant, and the wavelength emission was 10nm longer. Whereas, when we compare the third with the fourth structure, where the In composition was increased for the third QW while the others remained constant, similar behavior was observed. Comparing the first and the second structures, where the In content decreased in the second QW by 3% and increased in the third one by 2%, we observed a wavelength emission of 1nm shorter.

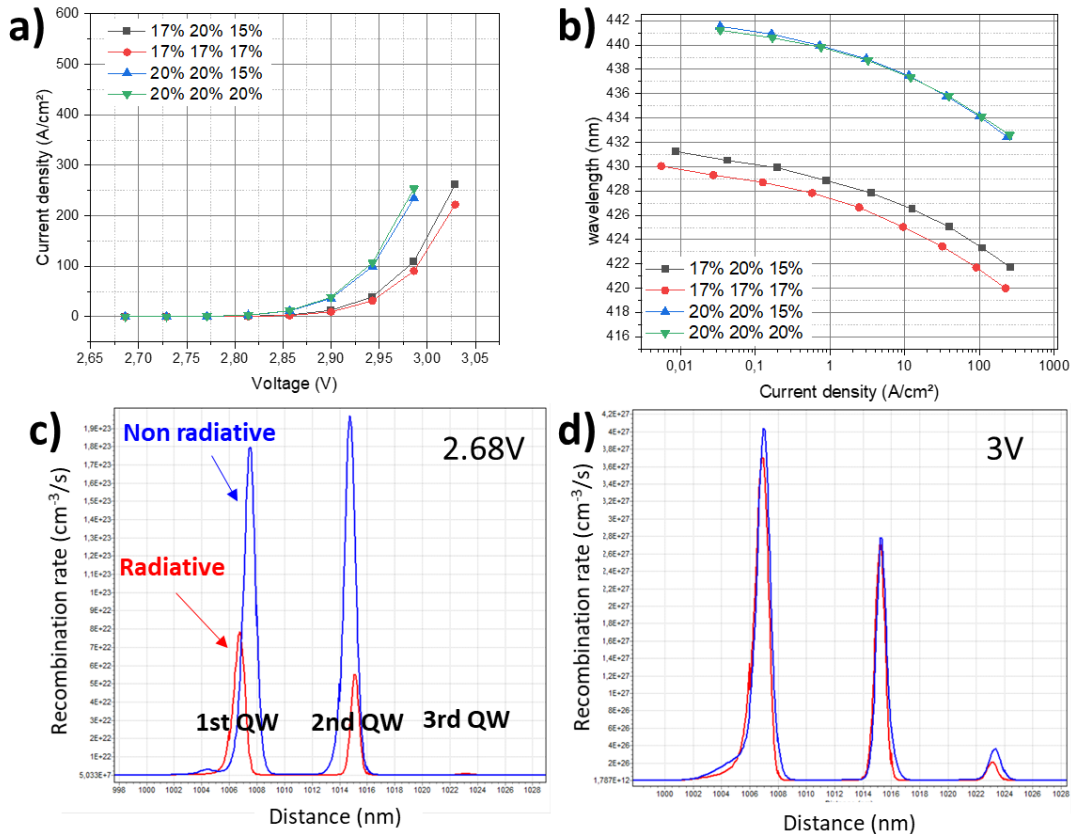


Figure 3-4: a) The current density-voltage b) the wavelength-current density characteristics of four LED structures having different In compositions in the three MQW. The carrier recombination rate for the first LED structure similar to our semipolar samples are shown in c) at the lowest and d) highest voltages.

These simulations show first the variation of In concentration in the MQWs is not the reason behind the wavelength shift as there are no significant differences between the structures. Second, the impact of the third QW on the wavelength emission is insignificant whereas the emission highly depends on the first QW. We observed by simulation that the first grown QW (close to the n-GaN side) is the main emitting QW at low and high injection currents as seen by the dominant radiative recombination in the first QW in **Figure 3-4.c** and **d** respectively, which is the contrary than in c-plane. Third, the screening of the remaining internal field in this semi-polar orientation seems to be responsible for some moderate blue shift since the emission did not change from one QW to another when J increased. However, other factors can also impact the amplitude of the shift, such as the MQW thicknesses. μ PL and μ EL characterizations were conducted to understand the origin of this wavelength shift.

V.3.c μ Photoluminescence

Power-dependent μ PL measurement has been conducted with the WITEC setup on a $5 \times 5 \mu m^2$ μ LED as depicted in **Figure 3-5**. It appears that when increasing the optical power from 10mW to 100mW, the

median wavelength is barely shifting by ~ 2 nm. This result on an LED structure is consistent with the one presented in **Chapter III** on a MQW structure, for which no large wavelength shift was observed in power-dependent PL measurements. It is also consistent with the band structure simulation that predicts just a few nm shifts for a change of injected carriers of one order of magnitude.

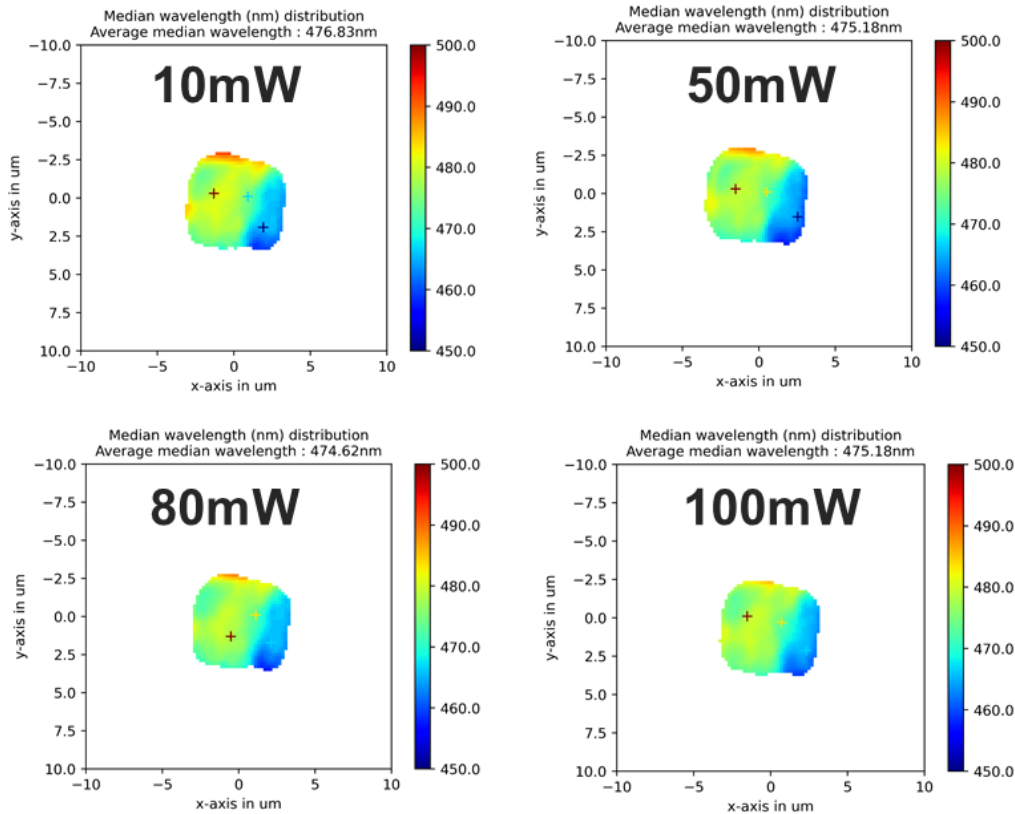


Figure 3-5: Median wavelength mapping of μ PL power-dependent measurements on a $5 \times 5 \mu\text{m}^2$ μ LED.

V.3.d μ Electroluminescence

Following μ PL measurements, using the WITEC, we performed μ EL measurements on the same μ LED to observe locally the wavelength shift for different applied voltages. **Figure 3-6** presents the wavelength mapping obtained when increasing the voltage from 7 to 9V. The median wavelength averaged over the whole μ LED decreased by ~ 8 nm with increasing voltage. The μ EL intensity mapping insets at each voltage show a non-uniform emission and a variation of this non-uniformity distribution with the applied voltage. In this specific case, it seems that the areas of the μ LED lighting up at higher applied bias also emit at shorter wavelength. Due to a lack of statistics, it is difficult to generalize. We can only conclude that it is difficult to obtain a direct correspondence between μ EL and μ PL carrier densities. Interestingly, the blue shift observed in μ EL on our semi-polar μ LEDs could have two origins. First a screening of the small remaining internal field that should be moderate and identical in PL and second a consequence of the In composition non-uniformities in the QWs possibly responsible for a progressive carrier injection from high to low In content area as the bias increases.

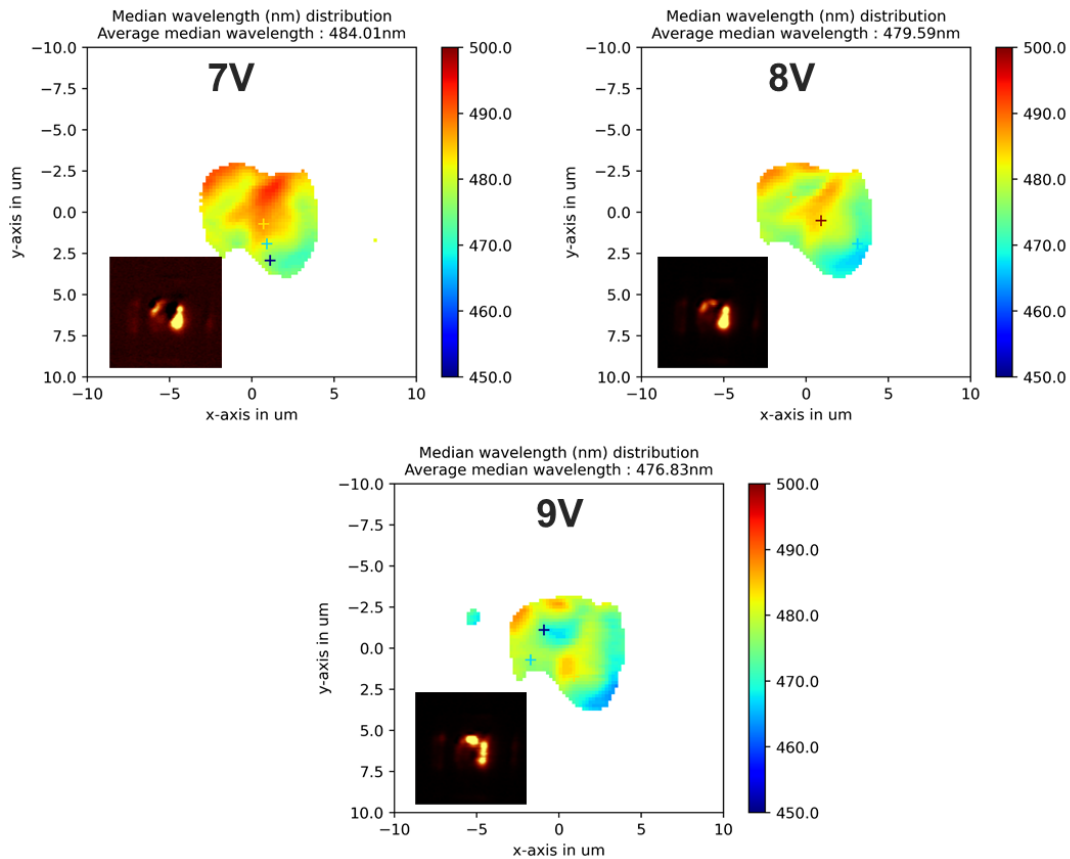


Figure 3-6: μ EL wavelength mapping of a $5 \times 5 \mu\text{m}^2$ μ LED with an image of the μ EL integrated intensity in the inset for 3 different applied biases.

V.4 μ LED-based applications

Chapter IV described the different types of devices present on the mask set which included an operational μ LED in a matrix environment, and RF μ LEDs. Despite the lack of time and complex epitaxial structure that prevented us from studying thoroughly these devices, we still managed to verify their functionality as described in this section.

V.4.a μ LED Matrix

The aim of this configuration was to study the efficiency of an operational μ LED in a matrix environment. However, due to the lack of time, I managed to conduct just μ EL measurements on a few matrices of the Aixtron sample emitting in blue. **Figure 4-1** presents the I-V characteristics before and after μ EL mapping acquisition on a $10 \times 10 \mu\text{m}^2$ μ LED having a $3 \mu\text{m}$ trench (space between each mesa). It is clear that the μ LED showed leakage current and a degraded quality after μ EL acquisition but not necessarily more than in individual μ LEDs.

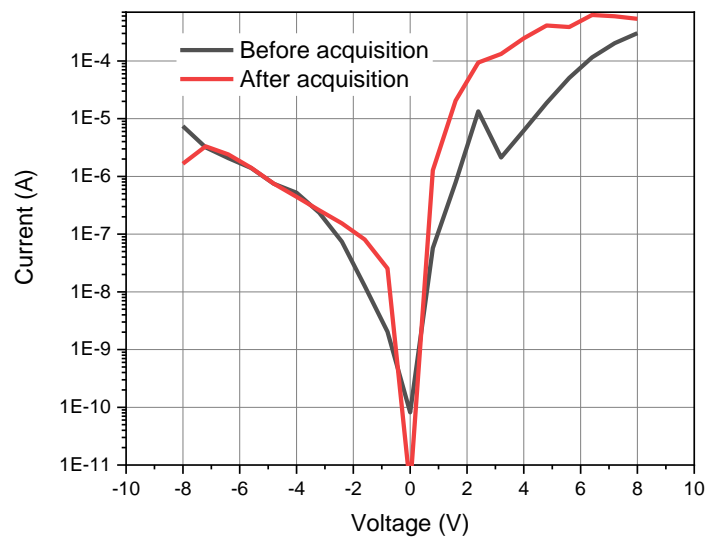


Figure 4-1: I-V characteristics of a $10 \times 10 \mu\text{m}^2$ μ LED before and after μ EL mapping acquisition at 8V.

Figure 4-2.a presents an optical microscope image during μ EL measurements at 8V. We can clearly observe the light extraction that might be caused by the stripes or the geometry of the mesa.[5] For micro-display applications, a metallization of the sidewalls after passivation would be necessary to reduce this crosstalk. Despite the leakage observed, we verified that the μ LED was indeed functional for $3\mu\text{m}$ and $5\mu\text{m}$ trenches as depicted in **Figure 4-2.b** and **c**, which is normally a critical fabrication step.

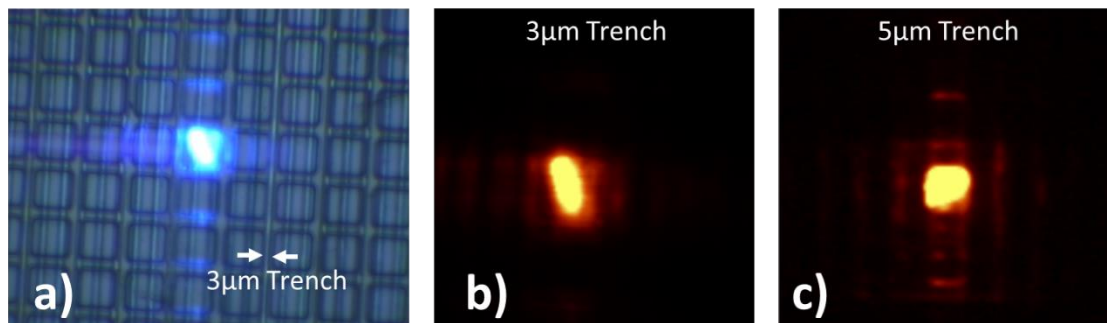


Figure 4-2:a) Optical microscope image of an operational $10 \times 10 \mu\text{m}^2$ μ LED in an 11×11 matrix with $3\mu\text{m}$ trench at 8V with its corresponding integrated intensity image in b). c) μ EL integrated intensity image of a $10 \times 10 \mu\text{m}^2$ μ LED in an 11×11 matrix with $5\mu\text{m}$ trench.

V.4.b Frequency response of semi-polar μ LED

The objective of this thesis was originally to fabricate semipolar μ LEDs for μ displays and displays applications. However, recently the laboratory's interest extended towards the field of data communication that requires high bandwidth emitters. That is why, due to the fast carrier recombination that semipolar orientations can offer, we decided to add μ LEDs with RF-optimized pads on the mask set to be able to characterize their frequency response. **Figure 4-3** shows an example of the transmission power versus the frequency modulation of a $30 \times 30 \mu\text{m}^2$ blue μ LED made out of a semipolar and polar GaN sample as presented in blue and red respectively. Both μ LEDs were fabricated using the same process flow as described in **Chapter IV**. At 10V, the modulation

bandwidth of the semipolar micro-LED was almost 1.4 GHz at $J=106.69 \text{ A/cm}^2$, compared to 101 MHz at $J=899.15 \text{ A/cm}^2$ for the polar micro-LED. This result is consistent with the optical differential lifetime (ODL) measurement of the MQWs, which showed a faster recombination rate for the semipolar MQW than for the polar MQW. In addition, the higher bandwidth at lower current density in semipolar compared to the polar is beneficial to obtain lower power consumption. It is worth mentioning that, both μ LEDs are emitting in the blue but to have a fair comparison between the two samples, we should have the same In composition within the QWs or similar QW thicknesses. Despite this fact, the results obtained by the ODL measurements in **Chapter III** and this RF measurements, are promising for the potential use of semi-polar μ LED in the field of data communication.

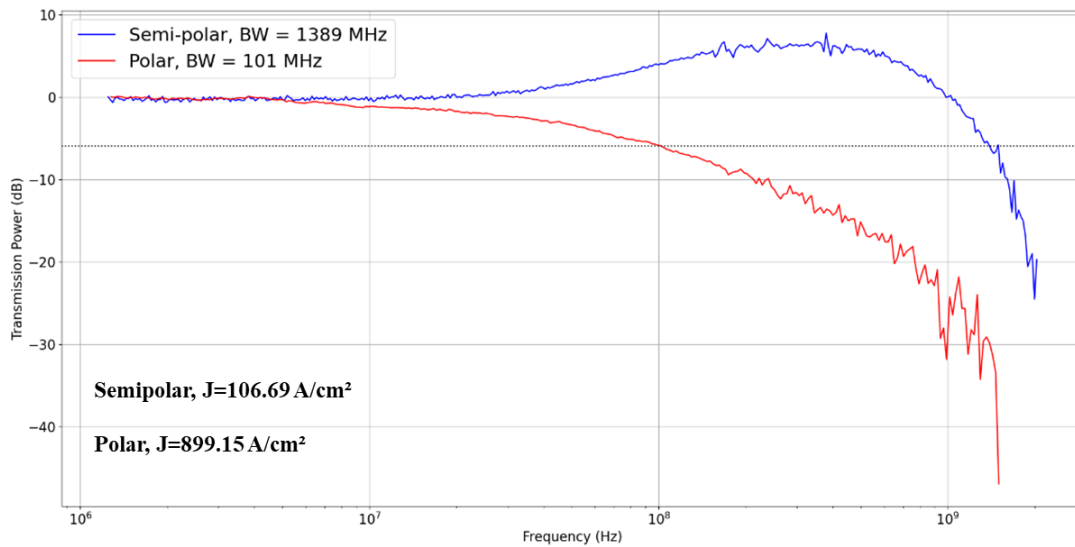


Figure 4-3: Normalized transmission power curve of a $30 \times 30 \mu\text{m}^2$ blue μ LED of the semipolar GaN presented in blue and a polar GaN in red.

V.5 Conclusion

In this chapter, we studied the electro-optical performance of the fabricated semipolar μ LEDs. First, we chose to focus our work on the Aixtron samples instead of the TS because of the 20nm wavelength shift obtained on the TS samples was mainly caused by the non-uniform MQWs. Despite the leakage observed on most of the μ LEDs that limited our analysis, we still managed to fabricate down to $4 \times 4 \mu\text{m}^2$ μ LEDs located in between the dislocation lines as attempted. We suspect that the leakage spot observed in some μ LED could be related to growth perturbation with a discontinuity of the number of QWs and QW thicknesses. An investigation on the $\sim 7\text{nm}$ wavelength blue shift detected by μ EL measurements was seen to be caused by the slight screening of the electric field expected along this orientation. In addition to the non-uniformity in EL emission and the variation of emission areas with respect to the applied voltage. Finally, we demonstrated a functional μ LED in a matrix environment and an RF semipolar μ LED with a modulation bandwidth reaching $\sim 1.4\text{GHz}$ which are very promising for both μ displays and VLC applications.

V.6 References

- [1] S.-W. H. Chen *et al.*, « Full-color micro-LED display with high color stability using semipolar (20-21) InGaN LEDs and quantum-dot photoresist », *Photonics Res.*, vol. 8, n° 5, p. 630, mai 2020, doi: 10.1364/PRJ.388958.
- [2] M. S. Wong, S. Nakamura, et S. P. DenBaars, « Review—Progress in High Performance III-Nitride Micro-Light-Emitting Diodes », *ECS J. Solid State Sci. Technol.*, vol. 9, n° 1, p. 015012, 2020, doi: 10.1149/2.0302001JSS.
- [3] F. Olivier, A. Daami, C. Licitra, et F. Templier, « Shockley-Read-Hall and Auger non-radiative recombination in GaN based LEDs: A size effect study », *Appl. Phys. Lett.*, vol. 111, n° 2, p. 022104, juill. 2017, doi: 10.1063/1.4993741.
- [4] A. E. Romanov *et al.*, « Basal plane misfit dislocations and stress relaxation in III-nitride semipolar heteroepitaxy », *J. Appl. Phys.*, vol. 109, n° 10, p. 103522, mai 2011, doi: 10.1063/1.3590141.
- [5] S. HANG, « On the impact of the beveled mesa for GaN-based micro-light emitting diodes: electrical and optical properties ».

General Conclusion

In this thesis, we report the first realization of functional $(10\bar{1}1)$ semipolar GaN-based μ LEDs on SOI-ART substrates. The presented work was carried out between two main laboratories, CEA-LETI and CRHEA. The patterning and the μ LED fabrication were accomplished in CEA-LETI whereas the MOVPE growth took place in CRHEA. Structural and electro-optical characterizations of the epi-structures and the resulted devices were conducted in both laboratories.

First, the patterning of the substrates was optimized for both regular and ART-SOI having the top silicon $(001)6^\circ$ off-axis. This was critical to improve the quality of the subsequent selective GaN growth. At CHREA, we used a two-step growth approach where we managed to obtain uniform and close-packed adjacent pyramidal stripes as a first step. In the second step, we tuned the growth conditions that enabled us to reach a 2D coalescence layer free of meltback etching, a relatively low surface roughness, and a high optical quality. This was accomplished by doing the coalescence using half-undoped and half-n-doped GaN. Despite the use of the ART as a dislocation-blocking approach, some dislocation was detected at the template level, in between the coalescence lines. Additionally, we observed chevron features and undulations along the surface. To improve the template quality, we suggested the use of SOI wafers with a 7° misorientation instead of 6° to better align the $(10\bar{1}1)$ semipolar GaN orientation. This might improve the surface morphology and avoid the formation of undulation and chevrons. On the other side, by tuning the growth conditions of the pyramidal stripes, we can favor the bending of the dislocations at the early growth stages which further reduces the dislocation density.

Second, MQWs and LED structures were grown on these templates. A turquoise-to-red MQW emission was achieved by tuning the growth temperature. These results have shown the ability to reach longer wavelength emissions using the $(10\bar{1}1)$ semipolar orientation. In addition, the MQW samples showed a fast recombination rate, wavelength stability, a low internal electric field as expected, and a decent IQE equal to 46% for the turquoise MQW. The wavelength was seen to be blue shifting along the arls of the chevrons and on the undulations present on the surface which we hopefully aim to solve by using the Si $(001) 7^\circ$. Additionally, the growth of metamorphic InGaN layers can help reach longer wavelengths with a better structure quality.

Third, we designed and fabricated a photolithography mask set which includes specific configurations to test single devices with various sizes, the impact of dislocation along the coalescence lines, μ LED in a matrix environment, and RF μ LEDs. This was followed by the development of a new μ LED process flow on c-plane GaN LED epi-structures, with no leakage observed when electro-optical measurements were conducted. This result validated the process flow by which we successfully fabricated down to $4 \times 4 \mu\text{m}^2$ functional semipolar μ LEDs.

Finally, we established different electro-optical characterizations on the fabricated semipolar μ LEDs that showed leakage in most of the devices and a blue shift of $\sim 7\text{nm}$. We suspect that the leakage is caused by the epitaxy as we identified a leakage spot in an area where the intended three MQWs turn into a single QW. On the other hand, the wavelength blue shift observed was due to the different areas emitting progressively with the increase of voltage by EL, and the impact of the screening of the remained electrical field. Despite this, we managed to obtain some good LEDs from $200 \times 200 \mu\text{m}^2$ to the smallest size μ LED on semipolar GaN.

General Conclusion

All of these results highlight the encouraging outcome in terms of In incorporation and low internal electric field, and the potential reproducibility of these results on a 200mm wafer, that pave the way for native color RGB μ display applications. In addition, the high modulated bandwidth of around 1.4GHz obtained along this orientation addresses fields of interests such as the communication applications.

Appendix A :

Process flow of SOI patterning :

Step	Recipe	Equipments	Comments	Comments
Substrate cleaning				
Observation MO				
Acetone	10min-Ultrasonic Bath	Solvent Workbench		
Acetone	Pressure gun 10s on vacuum holder	Solvent Workbench		
Isopropanol&de-ionized water rinse	Rinse	Solvent Workbench		
Caro	5min	Acid workbench		
Removing of the protection layer	BOE	Acid workbench	depends on the thickness	
Characterization of the thickness				
Observation MFD				
Resist Deposition				
HMD5	90°C 90 seconds	HMD5 vapor		
Resist Deposition	450ul,3000 rpm,10s	Delta 80	Result thickness around 1.8 µm	
Soft Bake	1min, 90°C	Delta 80	To solidify the resist	
Photolithography				
Exposure	90ul/cm ² ,888,Mask:GROOV small	Betasquared 2	Align the rotation axis of the Si (001) parallel to the mask	Vertical alignment
Develop	MF319, 1min	Dev workbench	Rinse with developer every 1.5s	
Cleaning	De-ionized water,2min			
Mask Opening				
Resist Cleaning	FLASH,2min	NE660	necessary to remove resist residuals to insure mask etching	
Mask Etching	SiO2-A2	NE660	CH3O2 50% 1.etching: 1.2 nm/sec	300nm-->150sec
Cleaning	FLASH,15s	NE660	necessary to remove carbon contamination after ICP etching	
Resist Removing				
DMSO	10min-Ultrasonic Bath	Solvent Workbench		80°C
Acetone	Pressure gun 10s on vacuum holder	Solvent Workbench		
Isopropanol	Rinse	Solvent Workbench		
Oxygen Plasma	Strip 2min	Tepia	organic contamination removal	
Caro	5min	Acid workbench		
Verify mask widths and openings	Optical Microscope	Olympus		
Si Facets Etching				
Cleaning	Flash BOE, 3s	Acid workbench	necessary to remove the native oxide layer that may block the etch	
KOH etching	KOH 37°C, 10wt%	KOH Workbench	around 2° 30' for our (111) facets	KOH:H2O/55.5:242ml (KOH 44%)
Rinse	5min	KOH Workbench		
Thickness Verification		Dektak		
SEM check + Optical scope				
Post KOH Cleaning				
Caro	4min	Acid workbench	Removal of crystallites from surface	
Inclined Masking Dep				
Samples orientations	180° from the notch		very important to cover the right facets	
1° facet Masking 100nm	at 11° without rotation and oscillation	IBS		59.22min=100nm
Final Cleaning				
Cleaning	Flash in diluted BOE 1:1.0, 3s	Acid workbench	necessary before growth to remove any unwanted SiO2 on the good facets	

Résumé:

Au début des années 1900, le concept d'émission spontanée a été introduit, qui se produit lorsqu'un électron se désactive d'un état d'énergie élevée à un état inférieur en émettant un photon. Ce principe appliqué aux semi-conducteurs a permis aux chercheurs de développer des diodes électroluminescentes (DEL, en anglais light emitting diode 'LED') pratiques en 1962, lorsque Nick Holonyak [1] de General Electric a obtenu la première LED visible émettant une lumière rouge. Suite à cette découverte, les chercheurs ont continué à développer cette technologie en atteignant une plus large gamme de couleurs. En 1994, l'équipe de Nichia dirigée par Shuji Nakamura a obtenu la première LED bleue à haute luminosité en utilisant le nitrure de gallium (GaN) comme matériau semi-conducteur. Cette invention a permis de compléter le spectre d'émission visible, ce qui a ensuite permis d'obtenir de la lumière blanche en combinant la LED bleue avec du phosphore jaune, atteignant des rendements externes supérieurs à 70%. Shuji Nakamura, Hiroshi Amano et Isamu Akasaki sont les trois pionniers qui ont reçu le prix Nobel 2014 pour leur contribution à l'invention de la LED bleue.[2]–[4]

Au début des années 2000, ces LEDs blanches ont commencé à être commercialisées et ont remplacé les sources d'éclairage traditionnelles, telles que les ampoules à incandescence, en raison de leur meilleur rendement, de leur durée de vie plus longue et de leur moindre génération de chaleur. La technologie LED est en constante évolution et des applications plus innovantes sont développées, telles que l'éclairage automobile, l'éclairage général, les écrans et la purification de l'eau.

Au cours des mêmes années, les écrans à cristaux liquides (en anglais liquid crystal display 'LCD') ont suffisamment progressé pour devenir la technologie dominante dans les grands écrans, remplaçant les tubes à rayons cathodiques (en anglais cathode ray tubes 'CRT'). Malgré leur domination, les LCD nécessitent une unité de rétroéclairage car ils ne sont pas émissifs, ce qui limite leur flexibilité en termes de taille. Le développement des diodes électroluminescentes organiques (en anglais organic LED 'OLED') est donc apparu et a commencé à concurrencer les LCD dans de nombreuses applications d'affichage. Toutefois, les deux technologies présentent des avantages et des inconvénients. Par exemple, les LCD offrent un coût inférieur, une durée de vie plus longue et une luminosité plus élevée, tandis que les OLED sont auto-émissifs, offrent un meilleur contraste et sont plus flexibles en taille. Les deux technologies sont en cours d'amélioration pour surmonter leurs inconvénients.

Récemment, les chercheurs ont commencé à se tourner vers les micro-DELs (en anglais micro-LEDs 'μLED'), qui sont considérées comme les écrans de nouvelle génération. Les écrans μLEDs sont constitués de LED miniatures, de diamètre inférieur à 50 micromètres et pouvant descendre jusqu'à 1 μm[5]. Ces μLEDs sont disposées selon un motif quelconque pour créer un écran. Bien qu'elles en soient à leurs premiers stades de développement, les μLEDs se sont avérées compactes, fiables et capables d'offrir une densité de pixels élevée, une luminosité élevée et un rapport de contraste élevé.[6]

En effet, il existe une demande croissante pour diverses applications, telles que la réalité augmentée, les smartphones, les montres intelligentes et les téléviseurs, qui peuvent bénéficier de ces μLEDs en raison de leurs avantages sur les LCD et les OLED. Au début des années 2000, des chercheurs ont présenté un écran de μLED InGaN de 12 μm. Depuis lors, de nombreuses équipes de laboratoire et entreprises, telles qu'Apple, Google, Sony et Samsung, ont travaillé au développement de cette technologie. Par exemple, Samsung a présenté un téléviseur microLED de 146 pouces et Sony a créé un écran microLED à panneau plat pouvant atteindre 21 mètres sur 5,5 mètres.[7]

D'un point de vue théorique, les μ LED étaient censées avoir un meilleur rendement et une meilleure consommation d'énergie que les LCD et les OLED. Cependant, cela n'a pas encore été atteint en raison de la forte densité de défauts sur les bords des μ LED gravées, ce qui entraîne une recombinaison non radiative des porteurs. Plus le rapport périmètre/surface est élevé, moins la μ LED est efficace.

Depuis près de 20 ans, les LEDs à puits quantiques (PQ) InGaN/GaN sont utilisées dans le domaine de l'éclairage. Leur développement continu leur a permis d'atteindre un niveau de maturité suffisant pour être intégrées dans les micro-LEDs destinées aux applications d'affichage. Cependant, la fabrication des trois couleurs primaires (rouge, vert et bleu (RGB)) nécessaires à l'émission de lumière blanche présente encore plusieurs défis. En plus de la réduction de la taille des μ LEDs, une perte d'efficacité est observée lorsqu'on cherche à atteindre des émissions à plus longue longueur d'onde. Même sur les LED de grande taille, l'efficacité quantique externe diminue de 80% dans le bleu à près de 50% dans le vert [8], [9]. D'autre part, l'efficacité dans le rouge dépasse rarement 10% [10] car une composition plus élevée en Indium est nécessaire dans les PQ pour atteindre le rouge, ce qui génère plus de défauts en raison du désaccord de maille entre InN et GaN. Bien que l'on atteigne une meilleure efficacité dans le rouge en utilisant des LED de grande taille à base d'AlGaInP/GaInP [11], l'objectif est de fabriquer des pixels RGB sur le même semi-conducteur afin de faciliter le transfert de masse.

Les chercheurs ont tenté plusieurs approches en utilisant des puits quantiques InGaN/GaN pour atteindre des longueurs d'onde plus longues sans dégrader la qualité des micro-LEDs. L'une de ces approches consiste à utiliser différentes orientations cristallographiques du GaN. L'orientation la plus mature et la plus couramment utilisée est appelée orientation polaire, qui est également responsable de la limitation de performance mentionnée précédemment. Dans ce cadre de thèse, nous utiliserons donc du GaN semi-polaire ($10\bar{1}1$), qui peut offrir plusieurs avantages par rapport au GaN polaire pour améliorer les performances des μ LEDs pour les applications d'affichage et de micro-affichage.

L'orientation semi-polaire du GaN présente plusieurs avantages par rapport à l'orientation polaire pour la fabrication de μ LEDs :

- **Champ électrique interne réduit dans les puits quantiques:** L'orientation semi-polaire entraîne un champ électrique interne réduit dans les PQ, ce qui se traduit par une recombinaison plus rapide des électrons et des trous. Cela devrait permettre de réduire la perte d'efficacité à haute densité de courant par rapport aux orientations polaires. Même à faible densité de courant, la recombinaison rapide limitera la recombinaison non radiative des porteurs sur les bords des μ LEDs, améliorant ainsi l'efficacité.
- **Incorporation plus élevée d'indium :** L'orientation semi-polaire ($10\bar{1}1$) permet d'incorporer des concentrations d'indium plus élevées dans les PQ, ce qui permet d'atteindre des émissions à plus longue longueur d'onde. Ces longueurs d'onde plus longues sont cruciales pour obtenir les couleurs verte et rouge nécessaires à l'émission de lumière blanche.

Ces avantages de l'orientation semi-polaire sont particulièrement intéressants pour les applications d'affichage et de communication à base de μ LEDs. Cependant, d'un point de vue industriel, la croissance du GaN semi-polaire se fait généralement sur des substrats de saphir ou de silicium, ce qui entraîne une densité élevée de défauts en raison de la croissance sur des substrats étrangers.

Plusieurs études ont cherché à obtenir du GaN semi-polaire de haute qualité à faible coût. Dans cette thèse, nous nous inspirons des travaux de Mantach et al. [12] qui ont obtenu la plus faible densité de défauts en utilisant la technique de " aspect-ratio-trapping " (ART) sur un substrat silicium sur isolant (en anglais 'SOI') pour faire croître le GaN semi-polaire ($10\bar{1}1$),.

L'objectif de ce travail est donc de fabriquer des μ LEDs basées sur du GaN semi-polaire ($10\bar{1}1$) sur des substrats SOI en suivant l'approche de Mantach et al. [12]

La thèse est organisée en cinq chapitres décrits comme suit :

Chapitre I : Contexte

Le premier chapitre fournit une vue d'ensemble des concepts physiques essentiels pertinents à cette thèse et met en évidence les principes clés qui soutiennent ce travail.

Chapitre II : Croissance de GaN semi-polaire sur substrats SOI texturés

Le deuxième chapitre décrit le développement et l'optimisation de la structuration des substrats SOI en salle blanche PFP du CEA-LETI ainsi que la croissance du template de GaN semi-polaire ($10\bar{1}1$) réalisée au laboratoire CRHEA.

Chapitre III : Caractérisation structurale et optique des structures épitaxiales MPQ et LED

Le troisième chapitre traite l'investigation des propriétés structurales et optiques des structures épitaxiales des MQW et LED.

Chapitre IV : Fabrication de microLED GaN semi-polaires.

Le quatrième chapitre présente la conception et la fabrication du jeu de masques de photolithographie incluant tous les dispositifs nécessaires. Il décrit également le développement du procédé de fabrication des μ LEDs et la fabrication des dispositifs eux-mêmes.

Chapitre V : Caractérisation électro-optique des μ LEDs semi-polaires

Le cinquième chapitre présente la caractérisation électro-optique des μ LEDs semi-polaires fabriquées et établit une corrélation entre leurs caractéristiques et les propriétés des structures épitaxiales obtenues.

Objectifs et démarche de la thèse

Dans ce travail, notre objectif est tout d'abord de trouver les conditions optimales pour reproduire et améliorer les approches SOI-régulières et ART-SOI (**Figure 1.a**) mentionnées précédemment afin d'atteindre des densités de défauts similaires. L'étape suivante consiste à passer à la fabrication des dispositifs, en fabriquant des μ LEDs de taille réduite, jusqu'à $4 \times 4 \mu\text{m}^2$. Cela nécessitera de localiser les μ LEDs dans une zone exempte de défauts, entre les lignes BSF et les DT comme présentés dans la **Figure 1.b**.

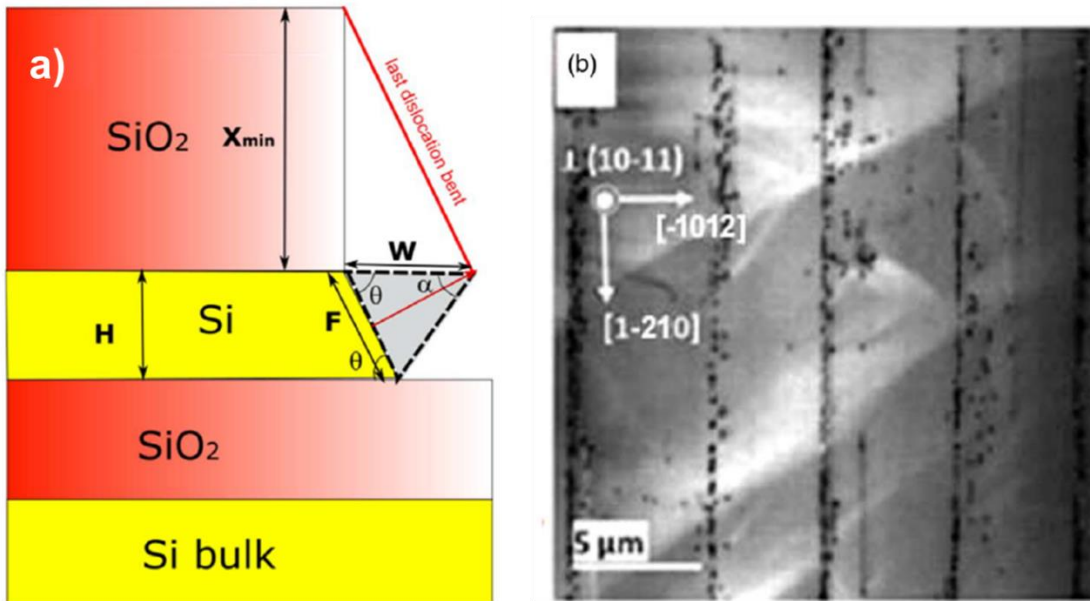


Figure 1: a) A schematic of the ART -SOI approach illustrating the dislocation bending. b) CL image at room temperature showing the TDs (black dots) along the coalescence line of the stripes. [12]

La fabrication d'une μ LED sur un substrat à haute qualité cristalline, en plus des avantages du GaN semi-polaire précédemment rapportés, ouvre la possibilité d'obtenir une μ LED haute performance et à haut rendement à des longueurs d'onde plus longues sur un substrat compatible avec l'industrie.

Chapitre II : Croissance de GaN semi-polaire sur substrats SOI texturés

Ce chapitre traite de la croissance de GaN semi-polaire sur des substrats SOI texturés, en s'appuyant sur les travaux de Mantach et al.

Dans un premier temps, nous avons présenté la méthode de croissance épitaxiale utilisée, en insistant sur l'approche de croissance par zone sélective. Cette technique permet un contrôle précis de la nucléation et de la croissance du GaN, ce qui est crucial pour obtenir des couches de haute qualité. Ensuite, nous avons détaillé les étapes de la structuration des substrats SOI par la technique ART. Cette technique permet de créer des motifs texturés sur la surface du silicium, ce qui favorise la croissance épitaxiale du GaN. Des substrats SOI structurés ont ensuite été utilisés pour étudier l'impact des conditions de croissance sur la formation des bandes de GaN et leur coalescence ultérieure. Cette étude a permis de déterminer les paramètres optimaux pour la croissance du GaN sur des substrats SOI texturés. Les paramètres de croissance optimisés ont ensuite été transférés aux substrats SOI ART. Cette étape a permis d'obtenir une croissance de GaN de haute qualité sur ces substrats texturés. La qualité du modèle final de GaN semi-polaire sur SOI a été évaluée par différentes techniques de caractérisation, notamment la microscopie électronique secondaire, la microscopie à force atomique, la spectroscopie de photoluminescence et la cathodoluminescence.

Conclusion de ce chapitre:

Les étapes de la structurations ont été adapté en se basant sur les résultats obtenus par Mantach et al. Après avoir reproduit leur travail, la qualité de la structuration a été améliorée, ce qui a permis d'améliorer la qualité de la croissance du template dans l'étape suivante.

Malgré les résultats obtenus par Mantach et al. sur la croissance du template, plusieurs difficultés ont été rencontrées lors de l'adaptation de leurs conditions, ce qui a conduit à développer et améliorer la croissance. Ce développement a été réalisé avec succès lors des premières campagnes de croissance sur des substrats SOI classiques, où divers paramètres de croissance ont été optimisés.

Après la première étape de croissance, des bandes de GaN uniformes et continues ont été obtenues malgré la différence de hauteur locale entre certaines bandes voisines, ce qui a conduit à la formation de motifs en chevron. De plus, en déposant la couche de SiO₂ inclinée avant la croissance d'AlN, et en passant du SOI classique à l'ART-SOI, une surface de GaN sans la présence du meltback etching après coalescence a été obtenue. En combinant du GaN non dopé et du GaN dopé au Si pour la coalescence 2D, des templates GaN sur SOI ART ont été obtenus avec une qualité structurale et optique assez bonne et une rugosité de surface relativement faible.

Malgré les efforts réalisés, il est possible d'améliorer encore la morphologie de surface du template GaN en utilisant un Si(001) à 7° hors axe, comme mentionné au chapitre I. Des wafers SOI avec Si(001) à 7° ont été fabriqués, mais la croissance de GaN n'a pas encore été effectuée.

Chapitre III : Caractérisation des structures épitaxiales PQM et LED

Le chapitre II décrivait le développement et l'optimisation d'un modèle GaN. Ce chapitre s'est concentré sur la croissance d'une structure LED. Pour obtenir des LED de bonne qualité épitaxiale, nous avons d'abord étudié la croissance de structures à puits quantiques multiples (PQM) sur deux réacteurs MOVPE au CRHEA.

Nous avons commencé par présenter les principales techniques de caractérisation utilisées pour étudier les structures PQM et LED. Nous avons ensuite exploré les paramètres de croissance des PQM et réalisé une caractérisation structurale et optique pour corrélérer l'impact des défauts structuraux sur la qualité optique des PQM et comparer les résultats obtenus avec les deux réacteurs. Enfin, nous avons détaillé et caractérisé la croissance des structures LED afin de préparer la fabrication des μ LED décrite dans le chapitre suivant.

Conclusion de ce chapitre :

Une comparaison de deux réacteurs de croissance a été réalisée sur deux lots de croissance de PQM. Les deux réacteurs ont présenté une morphologie de surface similaire à celle du template GaN, avec des ondulations, sans meltback etching et une faible rugosité. Un changement de température de croissance des PQM a montré un net décalage vers des longueurs d'onde plus longues pour les deux réacteurs. Cependant, l'utilisation du réacteur Aixtron a permis d'atteindre des concentrations plus élevées de dopant actif n et une meilleure uniformité d'épaisseur des PQM, comme observé par TEM. Des caractérisations optiques ont été menées sur différents échantillons de PQM pour étudier leur qualité. Les échantillons semi-polaires ont montré une efficacité quantique interne (IQE en anglais) décente, une stabilité de la longueur d'onde lors d'un changement de puissance d'excitation et une réponse de recombinaison plus rapide par rapport au GaN polaire. Ces résultats sont cohérents avec le faible champ électrique interne présent dans les orientations semi-polaires. Une caractérisation plus localisée a été réalisée sur un échantillon PQM rouge pour confirmer une émission rouge autour de 650 nm. La CL a mis en évidence l'effet de la morphologie en chevron sur l'émission de longueur d'onde. Enfin, une structure LED semi-polaire a été réalisée avec une morphologie de surface similaire à celle des structures PQM et une émission de longueur d'onde uniforme pour les deux réacteurs. Ces résultats ont constitué une démonstration de tous les éléments de base nécessaires à la fabrication

d'une structure épitaxiale LED semi-polaire, ce qui sera clé dans un avenir proche pour la réalisation de μ LEDs semi-polaires.

Chapitre IV : Fabrication de microLED GaN semi-polaires.

Ce chapitre présentait le développement et les progrès réalisés dans la fabrication de micro-LEDs (μ LEDs) tout au long de cette thèse.

Dans un premier temps, j'ai présenté une vue d'ensemble de la fabrication des dispositifs, en décrivant les étapes clés du procédé. Ensuite, j'ai présenté le jeu de masques de lithographie spécialement conçu pour contenir tous les dispositifs nécessaires à cette thèse. Des explications détaillées des différentes étapes du processus ont été fournies, accompagnées d'une discussion sur les défis rencontrés et les approches d'optimisation employées pour réaliser des μ LEDs à base de GaN semi-polaire.

Afin de valider la fonctionnalité du processus, des échantillons de GaN plan c ont également été traités. Enfin, les dispositifs fabriqués sur les deux orientations de GaN ont été caractérisés en conclusion de ce chapitre.

Conclusion de ce chapitre :

Ce chapitre présentait la fabrication et la caractérisation de micro-LEDs basées sur du GaN semi-polaire et polaire. Ces résultats constituaient une première démonstration de la viabilité du procédé développé. De plus, nous avons réussi à réaliser les premières μ LEDs semi-polaires bleues et vertes opérationnelles, avec une taille allant jusqu'à $4 \times 4 \mu\text{m}^2$.

L'objectif principal était d'évaluer la nécessité d'ajustements supplémentaires du procédé. Nous avons donc effectué des analyses préliminaires sur la qualité des contacts des μ LEDs en utilisant des structures TLMs linéaires. Ces analyses ont montré la présence de contacts Schottky sur les TLMs p et n, ce qui était attendu pour le type p. Une meilleure qualité de contact a été observée pour les TLMs n semi-polaires par rapport aux polaires, en raison d'une meilleure qualité de dopage.

Enfin, une étude a impliqué la réalisation des premières mesures I-V-L sur des échantillons de GaN semi-polaires et polaires. Les résultats ont montré des caractéristiques supérieures des LED polaires par rapport aux semi-polaires, ce qui pouvait être attribué à la structure épitaxiale des LED. Néanmoins, des micro-LEDs semi-polaires aussi petits que $4 \mu\text{m}$ étaient fonctionnels. Les différences observées pouvaient provenir de défauts ou de variations de la morphologie de surface des échantillons. Pour obtenir des informations plus approfondies, des investigations plus complètes sur les performances des μ LEDs semi-polaires seraient menées dans le chapitre suivant.

Chapitre V : Caractérisation électro-optique des μ LEDs semi-polaires

La caractérisation électro-optique des μ LEDs fabriquées était essentielle pour comprendre les principaux problèmes du dispositif et différencier ceux qui survenaient lors de la fabrication de ceux qui survenaient lors de l'épitaxie. Dans le chapitre IV, des mesures I-V ont été présentées sur des micro-LEDs polaires et semi-polaires. L'absence de fuite sur les dispositifs polaires confirmait un bon contrôle du processus. Cependant, la majorité des micro-LEDs semi-polaires fuyaient. Par conséquent, dans ce chapitre, nous avons étudié l'impact de la structure épitaxiale sur les performances et les caractéristiques de divers dispositifs. Ce chapitre s'est concentré sur la performance électro-optique des μ LEDs semi-polaires ($10\bar{1}1$) fabriquées.

Conclusion de ce chapitre :

Nous avons choisi de travailler avec les échantillons Aixtron plutôt que ceux de TS en raison du décalage de longueur d'onde de 20 nm observé sur ces derniers, principalement dû à l'hétérogénéité des PQM. Malgré les fuites observées sur la plupart des μ LEDs, limitant notre analyse, nous avons réussi à fabriquer des μ LEDs de taille $4 \times 4 \mu\text{m}^2$ situées entre les lignes de dislocations, comme prévu. Nous suspectons que les points de fuite observés sur certains μ LEDs pourraient être liés à des perturbations de croissance avec une discontinuité du nombre et de l'épaisseur des PQ. Une investigation du décalage de longueur d'onde bleu d'environ 7 nm détecté par les mesures μ EL a révélé qu'il était causé par le léger écrantage du champ électrique attendu dans cette orientation. En outre, nous avons observé une non-uniformité dans l'émission EL et une variation des zones d'émission en fonction de la tension appliquée. Enfin, nous avons démontré la fonctionnalité d'une μ LED dans un environnement matriciel et d'une μ LED semi-polaire RF avec une bande passante de modulation atteignant environ 1,4 GHz, ce qui était très prometteur pour les applications des μ displays et de la Communication par la lumière visible (en anglais visible light communication 'VLC').

Conclusion générale

Cette thèse présente la première réalisation de μ LEDs fonctionnelles à base de GaN semi-polaire sur des substrats SOI-ART. Les travaux présentés ont été menés conjointement par deux laboratoires principaux, le CEA-LETI et le CRHEA. La structuration et la fabrication des μ LEDs ont été réalisés au CEA-LETI, tandis que la croissance MOVPE a eu lieu au CRHEA. Les caractérisations structurales et électro-optiques des épitaxies et des dispositifs réalisés ont été effectuées dans les deux laboratoires.

Dans un premier temps, La structuration des substrats a été optimisé pour les SOI classiques et ART ayant le silicium supérieur à (001) 6° hors axe. Cette optimisation était cruciale pour améliorer la qualité de la croissance sélective ultérieure du GaN. Au CRHEA, nous avons utilisé une approche de croissance en deux étapes permettant d'obtenir des bandes pyramidales adjacentes uniformes et rapprochées dans un premier temps. Dans la deuxième étape, nous avons ajusté les conditions de croissance pour obtenir une couche de coalescence 2D sans la présence de meltback etching, une rugosité de surface relativement faible et une qualité optique élevée. Ceci a été réalisé en effectuant la coalescence avec du GaN à moitié non dopé et à moitié dopé n. Malgré l'utilisation de l'ART comme approche de blocage des dislocations, des dislocations ont été détectées au niveau du template, entre les lignes de coalescence. De plus, nous avons observé des motifs en chevron et des ondulations sur la surface.

Pour améliorer la qualité du template, nous avons suggéré l'utilisation de wafers SOI avec une désorientation de 7° au lieu de 6° pour mieux aligner l'orientation GaN semi-polaire. Cela pourrait améliorer la morphologie de la surface et éviter la formation d'ondulations et de chevrons. D'autre part, en ajustant les conditions de croissance des bandes pyramidales, on peut favoriser la courbure des dislocations aux premières étapes de croissance, ce qui réduit encore la densité de dislocations.

Deuxièmement, des structures PQM et LED ont été épitaxiées sur ces templates. Une émission PQM allant du turquoise au rouge a été obtenue en ajustant la température de croissance. Ces résultats ont montré la capacité d'atteindre des émissions de longueur d'onde plus longue en utilisant l'orientation semi-polaire. De plus, les échantillons PQM ont montré un taux de recombinaison rapide, une stabilité de longueur d'onde, un faible champ électrique interne comme prévu, et une efficacité quantique interne décente égale à 46% pour le PQM turquoise. On a observé un décalage bleu de la longueur d'onde sur les bords des chevrons et sur les ondulations présentes sur la surface, ce que nous espérons résoudre en utilisant le Si (001) 7° . De plus, la croissance de couches InGaN métamorphiques peut permettre d'atteindre des longueurs d'onde plus longues avec une meilleure qualité de structure.

Troisièmement, nous avons conçu et fabriqué un jeu de masques de lithographie comprenant des configurations spécifiques pour tester des dispositifs individuels de différentes tailles, l'impact des dislocations le long des lignes de coalescence, des μ LEDs en matrice et des μ LEDs RF. Nous avons ensuite développé un nouveau procédé de fabrication de μ LEDs sur des épitaxies LED GaN plan c, sans aucune fuite observée lors des mesures électro-optiques. Ce résultat a validé le procédé de fabrication par lequel nous avons réussi à fabriquer des μ LEDs semi-polaires fonctionnelles de $4 \times 4 \mu\text{m}^2$.

Enfin, nous avons réalisé différentes caractérisations électro-optiques sur les μ LEDs semi-polaires fabriquées, qui ont montré des fuites dans la plupart des dispositifs et un décalage bleu d'environ 7 nm. Nous suspectons que les fuites sont causées par l'épitaxie car nous avons identifié un point de fuite dans une zone où les trois PQM prévus se transforment en un seul PQ. D'autre part, le décalage bleu de la longueur d'onde observé est dû aux différentes zones émettant progressivement avec l'augmentation de la tension par EL, et à l'impact de l'écrantage du champ électrique restant. Malgré cela, nous avons réussi à obtenir de bonnes LED allant de $200 \times 200 \mu\text{m}^2$ à la plus petite μ LED sur GaN semi-polaire.

L'ensemble de ces résultats souligne des avancées encourageantes concernant l'incorporation d'indium et le faible champ électrique interne dans les structures à base de GaN semi-polaire. De plus, la reproductibilité potentielle de ces résultats sur des substrats de 200 mm ouvre la voie à la réalisation d'applications μ display RVB à couleurs natives. Enfin, la bande passante modulée élevée d'environ 1,4 GHz obtenue dans cette orientation répond aux besoins de domaines d'intérêt tels que les applications de communication.